Analyzing the Variations in Intensity-Duration-Frequency (IDF) Curves in the City of Saskatoon under Climate Change

By

Amin Elshorbagy, Alireza Nazemi, Md. Shahabul Alam

[1]Centre for Advanced Numerical Simulation (CANSIM), Department of Civil & Geological Engineering, University of Saskatchewan, Saskatoon, SK, Canada S7N 5A9

DISCLAIMER

This study, along with all results presented in this report and the accompanying Software tool, is based on a research conducted at the Centre for Advanced Numerical Simulation (CANSIM) in the Department of Civil and Geological Engineering, University of Saskatchewan. Part of this work was a result of an M.Sc. program of Md. Shahabul Alam under the supervision of Professor Amin Elshorbagy. The student, his supervisor (the principal investigator), and the co-investigator made every possible effort to adhere to good and widely acceptable practices of science and research with regard to the methodology adopted in this study. However, due to the nature of the study, the results and findings are subject to uncertainties due to various factors outlined in the study. The study aims at raising issues pertaining to climate change and bringing them to the attention of the city of Saskatoon. The use of the results reported here should be subject to the judgment, and solely on the responsibility, of the user.

EXECUTIVE SUMMARY

Intensity-Duration-Frequency (IDF) curves are among the standard design tools for various engineering applications, such as storm water management systems. The current practice is to use IDF curves based on historical extreme precipitation design values (quantiles). A warming climate, however, might change the extreme precipitation quantiles represented by the IDF curves, emphasizing the need for updating the IDF curves used for the design of urban storm water management systems in different parts of the world, including Canada.

This study attempts to construct the future IDF curves for Saskatoon, Canada, under possible climate change scenarios. For this purpose, LARS-WG, a stochastic weather generator, is used to spatially downscale the daily precipitation projected by Global Climate Models (GCMs) from coarse grid resolution to the local point scale. Ensembles of stochastically downscaled daily precipitation realizations were further disaggregated into ensemble hourly and sub-hourly (as fine as 5-minute) precipitation series, using a disaggregation scheme developed using the K-nearest neighbor (K-NN) technique. Another stochastic disaggregation method, developed within this study, was also employed to disaggregate the daily rainfall series into hourly resolution. This two-stage modeling framework (downscaling to daily, then disaggregating to finer resolution) is applied to construct the future IDF curves in the city of Saskatoon. By using the simulated hourly and sub-hourly precipitation series and the Generalized Extreme Value (GEV) statistical distribution, future changes in the IDF curves and associated uncertainties are quantified using a large ensemble of projections obtained for the Canadian and British GCMs (CanESM2 and HadGEM2-ES) based on three Representative Concentration Pathways (future climate change projections); RCP2.6, RCP4.5, and RCP8.5 available from CMIP5 – the most recent product of the Intergovernmental Panel on Climate Change (IPCC). The constructed IDF curves are then compared with the ones constructed using another method based on a symbolic regression technique, called genetic programming.

The results show that the sign and the magnitude of future variations in extreme precipitation quantiles in Saskatoon are sensitive to the selection of GCMs and/or RCPs, which seem to become intensified towards the end of the 21st century. Generally, the percentage change in precipitation intensities with respect to the historical intensities for CMIP5 climate models (e.g., CanESM2: RCP4.5) is less than those for the outdated CMIP3 climate models (e.g., CGCM3.1: B1), which might be due to the inclusion of climate policies (i.e., adaptation and mitigation) in CMIP5 climate models. The adopted framework enables quantification of uncertainty due to natural internal variability of precipitation, various GCMs and RCPs, and downscaling methods. In general, uncertainty in the projections of future extreme precipitation quantiles increases at shorter durations and for longer return periods. The two-stage method adopted in this study and the GP method reconstruct the historical IDF curves quite successfully during the baseline period (1961-1990); this suggests that these methods can be applied to construct IDF curves at the local scale under future climate scenarios. The most notable precipitation intensification in Saskatoon is projected to occur with shorter storm durations, up to one hour, and longer return periods of 25 years or more.

Compared to a historical (baseline) annual maximum precipitation (AMP) value of 117 mm/day for a 100-year storm, a maximum value of 144 mm/day is projected for the 2011-2040 period with CanESM2 and RCP2.6. Similarly, an intensity of 265 mm/hr for a 5-minute

historical storm with a 100-year return period is projected to increase to an intensity of 317 mm/hr for the 2011-2040 period with CanESM2 and RCP2.6, while an intensity of 275 mm/hr is projected for the same period with HadGEM2-ES and RCP2.6. During 2041-2070, the same historical storm is projected to intensify to values of 281 mm/hr and 381 mm/hr by RCP4.5 and RCP8.5, respectively, based on HadGEM2-ES. Compared to a 1-hr storm with a historical precipitation intensity of 84 mm/hr for a 100-year return period, an intensity of 140 mm/hr is projected for the 2071-2100 time period with the same GCM/RCP using the LARS-WG and K-NN-based downscaling-disaggregation method.

For improving the results of the research conducted in this study and for gaining more confidence in its recommendations, it is recommended that the current study be extended to include several other Global Climate Models (GCMs) available through CMIP5; improvement in the collection fine-resolution precipitation data at various gauges of the city; and dynamical downscaling methods using multiple regional climate models (RCMs).

ACKNOWLEDGMENT

TABLE OF CONTENTS

LIST OF FIGURES AND TABLES

1. INTRODUCTION

1.1. Background of the problem

The use of Intensity-Duration-Frequency (IDF) curves, which incorporate the frequency and intensity of maximum rainfall events of various durations, for design of hydrosystems is a standard practice in many places. The amounts of maximum daily and sub-daily rainfall values, similar to those represented by IDF curves, have shown increasing trends in many locations of the world including Canada (Arnbjerg-Nielsen, 2012; Denault et al., 2002; Waters et al., 2003). The frequency or the return period of a particular rainfall event (i.e., storm) is subject to change over time as a result of non-stationarity (Mailhot and Duchesne, 2010). The Intergovernmental Panel on Climate Change, IPCC (2012) concluded that the return period of a given Annual Maximum Precipitation (AMP) amount will decrease significantly by the end of the 21st century with extreme rainfall events occurring more frequently. For example, if an urban storm water collection system was designed 30 years ago based on the 50-year 10-min rainfall storm, the design might only satisfy up to 25-year design storm under non-stationary climatic conditions. Such conditions may significantly increase the vulnerability of urban storm water collection systems, which are associated with design-storm durations of less than a day and even less than an hour in many cases.

In the City of Saskatoon, the event of 24 June 1983 has been identified and selected as the design storm for the storm water retention ponds. However, the most recent rainfall events are not like the past as the total spring and summer rainfall in 2010, for example, is record breaking and is nearly 50% more than the previous maximum observed in 1920s. The wet summer of 2010, supported by other signs of possible climate change, emphasize the immediate need to revisit the design storm values in Saskatoon. Saskatoon's storm water collection system consists of minor and major sub-systems (City of Saskatoon, 2008). The minor systems are designed to withstand storm events of either 2 or 5-year return periods, whereas the major systems must control peak runoff situations of a 100-year return period. The City of Saskatoon, at present, uses the IDF curves based only on historical data up to 1986, assuming that the future will behave like the past. Recent studies reveal that extreme events might not be following the historical frequency.

Currently, there is no up-to-date study investigating the possible changes in the IDF curves and design storms in the city of Saskatoon under climate change or non-stationarity. The risk and rate of failure of systems designed using the historical design storms might be increased in face of non-stationary climatic condition (Mailhot et al., 2007; Adamowski et al., 2009). Characterization of the possible future changes in short-duration rainfall intensities faces several obstacles, and appropriate methods need to be developed for this purpose. First, the short-duration rainfall events in the Canadian prairies, which includes Saskatoon, are mostly convective during the summer months (Shook and Pomeroy, 2012). Global Climate Models (GCMs) are now the standard too to quantify the outcome of possible climate change scenarios in the future. GCMs have the ability to represent weather variables at coarse grid scale (usually greater than 200 kilometers). Therefore, GCM simulations might be insufficient to reproduce the rainfall for a small area (Olsson et al., 2009). Second, the outputs of GCMs for a given site and time period vary tremendously among various GCMs and representative emission scenarios. However, no GCM can be preferred without a detailed study (Semenov and Startonovitch, 2010).

Moreover, the outputs of GCMs are not available for durations shorter than a day in previous runs of GMs or several hours in case of the most recent runs. The uncertainty due to the choice of GCMs requires multi-model ensembles of climate projections with several modeling alternatives for characterizing the future rainfall events. Furthermore, hourly and even sub-hourly future rainfall scenarios are required for accurate modeling of the hydrological response of urban watersheds. Therefore, disaggregation of rainfall to fine temporal resolutions should be performed to assess the vulnerability of storm water collection systems in the City of Saskatoon with an estimation of uncertainty associated with the constructed IDF curves and the subsequent hydrological risks. *This study is part of a sole source project funded by the city of Saskatoon to fill the above-identified knowledge gap.*

The goal of this project is to construct the Intensity-Duration-Frequency (IDF) curves/design storms for the City of Saskatoon under climate change scenarios. The specific objectives are: (1) To inspect if there is any trend in Saskatoon's monthly, seasonal, and annual maximum rainfall across various durations from hourly to daily; (2) to evaluate the possibility of extending the historical trends into future and building a notion for future IDF curves; (3) to generate representative long time series of hourly and sub-hourly precipitation for the City of Saskatoon, during the baseline period and under projections of climate change scenarios; (4) To construct a set of potential future IDF curves for design purposes in Saskatoon; and (5) To assess and quantify the uncertainties in the constructed IDF curves.

This report is organized as follows: after the background presented in Section 1.1, the remainder of Section 1 summarizes some of the main methods and tools used worldwide for similar problems. The data and methods used in this study are presented and explained in details in Section 2, whereas the results and findings of the study are provided in Section 3. Finally, the conclusions and recommendations regarding future work are outlined in Section 4.

1.2. Solutions: Canada and worldwide

Understanding of the dynamics of hydrological processes and their impacts on urban storm water collection system requires a long record of fine resolution rainfall (Segond et al., 2006), but records of fine temporal and spatial resolution are often limited. Many regions have rainfall records at daily scale with limited hourly records. Obtaining sub-hourly rainfall records has become an important issue as climate change has been shown to cause increased rainfall intensities at fine temporal resolution in many parts of the world, including Canada (Waters et al., 2003). Global Climate Models (GCMs) have the ability to represent weather variables at coarse grid scale (usually greater than 200 kilometers), which is too coarse for climate change impact studies (Mladjic et al., 2011; Nguyen et al., 2008); especially in urban hydrology where the required scale is usually less than a few kilometers. The GCMs' outputs are usually downscaled to the local scale using various downscaling methods, for instance, weather generators, such as Long Ashton Research Station Weather Generator (LARS-WG; Semenov and Barrow, 1997) to obtain required information for impact investigations. Other possible downscaling methods include regional climate models (RCMs), regression-based methods, and weather typing methods. It is not uncommon that further disaggregation of downscaled precipitation to finer temporal scale (hourly and sub-hourly) is adopted. More details and discussion of the above-mentioned methods are provided in the sections below.

1.3. Global circulation models

Assessment of climate change is primarily based on Global Climate (or circulation) Models (GCMs). The GCMs are numerical models that can represent physical processes in the atmosphere, ocean, cryosphere, and land surface (IPCC, 2013). Currently, it is considered that the only scientifically sound way to predict the impact of increased greenhouse gas emissions on the global climate is through global scale simulation (Barrow, 2002). GCMs can simulate the responses of the global climate to increasing greenhouse gas concentrations (Taylor et al., 2012; Moss et al., 2010). GCMs are the most advanced tools currently available to climate research community thatcan incorporate the three dimensional nature of atmosphere and ocean simulating as many processes as possible. The coupling of atmosphere-ocean in GCMs (AOGCMs) is fully established with the inclusion of changes in biomes, atmosphere, ocean, and even soil chemistry (McGuffie and Henderson-Sellers, 2014). Global climate models with intermediate complexity are termed as Earth System Models (ESM).

Previously, the GCMs' simulations of climate variables based on three emission scenarios (A1B, A2, and B1) from Coupled Model Intercomparison Project Phase 3 (CMIP3) were commonly used. The Fourth Assessment Report (AR4) of the Intergovernmental Panel on Climate Change (IPCC) was supported by CMIP3 and the outputs of climate models included in CMIP3 were the basis of climate change impact studies conducted by the research community around the world since 2007 (IPCC, 2007; Taylor et al., 2012). The outputs of climate models from CMIP3 provided multi-model impact assessment comprehensively for climate change projections during the 21st century based on the IPCC Special Report's Emission Scenarios (SRES), i.e., A1B, A2, and B1. Scenarios describe plausible trajectories of the future climate conditions (Moss et al., 2010) and act as an appropriate analytical tool to assess the influence of driving forces on future emission results and associated uncertainties (IPCC, 2007). A1B, A2, and B1 scenarios represented "a rich world", "a very heterogeneous world", and "a convergent world", respectively (Nakicenovic et al., 2000). The models' outputs were contributed by some modeling centres and archived in the Program for Climate Model Diagnosis and Intercomparison (PCMDI: http://pcmdi9.llnl.gov/).

With the release of the Fifth Assessment Report (AR5) of the IPCC based on Phase 5 (CMIP5), a new set of GCMs' simulations was made freely available to the research community. CMIP5 climate models produce a comprehensive set of outputs with the inclusion of new emission scenarios, known as Representative Concentration Pathways (RCPs) (Moss et al., 2010; Taylor et al., 2012). With the introduction in September 2013 of AR5 based on CMIP5, updating the previous simulations of projected climate change based on CMIP3' climate models became a requirement. Generally, CMIP5 includes more than 50 sophisticated climate models (GCMs) from more than 20 modeling groups and a set of new forcing scenarios (Taylor et al., 2012). Examples of these GCMs includes: ACCESS1.0, BCC-CSM1.1, CanESM2, CESM1-BGC, CSIRO-Mk3.6.0, HadGEM2-ES, INM-CM4, MIROC-ESM, MRI-CGCM3 (CMIP5, 2013). The policy actions to achieve a wide range of mitigation were included in the RCPs aiming to have different radiative forcing targets by the end of the 21st century. The RCPs are denoted by the approximate radiative forcing (Wm^{-2}) they might reach by the end of the 21st century as compared to the year 1750. The values of radiative forcing represented by each RCP are indicative of the targets only by the end of year 2100. However, a range of 21st century climate

policies can be represented by the RCPs as compared with the no-policy AR4 emission scenarios. The relative projections due to AR4 and AR5 emission scenarios/RCPs are shown in appendix A.

The Integrated Assessment Models (IAMs) were used by the Integrated Assessment Modeling Consortium (IAMC) to produce the RCPs by considering various components, such as demographic, economic, energy, and climate (IPCC, 2013). Generally, IAMs combine a number of component models, which mathematically represent findings from different contributing sectors. IAMs are broadly of two categories: policy optimization models and policy evaluation models (Weyant et al., 1996); and policy alternatives for the control of climate change can be evaluated by combining technical, economic and social aspects of climate change in an IAM (Kelly and Kolstad, 1998).

1.4. Downscaling methods

Assessment of climate change is primarily based on outputs from GCMs, although the climate variables at the local scale – scale of influence for hydrological processes and infrastructure – show large differences when compared with those at the coarse scale of GCMs (Zhang et al., 2011; Hashmi et al., 2011). To overcome this problem, various downscaling approaches are usually used, and they are broadly of two categories: dynamical and statistical downscaling methods (Hashmi et at., 2011; Franczyk and Chang, 2009). A brief description of these downscaling methods is provided in the following sections.

1.4.1. Dynamical downscaling
Dynamical downscaling is performed by running Regional Climate Models (RCMs) of finer scales using the outputs of GCMs (Xue et al., 2014; Sharma et al., 2011) as boundary conditions. Originally, RCMs were developed as physically based downscaling tools; however, currently their use for simulating physical processes has been increased (Giorgi and Mearns, 1999). Examples of RCMs include Canadian regional climate model (CRCM), climate high resolution model (CHRM), Hadley center regional model (HadRM), regional climate model system (RegCM), and the Fifth Generation Pennsylvania State University/National Center for Atmospheric Research mesoscale model (MM5). Typically, the high resolution (10-50 km) RCMs are nested within the coarse resolution (typically greater than 200 km) GCMs for the purpose of dynamical downscaling, although the use of RCMs as a downscaling tool is computationally expensive.

Downscaling RCM outputs employs bias correction as biases in the GCMs' and RCMs' simulations restrict their direct use in climate change impact studies, which need what is known in the literature as "bias correction". In the simulations of RCMs, the biases could be due to the improper boundary conditions provided by the GCMs and lack of consistency in the representation of physics between GCMs and RCMs, and parameterizations of RCMs (Ehret et al., 2012). Out of many bias-correction methods available in the literature, the following list only provides a glimpse of the methods: correction of monthly mean (Fowler and Kilsby, 2007), delta change method (Hay et al., 2000; Olsson et al., 2012a), quantile-based method (Kuo et al., 2014; Sun et al., 2011). Biases in the output of RCMs may be overcome and /or reduced, if not fully, through reduction of bias by improving the model predictability, use of multi-model ensembles

of GCMs and/or RCMs (to estimate uncertainty bounds), and reduction of bias by processing the model output afterwards (Ehret et al., 2012). Fowler and Kilsby, 2007 applied simple monthly mean correction to the mean monthly precipitation from RCM (HadRM3H) and found it an effective method to estimate observed precipitation variability during the baseline period. They preferred this simple correction method to a complex quantile-based method (used by Wood et al., 2004) as a reasonable estimate of the observed climate variability was provided by the simple method with slight underestimation of the variability due to simplification of the method. However, the method used probability distributions for correcting model bias and assumed that they will remain stable over time, which may not be the case in reality.

Olsson et al. (2012a) demonstrated how precipitation from RCM projections can be further downscaled using the delta change approach to fine resolutions in time and space suitable for the impact assessment of climate change on urban hydrology. The delta change approach (also known as change factor) has been widely used and applied in climate change impact studies in many different ways, one of which is the multiplicative change factor. The multiplicative change factor (also called relative change factor) is the ratio between the future and the baseline simulations obtained from GCMs, which is then multiplied by the observed data (e.g., precipitation) to generate climate change scenarios of precipitation at the local scale (Anandhi et al., 2011). Kuo et al. (2014) concluded that the IDF curves constructed with bias corrected MM5 precipitation data using quantile-based method were consistent with the IDF curves at the rain-gauges in Edmonton. Sharma et al. (2011) used statistical downscaling method (SDSM) and a data-driven technique for downscaling the RCM data; and found that the further downscaled data were closer to the observed data than the raw RCM data.

1.4.2. Statistical downscaling
Statistical downscaling is based on the statistical relationship between the GCMs' outputs and the local scale observed data (e.g., precipitation) (Wilby et al., 1998). Statistical downscaling is classified into three sub-types: weather typing approaches, regression-based methods, and stochastic weather generators (Wilby and Wigley, 1997).

i. Weather typing approaches
Local meteorological data are categorized by weather type according to the patterns prevailing in the atmospheric circulation. Mean precipitation or the entire precipitation distribution is associated with a particular weather type of large-scale variables provided by GCMs. The downscaling method is founded on the relationships between the large-scale climate variables (predictor) and local scale observed weather variables (predictand). However, instead of creating continuous relationship between the variables, local scale climate variables (e.g., precipitation) are generated either by resampling from the observed data distribution conditioned on the atmospheric circulation patterns given by GCMs or by producing sequences of local scale weather patterns by Monte Carlo simulation method and then resampling from the observed data (Wilby and Dawson, 2004). To downscale a future daily precipitation event produced by a GCM, an analogous condition is searched in the observed data of climatic variables, and the local scale observed precipitation for the same event is selected as downscaled future precipitation. Generally, pressure fields produced by GCMs are used as predictors. So, weather types are classified using a classification scheme based on the pressure fields.

This weather typing downscaling method prevents the selection of an extreme precipitation event in future beyond the most extreme events in the historical records, only allowing the modification of the sequence and frequency of historical precipitation. However, the limitation can be overcome if the changes in the atmospheric circulation are considered along with changes in other atmospheric predictors (e.g., temperature, humidity) (Willems et al., 2012; Wilby and Dawson, 2004). Willems and Vrac (2011) compared the performance of weather typing downscaling method with that of quantile-perturbation based method (based on quantiles) in terms of changes in the IDF curves in Belgium. The changes in short-duration precipitation extremes were produced similarly by the two methods with the weather typing method using temperature as a large-scale predictor in addition to the atmospheric circulation.

ii. Regression-based methods
The regression-based methods are also known as transfer function methods, which involve developing relationships between the local scale (i.e., point station) variables (i.e., precipitation) and global scale (i.e., GCM) variables. Several studies used regression-based downscaling techniques, such as multiple linear regression (Wilby et al., 2002; Jeong et al., 2012), generalized linear models (GLM) (Chun et al., 2013; Yang et al., 2005; Chandler and Wheater, 2002), canonical correlation analysis (Busuioc et al., 2008; Von Storch et al., 1993), artificial neural networks (Schoof and Pryor, 2001; Hewitson and Crane, 1996), and genetic programming-based method (Hassanzadeh et al., 2014).

Artlert et al. (2013) used the SDSM, a multiple regression-based statistical downscaling model (Wilby et al., 2002), to establish relationship between the GCM-scale climate simulations and local scale precipitation characteristics. They analysed future precipitation characteristics based on the projected trends from the British GCM (HadCM3) and the Canadian CGCM3, which showed huge differences between the future precipitation projections. The differences in the future precipitation projections indicate a high uncertainty in the GCM-based climate simulations. The precipitation data obtained through downscaling are also uncertain, depending on the GCMs and downscaling methods used (Willems et al., 2012). Jeong et al. (2012) used a hybrid downscaling approach as a combination of a regression-based (multiple linear regression) and stochastic weather generation techniques to simulate precipitation at multiple sites in Southern Quebec, Canada. They found that the addition of stochastic generation approach to the multivariate multiple linear regression method improved the performance of downscaling daily precipitation from the Canadian CGCM3. The use of a hybrid downscaling approach can overcome the shortcomings of multivariate multiple linear regression and stochastic generation approach when they are used separately. Yang et al. (2005), and Chandler and Wheater (2002) used the GLM framework for generating daily precipitation sequences conditioned upon several external predictors, which offers superiority in simulating non-stationary sequences as the external predictors may have spatial and temporal variations.

Hewitson and Crane (1996) applied Artificial Neural Networks (ANNs) for learning the linkage between the atmospheric circulation produced by GCMs and the local scale precipitation. The ANNs were trained for each rain gauge station to predict daily precipitation values using the linkage learned by the ANNs. However, ANNs result in generalized relationships, which always predict the same precipitation for a given circulation. Chadwick et al. (2011) used ANNs to reproduce temperature and precipitation dynamically downscaled by nested RCM within a GCM

over Europe and concluded that ANNs were capable of reproducing the corresponding climate variables but missed high precipitation values over some mountain areas. The ANNs trained with only 1960-1980 data were not able to reproduce temperature or precipitation well for 1980-2000 or 2080-2100 periods, although the performance was improved by training ANNs using different time periods. The GP-based quantile downscaling (Hassanzadeh et al., 2014) using is a novel type of statistical downscaling methods because it maps the relationship between extreme precipitation (quantiles) at both global and local scale without having to generate the continuous precipitation record. GP has the advantage of producing explicit mathematical equations for the downscaling relationship.

iii. Stochastic weather generation
Quantification of the uncertainty due to internal natural weather variability based on stochastic weather generators has a number of applications in design and/or operation of many systems, such as, water resources systems, urban drainage systems, and land management changes (Srikanthan and McMahon, 2001). Historically, efforts were made to describe precipitation processes in constructing weather generators, since precipitation is the most critical climate variable for many applications, and very often, its value is precisely zero (Wilks and Wilby, 1999). The process of precipitation occurrence describes two states, wet and dry, which forces many weather generators to model separately the occurrence and intensity of precipitation (Wilks and Wilby, 1999).

The first statistical model for simulating the occurrence of daily precipitation was developed by Gabriel and Neumann (1962) using a first-order Markov chain model. They assumed that the probability of precipitation occurrence is conditioned only on the weather condition of the previous day, i.e., wet or dry. Later, the first-order Markov chain model of daily precipitation occurrence was combined with a statistical model (i.e., exponential distribution) of daily precipitation (with nonzero value) amounts by Todorovic and Woolhiser (1975). These initial models were constructed for the simulation of a single climate variable, generally daily precipitation, for hydrological analysis. The simulation of other climate variables (e.g., daily precipitation, temperature, and solar radiation) became possible using stochastic weather generators in the early 1980s, which were developed by Richardson (1981) and Racsko et al. (1991). Climate change increased interest in stochastic weather generators for stochastic simulation of local weather (Semenov and Barrow, 1997).

A stochastic weather generator is used to simulate daily time series of weather variables having statistical characteristics similar to the observed weather variables (Wilks and Wilby, 1999). Various tools (Semenov and Barrow, 1997; Wilks, 1999; Wilks and Wilby, 1999; Wilby and Dawson, 2007; Sharif and Burn, 2007; Hundecha and Bardossy, 2008; King et al, 2014) have been proposed as weather generators. Multiple regression models and stochastic weather generators are examples of the statistical downscaling techniques that are widely used (Wilks, 1992, 1999), since they are less computation intensive, easy to use, and efficient (Semenov et al., 1998; Dibike and Coulibaly, 2005). Hashmi et al. (2011) conducted a comparison between a multiple regression-based model (i.e., SDSM) (Wilby et al., 2002) and a weather generator (i.e., LARS-WG), which showed their (SDSM and LARS-WG) acceptability with reasonable confidence as downscaling tools in climate change impact assessment studies.

Two weather generators, LARS-WG and the Agriculture and Agri-Food Canada weather generator (AAFC-WG), were used by Qian et al. (2008) to reproduce daily extremes (maximum daily precipitation, the highest daily maximum temperature, and the lowest daily minimum temperature) over the period 1971-2000. Both weather generators were found to reproduce extreme daily precipitation values quite satisfactorily while LARS-WG was found to perform better in preserving the historical statistics (e.g., absolute maximum and minimum temperature, mean and standard deviation of precipitation) (Irwin et al., 2012). Chun et al. (2013) compared the downscaling abilities of LARS-WG and GLM-based weather generator (GLM-WG, Chandler and Wheater, 2002) using the climate variables during the baseline (1961-1990) and future (2071-2100) periods. GLM-WG, a stochastic precipitation model, was developed based on the GLM structure and two-stage precipitation model (first, modeling the sequence of wet/dry days using logistic regression and second, modeling the precipitation amount using gamma distributions, Coe and Stern, 1982). LARS-WG uses observed daily precipitation to generate synthetic daily precipitation series at a specific site (Semenov and Barrow, 2002), while GLM-WG simulates daily precipitation based on large-scale climate information at a particular time and location (Chandler and Wheater, 2002). In that particular study by Chun et al. (2013), both weather generators showed equal performance in simulating monthly and annual precipitation totals, while GLM-WG showed superiority in simulating annual daily maximum precipitations due to the information of large-scale climate used in GLM-WG.

Qian et al. (2004) and King et al. (2012) concluded that LARS-WG performed better in simulating daily precipitation but its performance in simulating temperature related statistics (e.g., absolute maximum and minimum temperature) was not adequate when compared to the corresponding performances of AAFC-WG, SDSM, and K-NN weather generator with Principal Component Analysis (WG-PCA). However, LARS-WG was found to perform well in simulating climatic extremes across Europe (Semenov and Barrow, 1997). The IPCC's Fourth Assessment Report (AR4) (Solomon et al., 2007) used multi-model ensemble, out of which 15 climate models have been incorporated in the new version (Version 5) of LARS-WG for climate projections. The model ensemble allows estimation of uncertainties associated with the impacts of climate change originating from uncertainty in climate predictions (Semenov and Stratonovitch, 2010).

Several studies, using LARS-WG for climate change impact assessment (Semenov and Barrow, 1997), suggested that LARS-WG can be used as a downscaling model with substantial confidence to conduct climate change impact assessment by extracting site-specific climatic characteristics (Hashmi et al., 2011; Semenov and Stratonovitch, 2010; Qian et al., 2008; Semenov and Barrow, 1997). LARS-WG can be used to generate synthetic daily precipitation data by calculating site-specific weather parameters from observed daily data of at least 20 years (Semenov and Barrow, 1997). The LARS-WG is capable of producing daily climate scenarios for the future at the local scale based on the GCMs' predictions and emission scenarios, providing the means for exploring the uncertainty in climate change impact assessment (Semenov and Stratonovitch, 2010).

LARS-WG was adopted for this research as a stochastic weather generator tool to simulate climate data (e.g., temperature, precipitation) in Saskatoon, Canada, during the baseline period and under future climatic conditions. Since LARS-WG was used for simulating daily

precipitation series in this study. The simulated data are in the form of synthetic daily time-series having similar characteristics to the observations. LARS-WG provides a computationally inexpensive platform for generating daily future climate data (e.g., temperature, precipitation) of many years under the projections of climate change scenarios, which are of spatial and temporal resolution suitable for local scale climate change impact studies. LARS-WG can reproduce changes in the mean climate and in the climate variability at the local scale. The first version of LARS-WG was developed in 1990, while the latest version was developed in 2002 incorporating series approach (Racsko et al., 1991), which in this context means that the weather generation begins with the simulation of wet/dry spell length and then the precipitation amount is modelled (Semenov and Barrow, 2002). The performance of LARS-WG was compared with the performance of another popular stochastic weather, WGEN (Richardson, 1981), over several sites with diverse climates and was found to perform as well as WGEN (Semenov et al., 1998).

The weather generation process in LARS-WG is based on semi-empirical distribution (SED), which is defined as the cumulative probability distribution function describing the probability that a random variable X with a given probability distribution takes on a value less than or equal to x. The semi-empirical distribution is represented by a histogram with 23 semi-closed intervals, $[a_{i-1}, a_i)$, where a_{i-1}, a_i indicates the number of events in the observed data in the i-th interval and i=1,2,……..,23. The values of the events are selected randomly from the semi-empirical distributions, where an interval is selected first using the fraction of events in every interval as the probability of choice and subsequently a value is chosen from that interval using a uniform distribution. SED provides a flexible distribution with a possibility to approximate a wide range of shapes through adjustment of the intervals, $[a_{i-1}, a_i)$. The choice of the intervals, $[a_{i-1}, a_i)$ is dependent on the weather variable type; for example, the intervals are evenly spaced in case of solar radiation, while the interval size is increased with the increase in i for the wet/dry spell lengths and for precipitation in order to restrict the use of very coarse resolution intervals for extremely small values (Semenov and Stratonovitch, 2010; Semenov and Barrow, 2002). The steps for generating daily precipitation time-series using LARS-WG are provided with in appendix B.

1.5. Rainfall disaggregation

To overcome the lack of high-resolution temporal and spatial precipitation data crucial for hydrological, meteorological, and agricultural applications, disaggregation of available data from one temporal and spatial scale to another seems to be the most efficient alternative (Sivakumar et al., 2001). Several disaggregation techniques exist in water resources literature enabled the generation of high-resolution temporal and spatial precipitation data using the widely available daily precipitation data. The disaggregation techniques include Bartlett-Lewis rectangular pulse model (Rodriguez-Iturbe et al., 1987, 1988; Khaliq and Cunnane., 1996; Bo et al., 1994), Generalized linear model (GLM) (Chandler and Wheater, 2002; Segond et al., 2006), the Multifractal cascade process (Shook and Pomeroy, 2010; Lavellee, 1991), the Chaotic approach (Sivakumar et al., 2001), and non-parametric methods such as, Artificial Neural Networks (Burian et al., 2000), and K-nearest neighbor (K-NN) technique (Lall and Sharma, 1996; Yates et al., 2003; Sharif and Burn, 2007; Buishand and Brandsma, 2001). In this study, downscaling refers to the generation of daily precipitation time series at the local scale using the daily precipitation series at the global scale, while disaggregation refers to the generation of

precipitation series from the coarse temporal scale to the fine temporal scale (e.g., transforming daily precipitation to hourly and to sub-hourly).

Yusop et al. (2013) and Abdellatif et al. (2013) used Bartlett Lewis Rectangular Pulse (refer to Rodriguez-Iturbe et al., 1987, 1988 for details) model to disaggregate daily precipitation into hourly precipitation. Segond et al. (2007, 2006) and Wheater et al. (2005) used GLM to simulate daily precipitation while the Poisson cluster process was used as a temporal disaggregation method to generate precipitation at finer resolutions (i.e., hourly). Lu and Qin (2014) used an integrated spatial-temporal downscaling-disaggregation approach based on GLM, K-NN, and MudRain (Koutsoyiannis et al., 2003) methods to evaluate future hourly precipitation patterns in Singapore. Olsson (1998) and Rupp et al. (2009) used cascade model for disaggregation of daily precipitation to hourly precipitation. Burian et al. (2000) implemented a disaggregation model in ANNs for the disaggregation of hourly precipitation to sub-hourly time steps (15 minutes). The ANN disaggregation model performed better, in obtaining the maximum depth and the time of 15-min precipitation, when compared with two empirical precipitation disaggregation models developed by Ormsbee (1989). It was not clear whether the ANN disaggregation model was able to preserve the historical statistics, specifically the variance of the historical precipitation.

Yates et al. (2003) developed and applied a non-parametric weather generator based on K-NN for the simulation of regional scale climate scenarios. Sharif and Burn (2007) made an improvement of the K-NN based weather generator, developed by Yates et al. (2003), by adding a random component in order to obtain precipitation data beyond the range of historical observations; which is important in simulating the hydrologic extremes (Irwin et al., 2012). Prodanovic and Simonovic (2007) used the improved K-NN based weather generator, developed by Sharif and Burn (2007), to simulate daily precipitation, and the same approach was used to disaggregate daily precipitation to hourly precipitation. The K-NN technique is a non-parametric method and easy to implement. Resampling from observed data forms the foundation of the method that enables the disaggregated precipitation data to preserve the statistical characteristics of the observed data with high likelihood (Prodanovic and Simonovic, 2007). The ability to preserve statistical characteristics of the observed data makes it a feasible approach to be adopted in this study to disaggregate precipitation data from daily scale to hourly and sub-hourly scale.

The K-NN technique is a form of nearest neighbour (NN) search, which is also known as closest-point or similarity or proximity search, whose aim is to identify the most similar or closest points to the point of interest. The similarity or closeness is measured by Euclidean or Mahalanobis distance or other distance metrics (Elshorbagy et al., 2000). The more similar the points, the closer they are to the point of interest. K-NN technique can be defined as follows: if a space S contains a set P of points and a point of interest k is k ∈ S, the K-NN finds the closest points (measured by the distance metrics) to k in P (Liu, 2006).

The days in the historical time series for which the observed weather variable is similar to the simulated weather variable of a given day are known as nearest neighbours. Generally, the K-NN technique involves finding K similar or closest points to the point of interest. K-NN wasoriginally used for pattern recognition; which was later demonstrated as a resampling (i.e., bootstrap) method by Lall and Sharma (1996). The resampling approach based on K-NN was extended to a stochastic weather generator for a single (Rajagopalan and Lall, 1999) and for

multiple sites (Yates et al., 2003; Buishand and Brandsma, 2001), which was further improved by Sharif and Burn(2007) as perturbation of historical data enabled extrapolation of weather data beyond the historical record. The method developed by Sharif and Burn (2007) was further adopted by Prodanovic and Simonovic (2007) for the disaggregation of precipitation from daily to hourly time scale. The K-NN technique was adopted in this study for temporal disaggregation of daily precipitation to hourly and sub-hourly scales.

2. DATA AND METHODS

This section provides a description of the study area, the precipitation data used for developing the two-stage downscaling-disaggregation method, trend analysis, and the methodology followed for conducting the modeling and the analysis needed to achieve the study objectives. The model development and analysis consist of two consecutive steps: (1) downscaling of daily precipitation from the coarse GCMs' scale (i.e., gridded precipitation) to the local scale (i.e., point/gauged precipitation); and (2) disaggregation of daily precipitation to hourly and subsequently to sub-hourly (i.e., 5-min) precipitation at the local scale. LARS-WG, the stochastic weather generator, was the main downscaling method used in this study. A method based on the K-nearest neighbour (K-NN) technique, previously used to disaggregate daily precipitation to hourly time scale and adopted in this study with few modifications for the disaggregation of precipitation from daily to hourly and subsequently, to sub-hourly (i.e., 5-minute), is presented in this section. The section also includes a description of the Generalized Extreme Value (GEV) distribution used for the construction of IDF curves in Saskatoon.

2.1. Data preparation

The Canadian Prairies are characterized by the grassland, numerous lakes, and relatively flat landscape. Relatively wet summer months and dry winter months are not uncommon in the region based on seasonal precipitation totals during 1961-2003 from four sites at Calgary, Banff, Saskatoon, and Winnipeg (Chun et al., 2013). The amount of annual precipitation in the prairies is generally less than 500 mm, since these provinces are too far away to receive cyclonic precipitation originated from either the west or the east coast (Gan, 2000). Approximately, 30% of the annual total precipitation occurs in the form of snowfall in the Canadian prairies including Saskatchewan. Saskatoon (106.70 W, 52.20 N, and approximately 218 km^2) is the largest city in Saskatchewan located on the banks of South Saskatchewan River (SSR) with mean annual precipitation amount of 352 mm during 1961-2003 according to the daily precipitation records available through the Canadian Daily Climate Data (CDCD) portal (www.climate.weatheroffice.gc.ca) and 421 mm according to the adjusted precipitation data available through the Adjusted and Harmonized Canadian Climate Data (AHCCD) data portal (http://www.ec.gc.ca/dccha-ahccd/). The SSR basin expects to observe extreme precipitation events more frequently under climate change (Martz et al., 2007). A study of daily precipitation during 1950-2009 showed increasing trend in the AMP in Saskatoon (Nazemi et al., 2011). However, data only up to 1986 were included in the construction of the current IDF curves; which are currently used for the design of storm water collection system in Saskatoon. The study area selected for this research, the City of Saskatoon, is shown in Figure 1.

The observed daily precipitation data at Saskatoon Diefenbaker Airport station during the baseline period (1961-1990), measured by Environment Canada (EC), were considered for the calibration and validation of the employed weather generator (LARS-WG). The data are freely available through Environment Canada's official website (climate.weather.gc.ca) for the entire baseline period after the data have been reviewed through quality control, which is done for majority of the Environment Canada's observed data. The daily precipitation data, in combination with observed hourly precipitation data (obtained from Environment Canada) for the months of April-September (1961-1990), were used in developing a model for the

disaggregation of precipitation from daily to hourly time scale. The City of Saskatoon operates tipping bucket rain gauges in the city to measure sub-hourly rainfall to capture the spatial variability of the fine temporal resolution rainfall in the city. The sub-hourly rainfall data from the rain gauges in Saskatoon between April-September were pre-processed and aggregated to obtain rainfall of 5-minute resolution. In this study, the 5-minute precipitation data at various city
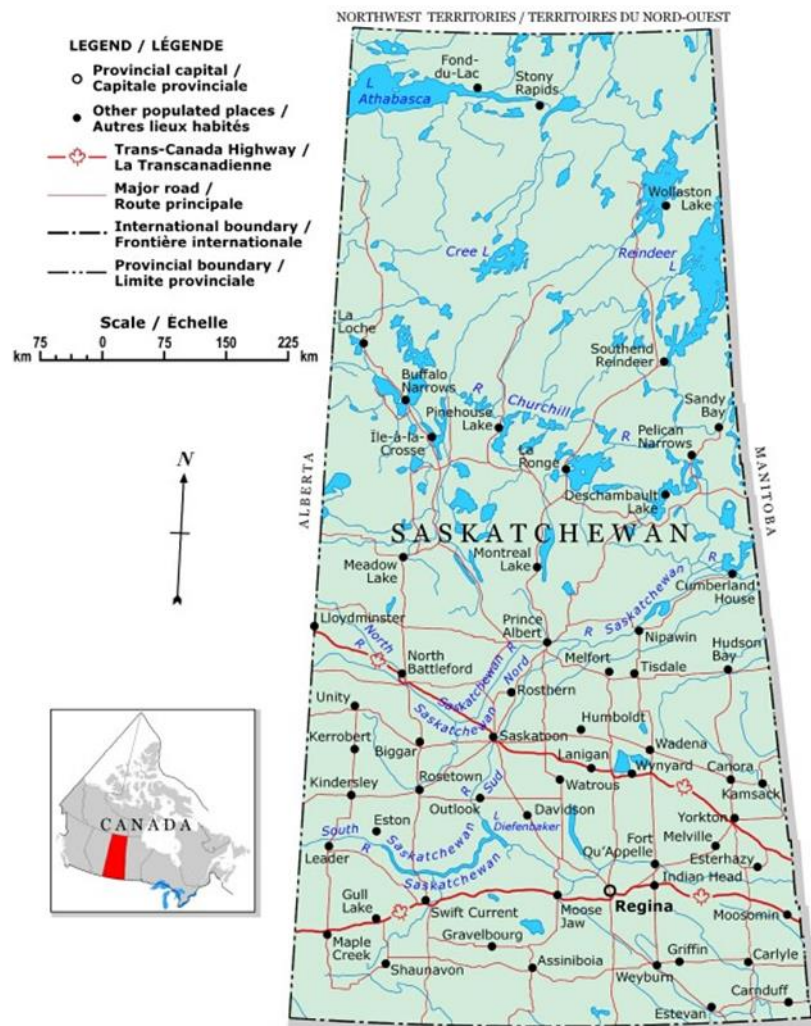
Figure 1. Location of the study area (Saskatoon, SK).

gauges were analyzed for consistency and length of records. The analysis showed that the sub-hourly rainfall recorded at Acadia Reservoir (shown as Acadia in Figure 2) rain gauge has the longest record (1992-2009), and it is more consistent with the Environment Canada's daily precipitation. However, there are missing data during the period of 2002-2004.

The 5-minute rainfall data recorded at Acadia Reservoir rain gauge were used in developing a model for the disaggregation of precipitation from hourly to the sub-hourly time scale in this study. Details of the precipitation consistency analysis are included in appendix C.

Figure 2. Location of rain gauges in Saskatoon (Source: City of Saskatoon).

The observed daily and hourly precipitation records at Saskatoon's Diefenbaker Airport station during 1961-1990 are plotted in Figure 3. The observed daily record contains precipitation data from January to December, while the observed hourly record contains rainfall data from April to September in each year. The hourly rainfall data were recorded during those months of the year only and made available to this study.

The observed daily and hourly precipitation record at the Saskatoon's Diefenbaker Airport station during 1961-1990 are described by the statistics presented in Table 1. Both the daily and hourly observed precipitation records are positively skewed. The annual mean precipitation amount is consistent with the precipitation characteristics in the prairie region, typically less than 500 mm.
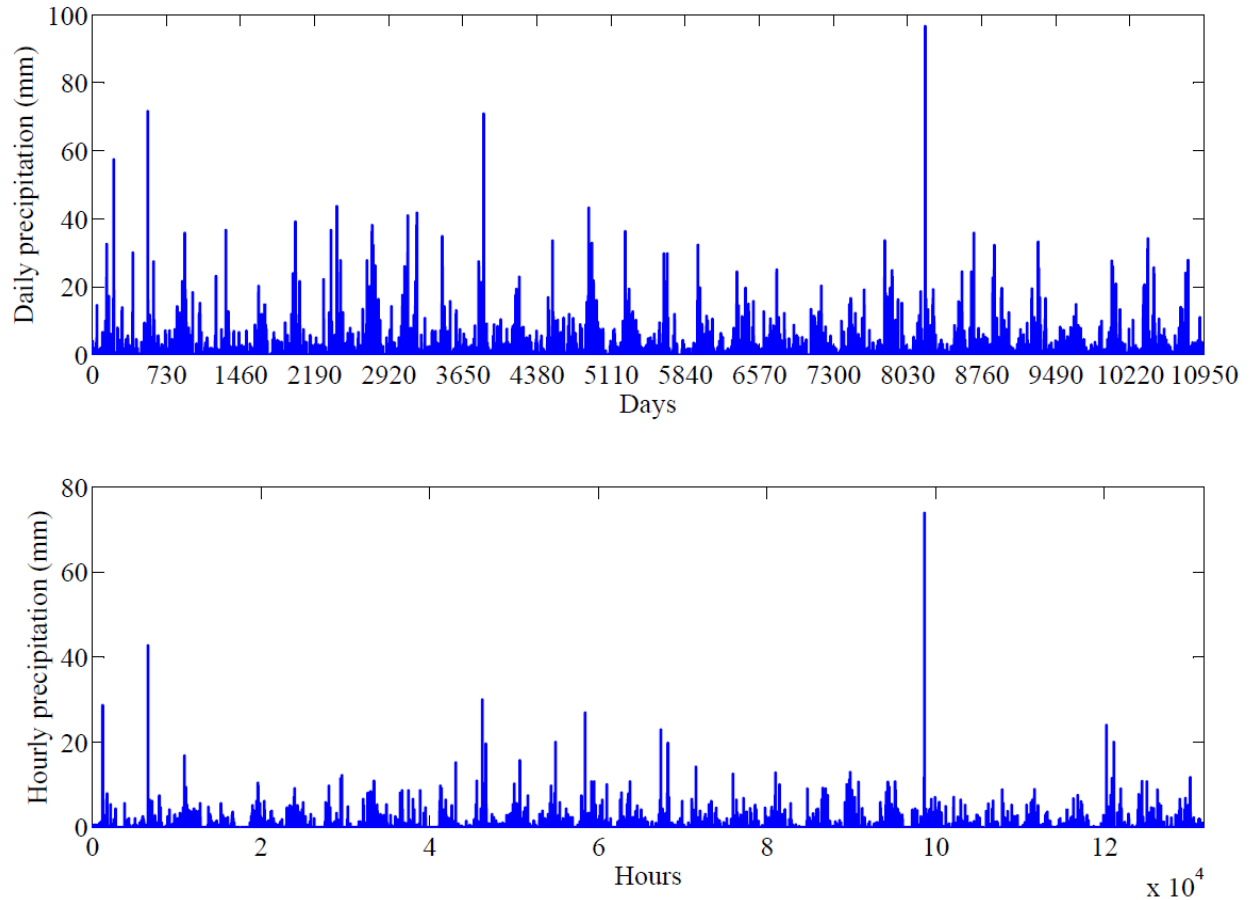
Figure 3. Observed daily (upper panel) and hourly (bottom panel) precipitation at Saskatoon's Diefenbaker Airport station during 1961-1990 (Source: Environment Canada).

Table 1: Statistics of the observed daily and hourly precipitation at Saskatoon's Diefenbaker Airport station during 1961-1990

Statistic	Daily record (Jan-Dec)	Hourly record (Apr-Sep)
Mean (mm)	0.95	0.05
Standard deviation (mm)	3.35	0.51
Coefficient of variation	3.53	9.98
Skewness	8.99	42.47
Annual mean (mm)	346.61	224.92
Maximum (mm)	96.60	73.90

2.2. Trend analysis

The most commonly addressed form of non-stationarity in hydroclimatic variables is the existence of monotonic trends. Trends in monthly, seasonal, and annual maximum precipitations (MMPs, SMPs, and AMPs, respectively) can portray significant changes in dynamics of extreme rainfall over time. Here the objectives of this section are (1) to inspect if there is any trend in Saskatoon's MMPs, SMPs, and AMPs across various durations from hourly to daily; (2) to evaluate the possibility of reconstructing the historical IDF curves using fitted trend models; and (3) to evaluate the possibility of extending the historical trends into future and building a notion for future IDF curves.

2.2.1. Methodology
Various methods are available in the literature to inspect significant trends in the data. Here we used simple linear regression and the Mann-Kendall non-parametric test with Sen's slope to inspect the significant trends in MMPs, SMPs, and AMPs across various durations. In simple linear regression, the evolution of data X over time can be described by a constant term, a temporal term, and a residual term. If the temporal term is significant at a specific confidence level, then there is a significant linear trend over time. The fundamental assumption of linear regression is the existence of independent and identically distributed residuals in the form of a white noise (i.e. normal distribution with zero mean). If this fundamental assumption is violated, then the results might not be reliable and extending the results into future is not justified – see the details in Chapter 12 of Helsel and Hirsch (1992).

We also used the popular Man-Kendall non-parametric trend test (Mann, 1945; Kendall, 1975). This 1-sample statistical test is a tool for determining if the central values in a time series tend to monotonically change within a time sequence or not – see the details in Chapter 12 of Helsel and Hirsch (1992). This test has been widely used in the literature to diagnose non-stationarity in hydroclimatic variables (e.g. Hirsch et al., 1982; Burn, 1994; Lettenmaier et al., 1994; Burn and Elnur, 2002). As Mann-Kendall test is a non-parametric test, test results do not depend on the distribution of the data and/or residuals; however, it can be affected by the possible autocorrelation in the time series (von Storch and Navarra, 1999). We investigated the existence of autocorrelation in Saskatoon's MMPs, SMPs, and AMPs and realized that the lag 1 auto-correlation is significant across various durations. This was considered in model development – see Table 2 below. The null hypothesis of Mann-Kendall test is rejection of trend in the data at a particular significance level, with the alternative hypothesis that the trend is significant. Trend tests are often accompanied by slope estimates, which determine the sign and magnitude of existing trends. Here we used the Sen's slope estimator, which selects the median slope among all lines through data samples. Sen's slope estimator is a robust method for linear regression and has been frequently used in quantifying trends in hydroclimatic variables (Cunderlik and Burn, 2003; Walvoord and Striegl, 2007; Hodgkins and Dudley, 2007; Klaus et al., 2014).

2.2.2. Data and modeling procedure
We considered Environment Canada's hourly rainfall total from 1960 to 1992, measured at Saskatoon's Diefenbaker airport and extracted 1-hour to 24-hour monthly maximum precipitation (MMPs) (i.e., April, May, June, July, August, and September), SMPs (Spring and Summer) and AMPs in Saskatoon. We were not able to extend the trend analysis to finer

durations (i.e. hourly and less) as the period of sub-hourly data is not sufficient for a reliable trend analysis. For the purpose of our analysis, we used both original and lag-transformed data. Combining these with two methods of trend analysis provides four models for inspecting monotonic evolutions of MMPs, SMPs and AMPs in each time duration – see Table 2.

Table 2. Models of trend analysis considered for inspecting the monotonic evolution in Saskatoon's monthly, seasonal, and annual maximum rainfall.

ID	Data/method	Formulation
L1	Original data/ linear regression	$X(t) = a + b \times t + \epsilon(t)$
L2	Log-transformed/linear regression	$\log\{X(t)\} = a + b \times t + \epsilon(t) \rightarrow$ $X(t) = e^{a+b\times t+\epsilon(t)}$
S1	Original data/Sen Slope	$X(t) = a + b \times t + c \times X(t-1) + \epsilon(t)$
S2	Log-transformed/ Sen Slope	$\log\{X(t)\} = a + b \times t + c \times \log\{X(t-1)\} + \epsilon(t) \rightarrow$ $X(t) = e^{a+b\times t+c\times\log\{X(t-1)\}+\epsilon(t)}$

2.2.3. Results and discussion
i. Inspected trends and associated significance levels

Figures 4 to 7 show the results of trend analysis using L1, L2, S1, and S2, respectively. Each figure contains two panels. Panel (a) shows the signed monotonic trends (mm/day/year or log((mm/day)/year); whereas panel (b) represents associated *p*-values obtained from the Mann-Kendall test. These *p*-values highlight the significance of trend. Higher *p*-value mean lower significance of the trend. For instance a *p*-value of 0.9 means that the there is only 10% chance that the identified trend is significant. In each panel, the horizontal axis is related to rainfall duration (i.e., 1-hr to 24-hr) and the vertical axis represents the period in which maximum rainfall is calculated (from bottom, April – A, May – M, June – J, July – J, August – A, September – S, Spring – SPR, Summer – SUM as well as Spring and Summer – Year). Slopes and p-values are shaded using the color schemes shown on the right side of each panel. In general, the estimated trends are dependent on the model considered for analyzing the trend. For instance, while L1 mainly shows decreasing linear trends; slope estimates obtained from S1 model are mainly positive. Similar argument can be made for L2 and S2. While L2 shows consistently decreasing trends in all spring months, S2 shows increasing trend in May. Regardless of these differences, associated *p*-values in all models do not confirm existence of any strong trend. None of the models shows significant trends at the 90% confidence level or higher in any of the considered durations.
.
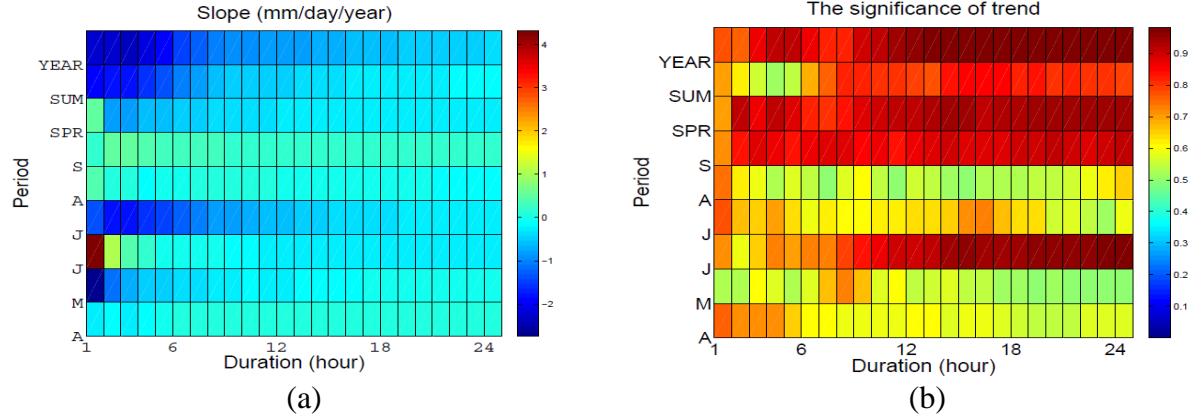
Figure 4. The results of trend analysis based on model L1; a) linear trends in original data; b) *p*-values associated to trend.
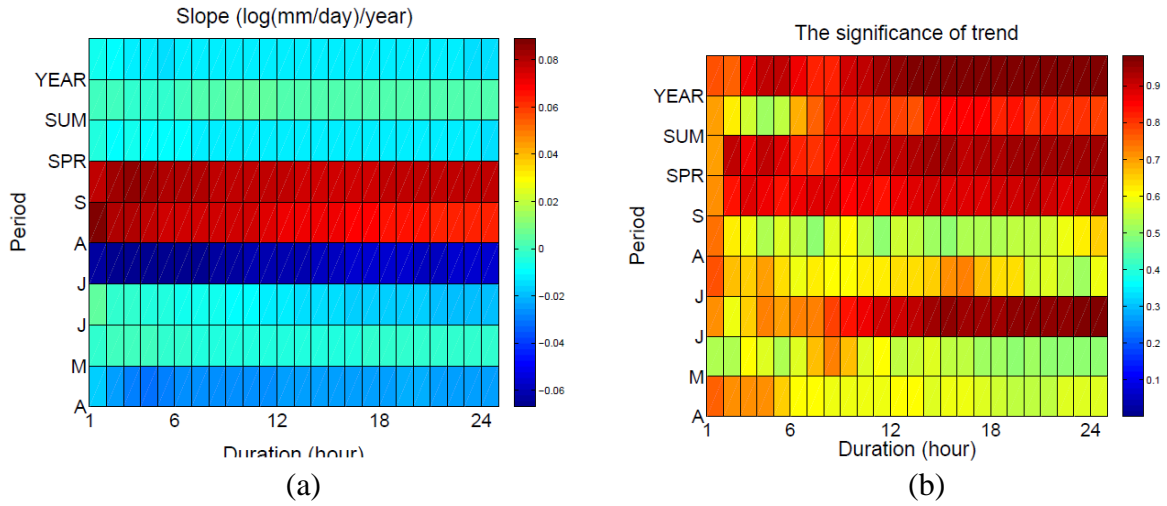
Figure 5. The results of trend analysis based on model L2; a) linear trends in log-transformed data; b) *p*-values associated to trend.
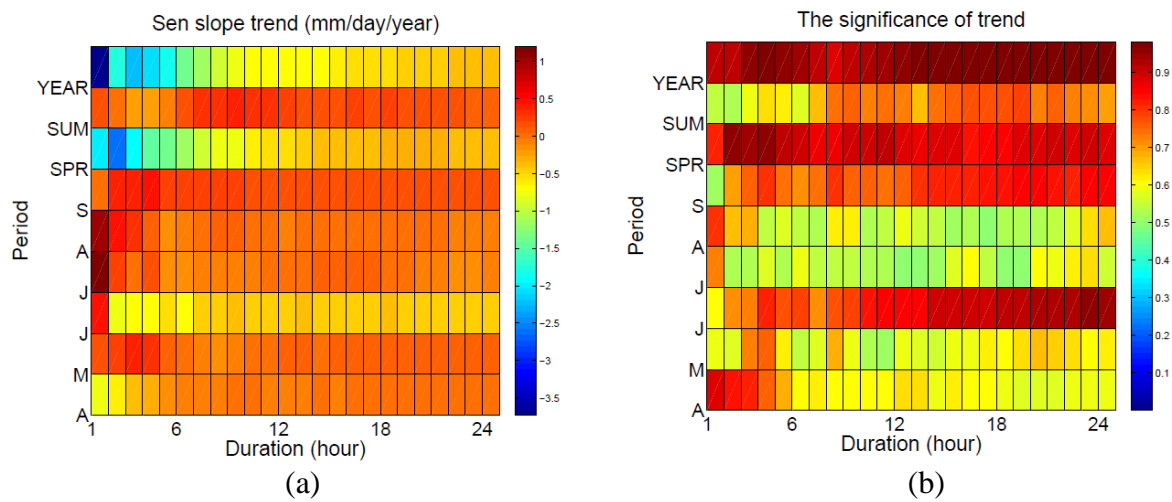
Figure 6. The results of trend analysis based on model S1; a) Sen's slopes in original data; b) *p*-values associated to trend.
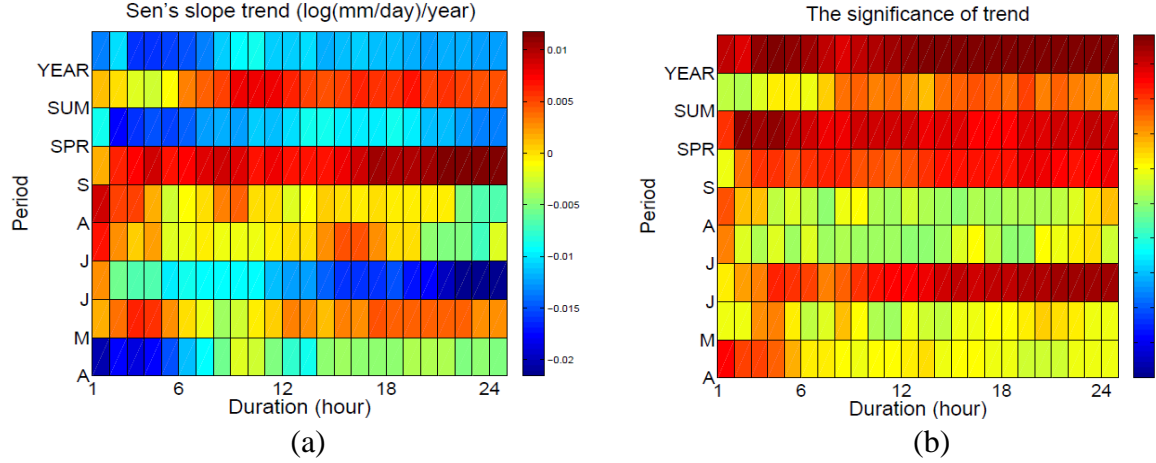
Figure 7. The results of trend analysis based on model S2; a) Sen's slopes in log-transformed data; b) *p*-values associated to trend.

In order to provide a better look at the feasibility of considered models, we visualized the fitted trends and associated residuals for AMPs across various durations. The fitted trends and associated residuals are obtained based on the considered models (L1, L2, S1, and S2, respectively). Figures G1 to G5 (Appendix G) show this analysis. We noticed that both L1 and L2 deviate from the assumption of identically distributed normal error terms. These models can be, therefore, falsified without further consideration. Models S1 and S2 do not require this assumption; however lower bound limits in S1 approach to negative values and therefore falsify the physical constraint of precipitation (i.e., rainfall cannot be lower than 0). S2, therefore, can be considered as the only non-falsified model, and is discussed further here. Based on S2 (see Figure 7), there are weak decreasing trends in months April, June (except 1-hr duration) and in general in the spring. Trends in summer months are, in contrast, increasing but with weak significance. Considering AMPs, there are weak decreasing trends. Regardless, it should be noted that variability in AMPs are increasing substantially with time - see also figure G4. This can provide conditions in which AMPs increase over time although the central tendency is to decline.

ii. Reconstructing the historical IDF curves using model S2
By considering the extracted Sen's slopes and associated lower and upper error bounds, various realizations for AMPs across different durations can be obtained by generating random error terms. We generated 100 realizations for random errors with the same length as the original data and considered them in model S2 to generated 100 realizations of AMPs during 1960 to 1992. Figure 8 shows the generated AMP realizations, in which the error in random realizations is more in short duration AMPs. It is again clear that the variability in AMPs increases by time, which can provide conditions in which the AMPs increase, despite declining trend. We further extracted the IDF curves based on these random realizations using the GEV distribution and compared the reconstructed IDF curves with the historical ones. Figure 9 shows this comparison, in which extreme intensities are largely underestimated in short durations.
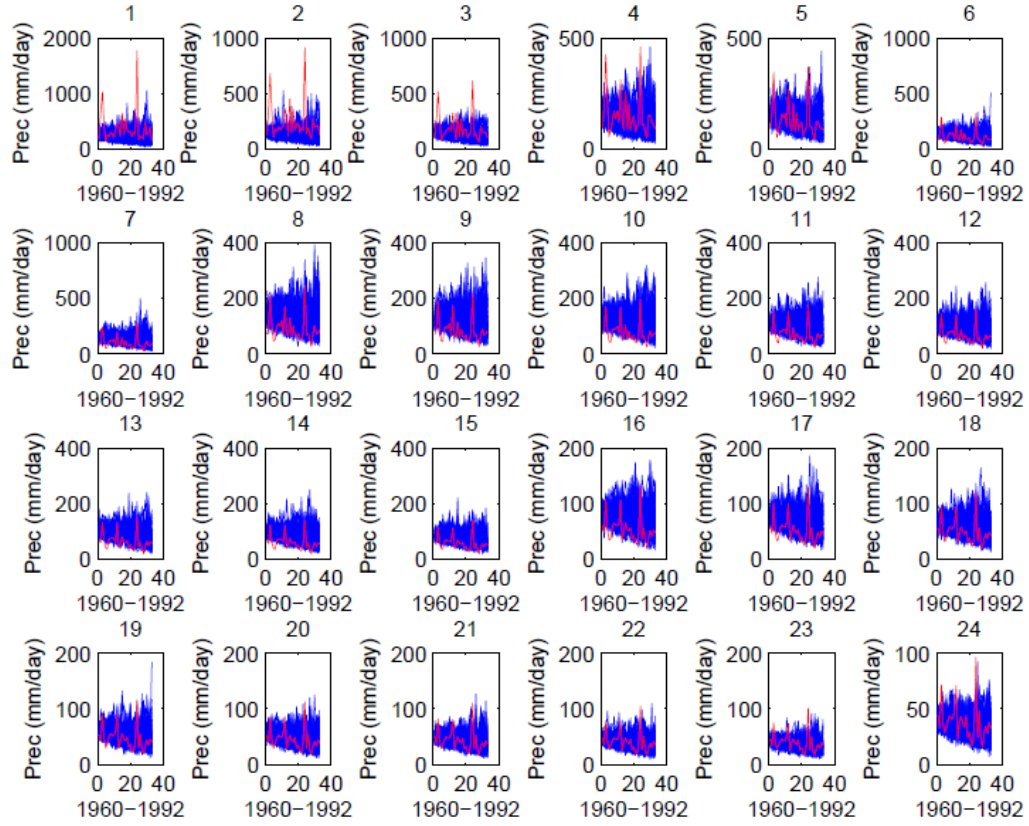
Figure 8. 100 realizations of 1-hr to 24-hr AMPs from 1960 to 1992. Blues lines show 100 random realizations and red lines show the historical AMPs.
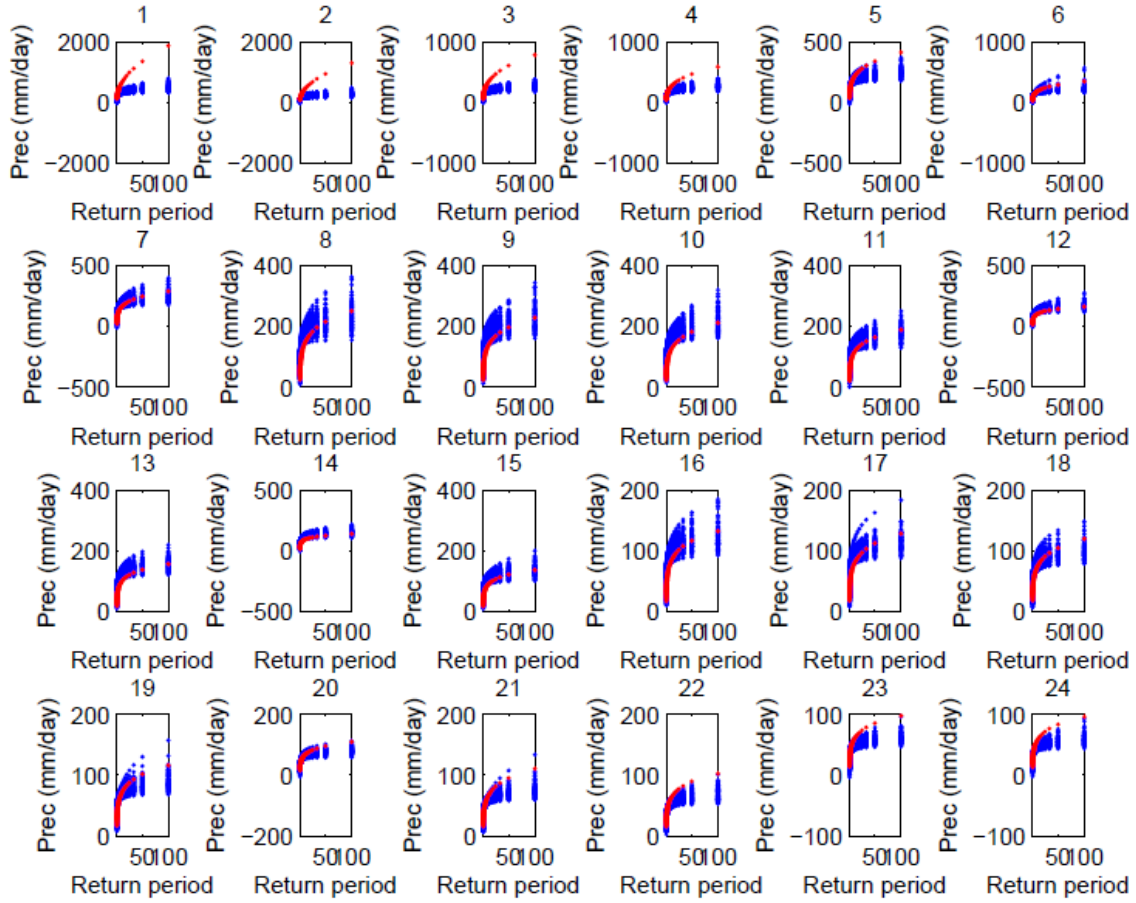
Figure 9. 100 realizations for 1-hr to 24-hr IDF curves obtained from 1960 to 1992. Blues dots show IDF curves from 100 random realizations and red dots show historical IDF relationships. Both generated and historical IDF relationships are extracted using the GEV distribution.

iii. *Possibility of projecting future IDF curves*

Despite large errors in reconstructing short duration IDF relationships, we considered extending the extracted trends to assess the possibility of identifying future IDF curves. As model S2 uses log-transformed data, the lower bound would be always above zero. Nonetheless, the upper bound can increase drastically and result in a substantially large uncertainty. Figure 10 shows an example in which the extracted trend during 1961 to 1990 (panel a) is extended into the future and used to generate 1000 realizations of daily AMPs during 2021 to 2050 (panel b). The uncertainty in generated AMP sequences is substantially larger during the future period, which consequently results in large uncertainty in IDF relationships, particularly at larger return periods – see Figure G5. We therefore reject the possibility of extending the existing trends into the future for projecting the future IDF relationships due to the large uncertainty between lower and upper confidence limit and unrealistically large upper bound limit, particularly in short durations and large return periods – see Figure G5 (Appendix G).

(a)

(b)
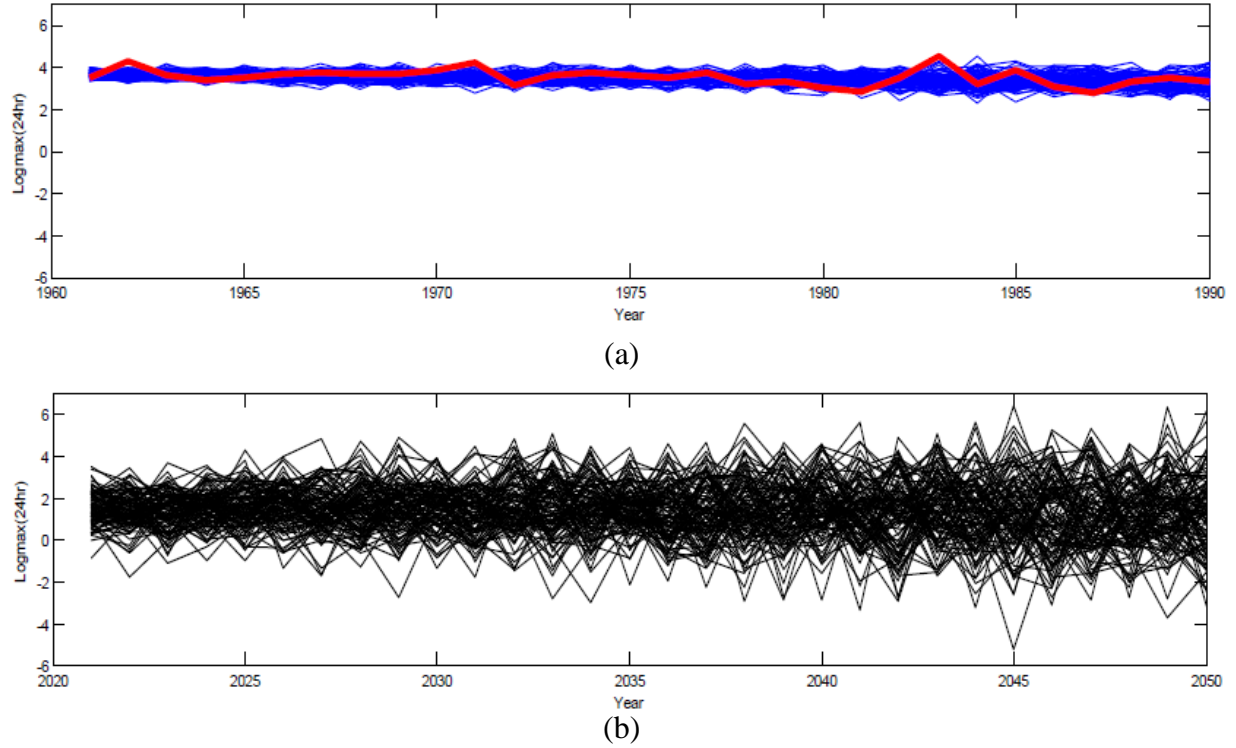
Figure 10. Extending the historical trends into future using S2 model; (a) 100 random realizations of 24-hr AMPs (blue lines) vs. historical AMPs (red line); (b) 100 random realizations of 24-hr AMPs from 2021 to 2050.

2.2.4. Conclusion and recommendations

We investigated the existence of monotonic trends in historical MMPs, SMPs and AMPs across various durations from hourly to daily. We showed that there have been weak decreasing trends during spring, weak increasing trends during summer and overall, weak decreasing trends during "spring and summer" months. Despite decreasing trend, we showed that there is an increasing variability in AMPs. This can provide conditions in which future AMPs can be larger than historical values. We explored the possibility of reconstructing the historical IDF curves using identified trends and showed that the reconstructed IDF curves underestimate the short duration extremes substantially. Apart from this limitation, we showed that by extending the historical trends into future, the uncertainty increases exponentially and projected IDF curves would not have any practical value due to large uncertainty envelope. We recommend using climate models' projections in conjunction with downscaling and disaggregation methods for constructing future IDF curves.

2.3. Projections of future precipitation using GCMs

In this study, the Canadian climate model CanESM2 and the British climate model HadGEM2-ES (the Second Generation Earth System Model) were used and their daily precipitation outputs were obtained from CMIP5 data portal (http://pcmdi9.llnl.gov/) for the baseline period (1961-1990) and for the projection period (2011-2100). The precipitation simulations were downloaded from the data portal for each of the selected GCMs based on three RCPs (RCP2.6, RCP4.5, and RCP8.5) and the first ensemble (run) out of five ensembles available. It is advisable to use

22

several GCMs/RCPs for assessing broader representations of possible future precipitation and for better assessment of possible future changes in precipitation intensities with reasonable confidence through estimation of uncertainties. For the purpose of this study, it is believed that the six scenarios (three RCPs based on two GCMs) with multiple realizations (through the stochastic weather generator) cover a wide range of variability that is assumed to be sufficient for the investigation of the adopted two-stage modeling approach. Eight daily precipitation time series were extracted; two for the baseline period from the two GCMs, and six series representing future precipitation based on three RCPs and 2GCMs.

2.4. Stochastic weather generation

In this study, the stochastic weather generator LARS-WG (Racsko et al., 1991; Semenov and Barrow, 1997), which was developed based on the series approach (Racsko et al., 1991), was used. Using the series approach, the sequence of wet or dry series length was modelled first and then, the precipitation amount was modelled for each wet spell. As a stochastic weather generator, LARS-WG is capable of simulating synthetic precipitation time-series with statistical characteristics corresponding to the observed statistics at a site (Semenov and Barrow, 2002). LARS-WG was employed in this research for generating multiple realizations of daily precipitation at the local scale in Saskatoon. A synthetic precipitation time-series of arbitrary length (30 years in this study) was generated using the computed set of parameters by randomly sampling values from the probability distributions (Semenov and Startonovitch, 2010).

LARS-WG uses relative change factors (RCFs) for each month to incorporate, at the local scale, possible changes in the future daily precipitation scenarios produced at the coarse scale by GCMs (Semenov and Barrow, 2002). RCFs are calculated based on the GCMs' output at the coarse-grid resolution. RCFs, in general, are the ratios of future values over baseline period values. For example, RCF for the month of June is the ratio of future average precipitation amount in the month of June to that of the baseline period. LARS-WG (Version 5.0) contains RCFs for CMIP3' GCMs and IPCC AR4 emission scenarios. For verification of the calculated RCFs, the RCFs for mean monthly precipitation amounts were calculated using the downloaded daily precipitation from CGCM3.1 (http://www.cccma.ec.gc.ca) based on three emission scenarios (A1B, A2, and B1) during the baseline period and under the projections of climate change; and compared with the RCFs embedded by the developers in LARS-WG. This verification step was needed because embedded RCFs are not available for CMIP5' GCMs, so these were calculated in this study.

The above-mentioned RCFs do not incorporate variability in future projections of precipitation due to wet and dry spell lengths. Therefore, average wet and dry spell lengths for each month were calculated during the baseline and future periods. Monthly ratio of the average lengths of wet or dry spells during the future period to the same during the baseline period represent the RCFs related to wet or dry spell lengths. Wet day is defined as a day with non-zero precipitation. Changes in the average wet and dry spell lengths for any month are supposed to alter the mean monthly precipitation of that month, and this is expected to incorporate more variability in the future daily precipitation. However, LARS-WG does not incorporate the RCFs for wet and dry spell lengths in its archive since it considers only monthly output from GCMs. Because of the availability of daily precipitation for CMIP5, RCFs for wet and dry spell lengths were calculated

in this study. The RCFs for mean monthly precipitation amounts, and wet and dry spell lengths were calculated, and used in this study, using two GCMs' (CanESM2 and HadGEM2-ES) precipitation available through CMIP5. The lengths of wet/dry spells were selected randomly from the probability distributions, constructed by LARS-WG, of wet/dry spells for the month in which the wet/dry spells begin.

The future realizations of climate data for Saskatoon were produced using LARS-WG in conjunction with GCMs. First, LARS-WG was calibrated based on the historical precipitation data of Saskatoon. In this context, this means constructing probability distributions for the precipitation data in Saskatoon based on the observed record, and multiple realizations (1000) of the daily precipitation record during the baseline period were generated. The constructed probability distributions were updated, using the RCFs, and perturbed to generate multiple (1000) realizations of future daily precipitation series in Saskatoon for each GCM/RCP combination. Accordingly, 6,000 realizations of future daily precipitation in Saskatoon were generated. The use of LARS-WG to produce future projections was considered as a "downscaling" method in this study.

It is worth noting here that the use of the term "downscaling" with stochastic weather generators is common in literature, but could be confusing to some readers. In the cases of dynamic and regression-based downscaling, actual "downscaling" occurs as models (RCMs or regression relationships) link data/variables at coarse spatial and temporal (global) scale to those at finer spatial and temporal (local) scale. The relationship developed based on the baseline period is used to downscale the future projections. However, the weather generator employs the statistical properties of observed variables at the local scale to generate multiple realizations at the same scale. Once future projections are produced by GCMs, a factor (RCF) is computed to quantify the shift in the data/variables from the baseline to the future periods. The same RCF is used to shift the variables/data generated at the local scale to produce the future projections. This argument is depicted graphically in Figure 11. Figure 11 (1) shows that a relationship is established between the global scale variable and the local scale variable during the baseline period, the relationship is then used to generate local scale future variable from the global scale future variable. In case of weather generator as shown in Figure 11 (2), RCFs are calculated for each month using global scale future and baseline scenarios, and these RCFs are applied to the local scale observed variable to generate local scale future variable.
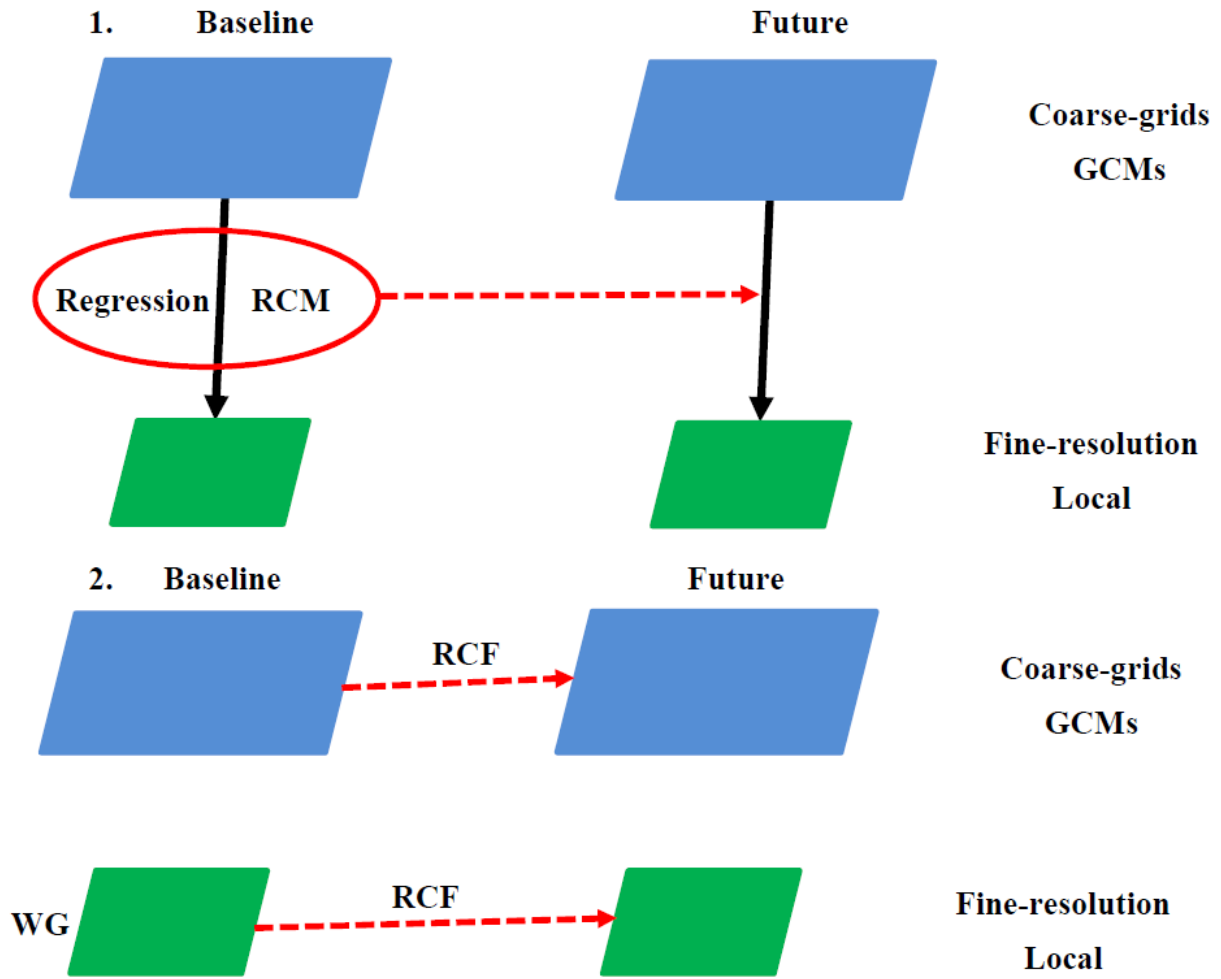
Figure 11: Generation techniques of future climate change scenarios at the fine resolution (local) scale from the coarse-grid GCMs' scale using (1) downscaling methods and (2) weather generators.

2.5. K-NN disaggregation model

2.5.1. Hourly disaggregation model

It is often necessary to disaggregate precipitation generated at certain timescales (e.g., daily) to finer timescales (e.g., hourly, sub-hourly). In this study, the K-nearest neighbor (K-NN) method (Lall and Sharma, 1996; Yates et al., 2003; Sharif and Burn, 2007) was used for disaggregating precipitation data from daily to hourly scale. The hourly K-NN disaggregation model, developed based on the work by Sharif and Burn (2007), was conducted for precipitation from a single precipitation station for disaggregating both baseline and future daily precipitation of n years to hourly precipitation. Development of the disaggregation method is explained below.

Let X_t be the vector of daily precipitation values x_t, where $t=1,\ldots\ldots\ldots, 365n$ (it excludes February 29 of a leap year); n is the total number of years in the daily precipitation time series.

The algorithm starts with the reading of each daily precipitation value from the X_t vector and it continues for all the 365n days in the daily precipitation time series. The steps of the algorithm as shown schematically in Figure 12 are as follows:

1. Suppose, Y_t^i be the vector of 24 hourly precipitation values y_t for day t of year i.

2. A window of w_d daily precipitation values in Figure 12 that includes x_t is identified to include the nearest neighbors to the selected daily precipitation x_t of a particular year i. If there is no rainy day within the window for the current year except x_t, the window size is increased each time by one day until it contains at least one rainy day. Accordingly, the corresponding hourly data block L from the time series Y_t of all years is identified. This way, the size of the hourly data block will be:

$$L_d = [(n*w_d)-1]*24 \qquad\qquad [1]$$

3. In the work of Sharif and Burn (2007), w_d (i.e. optimal window size) was chosen to be 15, including the x_t under consideration. So, if the current day of simulation is July 15, then all corresponding hourly profiles between July 8 and July 22 are selected from all n years of hourly record, excluding the corresponding hourly profile for July 15 for the current year (to prevent the possibility of generating the same hourly profile as that corresponding to the current day). However, in this study the optimal window size was investigated and selected for the City of Saskatoon based on the simulated and observed annual maximum precipitation (AMPs) of various durations during the baseline period rather than using an arbitrary window size. Although w_d is allowed to change dynamically whenever at least one rainy day is not available in the window, a fixed size of w_d is used for rest of the cases (containing at least one rainy day). The size of the fixed window is mentioned for easy understanding afterwards.

4. The daily precipitation amount (x_t) is compared with the set of neighboring hourly totals. The square of differences between x_t and each of the $[(n*w_d)-1]$ segments in the L_d block is calculated, and the segment showing the minimum squared difference compared to the daily precipitation amount is considered as the disaggregated hourly precipitation values for the current day. While doing so during the selection of optimal window size, more than one candidate among the nearest neighbors may be detected with the same minimum difference from the daily precipitation of the current day. So in addition to what was explained in Sharif and Burn (2007), the performance of the model can be assessed using both random (selection of a segment randomly from a number of candidate segments) and deterministic (i.e. selection of the first segment from a number of candidate segments) sampling approaches during the baseline period based on the simulated and observed AMPs of various durations. The hourly disaggregated precipitation sequences can be selected either randomly or deterministically from the hourly precipitation sequences of the nearest neighbors having equal minimum difference. The K-NN hourly disaggregation model was used to simulate the observed hourly precipitation sequences both randomly and deterministically using the optimal window size. The observed and simulated precipitation time series are accumulated to 24 different durations (1 to 24 hrs) and the corresponding AMPs are identified. AMPs obtained from both simulations (random/deterministic) can be compared with the observed AMPs of 24 durations to assess the effect of both selection approaches.

5. In case of climate change, when the future projected daily precipitation value is higher than the historical daily precipitation value, the hourly precipitation values may be scaled up by the same ratio as found for the daily scale. The steps (1-5) of the hourly disaggregation model are illustrated in Figure 12.
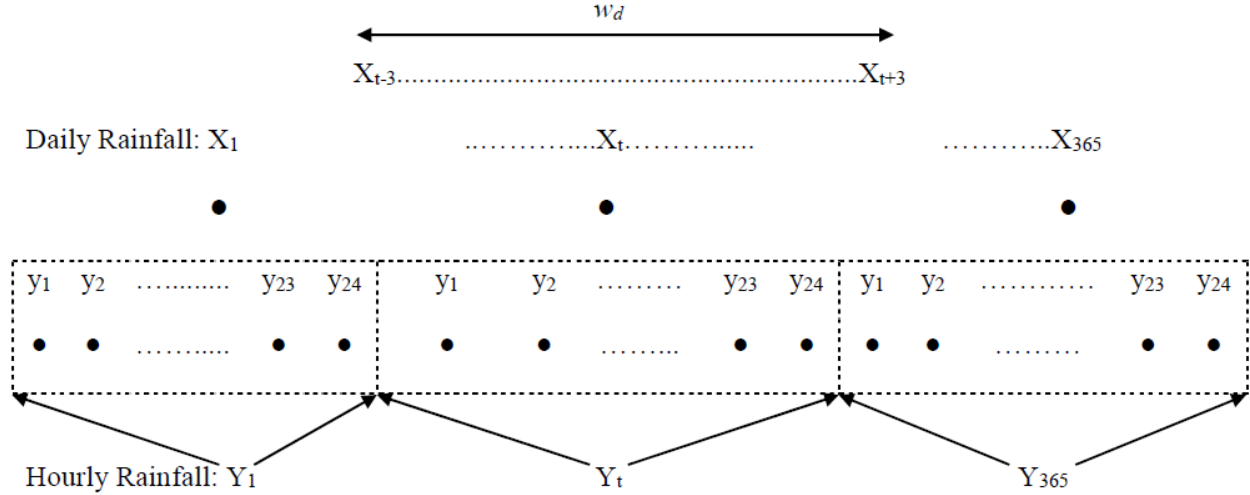
Figure 12. K-NN hourly precipitation disaggregation model for a typical year.

The steps (1-5) of the hourly disaggregation model were repeated for all days of all of the years in the daily precipitation time series. A set of 1000 realizations of the daily precipitation was generated using LARS-WG, and thus, ensembles of the hourly disaggregated precipitation values were created using the K-NN method.

2.5.2. Sub-hourly disaggregation model

The K-NN method was also used to disaggregate precipitation from hourly to sub-hourly (i.e., 5-min) values in the City of Saskatoon using the approach described in Section 3.3. The algorithm starts with the reading of each hourly precipitation value from the Y_t vector and it continues for the entire time series. Here, the steps of the algorithm (as described schematically in Figure 13) are similar to the K-NN hourly disaggregation model. Suppose, S_t^j be the vector of 12 sub-hourly (5-min) precipitation values for hour t of day j; where t denotes specific hour of the day and j denotes the specific day in a specific year. In this case, the size of the 5-min data block is:

$$L_h = [(n*w_h)*24-1]*12 \qquad\qquad [2]$$

Where w_h is the window size and n is the number of years in the hourly precipitation time series. The hourly precipitation amount (y_t) is compared with the set of neighboring totals of 5-min precipitation values. The squared of differences between y_t and each of the $[(n*w_h)*24-1]$ segments in the L_h block were calculated, and the segment showing the minimum square difference from the hourly precipitation amount was considered as the disaggregated 5-min precipitation values corresponding to the current hour. The extension of window size in absence of rainy hours, selection of optimal window size for Saskatoon, random/deterministic sampling,

27

and scaling of future sub-hourly precipitation values were considered for the K-NN sub-hourly disaggregation model in a similar way to that of the hourly model. The steps of sub-hourly disaggregation model are illustrated in the Figure 13. In Figure 13, t denotes a specific day of a specific year in selecting hourly and sub-hourly data block, and h denotes hours in a day in a specific year; where h=1,2,……….,24.

W_h

$Y_{t-56,h}$..$Y_{t+56,h}$

Hourly Rainfall: $Y_{1,h}$ …………...$Y_{t,h}$…………...... …………...$Y_{365,h}$

| S_1 | S_2 | ……...… | S_{11} | S_{12} | S_1 | S_2 | ……...… | S_{11} | S_{12} | S_1 | S_2 | ……...… | S_{11} | S_{12} |

5-min Rainfall: $S_{1,h}$ $S_{t,h}$ $S_{365,h}$
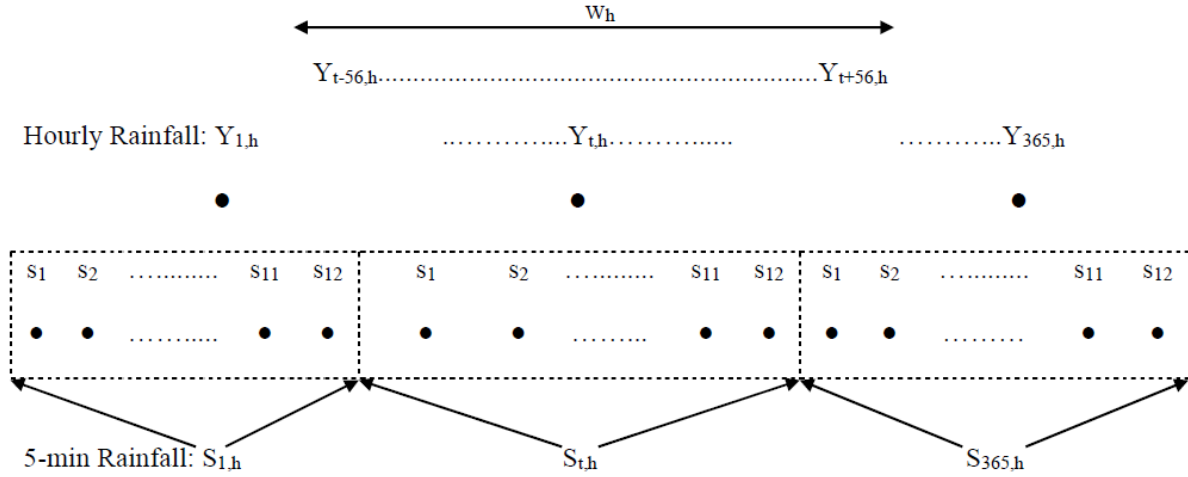
Figure 13: K-NN sub-hourly precipitation disaggregation model for a typical year.

2.6. Stochastic rainfall disaggregation

Stochastic rainfall disaggregation is an alternative method, developed in the course of this project, for sub-daily disaggregation of continuous daily rainfall. This method can be considered parallel to the sub-daily KNN disaggregation model. Similar to the sub-daily KNN disaggregation model, the newly developed stochastic disaggregation method gets the daily rainfall realizations and divides them into hourly segments. Underlying assumptions for distributing the daily rainfall into hourly estimates are different in KNN and the stochastic algorithms. In KNN disaggregation, the algorithm searches for the most similar daily event during a particular window of the baseline data and uses the historical hourly hyetograph of the identified "most-similar" rainfall to convert the daily rainfall realizations into hourly estimates. Stochastic disaggregation relaxes this assumption and distributes the daily rainfall into hourly values without considering the exact historical hyetograph; however, it uses the historical hourly distributions to come up with a basis to randomly generate new hyetographs. The stochastic disaggregation algorithm, therefore, acknowledges the fact that hourly rainfall distributions under future climate change conditions might be different from the most similar rainfall event during the baseline period. It should be noted that in principle, the stochastic disaggregation can be used for distributing the hourly rainfall into sub-hourly segments, similar to the KNN method. Nonetheless, our investigations showed that the length and quality of sub-hourly data in Saskatoon does not allow developing robust empirical basis, with which hourly cumulative rainfalls are disaggregated into 5-minute intervals. Therefore, we use this algorithm only for disaggregating daily rainfall totals into hourly hyetographs.

The proposed stochastic rainfall disaggregation is a non-parametric stochastic method, which is solely based on historical events during the baseline period. For a particular rainfall event, the algorithm considers the daily cumulative rainfall and the month, in which the event takes place. The algorithm then uses historical distributions of all daily rainfall events during that month to generate a new random rainfall distribution. The algorithm is based on the concept of Rainfall Distribution Functions (RDFs) that represents the empirical progression of a daily rainfall event in time and has the same characteristics as probabilistic Cumulative Distribution Function (CDFs). In simple words, a RDF determines ratios of the total daily rainfall that occurred in each hourly resolutions. RDFs can be simply computed using the historical rainfall events. Figure 14 shows how the RDF can be calculated based on a hypothetical rainfall event. In panel (a), an hourly rainfall hyetograph for a daily event with cumulative value of 70 mm is shown. This hyetograph can be converted into a cumulative rainfall distribution (panel b) and consequently, to an RDF, if cumulative hourly rainfalls are divided by the total daily value, i.e., 70 mm in this example.
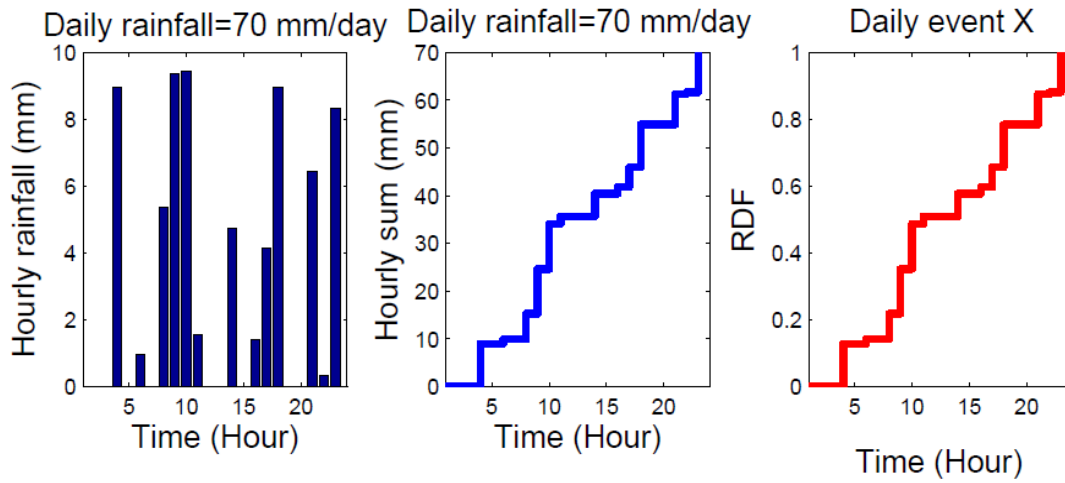
Figure 14. Calculation of an RDF from the hourly hyetograph of a daily rainfall event.

In principal, RDFs are normalized cumulative distributions; therefore, by considering empirical properties of RDFs during a certain month, a basis for random generation of rainfall distributions during that month can be obtained. Here, we try to explain this using a simple example. Figure 15 shows all RDFs that are obtained for the month of April during the baseline period (i.e. 1961 to 1990). For every hourly time step, a set of normalized ratios (i.e. between zero and one) are available that identify different proportions of daily rainfall, precipitated in each hour. By considering these historical hourly ratios, a set of secondary empirical distribution functions can be obtained that provide a basis for generating random realizations of rainfall ratios in each hour. As an example, Figure 16 shows the secondary empirical distributions of rainfall ratios during 6th, 13th and 20th hours during the month of April. By considering these empirical distributions during all 24 hours, new ratios can be randomly generated for every sub-daily time steps (i.e., hourly throughout this report).

It should be noted that the randomly generated distributions should satisfy the continuity condition and the mass balance. This means that the sum of randomly generated hourly ratios during a daily event should equal to one. To make sure the continuity condition is satisfied, we

developed an adaptive stochastic scheme that consider generating random rainfall ratios during each hour based on the sum of ratios generated in the previous hours. Figure 17 shows the step-by-step procedure of the developed framework through an algorithmic pseudo-code. Below, we try to explain this algorithm in simple words.
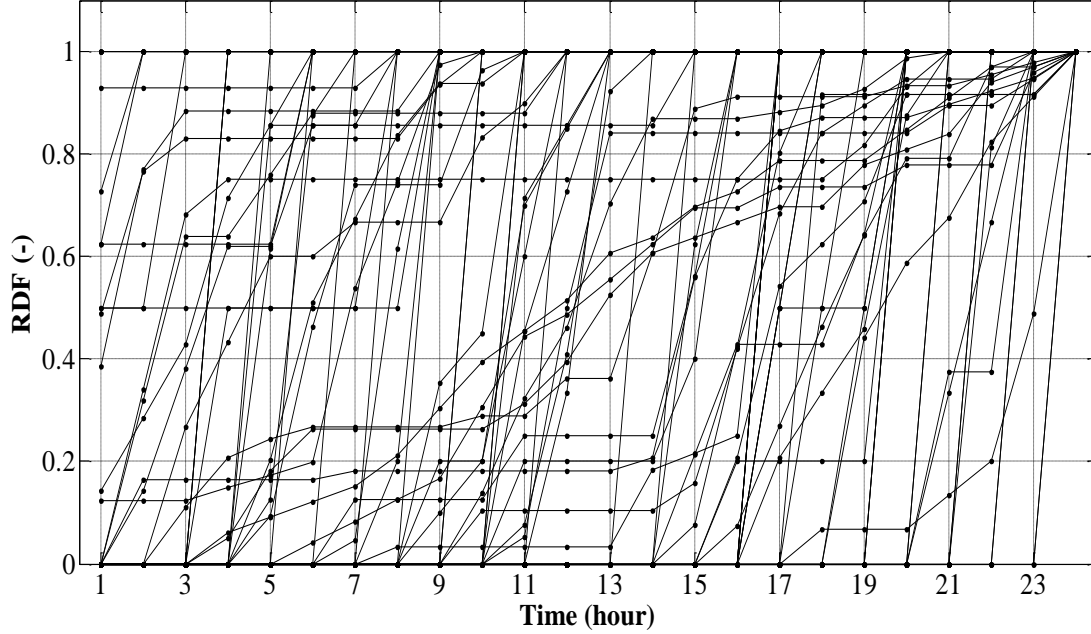
Figure 15. Daily RDFs for April in the city of Saskatoon during the baseline period (1961-1990).
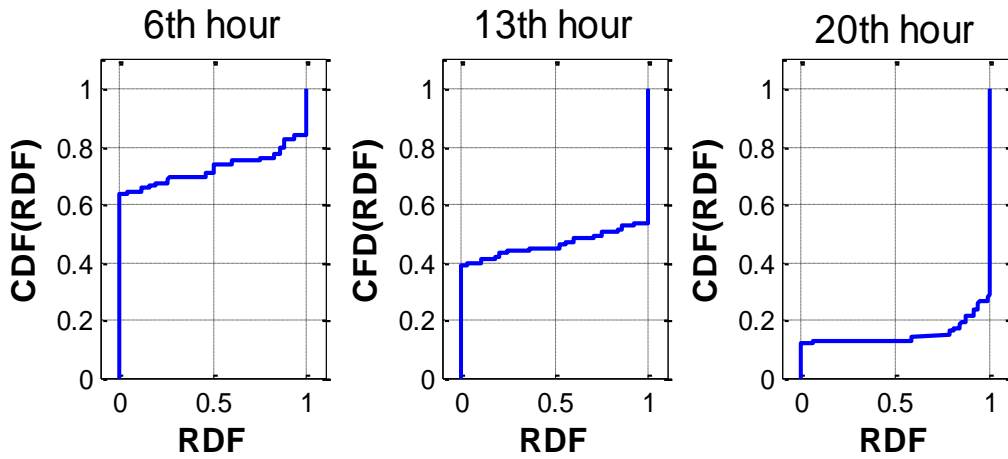
Figure 16. Empirical distributions of historical RDFs in 6th, 13th, and 20th hours of a typical daily rainfall event during Aprils of 1961 to 1990.

- Pre-simulation step: calculate RDFs of all rainfall events during the baseline period and categorize them into monthly maps as shown in Figure X2
- For every daily realization during baseline or future time episodes
- Consider the month of the daily event D
- Get $\sum_{i=1}^{24} Rain_{D,i}$
- For every hourly time step n=1:24
  - Sample a uniform random number $Z_n \in [0\ 1]$
  - find $X = \frac{\sum_{i=1}^{n-1} \%Rain_{D,i}}{100}$
  - Find $\{RDF^* | \sum_{i=1}^{n-1} RDF_i^* \geq X\}$
  - $\%Rain_{D,n} = 100 \times \min\left(\max\left[\langle CDF(RDF^*)\rangle_n^{-1}\{Z_n\}, 0\right], 1-X\right)$
- $\bigcup_{i=1}^{24}\{Rain_{D,i}\} = \frac{\sum_{i=1}^{24} Rain_{D,i}}{100} \times \bigcup_{i=1}^{24}\{\%Rain_{D,i}\}$

Figure 17. The pseudo-code of the developed stochastic disaggregation algorithm.

First the hourly RDFs for all daily event during the baseline period should be calculated according to the procedure shown in Figure 14, and accumulated together based on each month (April to September; See Figure 15 for the month of April). This pre-simulation step provides empirical distributions (Figure 16), with which the daily rainfall realizations can be disaggregated into hourly segments. For each daily rainfall event, first 24 random numbers are generated corresponding to 24 hourly time steps. For each time step, first, the sum of generated ratios up to the considered time step is calculated (zero for the first time step). Only RDFs that generate greater or equal cumulative ratios up to the considered time step are used for sampling random ratios in the this time step. Second, the rainfall ratio during the considered hourly step n is then generated by the following formula:

$$\%Rain_{D,n} = 100 \times \min\left(\max\left[\langle CDF(RDF^*)\rangle_n^{-1}\{Z_n\}, 0\right], 1-X\right) \qquad [3]$$

Equation 3 guarantees that the sum of ratios during a daily event equals to 1. The randomly generated hyetograph can be then identified by multiplying the total daily rainfall by the randomly generated ratios, calculated based on Equation 1. This process can be repeated multiple times to provide multiple realizations of the disaggregated rainfall.

2.7. Genetic programming

The concept of biological evolution led to the way for the development of Genetic programming (GP), which was introduced by Koza (1992) as an extension of genetic algorithms, which are optimization methods for searching for the global optimum of a function. GP, a data driven technique, was developed to induce computer programs as solutions to the search problems that uses intelligent and adaptive search. Depending on the search problem, GP takes on a special form called genetic symbolic regression (GSR) for establishing relationships as equations between the predictor and the predictand. The equations are optimized through adaptive random search providing the insight into the functional (structural) form of the regression relationships

31

between the input and the output, which is not the case for other regression methods. This technique of GP was utilized in this study for obtaining equations that express mapping relationships between the global scale daily AMP quantiles to the local scale sub-daily (1 to 24 hours) AMP quantiles.

Babovic and Keijzer (2000), Savic et al. (1999), and Koza (1992) provided detailed explanation of GP and GSR methods, while for detailed explanation of how GP can be applied to find relationships between local scale and global scale AMP quantiles, refer to Hassanzadeh et al. (2014). This study used GPLAB 3 package (Silva, 2007) for conducting experiments involving the local scale and global scale data.

Briefly, the GP search started with the creation of initial population of models (equations) in the form of parse trees without using prior information. The individual equations were assessed based on a goodness-of-fit measure, and the individuals with better fitness survive to create new individuals. Some operators originated from the concept of genetic evolution, specifically mutation and crossover, were considered for forming new parse trees using randomly selected parents during mating, and thus, the next generation was created. A threshold for the number of total function evaluations and the convergence criterion were predefined as stopping criteria for the GP search. Because GP-based method for producing future IDF curves for the City of Saskatoon was developed and published by Hassanzadeh et al. (2014), it was considered in this research to be a viable reference method for comparison with the developed two-stage modeling approach. In this study, various statistical error measures were used to evaluate the performance of the mapping equations (shown in appendix D).

Strong relationships were observed between the global scale's (using the daily output of CGCM3.1) AMP quantiles and the corresponding daily and sub-daily local values (Hassanzadeh et al., 2014). Based on the same rationale and hypothesis, the relationships between the global-scale (using the output of CanESM2 and HadGEM2-ES) and the corresponding daily and sub-daily local values were investigated in order to map GCM quantiles to the corresponding local daily and sub-daily quantiles. Figure 18 is a visual verification of the hypothesis of this GP-based downscaling method; it compares the global scale (using CanESM2) AMP quantiles and the corresponding daily and sub-daily local scale quantiles for the baseline period. The similar comparison using the output of HadGEM2-ES is shown in appendix D.
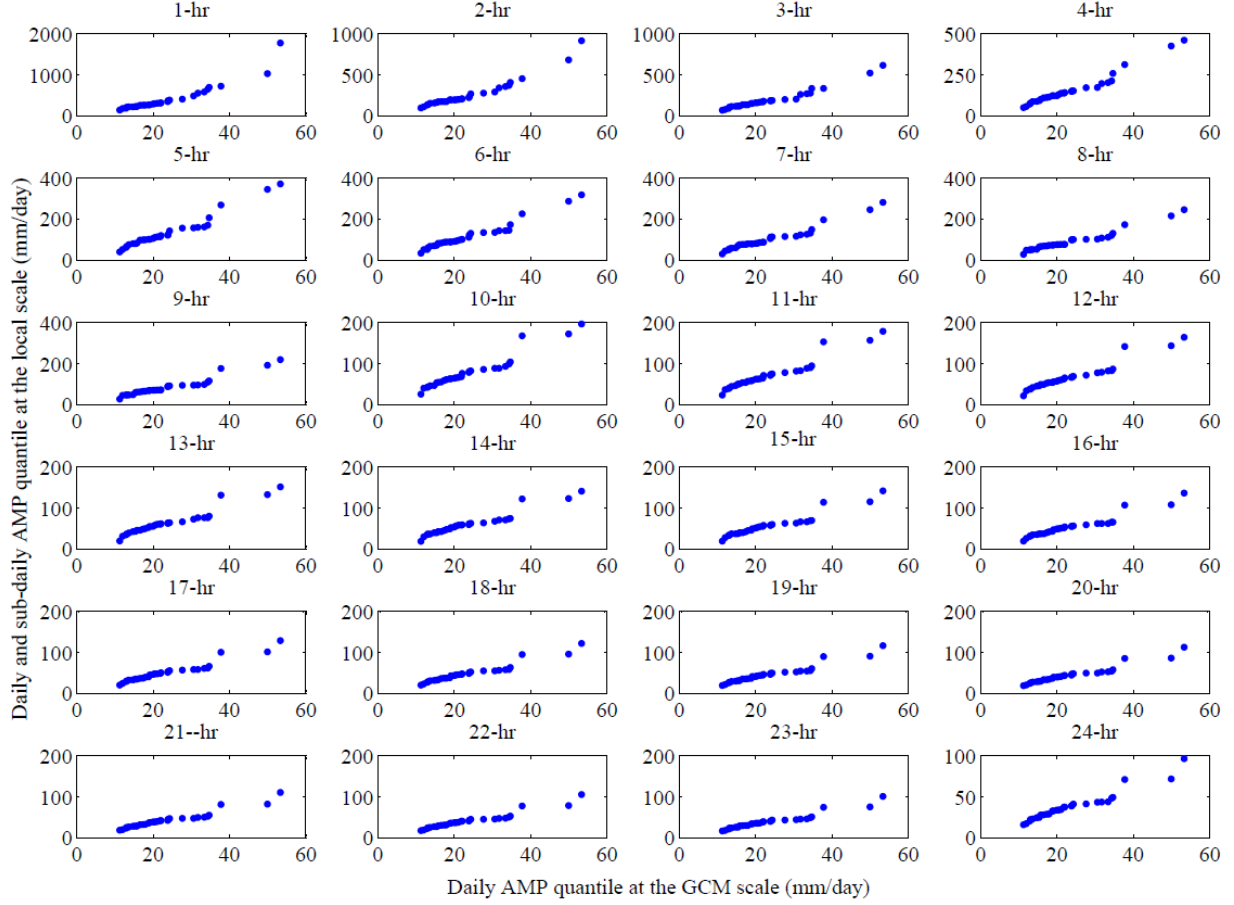
Figure 18. Quantile-Quantile plots of the GCM-scale (using output of CanESM2) daily AMP quantiles and the corresponding local-scale daily and sub-daily AMP quantiles during the baseline (1961-1990) period in Saskatoon (durations are indicated above the plots).

The daily AMP data were extracted from the 30 years' record during the baseline period. However, long record of data are required for the modeling purpose using the data-driven GP, which includes data for training and validation. GEV distributions were fitted to the observed 30 AMPs. For the modeling purpose, a set of 10,000 uniform random numbers was generated first to represent non-exceedance probability, $P \in [0 \ 1]$ and then the corresponding AMP quantiles were sampled from the GEV distributions at the GCM-scale daily precipitation, and the local-scale daily and sub-daily precipitation data. The first 6000 data pairs (i.e., the GCM-scale daily AMP quantiles, and the local-scale daily and sub-daily AMP quantiles) were chosen as the training dataset from the randomly selected 10,000 data pairs for extracting each of the mapping equations using GP. A total of 24 mapping equations were extracted to describe the relationships between the GCM-scale daily AMPs and the local-scale sub-daily AMPs. The GCM-scale daily AMPs was used as the inputs, while the outputs were the local-scale AMPs of a specified duration. The remaining 4000 data pairs were used as the validation dataset. In addition, the original 30 AMPs for the GCM-scale daily precipitation and the local-scale daily and sub-daily precipitation were used as a completely unseen testing dataset to verify the developed equations. For detailed explanation of the GP method implementation with setting internal parameters of the model, refer to appendix D.

2.8. GEV Distributions and the construction of IDF curves

Intensity-Duration-Frequency (IDF) curves were used in this study to represent extreme precipitation properties of short durations at the point scale. The construction of IDF curves involves collecting/generating precipitation time series of various durations. Once the precipitation data were collected/generated, annual maximum precipitation (AMP) values at various durations were extracted. The Generalized Extreme Value (GEV) distribution, which is a family of parametric probability distributions, was used to estimate the frequency of the AMP as a random variable. Gumbel, Fréchet, and Weibull probability distributions are combined in the GEV distribution, which takes the following form (Katz, 2012):

$$F(x, \mu, \sigma, \xi) = exp\left\{-\left[1 + \xi\left(\frac{x-\mu}{\sigma}\right)\right]^{-1/\xi}\right\}$$

[4]

where $1 + \xi\left(\frac{x-\mu}{\sigma}\right) > 0$, $F \in [0\ 1]$ denotes the non-exceedance probability of the random variable x, $\mu \in R$ is the location parameter, $\sigma > 0$ is the scale parameter, and $\xi \in R$ is the shape parameter. The shape parameter ξ controls the tail behaviour of the distribution. The GEV distribution converges to Gumbel, Fréchet, and Weibull distributions when $\xi = 0$, $\xi > 0$, and $\xi < 0$, respectively.

The GEV distribution with maximum likelihood method for parameter estimation was used in this study for the construction of IDF curves in the City of Saskatoon during the baseline period and the future projection period, as it was used successfully in previous studies (Beniston et al., 2007; Cameron et al., 2000, Hashmi et al., 2011; Hassanzadeh et al., 2014; Kharin and Zweris, 2005; Yilmaz and Perera, 2014). The GEV distribution was used for the construction of IDF curves, although it increases the computation intensity due to the involvement of three parameters (shape, scale, and location) instead of two parameters in Gumbel distribution. However, the GEV distribution provides better description of the upper tail behavior of the data by introducing an additional parameter (Overeem et al., 2008). Figure 19 shows the ability of GEV distribution to fit empirical cumulative distribution functions (ECDF) of daily and sub-daily AMPs in Saskatoon. The goodness of GEV fit to the AMPs was confirmed by the Kolmogorov-Smirnov test with 95% significance level.

IDF curves can be constructed based on the GEV fitting using the inverse of the fitted GEV distributions, given the return period (T) and precipitation quantiles (Q_x), as follows:

$$Q_x = GEV_x^{-1}\left(1 - \frac{1}{T}\right)$$

[5]
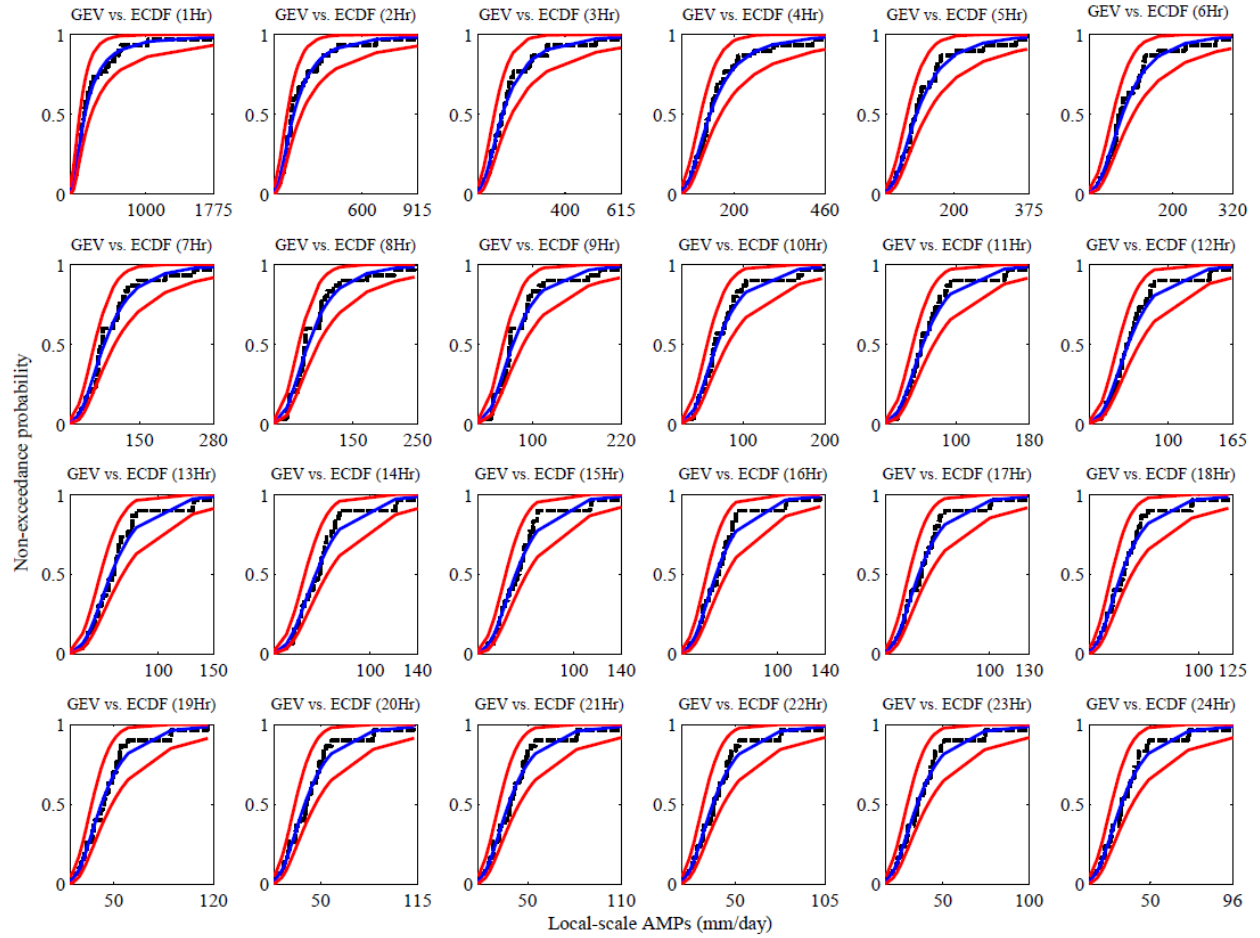
Figure 19. Comparison between the GEV (blue line) and empirical fit (black dots) for the local AMPs in Saskatoon with 95% confidence intervals of GEV fit shown by the red lines.

Eventually, the hourly and sub-hourly disaggregation models, based on the K-NN method, were used to generate long time-series of hourly and sub-hourly precipitation values for both baseline and future periods (2011-2100). The AMPs of the disaggregated hourly and sub-hourly precipitation time series were used to construct two different sets of IDF curves based on quantiles obtained from the GEV distribution: (a) the IDF curves derived from historical data (observations), which currently form the basis of the design and evaluation of Saskatoon's storm water collection system; and (b) the IDF curves based on the models developed in this study. Furthermore, a third set of IDF curves was constructed using the Genetic Programming (GP) method, which was introduced by Hassanzadeh et al. (2014) and was re-implemented in this study with new data based on CMIP5 simulations. The GP method employs a fundamentally different route for constructing the IDF curves because it generates AMPs at the local scale directly without having to generate the time series of continuous precipitation values. Accordingly, the GP method provides a solid reference for comparison with the two-stage modeling method developed in this study, and also helps show variability in IDF curves due to the adoption of various downscaling methods. The comparative analyses of the results took into consideration the various GCMs, RCPs, and the downscaling/disaggregation methods.

35

2.9. Likelihood of extreme storm events

The future IDF curves/tables were constructed using 1000 realizations of fine-resolution continuous rainfall series from the two disaggregation methods: (i) LARS-WG and K-NN and (ii) LARS-WG and Stochastic downscaling-disaggregation methods. So, the likelihood assessment of any storm represented by the IDF curve/table or the continuous series within the generated ensemble is conducted suing the 1000 realizations. The likelihood measure would characterize the probability of non-exceedance of a certain storm event for the selected GCMs, RCPs, time periods, disaggregation methods, and return periods. The LARS-WG and K-NN method generates hourly and 5-minute rainfall series, while the LARS-WG and Stochastic downscaling-disaggregation method generates only hourly rainfall series. The critical hourly and 5-minute rainfall profiles are calculated based on a pre-selected time window (2, 3, 4, 5, 6, 7, or 30 days) for the user defined combination.

2.9.1. Storm likelihood measurement
The GEV distribution is fitted to the 30 AMPs from each of the 1000 realizations to calculate quantiles for the selected GCMs, RCPs, return periods, storm durations, time periods, and disaggregation methods. The quantiles for each of the mentioned combinations are sorted in ascending order and the non-exceedance probability of the quantiles is calculated by $i/(1000+1)$, where I ranges from 1 to 1000. The quantiles are expressed as mm/hour and plotted against the probability calculated above, which shows the likelihood measure of the storm represented by the IDF curves/table. The mean of the quantiles from 1000 realizations was plotted as IDF curves in the remaining part of the report. The likelihood measures cannot be shown for GP method since it does not generate multiple realizations.

2.9.2. Calculation of critical profile
The critical profile within a fine-resolution (i.e., hourly or 5-minute) rainfall time series can be calculated using a time window of several days (e.g., 2, 3, 4, 5, 6, 7, and 30). For the selected time window, all the hourly or 5-minute data points within the time window of all moving windows are identified and accumulated. This search is conducted for the critical value of the window-accumulated rainfall along the entire time series, and the maximum value is identified, along with its time location. This procedure is repeated for the 1000 realizations; the 1000 critical values are sorted in ascending order and the non-exceedance probability is calculated in a similar way mentioned in the previous section. The cumulative values of the critical profiles are plotted against the probabilities to show the likelihood of the critical profiles. The procedure can be repeated for any pre-selected time window.

3. RESULTS AND ANALYSIS

The results of the stochastic weather generation, the disaggregation technique, and the GP method are presented in this section. The results related to the generated long time series of site-specific daily precipitation during the baseline period and under the projections of climate change scenarios for Saskatoon using LARS-WG are provided in Section 3.2. The hourly and sub-hourly disaggregation models developed using the K-nearest neighbours (K-NN) technique are presented and analyzed in Section 3.3. Variations in the future IDF curves, produced using both the K-NN and the GP method, as compared to the baseline IDF curves are presented and analyzed based on two GCMs and three RCPs during the 21st century in Section 3.4. Different sources of uncertainties and their contributions to the total uncertainty and uncertainties associated with the prediction of future IDF curves are included in Section 3.5.

3.1. Verification of the stochastic weather generator

LARS-WG was provided with Saskatoon's observed daily precipitation data during the baseline period (1961-1990) to obtain the parameters of the probability distributions of the local station's precipitation. This set of parameters was then used to generate 1000 realizations of the observed precipitation series. The performance of the calibrated model is shown in Figure 20. The weather generator was calibrated based on the p-value calculated for all statistics (e.g., KS-, t-, and f-statistics) concerning the hypothesis test (e.g., Kolmogorov–Smirnov test) to determine if the observed and simulated precipitation series belong to the same distribution. The model was then validated using Saskatoon's observed daily precipitation during the period of 1991-2009.
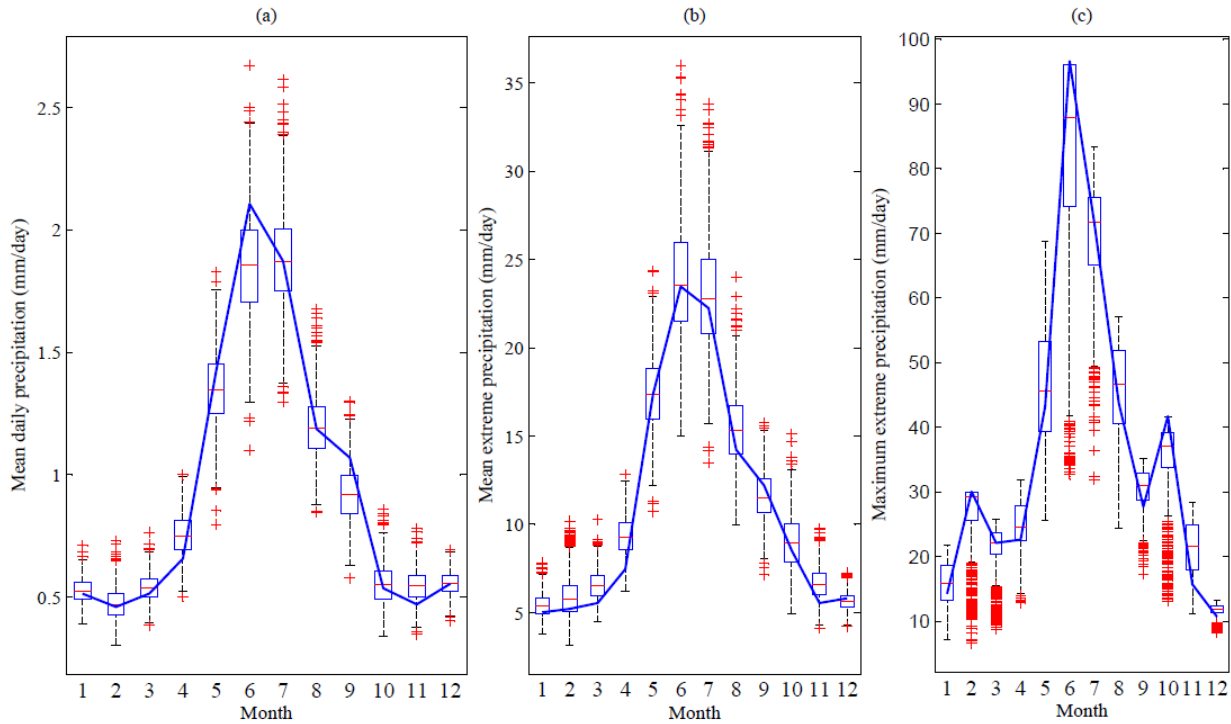
Figure 20. Performance of LARS-WG based on the observed monthly properties (solid lines) and 1000 realizations of synthetic (box plots) precipitation time-series during the baseline period (1961-1990) in Saskatoon.

Figure 20 shows a comparison between the observed mean daily precipitation (20a) and mean of extreme daily precipitation (20b) in each month and the corresponding ones of the synthetic daily precipitation in each month shown as boxplots based on 1000 realizations obtained from LARS-WG during the baseline period. The mean daily precipitation was calculated as the mean of daily precipitation in each month over a period of 30 years (1961-1990), the 30 years have 30 AMPs and the mean of 30 AMPs in each month was termed as mean extreme precipitation, while the maximum of the 30 AMPs in each month was denoted as maximum extreme precipitation in Figure 20. The figures show that LARS-WG generated the mean and mean of the extreme precipitation properties quite well during the baseline period. However, LARS-WG seems to slightly underestimate the maximum of the extreme precipitation in the month of June (Figure 20c) due to low success rate of the weather generator in reproducing maximum of the extreme precipitation values, which might contribute to some uncertainty in simulating the future maximum extreme precipitation. Other months outside the summer season are not considered of importance for this study.

Generation of daily precipitation series using LARS-WG requires calculation of relative change factors (RCFs) related to the precipitation amounts, wet spell lengths, and dry spell lengths for each month. The relative change factors (RCFs) related to monthly precipitation amounts for 15 GCMs from CMIP3 are embedded in the current version of LARS-WG. Nevertheless, the RCFs for the GCMs from CMIP5 are not included in LARS-WG archive, which need to be calculated using downloaded output of the corresponding GCMs. For verification, the downloaded output of CGCM3.1 (a CMIP3 model) was used to calculate the RCFs related to the monthly precipitation amounts and compared with the corresponding values embedded in LARS-WG.

Table 3 shows a comparison between the relative change factors (RCFs), for each month, based on the embedded and downloaded precipitation values of GCMs. The comparison shows that the sign and magnitude of change in mean monthly precipitation amount as presented by the calculated RCFs are not very different from those embedded in LARS-WG.

Table 3: Relative changes in monthly precipitation amounts between baseline and future (2020s, 2050s, and 2080s) climate as calculated from CGCM3.1 output (ratio of A1B future scenario to baseline scenario) as compared to the RCFs embedded in LARS-WG.

Month	(2011-2040)		(2041-2070)		(2071-2100)	
	LARS-WG	Calculated	LARS-WG	Calculated	LARS-WG	Calculated
Jan	1.17	1.20	1.18	1.16	1.21	1.15
Feb	1.15	1.20	1.21	1.20	1.26	1.16
Mar	1.15	1.12	1.25	1.14	1.47	1.22
Apr	1.17	1.20	1.36	1.44	1.63	2.02
May	1.14	1.16	1.41	1.74	1.43	1.58
Jun	1.03	1.10	1.24	1.28	1.10	1.14
Jul	0.98	0.97	1.06	0.95	0.96	0.91
Aug	0.96	0.97	1.01	1.23	0.95	0.86
Sep	1.00	0.96	1.01	0.90	1.07	0.97

Oct	1.08	1.07	1.11	1.16	1.24	1.27
Nov	1.11	0.99	1.17	1.12	1.27	1.20
Dec	1.15	1.23	1.15	1.10	1.24	1.32

The calculated RCFs for the mean monthly precipitation amounts, and wet and dry spell lengths are shown in Table 4, which were used in LARS-WG to generate realizations of future daily precipitation scenarios using CanESM2 (shown in Table 4) and HadGEM2-ES (shown in Appendix D) based on three RCPs (i.e. RCP2.6, RCP4.5, and RCP8.5).

Table 4: Relative change factors for CanESM2 during 2011-2040.

Month	Mean monthly precipitation			Wet spell length			Dry spell length		
	RCP2.6	RCP4.5	RCP8.5	RCP2.6	RCP4.5	RCP8.5	RCP2.6	RCP4.5	RCP8.5
Jan	0.88	1.15	1.16	0.93	1.01	1.20	0.96	0.93	1.00
Feb	1.03	1.00	0.91	0.96	0.94	0.97	0.93	0.97	1.12
Mar	1.61	1.11	1.29	1.37	1.39	1.19	0.94	1.11	0.92
Apr	1.33	1.49	1.80	0.88	1.15	1.05	0.91	0.88	0.76
May	1.07	1.16	0.96	0.92	0.90	0.93	0.87	1.08	0.98
Jun	0.91	0.72	0.81	0.88	0.75	0.93	0.83	1.20	1.06
Jul	1.08	1.10	1.03	1.09	1.25	0.97	1.34	1.27	1.11
Aug	0.98	0.88	0.88	0.98	0.88	0.88	0.87	0.76	1.04
Sep	0.85	0.87	1.19	1.01	1.07	1.08	0.95	0.97	1.00
Oct	1.24	1.19	1.41	1.01	1.05	1.22	1.00	0.92	0.81
Nov	1.05	1.05	1.06	1.14	1.13	1.09	1.06	1.09	1.05
Dec	1.25	1.42	1.41	1.08	1.05	1.33	0.86	0.88	0.90

Two sets of relative change factors were calculated for each GCM of the CMIP5 based on all RCPs, one including wet and dry spell lengths together with the mean monthly precipitation amount, and another by considering the mean monthly precipitation amounts only. The 1000 realizations of future daily precipitation time series for the GCMs/RCPs were simulated using each of the two sets of relative change factors were used to differentiate between the contributions of changes in the mean monthly precipitation amounts and changes in wet/dry spell durations.

The annual maximum precipitation (AMPs) of the realizations of future daily precipitation projections, obtained from the simulations based on CanESM2 with and without using RCFs related to wet/dry spell lengths, were used to estimate the expected values and 95% confidence intervals using the Generalized Extreme Value (GEV) distribution as shown in Figure 21. Although the RCFs of mean monthly precipitation amounts are the major contributors to the changes in the future daily precipitation values, the RCFs of wet/dry spell lengths can affect the

changes in the future daily precipitation values. The expected values and 95% confidence intervals of extreme precipitation quantiles for CanESM2 based on three RCPs seem to change when the RCFs of wet/dry spell lengths are used, particularly in longer return periods.

The uncertainty in determining the sign and magnitude of change in future extreme precipitation seems to be more dependent on the RCPs and time periods. For the CanESM2 and a 100-year return period as shown in Figure 21, the future expected precipitation intensities during 2041-2070 – using the RCFs related to wet/dry spell lengths for RCP2.6, RCP4.5, and RCP8.5, compared to the observed expected precipitation intensity of 115 mm/day during the baseline period – are 115, 96, and 123 mm/day, respectively. The corresponding future expected precipitation intensities, without using RCFs related to wet/dry spell lengths for RCP2.6, RCP4.5, and RCP8.5 are; 114, 84, and 107 mm/day, respectively. Future expected precipitation intensities, using RCFs related to wet/dry spell lengths during the time slices 2011-2040, 2041-2070, and 2071-2100, are 118, 95, and 96, respectively, using the RCP4.5 of CanESM2 and a 100-year return period. The corresponding future expected precipitation intensities without using RCFs related to wet/dry spell lengths into consideration for 2011-2040, 2041-2070, and 2071-2100 are 105, 84, and 96 mm/day, respectively, when the RCP4.5 of CanESM2 and a 100-year return period are considered. The results for HadGEM2-ES are shown in Appendix B.
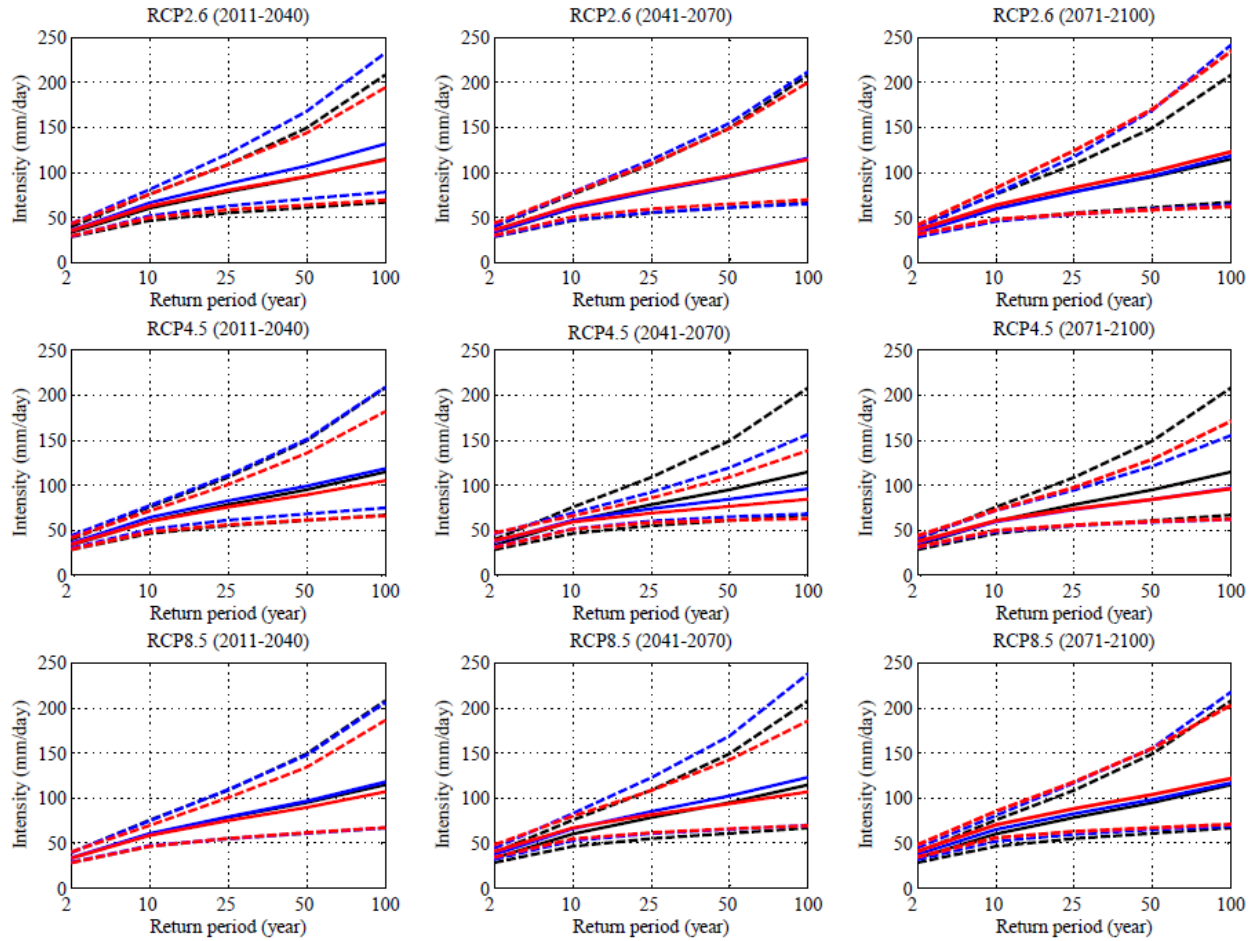
Figure 21: Variations in the future projections of daily AMP quantiles in the City of Saskatoon according to CanESM2 forced with three RCPs using two sets of change factors: with wet/dry spell (blue) and without wet/dry spell (red) effects. The expected quantiles (solid lines) and their 95% confidence intervals (dashed lines) are shown with the corresponding quantiles during the baseline period (black).

The AMP quantiles of 1000 realizations of daily precipitation obtained from LARS-WG based on CanESM2 and HadGEM2-ES, forced with three RCPs using both sets of RCFs, were calculated. Figure 22 shows the variability of the 2-year storm value (shown in the boxplots). The quantiles were estimated by fitting GEV distributions to the daily AMPs from LARS-WG. The figure for the 100-year return period is presented in Appendix E. The extreme daily precipitation quantiles seem to vary depending on whether wet/dry spell effects were considered or not in the case of both GCMs and all three RCPs. The sign and magnitude of variation due to the inclusion of RCFs related to wet/dry spell lengths depend largely on the choice of GCM/RCP, return period, and time slice. Hence, the future daily precipitation simulated with consideration of wet/dry spell effects shows differences from the same values simulated without considering the wet/dry spell effects, which might cause variations in the future IDF curves. Figure 22 also reveals that in most cases, the variabilities in the future IDF curves due to the choice of GCMs can be larger than those due to the inclusion/exclusion of wet and dry spells. Including the wet/dry spell effects in a 100-year return period, the future expected precipitation

intensity is 131 mm/day for CanESM2 and RCP2.6 during 2011-2040, compared to the observed expected precipitation intensity of 115 mm/day during the baseline period, which is 100 mm/day for HadGEM2-ES and RCP2.6 during 2011-2040. Considering a 2-year return period, the future expected precipitation intensity is 35 mm/day for CanESM2 and RCP2.6 during 2011-2040, compared to the observed expected precipitation intensity of 33 mm/day during the baseline period, which is 37 mm/day for HadGEM2-ES and RCP2.6 during 2011-2040. The variations due to the choice of GCMs seem to increase with an increase in the return period.
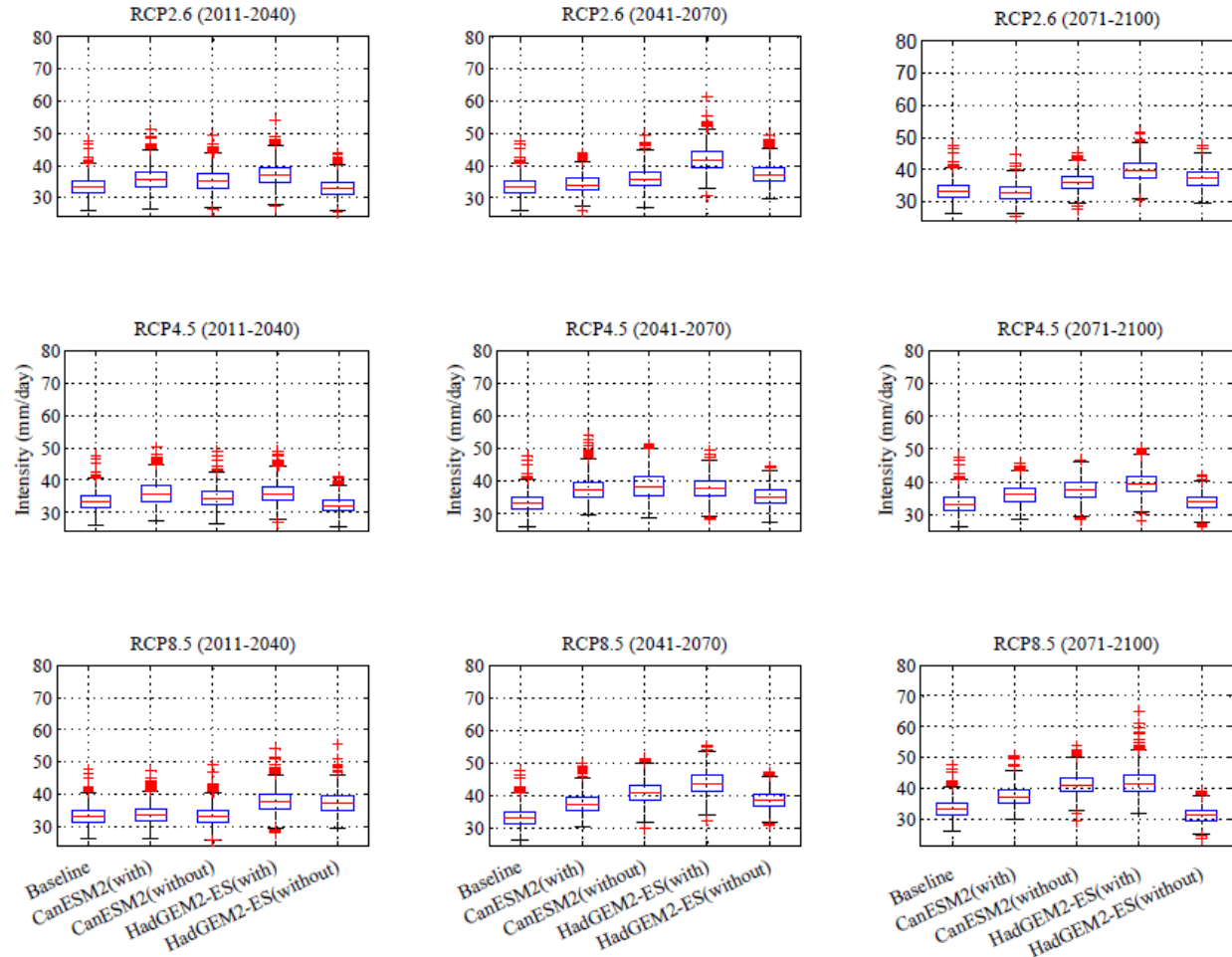
Figure 22: Variations in the future projections of daily AMP quantiles for 2-year return period in the City of Saskatoon according to CanESM2 and HadGEM2-ES forced with three RCPs using two sets of change factors, i.e. with wet/dry spell and without wet/dry spell effects along with the expected quantiles during the baseline period.

3.2. K-NN Disaggregation models

3.2.1. Selection of optimum window size
In order to develop the most appropriate K-NN hourly disaggregation model, the optimal window size (i.e. number of nearest neighbors to the current day of disaggregation) was selected using the observed daily and hourly precipitation data during the baseline period (1961-1990).

The K-NN hourly disaggregation model was used to disaggregate the observed daily precipitation to hourly precipitation sequences using 30 different window sizes (i.e., 3 days to 61 days) to identify the most appropriate memory length of the hydrological system for the City of Saskatoon. Each window size was used to generate the hourly precipitation sequences based on the daily precipitation values. Subsequently, the corresponding AMPs were identified for different durations (i.e., 1-hour to 24-hour). The simulated AMPs of various durations were then compared with the corresponding observed AMPs, and the performance of each window size was evaluated based on the Root Mean Squared Error (RMSE in Equation 6, where X= normalized AMPs and i=1, 2, 3,……,n (total number of years in the time series).

$$X = \frac{(AMP_i - Minimum\ value)}{(Maximum\ value - Minimum\ value)}$$ [6]

The RMSE values resulted from 30 widow sizes, as shown in Figure 23, were evaluated to determine the optimal window size for the K-NN hourly disaggregation model. Among the 30 windows, the window with 3 days (half window) on both sides of the current disaggregation day, i.e., a window of 7 days, provided the lowest RMSE of 0.12 when compared with other window sizes. Therefore, the optimal window size of 7 days was chosen for the K-NN hourly disaggregation model.
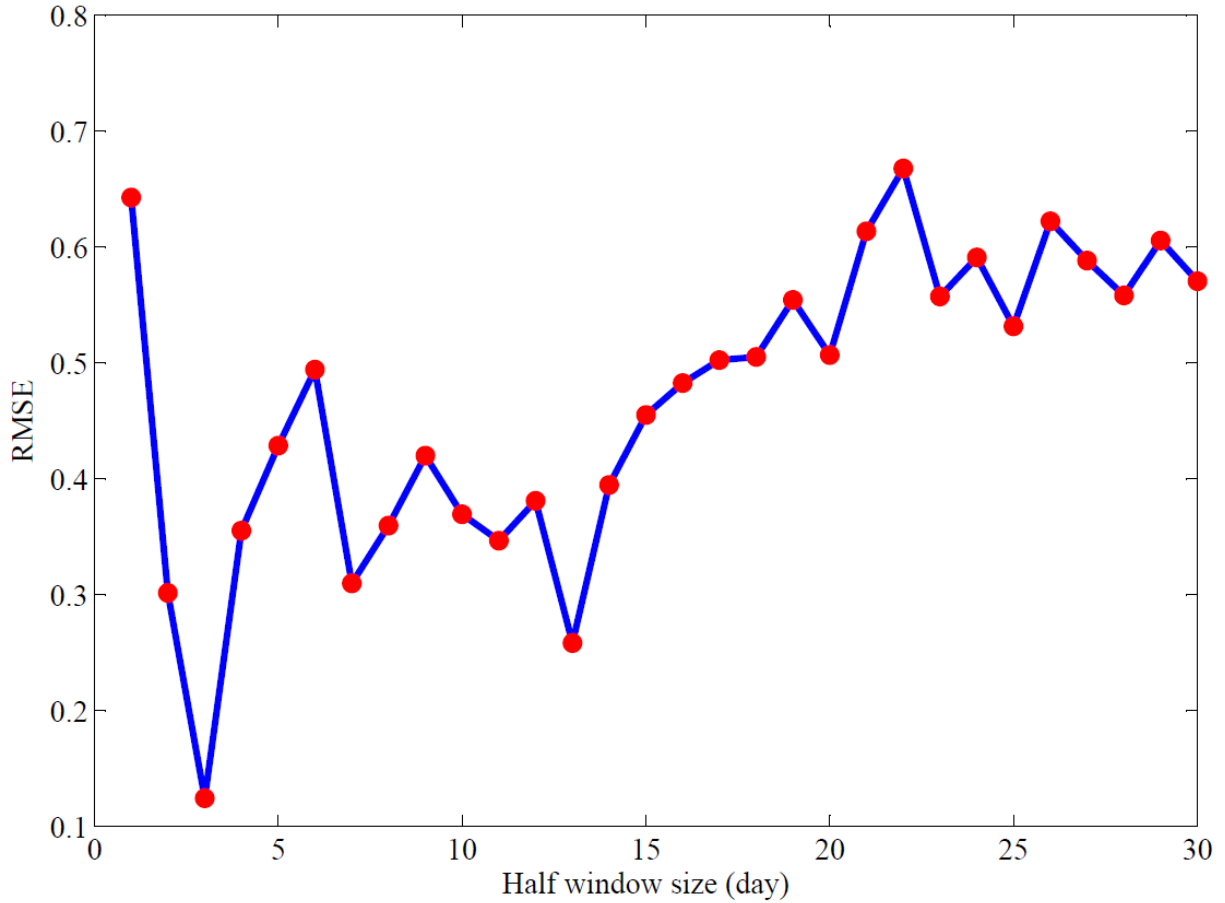
Figure 23: The performance of various windows obtained for selecting optimal window size for the K-NN hourly disaggregation model.

The K-NN hourly disaggregation model was used to simulate the observed hourly precipitation sequences both randomly and deterministically using the optimal window size. As far as the extreme precipitation quantiles were concerned, it was found that random selection of hourly precipitation sequences had no significant effect on the hourly disaggregation simulations. Also the use of deterministic or random sampling approach produced the same optimal window size based on the RMSE measure. However, random sampling can result in selecting a wide range of possible hourly disaggregated precipitation sequences than the deterministic sampling approach. Hence, the sampling in K-NN hourly disaggregation model using random selection approach of one sequence can be adopted using a single random realization, which reduces the modeling complexity and computational time tremendously without compromising the efficiency of the model.

The calculation of optimum window size was repeated with sub-hourly precipitation data. The RMSE values resulted from investigating 120 different widow sizes, shown in Figure 24, were evaluated to determine the optimal window size for the K-NN sub-hourly disaggregation model. Among the 120 windows, the window with 110 hours (half window) on both sides of the disaggregation hour, i.e., a window of 221 hours in total shows the minimum RMSE of 0.165.

However, a window size of 221 hours would be too large for a sub-hourly disaggregation model because it increases the model complexity as well as the computational time. Any smaller window with reasonably good performance (with reasonable RMSE) can be more acceptable choice for the K-NN sub-hourly disaggregation model. Keeping these criteria in mind, the half window size of 56 hours, i.e., a window of 113 hours shows an RMSE of 0.219. This window size is almost half of the optimum window size and has a very similar RMSE. Therefore, the optimal window size of 113 hours was chosen for the K-NN sub-hourly disaggregation model. Similar to the K-NN hourly disaggregation model, the K-NN sub-hourly disaggregation model was used to simulate the observed sub-hourly precipitation sequences randomly and deterministically using the selected optimal window size. These simulations revealed that the random selection of sub-hourly precipitation sequences had no significant effect on the sub-hourly disaggregation simulations, when compared with the deterministic selection, as far as the extreme precipitation quantiles were concerned.
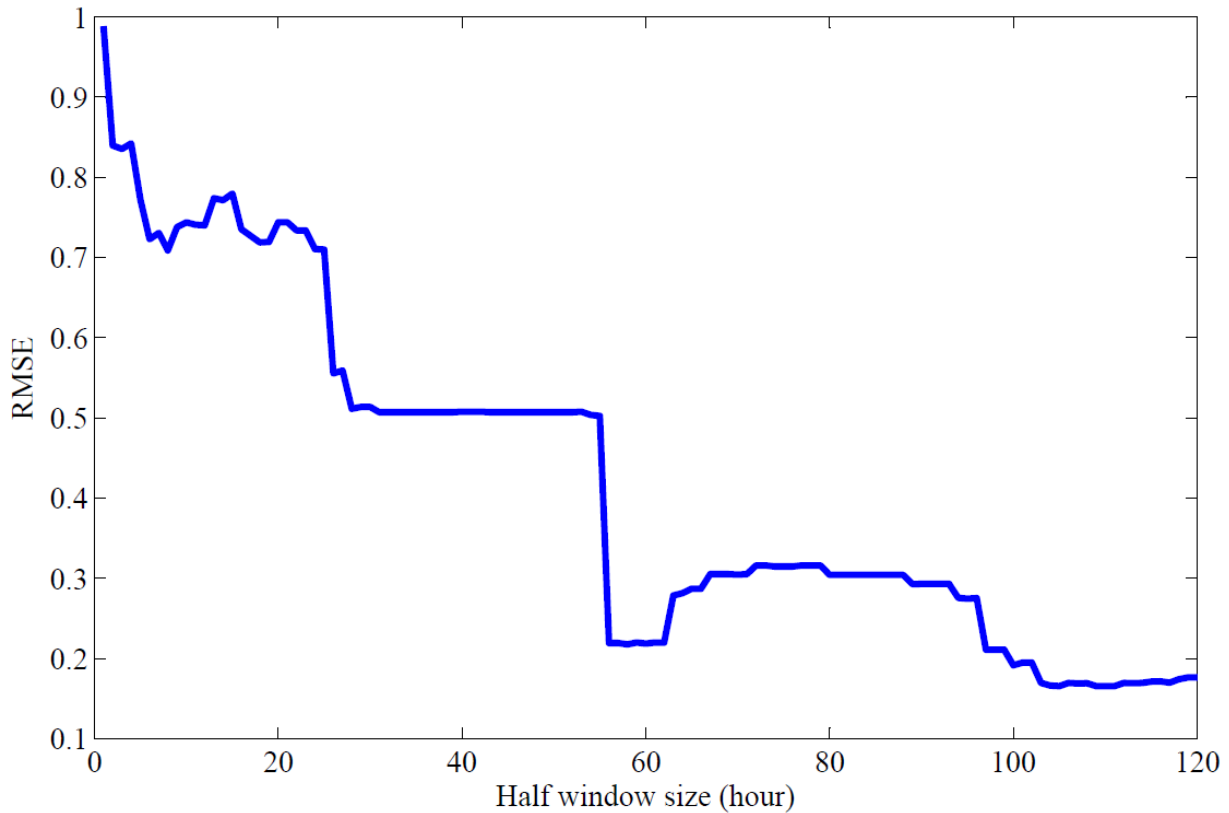
Figure 24: The performance of various windows obtained in selecting optimal window size for the K-NN sub-hourly disaggregation model.

3.2.2. Performance of the disaggregation models

The K-NN hourly disaggregation model was provided with 1000 realizations of daily precipitation obtained from LARS-WG and the Saskatoon's observed hourly precipitation data during the baseline period (1961-1990) to obtain 1000 realizations of hourly precipitation during the same baseline period. The disaggregation model used the optimal window size to generate 1000 realizations of observed hourly precipitation series. The performance of the calibrated

model is shown in Figure 25 during the spring and summer months (April-September). The K-NN hourly disaggregation model seems to simulate the observed mean hourly precipitation, the mean of maximum hourly precipitation, and the maximum extreme precipitation quite well except in June with regard to the maximum of the extreme precipitation.
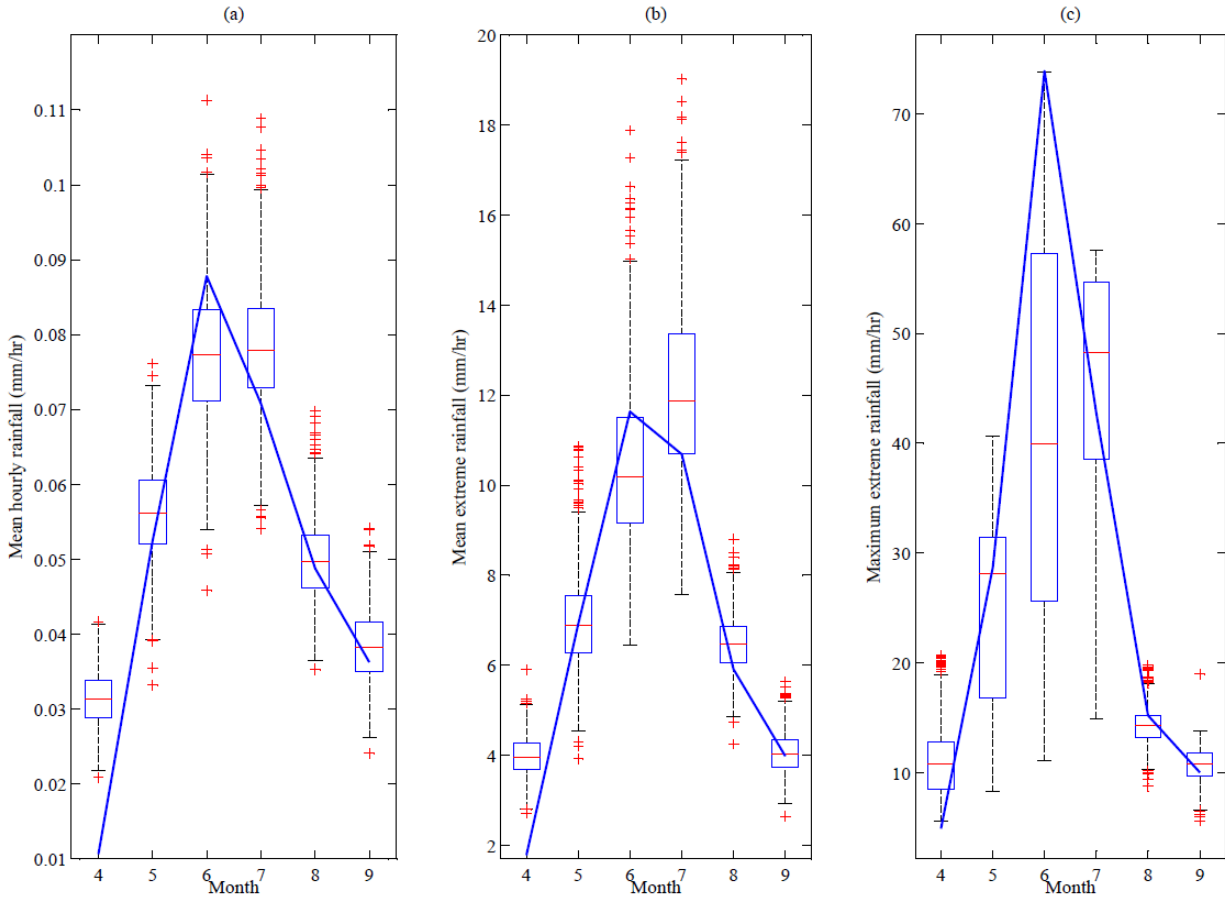
Figure 25: Performance of K-NN hourly disaggregation model based on the observed monthly properties (solid lines) and 1000 realizations of disaggregated (box plots) hourly precipitation time-series during the baseline period (1961-1990).

Similarly, the K-NN sub-hourly disaggregation model was provided with 1000 realizations of hourly precipitation obtained from the K-NN hourly disaggregation model and the Saskatoon's observed 5-min precipitation data during the period 1992-2009 (May-September) to obtain 1000 realizations of 5-min precipitation values during the same period. The disaggregation model used the selected optimal window size to generate 1000 realizations of the 5-min precipitation series. The performance of LARS-WG and the K-NN hourly and sub-hourly disaggregation models are shown in Figure 26 during the period 1992-2009 (May-September). The 5-min precipitation data from Acadia Reservoir rain gauge were aggregated to daily and hourly precipitation to conduct this part of the study.

Similar comparisons to those shown in Figure 20 and Figure 25 are shown in Figure 26(a-f) in addition to comparison between the observed and simulated 5-min precipitation in each of the

five months based on 1000 realizations obtained from K-NN sub-hourly disaggregation model during the period 1992-2009 (Figure 26g-i). All figures show that LARS-WG, K-NN hourly, and K-NN sub-hourly disaggregation models generated mean, mean extreme, and maximum extreme precipitation properties reasonably well during the period 1992-2009, except Figure 26(c), where LARS-WG appears to underestimate the maximum extreme precipitation in most of the months, which might contribute to the uncertainty in simulating the future maximum extreme precipitation. Only 14 years of 5-minute precipitation data were available for conducting this part of the study; however, 20-30 years of daily precipitation data are generally required in order to simulate synthetic daily precipitation series in LARS-WG and capture the climate properties of the precipitation station (Semenov and Barrow, 2002). Since the baseline period used in this study is 30 years (1961-1990), this issue of underestimation can be minimized during the baseline period as shown in Figure 20(c).
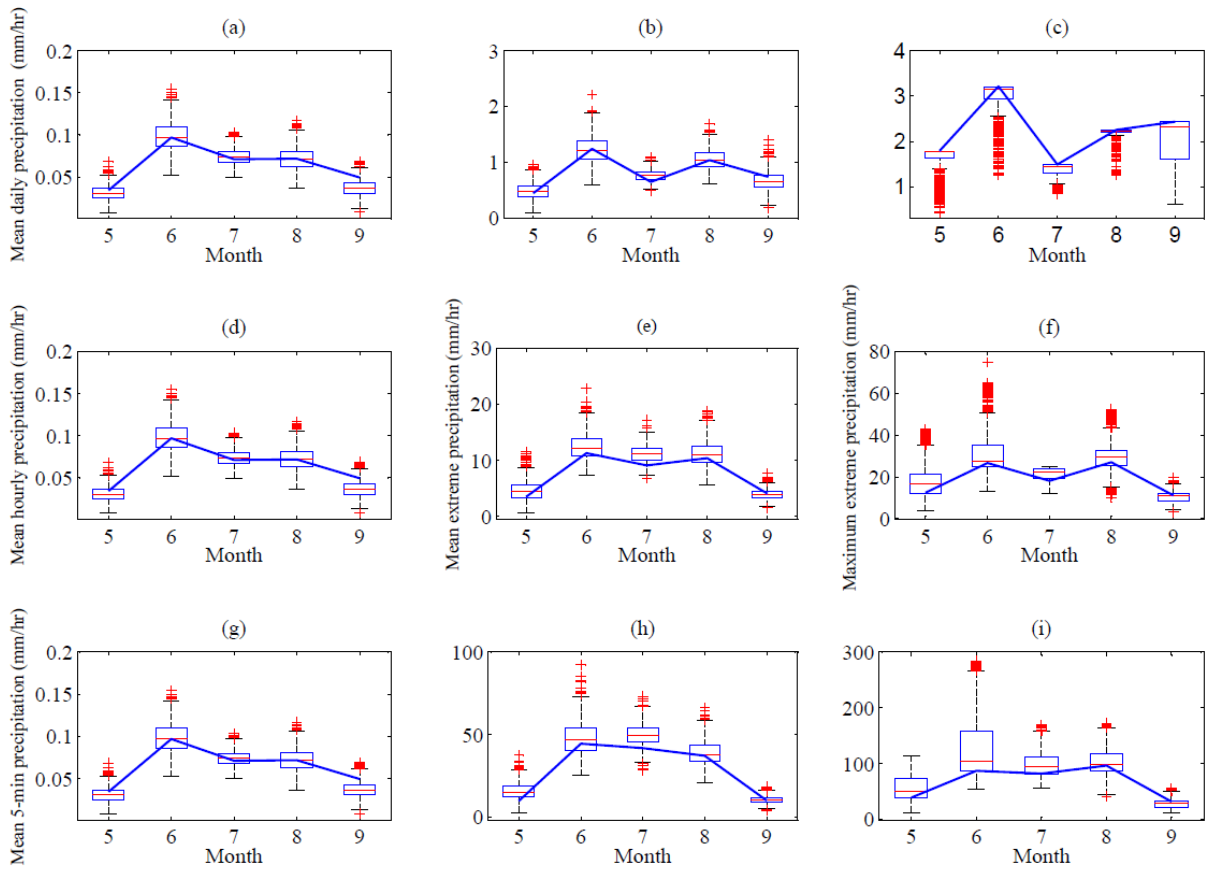
Figure 26: Performance of LARS-WG (1st panel), K-NN hourly disaggregation model (2nd panel), and K-NN Sub-hourly Disaggregation Model (3rd panel) based on the observed monthly properties (solid lines) and 1000 realizations of downscaled/disaggregated (box plots) daily, hourly, and 5-min precipitation time-series, respectively, during 1992-2009.

After developing/calibrating K-NN sub-hourly disaggregation model (Figure 26), an attempt was made to validate the K-NN sub-hourly disaggregation model as shown in Figure 27. The K-NN sub-hourly disaggregation model was provided with 1000 realizations of hourly precipitation obtained from the K-NN hourly disaggregation model during the baseline period (1961-1990)

and the Saskatoon's observed 5-min precipitation data during the period 1992-2009 (April-September) to obtain 1000 realizations of 5-minute precipitation during the baseline period. The simulated 5-min precipitation was aggregated to obtain 1000 realizations of hourly precipitation series during the baseline period. Thus, the performance of the validated model is shown in Figure 27 during the spring and summer months (April-September) of the baseline period.

Similar comparisons to those shown in Figure 25 are shown in Figure 27. Figure 27 (a-c) shows that the hourly (i.e., by aggregating 5-min precipitation to hourly time-scale) mean, mean extreme, and maximum extreme precipitation properties were successfully reproduced by the K-NN sub-hourly disaggregation model during the baseline period. The use of 5-min precipitation from a different time period seems to be applicable in generating 5-min precipitation of other time periods. Hence, the same 5-min precipitation series can be used to generate future 5-min precipitation in order to create future IDF curves based on the performance of the K-NN hourly and sub-hourly disaggregation models.
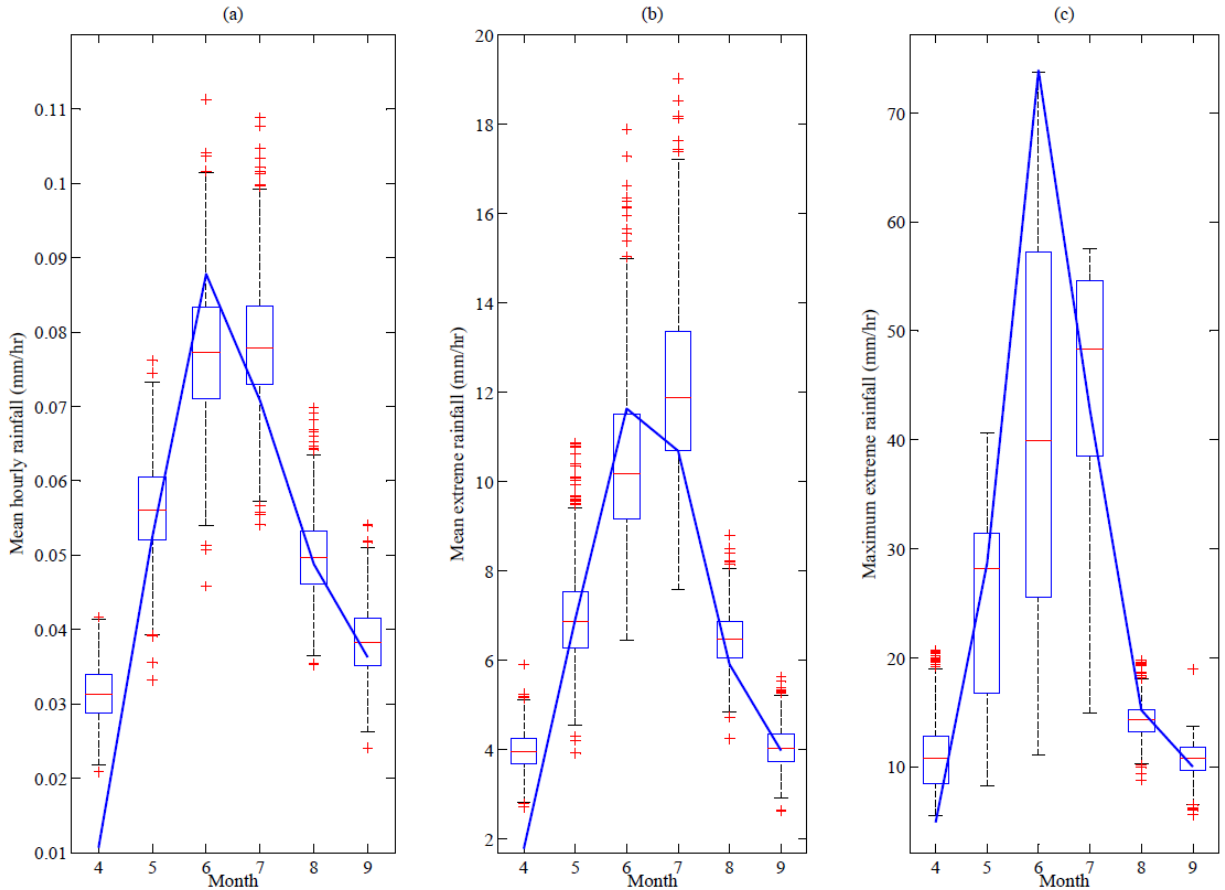
Figure 27: Performance of K-NN Sub-hourly Disaggregation Model based on the observed monthly properties (solid lines) of hourly precipitation time-series and 1000 realizations of disaggregated (box plots) 5-min precipitation time-series (aggregated to produce hourly precipitation) during the baseline period (1961-1990).

3.3. The IDF-curves under future climate scenarios

3.3.1. Variations obtained for CMIP5 climate models

Intensity-Duration-Frequency (IDF) curves for the City of Saskatoon were constructed using the GEV distribution for the baseline and the projection periods based on two GCMs (CanESM2 and HadGEM2-ES) and three RCPs (RCP2.6, RCP4.5, and RCP8.5) for nine selected durations (5-, 10-, 30-min, 1-, 2-, 3-, 6-, 18-, and 24-hour) and four different return periods (2-, 5-, 25-, and 100-year). The IDF curves are shown in Figure 28, and the design values during the baseline and projection periods are presented in Table 5 and Table 6, respectively. It can be seen that variations in the future precipitation quantiles, as represented by the IDF curves, are more significant at shorter durations and for longer return periods, which (the variations) seem to get intensified towards the end of the 21st century. The significant variations in the quantiles emphasize the importance of disaggregation to fine temporal resolution; e.g., 5-min precipitation as GCMs provide precipitation mostly in the daily temporal scale. The sign and the magnitude of future variations in extreme precipitations at different durations and/or return periods are highly sensitive to the selection of GCMs and/or RCPs.
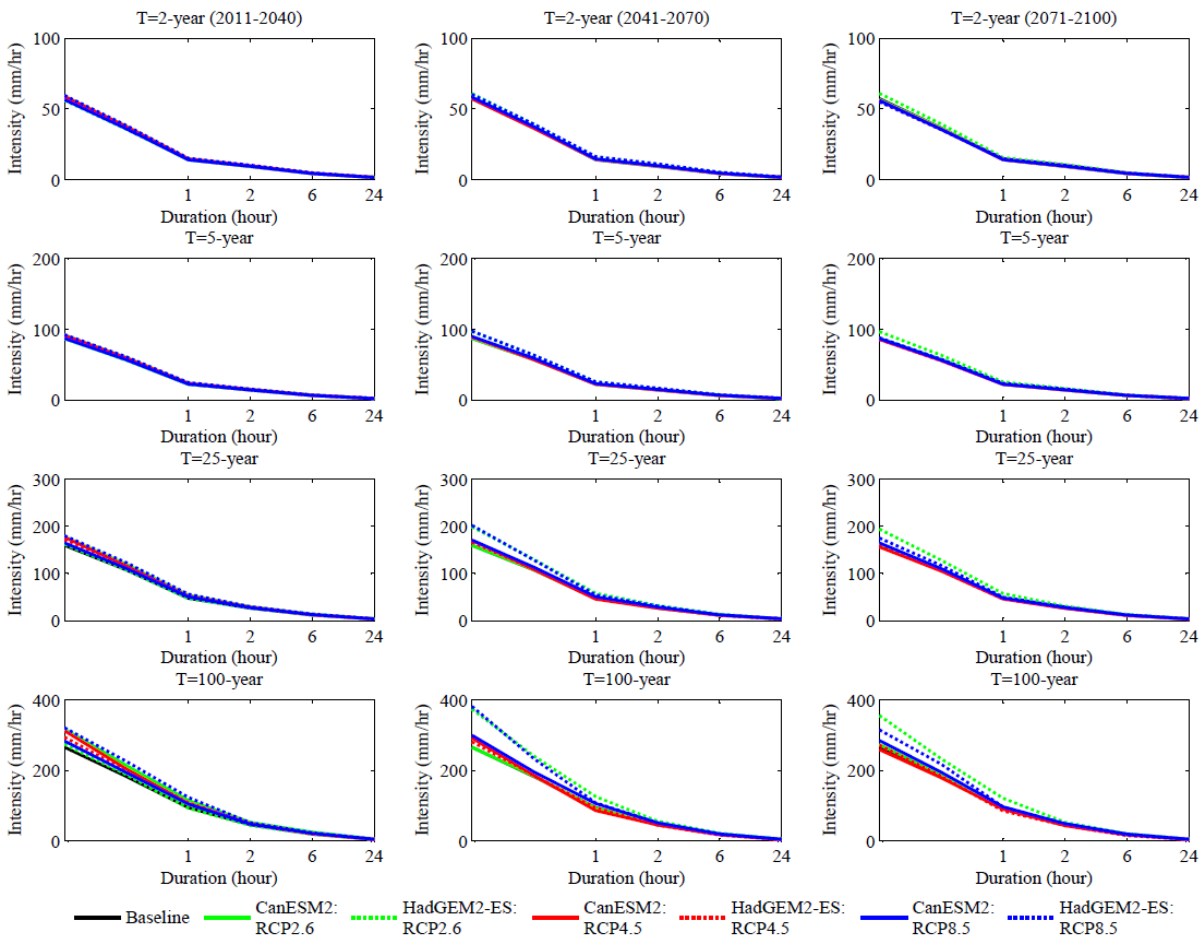
Figure 28: Variations in the future IDF curves in the City of Saskatoon according to CanESM2 and HadGEM2-ES based on three RCPs.

Generally, it is observed that there are changes (increase/decrease) in precipitation intensities in future compared to the baseline period (i.e., historical intensities) for all the return periods. The HadGEM2-ES: RCP8.5 IDF curve shows the highest relative change (i.e., 43.5%) in precipitation intensity for 5-min duration and 100-year return period during 2041-2070, while CanESM2: RCP2.6 shows the highest relative change (i.e., 31.5%) in precipitation intensity for 6-hour duration and 100-year return period during 2011-2040. HadGEM2-ES: RCP4.5 shows the biggest relative decrease (i.e., 20.8%) in precipitation intensity for 6-hour duration and 100-year return period during 2071-2100, while CanESM2: RCP4.5 shows the biggest relative decrease (i.e., 15.6%) in precipitation intensity for 24-hour duration and 100-year return period during 2041-2070. The relative change in precipitation intensities with respect to the historical intensities for the GCMs/RCPs is dependent on the duration, return period, and time periods during the 21st century.

The results based on two GCMs (CanESM2 and HadGEM2-ES) and three RCPs (RCP2.6, RCP4.5, and RCP8.5) show changes (increase/decrease) in the future IDF curves for the City of Saskatoon. However, the relative changes in the extreme precipitation intensities (represented by the IDF curves) with respect to the historical intensities is dependent on the duration, return period, and time slice. The future IDF curves at sub-hourly (e.g., 5-min and 15-min) durations show increase in future precipitation intensities for most of the GCMs/RCPs during the 21st century with a maximum value of 43% (for HadGEM2-ES: RCP8.5 for 5-minute duration and 100-year return period during 2041-2070) increase as compared to the historical intensities. The historical 5-min precipitation intensity during the baseline period (1961-1990) for 100-year return period in Saskatoon is 265 mm/hr, which might increase up to 320, 381, and 356 mm/hr as shown by the future IDF curves during 2011-2040, 2041-2070, and 2071-2100, respectively. The existing urban storm water collection systems are designed based on the historical IDF curves, so the projected increases in future sub-hourly precipitation intensities would make the urban systems more vulnerable when the variations in the future IDF curves are taken into account. However, the extent of the estimated vulnerability depends on the choice of GCMs/RCPs, return period, duration, and time slice.

Table 5: The precipitation intensity (mm/hr) during the baseline period (1961-1990) for various return periods.

Duration	Return period (year)			
	2	5	25	100
5-min	57.2	87.2	159.6	265.5
15-min	36.5	57.2	107.6	183.1
1-hr	13.9	22.2	47.4	94.5
2-hr	9.2	14.0	26.5	46.3
6-hr	4.2	6.4	11.7	19.6
24-hr	1.4	2.1	3.4	4.9

Table 6: The expected precipitation intensity (mm/hr) for CanESM2 based on three RCPs obtained from CMIP5 during the 21st century for various return periods.

	(2011-2040)				(2041-2070)				(2071-2100)				(2011-2040)				(2041-2070)				(2071-2100)			
	Return period (year)																							
	2	5	25	100	2	5	25	100	2	5	25	100	2	5	25	100	2	5	25	100	2	5	25	100
	CanESM2: RCP2.6												HadGEM2-ES: RCP2.6											
5-min	59	92	178	317	57	87	160	265	56	87	162	274	56	87	162	275	61	97	199	373	61	97	194	356
15-min	37	60	119	214	37	57	108	185	36	57	109	189	35	56	108	189	39	64	130	241	39	64	128	233
1-hr	15	24	54	115	14	22	47	94	14	23	48	93	14	22	47	93	16	26	58	126	16	25	57	121
2-hr	10	15	29	53	9	14	27	47	10	15	27	46	9	14	26	44	11	16	32	56	11	16	31	53
6-hr	4	7	14	26	4	7	12	19	4	6	11	19	4	6	11	19	5	7	14	22	5	7	13	21
24-hr	1	2	4	6	1	2	3	5	1	2	3	5	2	2	3	4	2	2	4	5	2	2	4	5
	CanESM2: RCP4.5												HadGEM2-ES: RCP4.5											
5-min	59	91	177	312	57	89	170	291	56	86	156	259	58	91	172	294	57	89	166	281	55	86	161	272
15-min	37	59	116	204	36	57	109	186	36	56	105	179	37	59	114	199	37	58	109	185	35	56	106	184
1-hr	15	24	52	106	14	22	45	86	14	22	46	90	14	23	52	109	14	23	47	94	15	23	46	85
2-hr	10	15	28	49	9	14	27	46	9	14	26	44	10	15	28	49	10	15	27	45	10	15	27	44
6-hr	4	7	13	21	4	6	11	18	4	6	11	17	4	7	12	21	4	7	11	17	5	7	11	16
24-hr	2	2	4	5	2	2	3	4	1	2	3	4	1	2	4	5	2	2	3	4	2	2	3	4
	CanESM2: RCP8.5												HadGEM2-ES: RCP8.5											
5-min	56	87	165	283	58	90	171	299	56	87	165	285	59	93	180	320	60	97	202	381	55	88	175	315
15-min	36	57	111	194	37	59	113	196	35	56	110	195	38	61	123	226	39	63	128	233	35	58	117	218
1-hr	14	23	50	105	14	23	51	106	14	22	48	97	15	25	56	124	16	26	54	108	15	24	49	96
2-hr	9	14	27	48	10	15	29	51	9	14	28	49	10	15	30	52	11	17	31	52	10	15	29	49
6-hr	4	6	12	22	4	7	12	20	4	6	12	20	5	7	13	23	5	7	12	18	5	7	12	18
24-hr	1	2	3	5	2	2	4	5	1	2	3	5	2	2	4	5	2	3	4	5	2	2	4	5

3.3.2. Variations obtained with the GP method and the K-NN hourly disaggregation model

The adopted downscaling/disaggregation (LARS-WG and K-NN) method was compared with the GP method developed by Hassanzadeh et al. (2014), and re-implemented in this study, in terms of variations in the constructed future IDF curves according to two GCMs and three RCPs for various return periods. As an example, a return period of 2-year is shown in Figure 29. Generally, the IDF curves constructed using two different approaches seem comparable in quantifying historical IDF curves as shown in Table 7. The GP method uses sets of equations evolved to map the global scale daily AMP values directly to the local scale daily and sub-daily AMPs (1 to 24 hrs durations). The GP method seems to be more accurate for larger return periods (i.e. 100-year) and at shorter durations. The historical precipitation intensity of 1-hr duration and 100-year return period is 84.6 mm/hr, which was simulated as 88.4 mm/hr and 84.7 mm/hr by two sets of GP extracted equations (based on CanESM2 and HadGEM2-ES output during baseline period) while the same was simulated as 105.2 mm/hr by the K-NN hourly disaggregation model. However, both methods reconstruct the historical IDF curves successfully during the baseline period (1961-1990) with less than 10% absolute error.
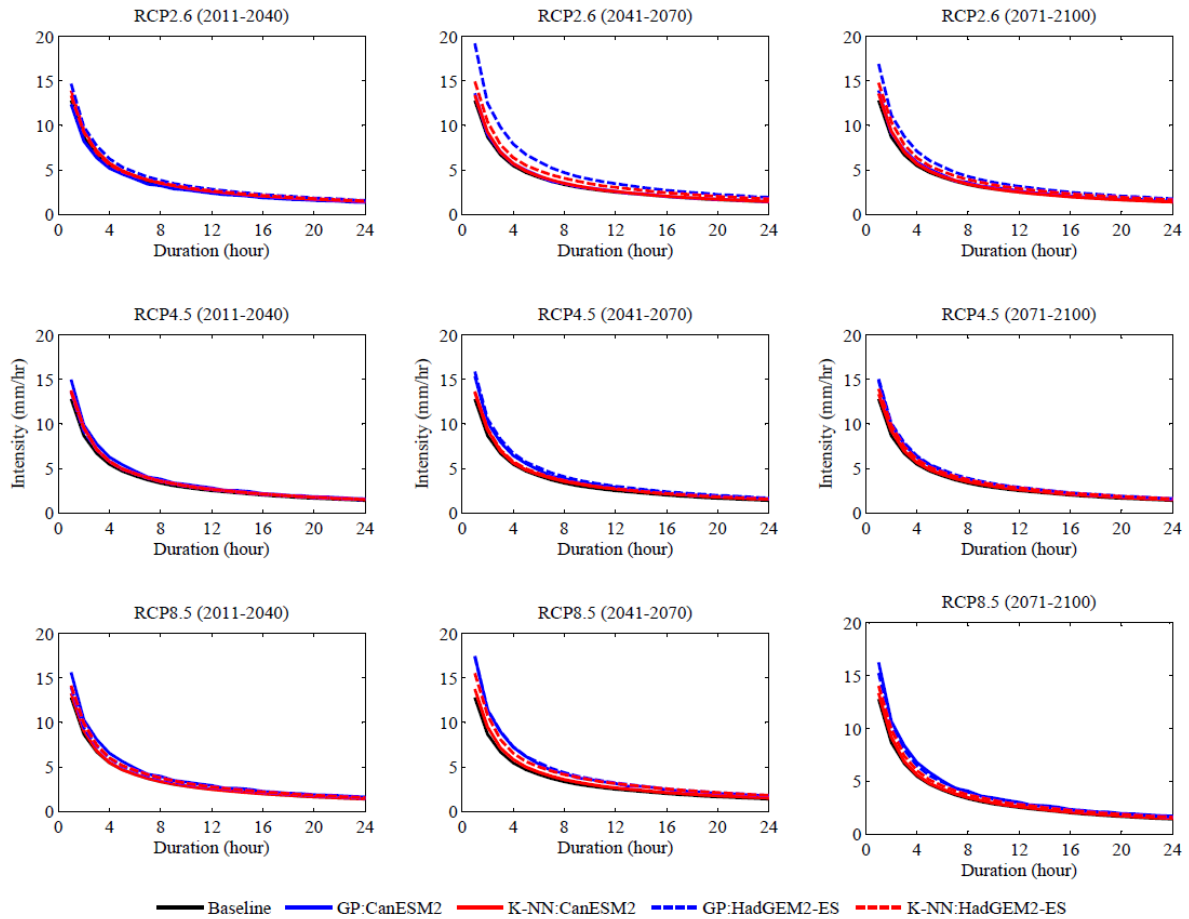
Figure 29: Comparison between the future IDF curves (2011-2100) according to CanESM2 (solid lines) and HadGEM2-ES (dashed lines) based on three RCPs and 2-year return period obtained using two different downscaling approaches, i.e. GP method and LARS-WG combined with K-NN Hourly Disaggregation Model.

Table 7: Comparison between the performance of K-NN hourly disaggregation model and GP method in simulating the expected precipitation intensity (mm/hr) during the baseline period (1961-1990) for various durations and return periods.

	Return period (year)				Return period (year)			
	2	5	25	100	2	5	25	100
Duration	Historical precipitation (1961-1990)	(observed)		hourly	Simulated hourly precipitation (Using K-NN Hourly Disaggregation Model) (1961-1990)			
1-hr	12.8	21.0	44.9	84.6	13.2	21.5	48.6	105.2
2-hr	8.7	13.5	25.5	42.7	9.0	13.8	26.2	46.2
3-hr	6.7	10.4	18.7	29.3	6.8	10.4	20.2	36.8
4-hr	5.5	8.5	15.0	22.8	5.5	8.4	15.9	28.1
6-hr	4.2	6.3	10.3	14.7	4.2	6.3	11.7	19.7
12-hr	2.5	3.6	5.4	7.3	2.5	3.7	6.2	9.6
18-hr	1.8	2.5	3.9	5.3	1.8	2.6	4.4	6.5
24-hr	1.4	2.0	3.0	4.1	1.4	2.1	3.4	4.9
	Simulated hourly precipitation (Using GP for CanESM2) (1961-1990)				Simulated hourly precipitation (Using GP for HadGEM2-ES) (1961-1990)			
1-hr	13.0	20.9	45.9	88.4	12.7	20.6	43.9	84.7
2-hr	8.6	13.3	25.0	41.7	8.7	13.2	25.6	43.5
3-hr	6.7	10.5	18.8	29.3	6.7	10.4	18.7	29.4
4-hr	5.4	8.4	14.9	22.9	5.5	8.4	14.9	23.0
6-hr	4.2	6.1	10.1	14.8	4.1	6.3	10.4	14.7
12-hr	2.5	3.5	5.3	7.1	2.5	3.6	5.5	7.2
18-hr	1.8	2.5	4.0	5.4	1.8	2.6	3.9	5.2
24-hr	1.4	2.0	3.1	4.1	1.4	2.0	3.1	4.2

The relative changes in future precipitation intensities with respect to the historical intensities range from a minimum of -8.9% to a maximum of 81.7% using the GP Method, whereas from -0.6% to 75.6% using the K-NN hourly disaggregation model as shown in

Table 8. The GP method shows the highest precipitation intensity of 154 mm/hr for CanESM2: RCP4.5 of 1-hour duration and 100-year return period during 2071-2100, while the K-NN hourly disaggregation model shows the highest precipitation intensity of 126 mm/hr for CanESM2: RCP2.6 of 1-hour duration, and 100-year return period during 2011-2040. Similar to the K-NN hourly disaggregation model, the changes in the future precipitation intensities obtained from the GP method depend on the selection of GCMs/RCPs, duration, return period, and time period. The difference in the results of the two methods in generating future precipitation intensities might be due to different approaches used for developing the disaggregation methodology, which contribute to the uncertainty in creating future IDF curves using different methods.

Generally, the IDF curves constructed using two different approaches (the GP-based method and the two stage method adopted in this study) seem comparable in quantifying variations in the future IDF curves. However, some differences were observed in the results produced by the two methods due to different underlying approaches used for developing the methods. The adopted two-stage downscaling/disaggregation method was based on the combination of a stochastic precipitation generator (LARS-WG) and a disaggregation model (K-NN) for generating continuous precipitation series, while the GP method was based on the genetic programming (GP) used to map the daily extreme precipitation qauntiles at the global scale to the corresponding daily and sub-daily extreme precipitation quantiles at the local scale. The AMP quantiles of various durations (1 to 24 hrs) extracted from the adopted method (K-NN and LARS-WG) are largely dependent on the downscaled daily precipitation series from the global to the local scale by LARS-WG as it could be the main contributor to the total uncertainty. On the other hand, the performance of the GP method entirely depends on how perfectly the extreme precipitation quantiles at the global scale were mapped to the same at the local scale in the form of data driven equations extracted from genetic programming (Hassanzadeh et al., 2014). So, the different approaches used in the two methods would contribute to quantifying the uncertainty in creating future (2011-2100) IDF curves, although the two methods seem to reconstruct the historical IDF curves successfully during the baseline period (1961-1990). The use of two methods provides two sets of IDF curves that cover a wider range of likelihoods associated with the future designs of urban storm water collection systems under the plausible climate change scenarios.

Table 8: Comparison between the K-NN hourly disaggregation model and the GP method in simulating the expected precipitation intensity (mm/hr) for CanESM2 based on three RCPs during the 21st century for various durations and return periods.

	GP Method												K-NN Hourly Disaggregation Model											
	(2011-2040)				(2041-2070)				(2071-2100)				(2011-2040)				(2041-2070)				(2071-2100)			
	Return period (year)												Return period (year)											
	2	5	25	100	2	5	25	100	2	5	25	100	2	5	25	100	2	5	25	100	2	5	25	100
CanESM2: RCP2.6																								
1-hr	12	18	34	60	14	22	46	82	14	23	43	67	14	23	55	126	13	22	48	103	14	22	49	101
2-hr	8	12	20	31	9	14	25	39	9	14	24	34	10	15	29	52	9	14	27	47	9	14	27	46
3-hr	6	9	15	23	7	11	19	28	7	11	18	24	7	11	23	44	7	11	20	36	7	11	20	36
4-hr	5	7	12	18	6	9	15	22	6	9	14	19	6	9	18	35	6	9	16	27	6	9	16	28
6-hr	4	5	8	12	4	6	10	14	4	6	10	13	4	7	14	26	4	6	12	19	4	6	11	19
12-hr	2	3	5	6	3	4	5	7	3	4	5	6	3	4	7	12	3	4	6	9	2	4	6	10
18-hr	2	2	3	5	2	3	4	5	2	3	4	5	2	3	5	8	2	3	4	7	2	3	4	7
24-hr	1	2	3	3	1	2	3	4	1	2	3	4	1	2	4	6	1	2	3	5	1	2	3	5
CanESM2: RCP4.5																								
1-hr	15	24	48	81	15	25	50	83	15	26	70	154	14	23	54	122	14	22	46	93	13	21	47	99
2-hr	10	15	26	39	10	15	26	40	10	16	35	66	10	15	28	49	9	14	26	45	9	14	26	44
3-hr	8	12	20	28	8	12	20	28	8	13	25	43	7	11	22	39	7	11	20	36	7	10	19	35
4-hr	6	9	15	22	6	10	16	22	6	10	20	33	6	9	17	31	6	8	16	27	6	8	15	25
6-hr	5	7	10	14	5	7	11	14	5	7	13	20	4	7	13	21	4	6	11	18	4	6	11	17
12-hr	3	4	5	7	3	4	5	7	3	4	6	9	3	4	7	10	3	4	6	8	3	4	6	8
18-hr	2	3	4	5	2	3	4	5	2	3	5	6	2	3	5	7	2	3	4	5	2	3	4	6
24-hr	2	2	3	4	2	2	3	4	2	2	4	5	2	2	4	5	2	2	3	4	1	2	3	4
CanESM2: RCP8.5																								

1-hr	16	23	37	50	17	28	59	105	16	25	49	84	13	22	51	120	14	22	52	115	13	22	49	105
2-hr	10	15	21	27	11	17	30	48	11	16	26	40	9	14	26	47	10	15	29	52	9	14	27	50
3-hr	8	11	16	20	9	13	22	33	8	12	20	28	7	11	21	39	7	11	22	40	7	11	21	40
4-hr	7	9	13	16	7	11	18	26	7	10	16	22	5	8	17	30	6	9	17	30	6	9	17	30
6-hr	5	7	9	11	5	7	12	16	5	7	11	14	4	6	12	22	4	7	12	20	4	6	12	20
12-hr	3	4	5	5	3	4	6	8	3	4	5	7	2	4	7	10	3	4	7	10	3	4	6	10
18-hr	2	3	4	4	2	3	5	6	2	3	4	5	2	3	4	7	2	3	5	7	2	3	4	7
24-hr	2	2	3	3	2	2	3	4	2	2	3	4	1	2	3	5	2	2	4	5	1	2	3	5

3.4. Uncertainty analysis

3.4.1. Uncertainty due to natural weather variability

The two-stage modeling scheme (downscaling-disaggregation) can be used to estimate various sources of uncertainty contributing to the projections of extreme precipitation quantiles represented by the IDF curves. One of the advantages of stochastic weather generators (e.g., LARS-WG) is their ability to synthesize a time series of a variable, such as precipitation, and generate multiple realizations of a variable such as precipitation. Such realizations can be considered representations of possible sequences of precipitation at the same location, which is a realistic way of representing the natural internal variability (caused due to stochastic nature) of precipitation. The effect of such variability (uncertainty) on the IDF curves due to the natural variability of precipitation can be quantified using AMP quantiles extracted from each of the 1000 realizations of daily precipitation obtained from LARS-WG during the baseline period for different return periods (2-, 5-, 25-, and 100-year) using the GEV distribution. The simulated AMP quantiles for various return periods were obtained by fitting GEV distribution to AMPs corresponding to the 1000 simulated 1000 realizations of daily precipitation, each realization having 30 years of daily precipitation. The mean of the AMP quantiles corresponding to the simulated 1000 realizations represents the expected intensity, while 97.5th and 2.5th percentiles represent the upper and lower bounds of 95% confidence interval. The observed AMP quantiles for various return periods were obtained by fitting GEV distribution to AMPs corresponding to the observed daily precipitation series.

In the case of the observed AMP quantiles, each of the three parameters of GEV distribution with three values were was used to obtain the expected intensity, upper, and lower bounds of the 95% confidence interval. Figure 30 shows the expected values and the 95% confidence intervals obtained from LARS-WG simulations as compared to the corresponding theoretical quantiles derived for the observed daily AMPs. The simulated expected values slightly overestimate the theoretical expected quantiles, while the simulated confidence intervals systematically slightly underestimate the theoretical 95% bounds particularly at larger return periods. Two points are worth noting in Figure 30: first, the stochastic realizations produced by LARS-WG approached the theoretical confidence interval of the GEV distribution, and second, confidence intervals should be treated and understood carefully as Figure 30 clearly demonstrates wide variability around the baseline/historical IDF curves. Therefore, such variability around projected future IDF curves should not be attributed to uncertainty due to climate change.
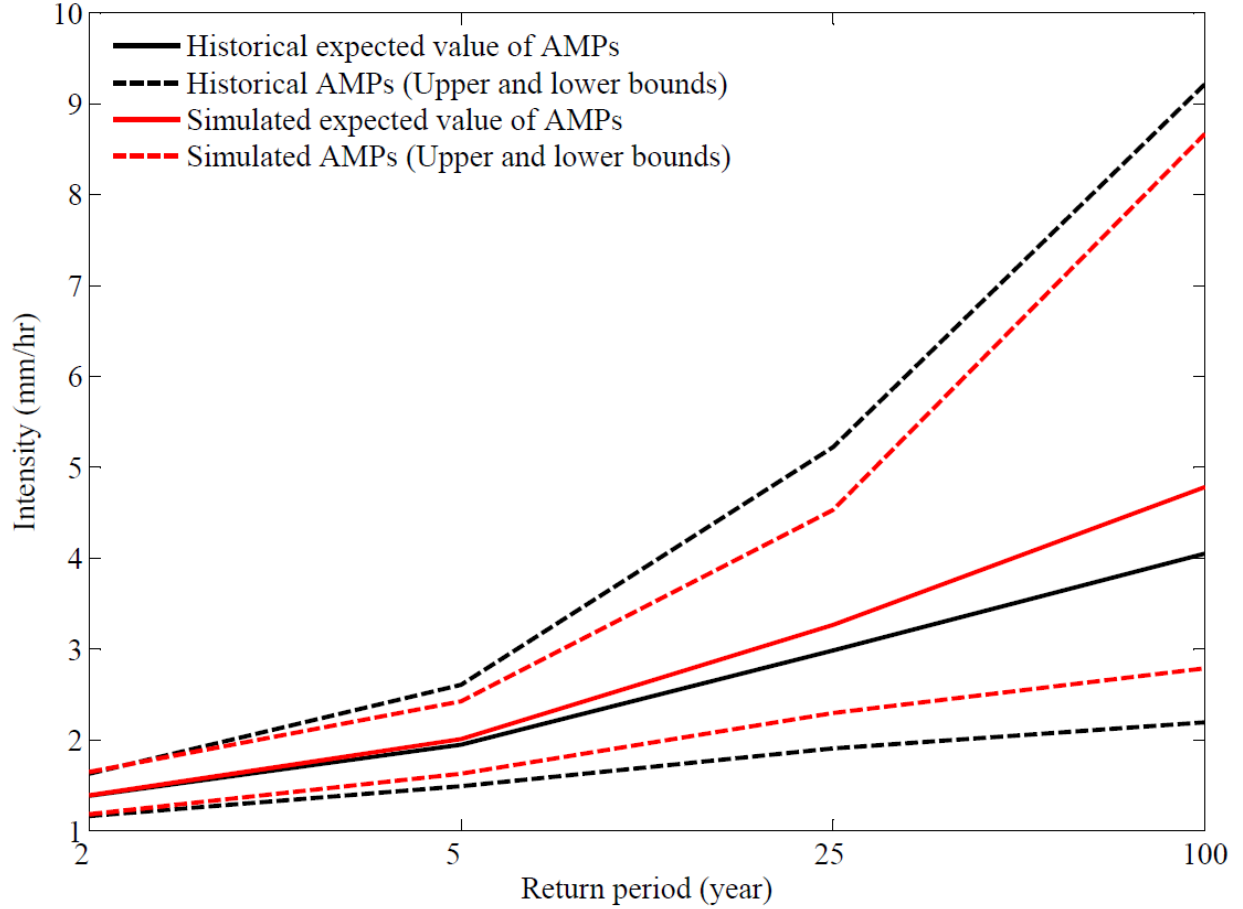
Figure 30: Theoretical GEV estimation of extreme quantiles based on the historical AMPs (black) and simulated AMPs obtained from 1000 realizations of daily precipitation time series during the baseline period using LARS-WG (red) with the corresponding 95% confidence intervals (dashed lines).

3.4.2. Uncertainty due to natural variability and disaggregation models

The K-NN hourly disaggregation model was provided with 1000 realizations of daily precipitation values obtained from LARS-WG to create 1000 realizations of hourly precipitation sequences during the baseline period. The simulated hourly AMP values were extracted from the disaggregated series and GEV distributions were fit to them. The mean and the 95% upper and lower bounds of 1000 realizations were obtained in a similar way as discussed previously.

Figure 31 shows a comparison between the simulated hourly AMP quantiles (expected value and 95% confidence intervals) and the corresponding historical hourly quantiles. Similar to the daily values, the simulated expected values slightly overestimate the historical expected quantiles, while the simulated confidence intervals slightly underestimate the theoretical 95% bounds, particularly in larger return periods, with some exceptions (3-, 6-, 8-, and 12-hour durations).
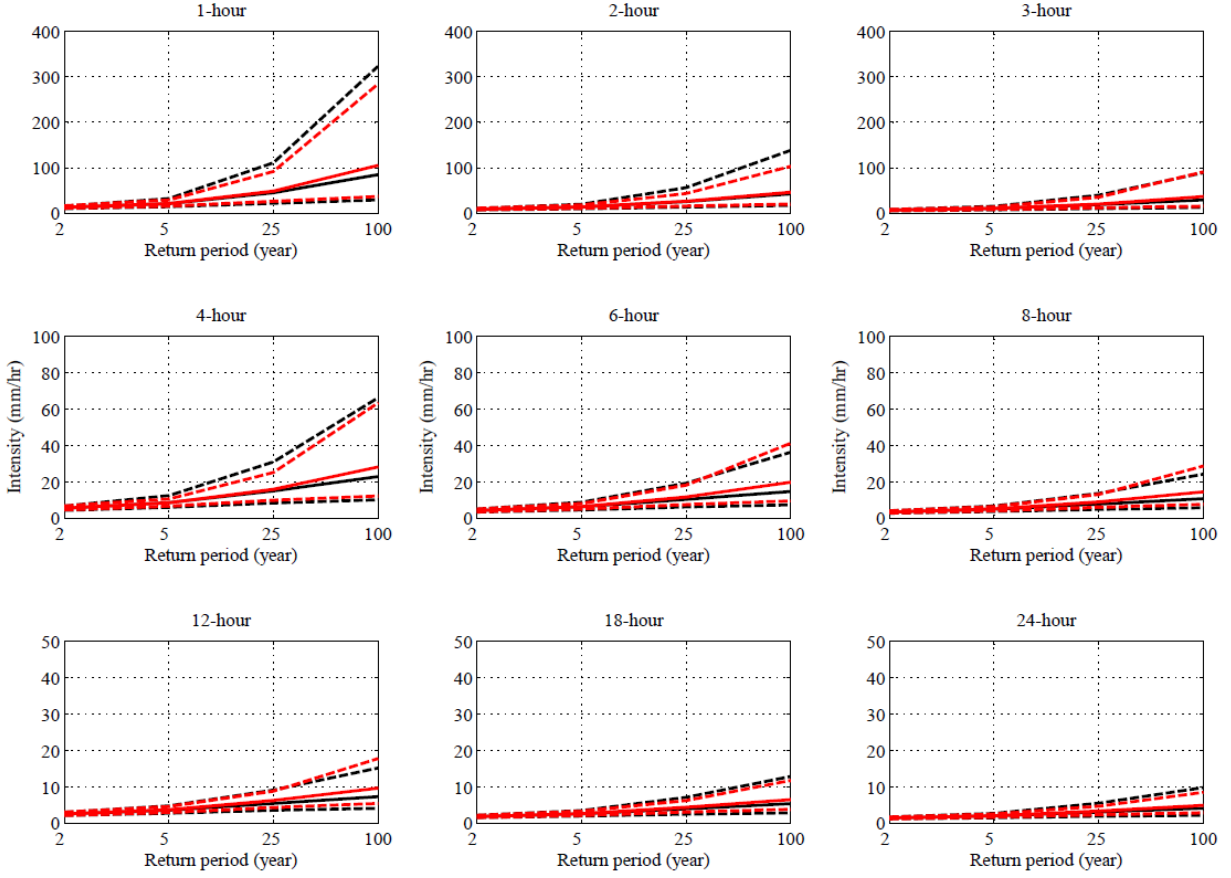
Figure 31: The IDF curves based on historical AMPs (black) as compared to the simulated values obtained from 1000 realizations of baseline time series from K-NN hourly disaggregation model and LARS-WG (red) with corresponding 95% confidence intervals (dashed lines).

The K-NN sub-hourly disaggregation model was provided with 1000 realizations of hourly precipitation obtained from LARS-WG and K-NN hourly disaggregation model to create 1000 realizations of sub-hourly (i.e. 5-min) precipitation sequences during the baseline period (1961-1990). The observed hourly precipitation was also provided to the K-NN sub-hourly disaggregation model to generate 5-min precipitation during the same baseline period (1961-1990), which was used to estimate the historical 5-min quantiles. A similar process, mentioned above for the hourly precipitation quantiles, was repeated with the 30 years of 5-min precipitation series, both for simulated 1000 realizations and the observed precipitation. Figure 32 shows a comparison between the simulated sub-hourly AMP quantiles and the corresponding sub-hourly quantiles for the gauged precipitation. In general, the simulated expected values and the lower bounds overestimate the gauged precipitation expected quantiles and their lower bounds in the shorter durations and longer return periods. However, the upper bounds of the simulated confidence intervals systematically underestimate the 95% upper bounds of the gauged precipitation in all durations and return periods, while the lower bounds systematically underestimate the theoretical lower bounds in the larger durations. The overestimation of the expected values seems to diminish as the storm durations increase.
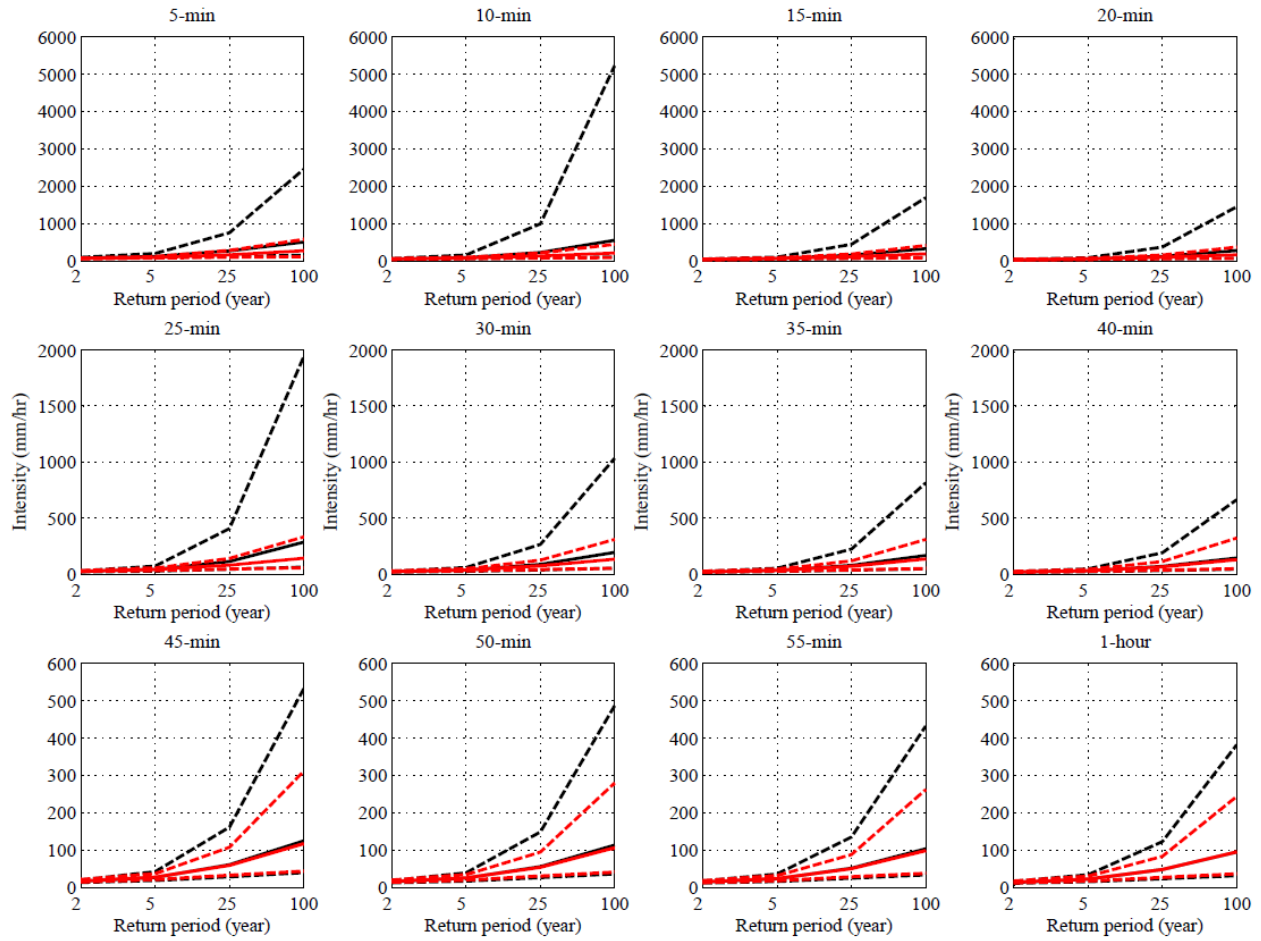
Figure 32: The sub-hourly IDF curves based on observed AMPs (black) as compared to the simulated values obtained from 1000 realizations of baseline time series from K-NN hourly and sub-hourly disaggregation models and LARS-WG (red) with corresponding 95% confidence intervals (dashed lines).

Regardless of the downscaling method, it is important to verify the results obtained by a downscaling method before using the results for purposes in order to reduce the associated risks. In this study, the results of the adopted two-stage downscaling-disaggregation method using LARS-WG and K-NN were compared with results obtained from a published method based on GP. Comparing the results of GP and K-NN can be considered a way to quantify uncertainty/variability due to disaggregation from daily to hourly precipitation. Hence, the expected hourly precipitation quantiles corresponding to 1000 realizations from LARS-WG and K-NN hourly disaggregation model , and the expected hourly precipitation quantiles from the GP method of 2-year return period for CanESM2 based on three RCPs during 2011-2040, 2041-2070, and 2071-2100 periods are compared in Figure 33. The results for HadGEM2-ES and other return periods are provided in appendix F. The internal variability of precipitation represented by 1000 realizations can be better explained by the box plots in Figure 33 and the values within the whiskers of the box plots seem to contain the simulations of the GP method for almost all the

cases. This would provide more confidence in using the simulations from the adopted method of this study as these are comparable to the results of the GP method.
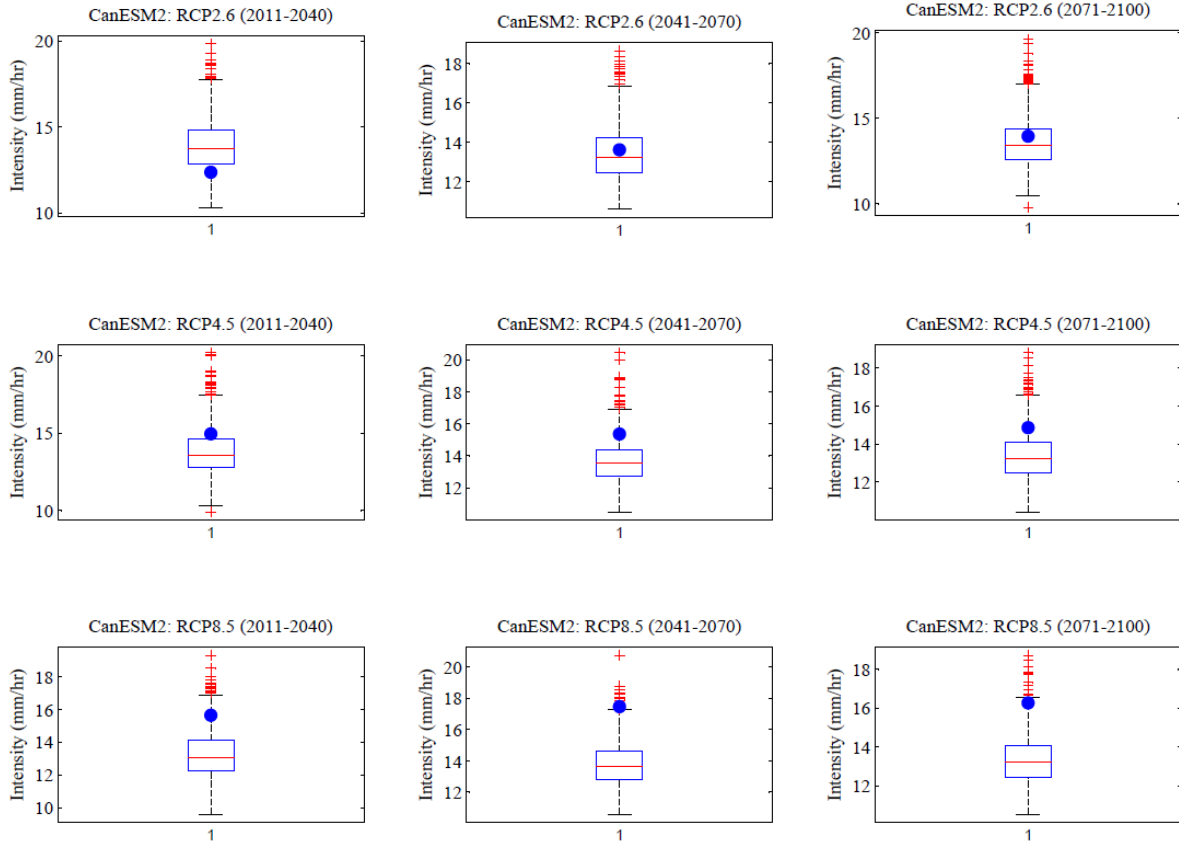
Figure 33: Expected 1-hr AMP corresponding to 1000 realizations from LARS-WG and K-NN hourly disaggregation model (boxplot), and the same from GP method (blue dots) of 2-year return period for CanESM2 based on three RCPs during the 21st century.

3.4.3. *Uncertainty in the projections of future IDF curves*

The K-NN sub-hourly disaggregation model was provided with 1000 realizations of hourly precipitation obtained from LARS-WG and the K-NN hourly disaggregation model to create 1000 realizations of 5-min precipitation sequences during the projection period (2011-2100) according to two GCMs (CanESM2 and HadGEM2-ES) and three RCPs. The simulated AMP quantiles were extracted from the disaggregated sub-hourly precipitation series related to various return periods using the GEV distribution as explained earlier.

Figure 34 shows comparison between the simulated sub-hourly AMP quantiles for both GCMs and the corresponding theoretical quantiles obtained from the GEV distribution fitted to the observed (historical) AMPs for 2-year return periods. The graphs representing other return periods and longer durations are provided in Appendix G. In general, uncertainty in the projections of future extreme precipitation quantiles increases at shorter durations and for longer return periods. Projections are highly sensitive to the choice of GCMs and/or RCPs. This includes uncertainty in projecting both the sign and the magnitude of future variations (relative change) in extreme precipitation quantiles at different durations and/or return periods.
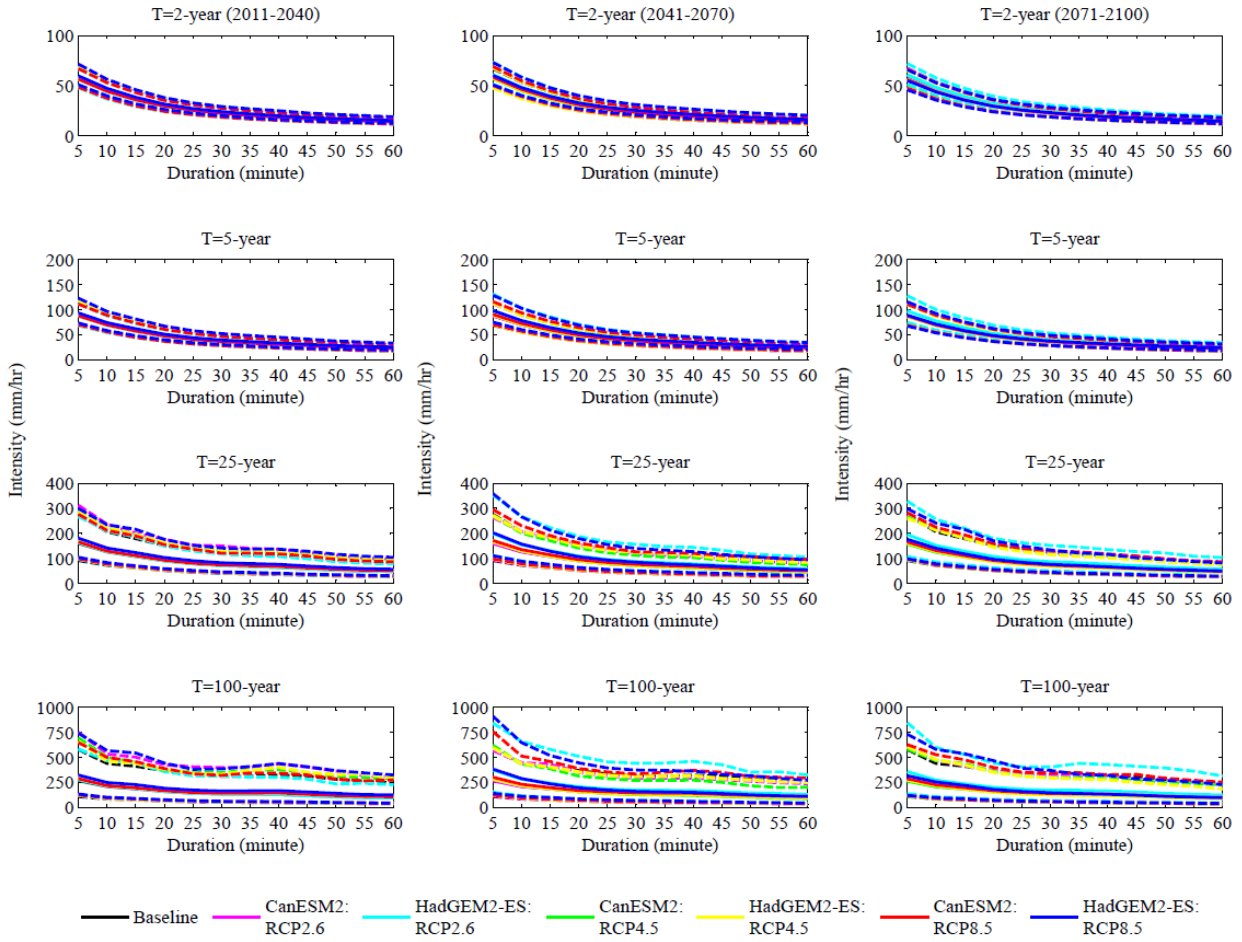
Figure 34: Uncertainty in the projections of future extreme precipitation quantiles based on two GCMs and three RCPs obtained from CMIP5 and quantified by using GEV shown as 95% confidence intervals (dashed lines) with expected quantiles (solid lines).

3.5. Discussion

Generally, it is observed that there are changes in fine-resolution precipitation intensities in future with respect to the precipitation intensities during the baseline period (i.e., historical intensities) for all return periods. When the expected precipitation quantiles are compared, HadGEM2-ES: RCP8.5 shows the highest relative change (i.e., 43%) in precipitation intensity for 5-min duration and 100-year return period during 2041-2070, while CanESM2: RCP2.6 shows the highest relative change (i.e., 25%) in precipitation intensity for 45-min duration and 100-year return period during 2011-2040. HadGEM2-ES: RCP4.5 shows the biggest relative decrease (11%) in precipitation intensity for 35-min duration and 100-year return period during 2071-2100, while CanESM2: RCP4.5 shows the highest relative decrease (9%) in precipitation intensity for 35-min duration and 100-year return period during 2071-2100.

The relative changes in precipitation intensity with respect to the historical intensities and the uncertainty bounds in the projections of future IDF curves for the GCMs/RCPs are dependent on the duration, return period, and time periods. These dependencies might be useful to consider while selecting the design values of storms (i.e., IDF curves) for the design of urban storm water collection systems in the City of Saskatoon. From a practical point of view, Table 9 provides an overall summary of possible changes in design values of rainfall intensities in Saskatoon due to climate change. The projected increase in future rainfall intensities intensifies at shorter durations and longer return periods. Shorter duration storms are of significance to minor system (e.g., street drainage inlets and storm sewers) and storms of longer return periods are of significance to major systems (e.g., storm detention ponds) (City of Saskatoon, 2012).

Table 9. Historical and projected rainfall intensities for selected durations and return periods of storms in Saskatoon. *Base* means historical values, *Min* means the lowest of future projection, and *Max* is the highest value of future projections. The "bold" values represent the projected highest change.

Duration	Intensity (mm/hr)											
	2-year			5-year			25-year			100-year		
	Base	Min	Max	Base	Min	Max	Base	Min	Max	Base	Min	Max
15 min	37	35	39	57	56	64	108	105	**130**	183	179	**241**
1-hour	14	14	16	22	22	26	47	45	**58**	94	85	**126**
2-hour	9	9	11	14	14	17	27	26	32	46	44	**56**

3.6. Model verification for the Stochastic rainfall disaggregation

We tested the proposed stochastic disaggregation procedures in two different modes, i.e. uncoupled and coupled with the LARS-WG model. In the uncoupled mode, we disaggregated historical daily rainfall totals during the baseline period (1961-1990) into hourly time-steps using 100 realizations of the proposed stochastic algorithm. Accordingly, we compared historical AMPs with the simulated envelope of AMPs during the baseline period. Figure 35 shows the results of this analysis for 1-hr, 3-hr, 6-hr, 12-hr, 18-hr and 24-hr rainfall durations. For each sub-daily duration, the simulated AMP envelope (grey area) contains the corresponding historical time series (black solid line). It should be noted that uncertainty bounds in the simulated envelopes are wider at shorter durations. For 1-hr AMPs, the simulated envelope might slightly overestimate extremely low AMPs (e.g., for 1-hr AMPs around 1965). The algorithm, however, can capture average and large AMPs during all hourly durations quite well.
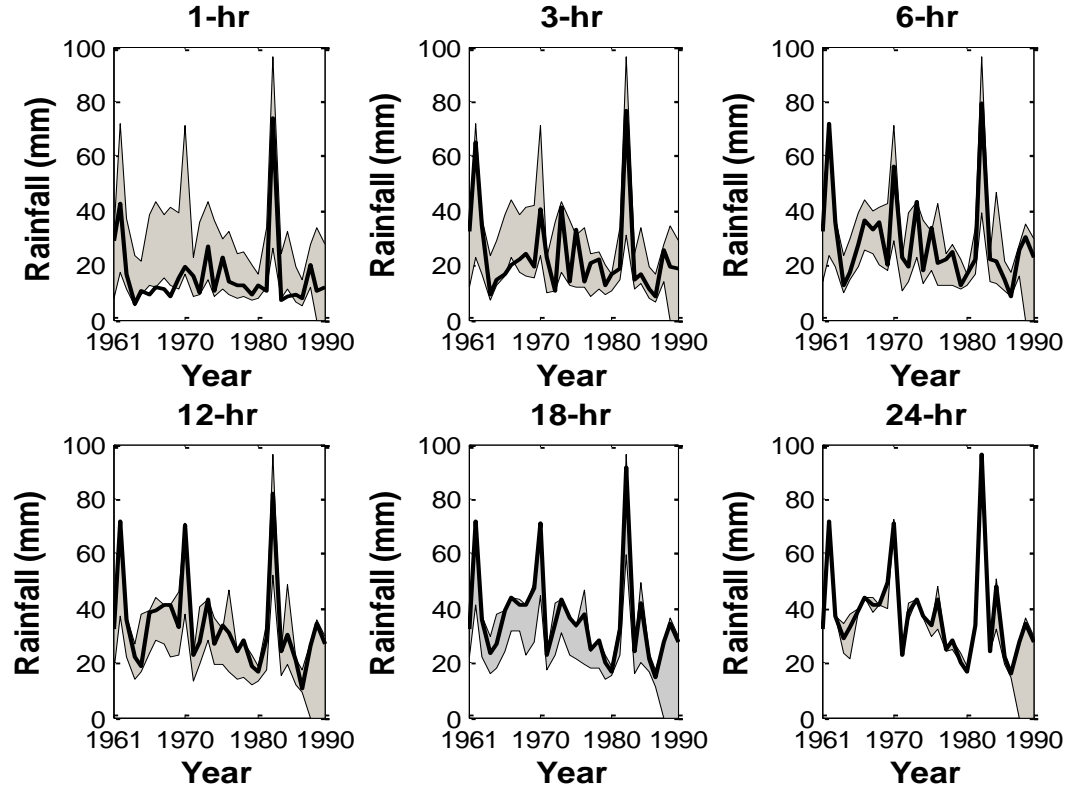
Figure 35. Comparison between historical AMPs (black solid lines) and corresponding simulated AMP envelopes (grey areas) obtained based on 100 realizations using the proposed stochastic disaggregation algorithm.

To further investigate the efficiency of the proposed stochastic disaggregation method, we considered a coupled experimentation, in which multiple daily LARS-WG realizations during the baseline period are introduced to the stochastic model and disaggregated into hourly rainfall profiles. Accordingly, we compared historical and simulated AMPs across various rainfall durations and/or return periods. Figure 36 shows the results of this experimentation, in which 100 realizations of the historical daily rainfall based on LARS-WG are disaggregated. Each daily realization is disaggregated 100 times, resulting into 10,000 realizations of hourly rainfall time series from 1961 to 1990. For each hourly realization, we extracted 1-hr, 3-hr, 6-hr, 12-hr, 18-hr and 24-hr AMPs and used the GEV distribution to quantify the AMPs across various return periods from 2-year to 100-year. In each panel of Figure 36, the black solid line shows the historical extremes based on fitting the GEV distribution to the observed AMPs. These lines can be compared with blue and red solid lines, which show the mean and median of simulated ensemble extremes, respectively. Similarly, dashed black lines in each panel show the theoretical 95% confidence intervals obtained by fitting the GEV distribution to the historical AMPs. These intervals can be compared with the grey envelope that represent the simulated 95% confidence interval obtained from the disaggregated ensemble. As it can be observed, the simulated envelopes overestimate theoretical lower bounds and underestimate theoretical upper bounds. This behavior is mainly due to the quality of LARS-WG simulations (see Figure 19) that propagate into shorter durations through disaggregation; nonetheless, the ensemble mean and median estimates match the historical extremes quite well, although they slightly overestimate the historical extremes during long return periods. In summary, the proposed method can

sufficiently reproduce the historical daily and sub-daily AMPs; and the efficiency of the proposed method is comparable with the KNN model. Moreover, the fully coupled stochastic downscaling/disaggregation framework can reproduce expected AMP qunatiles during the baseline period and across different durations and/or return periods.
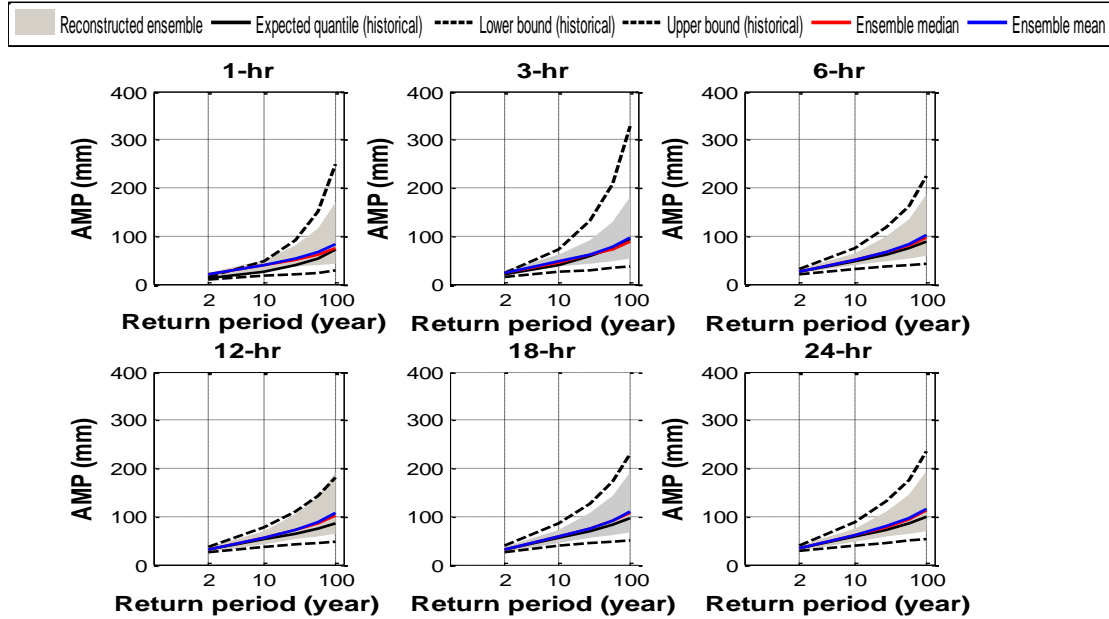
Figure 36. Comparison between observed and simulated extremes during baseline period and their corresponding 95% confidence intervals across various hourly durations and/or return periods.

3. 7 Future simulations of the Stochastic rainfall disaggregation

We linked the stochastic disaggregation method to downscaled realizations of Saskatoon's daily rainfall from 2011 to 2100 according to projections obtained from 6 GCM/RCP combinations considered in the course of this study. For each GCM/RCP combination, we considered 100 daily realizations obtained from LARS-WG and disaggregated each realization 100 times. This resulted into 10,000 realizations of hourly rainfall from 2011 to 2100. For each sub-daily duration, we extracted AMPs during three future control periods, i.e. 2011-2040, 2041-2070 and 2071-2100. We further used the GEV distributions to calculate extreme rainfalls and corresponding 95% confidence intervals across various hourly durations and/or return periods. Estimated extremes and their corresponding 95% confidence intervals were then compared with those obtained for the baseline period (Figure 36). Figures 37 and 38 show parts of this analysis for projections obtained from CanESM2 and HadGEM2-ES, respectively (see Tables H1 to H6 in appendix H for more extended results for each GCM/RCP combination). In these figures, rows and columns correspond to return periods (2-yr, 10-yr and 100-yr) and future control periods (2011-2040, 2041-2070 and 2071-2100), respectively. In each panel, solid lines represent the mean of the simulated ensemble of AMPs and dashed lines correspond to 95% confidence intervals, derived empirically from 10000 simulations. In addition, black lines are related to baseline simulations and red, green, and blue lines correspond to future projections based of RCP2.6, RCP4.5 and RCP8.5, respectively. Considering the overall results, projections largely vary depending on the particular GCM/RCP combination considered. Based on the results

65

obtained from 6 GCM/RCP combinations used, it can be concluded that the extreme rainfall quantiles in Saskatoon are subject to change during the 21st century; however, projected changes in sign, magnitude, and variability of AMPs differ across sub-daily durations and/or different return periods, and are highly sensitive to the choice of the GCM/RCP combination. In general, for all considered combinations, the magnitude and variability of change in AMPs are more pronounced at shorter duration and longer return periods. Comparing the results obtained from the two GCMs, projected changes and differences between three RCPs are stronger in HadGEM2-ES model.
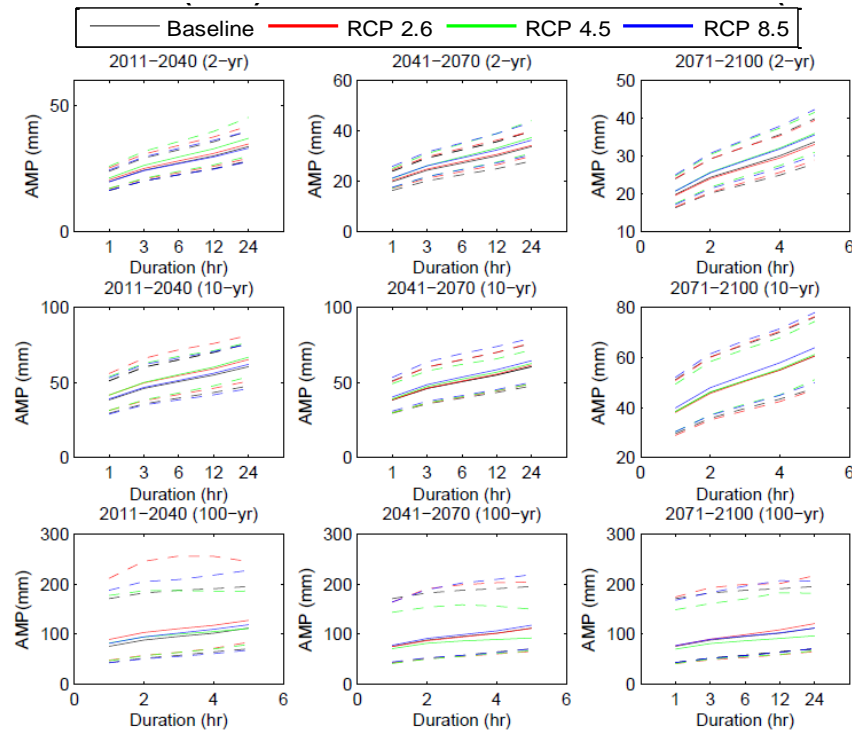
Figure 37. Comparison between baseline and future AMPs according to projections of CanESM2 across various duration and return periods.
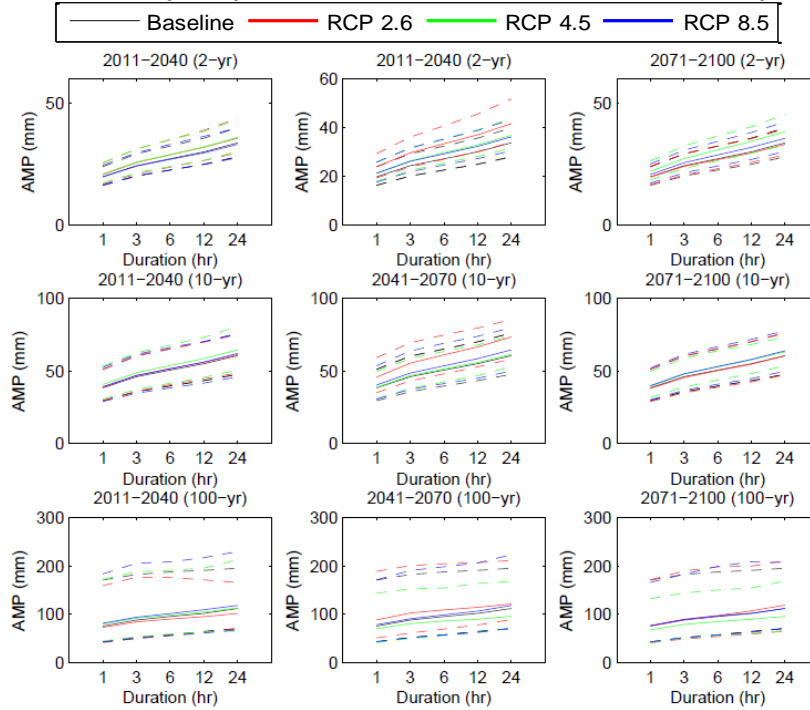
Figure 38. Comparison between baseline and future AMPs according to projections of HadGEM2-ES across various duration and return periods.

Having a large ensemble for future projections can enable a detailed analysis of future rainfall likelihood across different sub-daily durations and/or return period, as presented earlier in this report. This analysis extends the analysis provided in Figures 37 and 38 and look inside the ensemble projections within simulated envelopes. This analysis not only reflects the differences in future extreme rainfalls across different GCM/RCP combinations, but also can provide a basis for choosing a particular design rainfall according to the risk accepted in the design and operation of storm water system. Here, we just compare empirical distributions of 1-hr AMPs in three different return periods (for complete likelihood information please refer to the accompanying software tool (SaskIDF)). Figures 39 and 40 show this analysis for CanESM2 and HadGEM2-ES, respectively. In both figures rows and columns correspond to return periods (2-yr, 10-yr and 100-yr) and future time episodes (2011-2040, 2041-2070, and 2071-2100), respectively. In each panel, blue, green, and red lines correspond to RCP2.6, RCP4.5, and RCP8.5, respectively. While the simulated envelops can be almost similar in some corresponding cases, the empirical characteristics of simulated envelopes can be largely different from one-another. Moreover, the differences across different GCMs, forced with a particular RCP, can be quite substantial, highlighting a large uncertainty in the future projections obtained from GCMs. This can reflect the need for considering the IDF curves obtained from various GCM/RCP combinations and analyzing the corresponding likelihood information to choose a sub-daily design storms based on the risk accepted in design and operation.
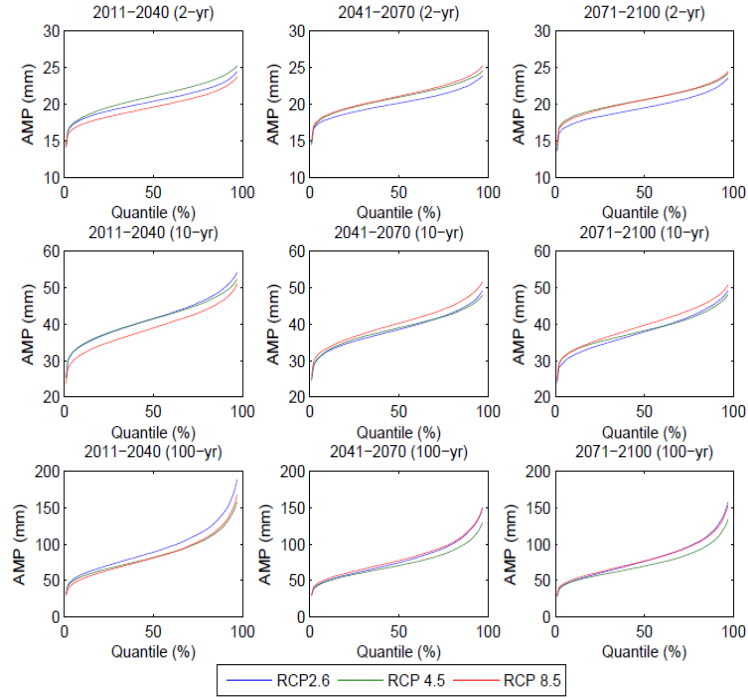
Figure 39. Comparison between future 1-hr AMPs according to projections of CanESM2 across three different RCPs (2.6, 4.5 and 8.5), three different control periods (2011-2040, 2041-2070 and 2071-2100) and three different return periods (2-yr, 10-yr and 100-yr).
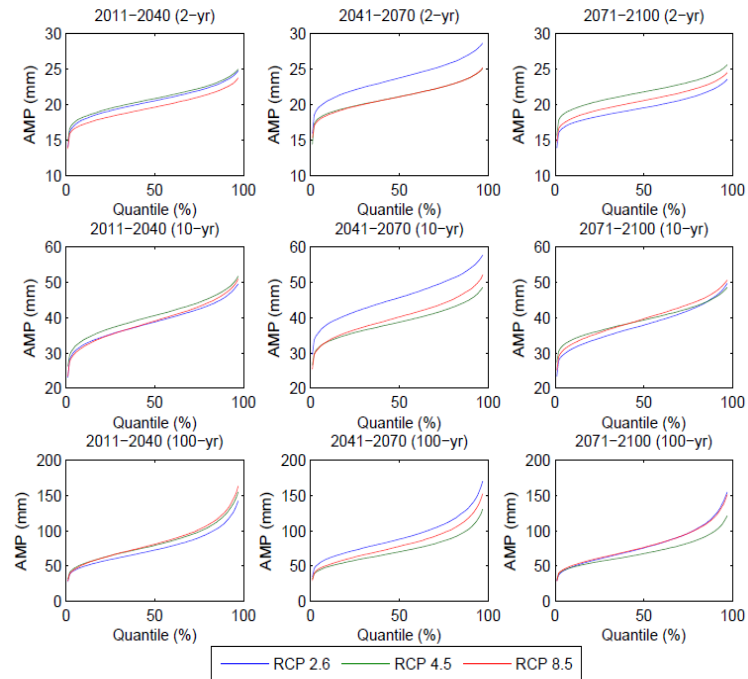
Figure 40. Comparison between future 1-hr AMPs according to projections of HadGEM2-ES across three different RCPs (2.6, 4.5 and 8.5), three different control periods (2011-2040, 2041-2070 and 2071-2100) and three different return periods (2-yr, 10-yr and 100-yr).

4. CONCLUSIONS AND RECOMMENDATIONS

4.1. Conclusions

The two-stage downscaling-disaggregation method is a promising approach for generating long records of hourly and sub-hourly precipitation and constructing a set of IDF curves for design purposes in Saskatoon. This approach also enabled the quantification of uncertainties due to the natural internal variability of precipitation, and enabled a comparison with the GP method to quantify uncertainty in the disaggregation methods.

LARS-WG performed well in reproducing the mean daily precipitation, mean extreme daily precipitation, and maximum extreme daily precipitation, underestimating variability of the maximum extreme daily precipitation only in the month of June. Including the distributions of wet and dry spell lengths helped in widening the range of variabilities of extreme precipitation generated by LARS-WG. Compared to a historical (baseline) AMP value of 117 mm/day for a 100-year storm, a maximum value of 144 mm/day was projected for the 2011-2040 period with CanESM2 and RCP2.6.

For the K-NN method of disaggregation, optimum window sizes for hourly and sub-hourly disaggregation models were found to be 7 days and 113 hours, respectively. Based on the sub-hourly precipitation series, it was found that variations in the future extreme precipitation quantiles, as represented by the IDF curves, are more significant at shorter durations and for larger return periods when compared to historical IDF curves. The variations in future extreme precipitation quantiles seem to intensify toward the end of the 21st century. The sign and the magnitude of variations in future extreme precipitation quantiles at different durations and/or return periods are highly sensitive to the selection of GCMs and/or RCPs.

A 15-minute storm with historical precipitation intensities of 37 mm/hr and 183 mm/hr for 2-year and 100-year return periods, respectively, is projected to intensify to values of 39 mm/hr and 241 mm/hr. The same for a 1-hour storm are projected to increase to 16 mm/hr and 126 mm/hr from historical values of 14 mm/hr and 94 mm/hr for the 2-year and 100-year return periods, respectively. The intensification is apparently more pronounced for shorter durations and longer return period storms.

In general, uncertainty in the projections of future extreme precipitation quantiles increases at shorter durations and for longer return periods. Compared to an intensity of 265 mm/hr for a 5-minute historical storm with a 100-year return period, an intensity of 317 mm/hr was projected for the 2011-2040 period with CanESM2 and RCP2.6, while an intensity of 275 mm/hr was projected for the same period with HadGEM2-ES and RCP2.6. During 2041-2070, the same return period storm is projected to intensify to values of 281 mm/hr and 381 mm/hr by RCP4.5 and RCP8.5, respectively, based on HadGEM2-ES. Compared to a 1-hr storm with a historical precipitation intensity of 84 mm/hr for a 100-year return period, an intensity of 84.6 mm/hr was projected for 2071-2100 with HadGEM2-ES and RCP2.6 using a GP-based downscaling method, while an intensity of 140 mm/hr was projected for the same period with the same GCM/RCP using the LARS-WG and K-NN-based downscaling-disaggregation method.

The contribution of internal precipitation variability, represented by 1000 realizations using LARS-WG, to the uncertainty of AMP values should be taken into account and understood carefully. These realizations provide a wider uncertainty in future projections than other sources of uncertainty. However, a similar wide range of variability in the constructed IDF curves was produced during the baseline (historical) period; therefore, the uncertainty cannot be attributed to possible climate change. If such variability was always present, and the historical IDF curves were successfully employed, it is logical to consider this source of projected future variability as a source of additional information. Thus, the mean of the realizations can be considered for representation of the IDF curves; this is the approach adopted in this study for assessing future values of AMPs.

4.2. Limitations of the study

The assumptions and limitations of the current study are as follows.
- The development of the K-NN sub-hourly disaggregation model used only 14 years of 5-minute precipitation data, which might not be optimum for model calibration and validation. This was due to the data recorded over a limited time period (1992-2009 with some missing years).
- Out of eight rain gauges in Saskatoon, only sub-hourly precipitation from the Acadia Reservoir rain gauge was considered in this study. This might not adequately represent the spatial variability in precipitation throughout the city; thus caution should be exercised in deciding on design criteria for urban storm water collection systems based on the variations observed in the future IDF curves in this study. However, the precipitation, when available, from any rain gauge can easily be included in the two-stage downscaling-disaggregation method adopted in this research. The general method adopted in this study can be applied to any rain gauge in the city considering any other GCM/RCP for constructing multiple sets of future IDF curves in order to produce a wider range of variations for future extreme precipitation quantiles in Saskatoon.
- Two GCMs (the Canadian CanESM2 and the British HadGEM2-ES) were considered in this study, assuming that the two GCMs and the corresponding six RCPs (RCP2.6, RCP4.5, and RCP8.5) with multiple realizations would cover a wide range of variability, which was assumed to be sufficient to investigate the adopted two-stage modeling approach. However, the two-stage modeling approach adopted in this research can be implemented using other multiple GCMs.
- Only LARS-WG was adopted as a downscaling technique. Other downscaling approaches, as presented earlier, can be used for better quantification of uncertainty due to the downscaling process.

4.3. Recommendations

For improving the results of the research conducted in this study and for gaining more confidence in its recommendations, it is recommended that the current study be extended in the following ways:
- Inclusion of several other Global Climate Models (GCMs) available through PCMDI under CMIP5 to better understand the impact of climate change on the IDF curves in the City of Saskatoon, with better estimation of uncertainty due to GCMs using a multi-

model ensemble. This is not difficult, given the framework already developed in this study.

- Improvement in the collection of fine-resolution precipitation data at various gauges of the city should be done by performing quality check of the data, followed by spatial analysis to construct a representative precipitation record of fine temporal resolution.
- The study may consider dynamical downscaling methods using multiple RCMs, and comparing the results with the statistical downscaling methods adopted in this study.
- There is a body of literature (Westra et al., 2014) suggesting that intensification of sub-daily extreme rainfall intensities occurs as a result of an increase in atmospheric temperature. With global warming in the northern hemisphere, it is recommended to investigate the rate of temperature increase in the Canadian prairies under climate change, and the empirical evidence of a relationship between increasing temperatures and extreme sub-daily rainfall intensities.

References

Abdellatif, M., Atherton, W., & Alkhaddar, R. (2013). Application of the stochastic model for temporal precipitation disaggregation for hydrological studies in north western England. Journal of Hydroinformatics, 15(2), pp. 555-567. doi:10.2166/hydro.2012.090.

Adamowski, J., Adamowski, K., and Bougadis, J. (2009). Influence of Trend on Short Duration Design Storms. Water Resources Management, 24(3), pp. 401–413.

Anandhi, A., Frei, A., Pierson, D. C., Schneiderman, E. M., Zion, M. S., Lounsbury, D., & Matonse, A. H. (2011). Examination of change factor methodologies for climate change impact assessment. Water Resources Research, 47(3), pp. 1-10. doi:10.1029/2010WR009104

Arnbjerg-Nielsen, K. (2012). Quantification of climate change effects on extreme precipitation used for high resolution hydrologic design. Urban Water Journal, 9(2), pp. 57–65. doi:10.1080/1573062X.2011.630091

Artlert, K., Chaleeraktrakoon, C., & Nguyen, V.-T.-V. (2013). Modeling and analysis of precipitation processes in the context of climate change for Mekong, Chi, and Mun River Basins (Thailand). Journal of Hydro-environment Research, 7(1), pp. 2–17. doi:10.1016/j.jher.2013.01.001.

Babovic, V., and Keijzer, M. (2000). Genetic programming as model induction engine. J. Hydroinf., 2(1), pp. 35–60.

Barrow, E. (2002). Scenarios of climate change, In Proceeding of Climate Change and Water Resources in South Saskatchewan River Basin, Saskatoon, Saskatchewan, Canada, April 2002, pp. 22-45.

Beniston, M., et al. (2007). Future extreme events in European climate: an exploration of regional climate model projections. Clim. Change, 81(1), pp. 71–95.

Bo, Z., Islam, S., and Eltahir, E. A. B. (1994). Aggregation-disaggregation properties of a stochastic precipitation model, Water Resour. Res., 30 (12), pp. 3423-3435.

Buishand, T. A. and Brandsma, T. (2001). Multisite simulation of daily precipitation and temperature in the Rhine basin by nearest-neighbor resampling. Water Resour. Res., 37(11), pp. 2761–2776.

Burian, B. S. J., Durrans, S. R., Nix, S. J., and Pitt, R. E. (2001). Training of Artificial Neural Networks to Perform Precipitation Disaggregation, J. Hydrol. Eng. 6, pp. 43-51.

Burian, B. S. J., Durrans, S. R., Tomic, S., Pimmel, R. L., & Wai, C. N. (2000). Precipitation disaggregation using Artificial Neural Networks. Journal of Hydrologic Engineering, 5, pp. 299–307.

Burn, D. H. (1994). Hydrologic effects of climatic change in west-central Canada. Journal of Hydrology, 160(1), pp. 53-70.

Burn, D. H., & Hag Elnur, M. A. (2002). Detection of hydrologic trends and variability. Journal of hydrology, 255(1), pp. 107-122.

Busuioc, A., Tomozeiu, R., & Cacciamani, C. (2008). Statistical downscaling model based on canonical correlation analysis for winter extreme precipitation events in the Emilia-Romagna region, 464 (July 2007), pp. 449–464. doi:10.1002/joc

Cameron, D., Beven, K., and Tawn, J. (2000). Modelling extreme precipitations using a modified random pulse Bartlett-Lewis stochastic precipitation model (with uncertainty). Adv. Water Resour., 24(2), pp. 203–211.

Chadwick, R., Coppola, E., & Giorgi, F. (2011). An artificial neural network technique for downscaling GCM outputs to RCM spatial scale. Nonlinear Processes in Geophysics, 18(6), pp. 1013–1028. doi:10.5194/npg-18-1013-2011

Chandler, R. E., and Wheater, H. S. (2002). Analysis of precipitation variability using generalized linear models: A case study from the west of Ireland. Water Resour. Res., 38(10), 1192, pp. 10-1-10-11. doi:10.1029/2001WR000906.

Chun, K. P., Wheater, H. S., Nazemi, a., & Khaliq, M. N. (2013). Precipitation downscaling in Canadian Prairie Provinces using the LARS-WG and GLM approaches. Canadian Water Resources Journal, 38(4), 311–332. doi:10.1080/07011784.2013.830368.

City of Saskatoon, 2008. New Neighborhood Design and Development Standards Manual, Storm Water Drainage System, Section six.

CMIP5 (2013). CMIP5 Coupled Model Intercomparison Project, Data Access, Availability. Available at: http://cmip-pcmdi.llnl.gov/cmip5/availability.html. Accessed on 12 December 2014.

Coe, R. and Stern, R. D. (1982). Fitting Models to Daily Precipitation Data. Journal of Applied Meteorology, 21 (7), pp. 1024–1031.

Cunderlik, J. M., & Burn, D. H. (2003). Non-stationary pooled flood frequency analysis. Journal of Hydrology, 276(1), pp. 210-223.

Denault, C., Millar, R. G., & Lence, B. J. (2002). Climate change and drainage infrastructure capacity in an urban catchment. In Proc. Annual Conference of the Canadian Society for Civil Engineering, pp. 5-6. [http://pedago.cegepoutaouais.qc.ca/media/0260309/0378334/SCGC-BON/Documents/GE110-Denault.pdf]

Dibike Y.B., Coulibaly, P. (2005). Hydrologic impact of climate change in the Saguenay watershed: comparison of downscaling methods and hydrologic models. J Hydrol., 307, pp. 145–163.

Ehret, U., Zehe, E., Wulfmeyer, V., Warrach-Sagi, K., & Liebert, J. (2012). Should we apply bias correction to global and regional climate model data? Hydrology and Earth System Sciences, 16(9), pp. 3391–3404. doi:10.5194/hess-16-3391-2012

Elshorbagy, A., Panu, U., and Simonovic, S. (2000). Group-based estimation of missing hydrological data: I. Approach and general methodology. Hydrological Sciences Journal, 45(6), 849 – 866.

Fowler, H. J. and Kilsby, C. G. (2007). Using regional climate model data to simulate historical and future river flows in northwest England. Climatic Change, 80(3-4), pp. 337–367. doi:10.1007/s10584-006-9117-3

Franczyk, J. and Chang, H. (2009). The effects of climate change and urbanization on the runoff of the Rock Creek basin in the Portland metropolitan area, Oregon, USA. Hydrological Processes, 23 (6), pp. 805–815.

Gabriel, K. R. and Neumann, J. (1962). A markov chain model for daily precipitation occurrence at Tel Aviv. Quarterly Journal of the Royal Meteorological Society, 88, pp. 90–95.

Gan, T. Y. (2000). Reducing vulnerability of water resources of Canadian prairies to potential droughts and possible climatic warming. Water Resources Management, 14(2), pp. 111-135.

Giorgi, I. F. and Mearns, L. O. (1999). Introduction to special section- Regional climate modeling revisited in the issue illustrate a wide range of applications. Journal of Geophysical Research, 104(D6), pp. 6335–6352.

Hashmi, M. Z., Shamseldin, A. Y., and Melville, B. W. (2011). Comparison of SDSM and LARS-WG for simulation and downscaling of extreme precipitation events in a watershed. Stochastic Environmental Research and Risk Assessment, 25(4), pp. 475–484. doi:10.1007/s00477-010-0416-x

Hassanzadeh, E., Nazemi, A., and Elshorbagy, A. (2014). Quantile-Based Downscaling of Precipitation using Genetic Programming: Application to IDF Curves in the City of Saskatoon. J. Hydrol. Eng., pp. 943-955. doi:10.1061/(ASCE)HE.1943-5584.0000854

Hay, L. E., Wilby, R. J. L., and Leavesley, G. H. (2000). A comparison of delta change and downscaled GCM scenarios for three mountainous basins in the United States. J. Am. Water Resour. Assoc., 36, pp. 387–397, doi:10.1111/j.1752-1688.2000.tb04276.x

Helsel, D. R., & Hirsch, R. M. (1992). Statistical methods in water resources (Vol. 49). Elsevier.

Hewitson, B. C. and Crane, R. G. (1996). Climate downscaling: techniques and application. Climate Research, 7, pp. 85-95.

Hirsch, R. M., Slack, J. R., & Smith, R. A. (1982). Techniques of trend analysis for monthly water quality data. Water resources research, 18(1), pp. 107-121.

Hodgkins, G. A., & Dudley, R. W. (2006). Changes in the timing of winter–spring streamflows in eastern North America, 1913–2002. Geophysical Research Letters, 33(6).

Hundecha, Y. and Bardossy, A. (2008). Statistical downscaling of extremes of daily precipitation and, Int. J. Climatology, (28), 589–610. doi: 10.1002/joc.1563.

Intergovernmental Panel on Climate Change (IPCC). (2013). Climate change 2013: the physical science basis. Contribution of Working Group I to the Fifth Assessment Report of the Intergovernmental Panel on Climate Change. Stocker et al., eds., Cambridge University Press, Cambridge, United Kingdom and New York, NY, USA, pp. 1535.

Intergovernmental Panel on Climate Change (IPCC). (2012). Managing the risks of extreme events and disasters to advance climate change adaptation. A special report of working groups I and II of the Intergovernmental Panel on Climate Change, C. B. Field, et al., eds., Cambridge University Press, New York.

Intergovernmental Panel on Climate Change (IPCC). (2007). Climate change (2007) synthesis report, contribution of working groups I, II and III to the fourth assessment report of the Intergovernmental Panel on Climate Change, Geneva, Switzerland.

Irwin, S. E., Sarwar, R, King, L. M., and Simonovic, S.P. (2012). Assessment of climatic vulnerability in the Upper Thames River basin: Downscaling with LARS-WG, Department of Civil and Environmental Engineering, The University of Western Ontario, London, Ontario, Canada, Report 081, April 2012.

Jeong, D. I., St-Hilaire, a., Ouarda, T. B. M. J., & Gachon, P. (2012). Multisite statistical downscaling model for daily precipitation combined by multivariate multiple linear regression and stochastic weather generator. Climatic Change, 114(3-4), pp. 567–591. doi:10.1007/s10584-012-0451-3

Katz, R. (2012). Statistical methods for nonstationary extremes. Extremes in a changing climate: Detection, analysis and uncertainty, A. AghaKouchak, D. Easterling, K. Hsu, S. Schubert, and S. Sorooshian, eds., Springer, Dordrecht, Netherlands.

Kelly, D.L. and Kolstad, C.D. (1998). Integrated assessment models for climate change control. Retrieved from http://www.econ.ucsb.edu/papers/wp31-98.pdf on September 7, 2014.

Kendall, M. G. (1975). Rank correlation measures. Charles Griffin, London, pp. 202.

Khaliq, M. N., & Cunnane, C. (1996). Modelling point precipitation occurrences with the modified Bartlett-Lewis rectangular pulses model. Journal of Hydrology, 180(1-4), pp. 109–138. doi:10.1016/0022-1694(95)02894-3.

Kharin, V. V., and Zwiers, F. W. (2005). Estimating extremes in transient climate change simulations. J. Clim., 18(8), pp. 1156–1173.

King, L. M., McLeod, a. I., & Simonovic, S. P. (2014). Simulation of historical temperatures using a multi-site, multivariate block resampling algorithm with perturbation. Hydrological Processes, 28(3), 905–912. doi:10.1002/hyp.9596.

King, L. M., Irwin, S., Sarwar, R., McLeod, A. I., & Simonovic, S. P. (2012). The Effects of Climate Change on Extreme Precipitation Events in the Upper Thames River Basin: A Comparison of Downscaling Approaches. Canadian Water Resources Journal, 37(3), 253–274. doi:10.4296/cwrj2011-938.

Klaus, J., Chun, K. P., & Stumpp, C. (2014). Temporal trends in δ18O composition of precipitation in Germany: insights from time series modelling and trend analysis. Hydrological Processes.

Koutsoyiannis, D., Onof, C., & Wheater, H. S. (2003). Multivariate precipitation disaggregation at a fine timescale. Water Resources Research, 39(7), SWC 1, 1-18. doi:10.1029/2002WR001600

Koza, J. R. (1992). Genetic programming: On the programming of computers by means of natural selection, MIT Press, Cambridge, MA.

Kuo, C.-C., Gan, T. Y., & Hanrahan, J. L. (2014). Precipitation frequency analysis based on regional climate simulations in Central Alberta. Journal of Hydrology, 510, 436–446. doi:10.1016/j.jhydrol.2013.12.051

Lall, U., and Sharma A. (1996). A nearest neighbor bootstrap for time series resampling, Water Resour. Res., 32(3), pp. 679– 693.

Lavellee, D. (1991). Multifractal analysis and simulation techniques and turbulent fields. PhD thesis, McGill University, Montreal, Canada.

Lettenmaier, D. P., Wood, E. F., & Wallis, J. R. (1994). Hydro-climatological trends in the continental United States, 1948-88. Journal of Climate, 7(4), pp. 586-607.

Lin, Y, and Wei, X. (2008). The impact of large-scale forest harvesting on hydrology in the Willow watershed of Central British Columbia, Journal of hydrology, 359, pp. 141-149.

Liu, T. (2006). Fast Nonparametric Machine Learning Algorithms for High-dimensional Massive Data and Applications. Doctoral thesis, Carnegie Mellon University, Pittsburgh, PA 15213, USA.

Lu, Y., & Qin, X. S. (2014). Multisite precipitation downscaling and disaggregation in a tropical urban area, Journal of Hydrology (509), 55–65.

Mailhot A., Duchesne S. (2010). Design Criteria of Urban Drainage Infrastructures under Climate Change, Journal of Water Resources Planning and Management, 136(2), pp. 201-208. doi: 10.1061/(ASCE)WR.1943-5452.0000023

Mailhot, A., Duchesne, S., Caya, D., & Talbot, G. (2007). Assessment of future change in intensity–duration–frequency (IDF) curves for Southern Quebec using the Canadian Regional Climate Model (CRCM). Journal of Hydrology, 347(1-2), pp. 197–210.

Mann, H. B. (1945). Nonparametric tests against trend. Econometrica: Journal of the Econometric Society, pp. 245-259.

Martz, L., Bruneau, J., and Rolfe, J. T. (2007). Climate change and water: SSRB, final technical report. [http://www.parc.ca/ssrb/] (Jun. 11, 2014).

McGuffie, K. and Henderson-Sellers, A. (2014). The Climate Modelling Primer, Fourth Edition, John Wiley & Sons, Ltd.

Mladjic, B., Sushama, L., Khaliq, M. N., Laprise, R., Caya, D., & Roy, R. (2011). Canadian RCM Projected Changes to Extreme Precipitation Characteristics over Canada. Journal of Climate, 24(10), pp. 2565–2584. doi:10.1175/2010JCLI3937.1

Moss, R. H., Edmonds, J. A, Hibbard, K. A, Manning, M. R., Rose, S. K., van Vuuren, D. P., Wilbanks, T. J. (2010). The next generation of scenarios for climate change research and assessment. Nature, 463(7282), pp. 747–56. doi:10.1038/nature08823

Nakicenovic, N., and Davidson, O., eds. (2000). Summary for Policymakers (Emission Scenarios): A Special Report of Working Group III of the Intergovernmental Panel on Climate Change (IPCC).

Nazemi, A., Elshorbagy, A. and Pingale, S. (2011). Uncertainties in the estimation of future annual extreme daily precipitation for the city of Saskatoon under climate change effects. In proceedings of the 20th annual Hydrotechnical Conference, Canadian Society of Civil Engineering Conference, 14-17 June 2011, Ottawa, Canada.

Nguyen, V.T.V., Desramaut, N., & Nguyen, T.D. (2008). Estimation of Design Storms in Consideration of Climate Variability and Change. 11th International Conference on Urban Drainage, Edinburgh, Scotland, UK, 2008, pp. 1–10.

Olsson, J., Gidhagen, L., Gamerith, V., Gruber, G., Hoppe, H., & Kutschera, P. (2012a). Downscaling of Short-Term Precipitation from Regional Climate Models for Sustainable Urban Planning. Sustainability, 4(12), 866–887. doi:10.3390/su4050866

Olsson, J., Berggren, K., Olofsson, M., & Viklander, M. (2009). Applying climate model precipitation scenarios for urban hydrological assessment: A case study in Kalmar City, Sweden. Atmospheric Research, 92, pp. 364–375.

Olsson, J. (1998). Evaluation of a scaling cascade model for temporal precipitation disaggregation. Hydrology and Earth System Sciences, 2(1), pp. 19–30.

Ormsbee, L. E. (1989). Precipitation disaggregation model for continuous hydrologic modeling. Journal of Hydraulic Engineering, 115(4), pp. 507–525.

Overeem, A., Buishand, A., & Holleman, I. (2008). Precipitation depth-duration-frequency curves and their uncertainties. Journal of Hydrology, 348(1-2), pp. 124–134. doi:10.1016/j.jhydrol.2007.09.044

Prodanovic, P. and Simonovic, S. P. (2007). Development of precipitation intensity duration frequency curves for the City of London under the changing climate, Department of Civil and Environmental Engineering, The University of Western Ontario, London, Ontario, Canada, Report 058, November 2007.

Qian, B., Gameda, S., and Hayhoe, H. (2008). Performance of stochastic weather generators LARS-WG and AAFC-WG for reproducing daily extremes of diverse Canadian climates. Climate Research, 37 (September), pp. 17–33. doi:10.3354/cr00755

Qian, B., Gameda, S., Hayhoe, H., Jong, R. De, & Bootsma, A. (2004). Comparison of LARS-WG and AAFC-WG stochastic weather generators for diverse Canadian climates, Climate Research, 26, pp. 175–191.

Racsko, P., Szeidl, L., and Semenov, M. (1991) A serial approach to local stochastic weather models. Ecol Model, 57, pp. 27–41.

Rajagopalan, B. and Lall, U. (1999). A k-nearest-neighbor simulator for daily precipitation and other weather variables. Water resources research, 35 (10), pp. 3089-3101.

Richardson, C. W. (1981).Stochastic Simulation of Daily Precipitation, Temperature and Solar Radiation. Water Resources Research, 17, pp. 182–190.

Rodriguez-Iturbe, I., Cox, D. R., and Isham, V. (1988). A point process model for precipitation: Further developments. Proc. R. Soc. London, Ser. A , 417, pp. 283-298.

Rodriguez-Iturbe, I., Cox, D. R., and Isham, V. (1987). Some models for precipitation based on stochastic point processes. Proc. R. Soc. London, Ser. A, 410, pp. 269-288.

Rogelj, J., Meinshausen, M., & Knutti, R. (2012). Global warming under old and new scenarios using IPCC climate sensitivity range estimates. Nature Climate Change, 2(4), pp. 248–253. doi:10.1038/nclimate1385

Rupp, D. E., Keim, R. F., Ossiander, M., Brugnach, M., & Selker, J. S. (2009). Time scale and intensity dependency in multiplicative cascades for temporal precipitation disaggregation. Water Resources Research, 45(7), pp. W07409 (1-14). doi:10.1029/2008WR007321

Savic, D. A., Walters, G. A., and Davidson, J. W. (1999). A genetic programming approach to precipitation-runoff modeling. Water Resour. Manage., 13(3), pp. 219–231.

Schoof, J. T., & Pryor, S. C. (2001). Downscaling temperature and precipitation: a comparison of regression-based methods and artificial neural networks. International Journal of Climatology, 21(7), pp. 773–790. doi:10.1002/joc.655

Segond, M.-L., Neokleous, N., Makropoulos, C., Onof, C., & Maksimovic, C. (2007). Simulation and spatio-temporal disaggregation of multi-site precipitation data for urban drainage applications. Hydrological Sciences Journal, 52(5), pp. 917–935. doi:10.1623/hysj.52.5.917.

Segond, M.-L., Onof, C., and Wheater, H. S. (2006). Spatial–temporal disaggregation of daily precipitation from a generalized linear model. Journal of Hydrology, 331, pp. 674– 689.

Semenov, M. A., Stratonovitch, P. (2010). Use of multi-model ensembles from global climate models for assessment of climate change impacts, Climate Research, 41, pp. 1-14.

Semenov M. A., Barrow, E. M. (2002) LARS-WG: A Stochastic Weather Generator for Use in Climate Impact Studies, User Manual for Version 3.0, August 2002, [http://www.rothamsted.ac.uk/mas-models/download/LARS-WG-Manual.pdf].

Semenov, M. A., Brooks, R. J., Barrow, E. M., and Richardson, C. W. (1998). Comparison of the WGEN and LARS-WG stochastic weather generators for diverse climates, Climate Research, 10, pp. 95–107.

Semenov, M. A., & Barrow, E. M. (1997). Use of a stochastic weather generator in the development of climate change scenarios, Climate Change, 35, pp. 397–414.

Sharif, M. and Burn, D. H. (2007). Improved K-nearest neighbor weather generating model. Journal of Hydrologic Engineering, 12, pp. 42-51.

Sharma, M., Coulibaly, P., and Dibike, Y. (2011). Assessing the Need for Downscaling RCM Data for Hydrologic Impact Study. Journal of Hydrologic Engineering, 16, pp. 534–539. doi:10.1061/(ASCE)HE.1943-5584.

Shook, K., & Pomeroy, J. (2012). Changes in the hydrological character of rainfall on the Canadian prairies. Hydrological Processes, 26(12), pp. 1752–1766. doi:10.1002/hyp.9383

Shook, K. and Pomeroy, J. W. (2010). Hydrological effects of the temporal variability of the multiscaling of snowfall, Hydrol. Earth Syst. Sci., 14, pp. 1195–1203.

Silva, S. (2007). GPLAB- A genetic programming toolbox for MATLAB. ⟨http://gplab.sourceforge.net⟩ (August 22, 2014).

Sivakumar, B., Sorooshian, S., Gupta, H. V., and Gao, X. (2001) A chaotic approach to precipitation disaggregation, Water Resources Research, 37 (1), pp. 61-72.

Solomon, S., Qin, D., Manning, M., Marquis, M., and others (eds) (2007). Climate Change 2007: the physical science basis. Contribution of Working Group I to the Fourth Assessment Report of the Intergovernmental Panel on Climate Change. Cambridge University Press, Cambridge.

Srikanthan, R., McMahon, T.A. (2001) Stochastic generation of annual, monthly and daily climate data: A review, Hydrology and Earth System Sciences, 5(4), pp. 653–670.

Sun, F., Roderick, M. L., Lim, W. H., & Farquhar, G. D. (2011). Hydroclimatic projections for the Murray-Darling Basin based on an ensemble derived from Intergovernmental Panel on Climate Change AR4 climate models. Water Resources Research, 47(12), pp. 1-14. doi:10.1029/2010WR009829

Taylor, K. E., Stouffer, R. J., & Meehl, G. A. (2012). An Overview of CMIP5 and the Experiment Design. Bulletin of the American Meteorological Society, 93(4), pp. 485–498. doi:10.1175/BAMS-D-11-00094.1

Todorovic, P. and Woolhiser, D. A. (1975). A stochastic model of n-day precipitation. J. Appl. Meteorol., 14(1), pp. 17-24.

von Storch, H., & Navarra, A. (Eds.). (1999). Analysis of climate variability: applications of statistical techniques. Springer.

von Storch, H., Zorita, E., and Cubasch, U. (1993). Downscaling of global climate change estimates to regional scale: An application to Iberian precipitation in wintertime. Journal of Climate, 6, pp. 1161–1171.

Walvoord, M. A., & Striegl, R. G. (2007). Increased groundwater to stream discharge from permafrost thawing in the Yukon River basin: Potential impacts on lateral export of carbon and nitrogen. Geophysical Research Letters, 34(12).

Waters, D., Watt, W. E., Marsalek, J., & Anderson, B. C. (2003). Adaptation of a Storm Drainage System to Accommodate Increased Precipitation Resulting from Climate Change. Journal of Environmental Planning and Management, 46(5), pp. 755–770. doi:10.1080/0964056032000138472.

Westra, S., Fowler, H. J., Evans, J. P., Alexander, L. V., Berg, P., Johnson, F., Kendon, E. J., Lenderink, G., and Roberts, N. M. (2014). Future changes to the intensity and frequency of short-duration extreme rainfall. Reviews of Geophysics, 52(3), 522–555. doi:10.1002/2014RG000464

Weyant, et. al. (1996) "Integrated Assessment of Climate Change: An Overview and Comparison of Approaches and Results," pp. 367-439 in J. P. Bruce, et. al. (eds), Climate Change 1995: Economic and Social Dimensions of Climate Change, Cambridge University Press, Cambridge.

Wheater, H. S., Chandler, R. E., Onof, C. J., Isham, V. S., Bellone, E., Yang, C., Lekkas, D., Lourmas, G., and Segond, M.-L. (2005). Spatial-temporal precipitation modelling for flood risk

estimation. Stochastic Environmental Research and Risk Assessment, 19(6), pp. 403–416. doi:10.1007/s00477-005-0011-8

Wilby, R. L. and Dawson, C. W. (2007). SDSM 4 .2-A decision support tool for the assessment of regional climate change impacts, Version 4.2 user manual, pp. 1–94.

Wilby, R. L. and Dawson, C. W. (2004). Using SDSM Version 3.1-A decision support tool for the assessment of regional climate change impacts, User Manual, pp. 1–67.

Wilby, R., Dawson, C., & Barrow, E. (2002). SDSM — a Decision Support Tool for the Assessment of Regional Climate Change Impacts. Environmental Modelling & Software, 17(2), pp. 145–157. doi:10.1016/S1364-8152(01)00060-3.

Wilby, R. L., Wigley, T. M. L., Conway, D., Jones, P. D., Hewitson, B. C., Main, J., & Wilks, D. S. (1998). Statistical downscaling of general circulation model output: A comparison of methods. Water Resources Research, 34(11), pp. 2995–3008. doi:10.1029/98WR02577.

Wilby, R. L., & Wigley, T. M. L. (1997). Downscaling general circulation model output: a review of methods and limitations. Progress in Physical Geography, 21(4), pp. 530–548. doi:10.1177/030913339702100403

Wilks, D. S. (1999). Multisite downscaling of daily precipitation with a stochastic weather generator. Climate Research, 11(2), 125-136.

Wilks, D.S. (1992) Adapting stochastic weather generation algorithms for climate changes studies. Clim Change, 22, pp. 67–84.

Wilks, D. S., & Wilby, R. L. (1999). The weather generation game: a review of stochastic weather models. Progress in Physical Geography, 23(3), 329–357. doi:10.1177/030913339902300302

Willems, P., Arnbjerg-Nielsen, K., Olsson, J., & Nguyen, V. T. V. (2012). Climate change impact assessment on urban precipitation extremes and urban drainage: Methods and shortcomings. Atmospheric Research, 103, pp. 106–118. doi:10.1016/j.atmosres.2011.04.003.

Willems, P., & Vrac, M. (2011). Statistical precipitation downscaling for small-scale hydrological impact investigations of climate change. Journal of Hydrology, 402(3-4), pp. 193–205. doi:10.1016/j.jhydrol.2011.02.030

Wood, A.W., Leung, L. R., Sridhar, V., and Lettenmaier, D. P. (2004) Hydrologic implications of dynamical and statistical approaches to downscaling climate model outputs. Climatic Change, 62, pp. 189–216.

Xue, Y., Janjic, Z., Dudhia, J., Vasic, R., & De Sales, F. (2014). A review on regional dynamical downscaling in intraseasonal to seasonal simulation/prediction and major factors that affect

downscaling ability. Atmospheric Research, 147-148, 68–85. doi:10.1016/j.atmosres.2014.05.001

Yang, C., Chandler, R. E., Isham, V. S., & Wheater, H. S. (2005). Spatial-temporal precipitation simulation using generalized linear models. Water Resources Research, 41(11), pp. W11415 (1-13). doi:10.1029/2004WR003739

Yates, D., Gangopadhyay, S., Rajagopalan, B., Strzepek, K. (2003). A technique for generating regional climate scenarios using a nearest-neighbor algorithm. Water Resources Research 39 (7), pp. SWC 7-1–SWC 7-14.

Yilmaz, A. G., and Perera, B. J. C. (2014). Extreme Precipitation Nonstationarity Investigation and Intensity – Frequency – Duration Relationship. J. Hydrol. Eng., 19 (6), pp. 1160–1172. doi:10.1061/(ASCE)HE.1943-5584.0000878

Yusop, Z., Nasir, H., & Yusof, F. (2013). Disaggregation of daily precipitation data using Bartlett Lewis Rectangular Pulse model: a case study in central Peninsular Malaysia. Environmental Earth Sciences. doi:10.1007/s12665-013-2755-7

Zhang, M., Wei, X., Sun, P., & Liu, S. (2012). The effect of forest harvesting and climatic variability on runoff in a large watershed: The case study in the Upper Minjiang River of Yangtze River basin. Journal of Hydrology, 464, pp. 1-11.

Zhang, H., Huang, G. H., Wang, D., & Zhang, X. (2011). Uncertainty assessment of climate change impacts on the hydrology of small prairie wetlands. Journal of Hydrology, 396(1-2), 94–103. doi:10.1016/j.jhydrol.2010.10.037

Appendix A
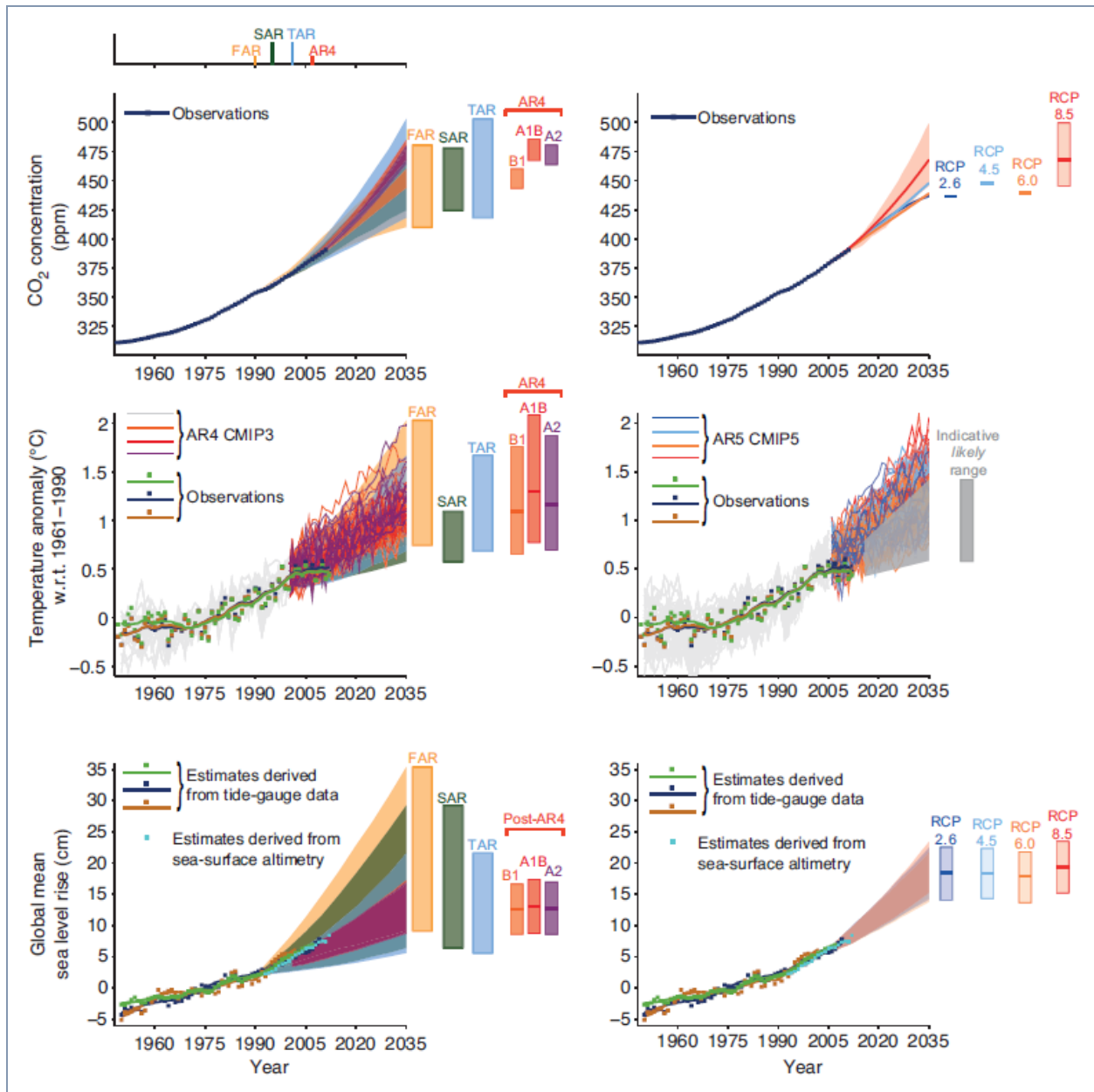
Figure A.1: Comparison of the observed globally and annually averaged CO2 concentration, temperature anomaly, and mean sea level rise and those under the projections of climate change scenarios obtained from various IPCC assessment reports (e.g., AR4, AR5) (Source: IPCC Fifth Assessment Report, Climate Change 2013 with permission).
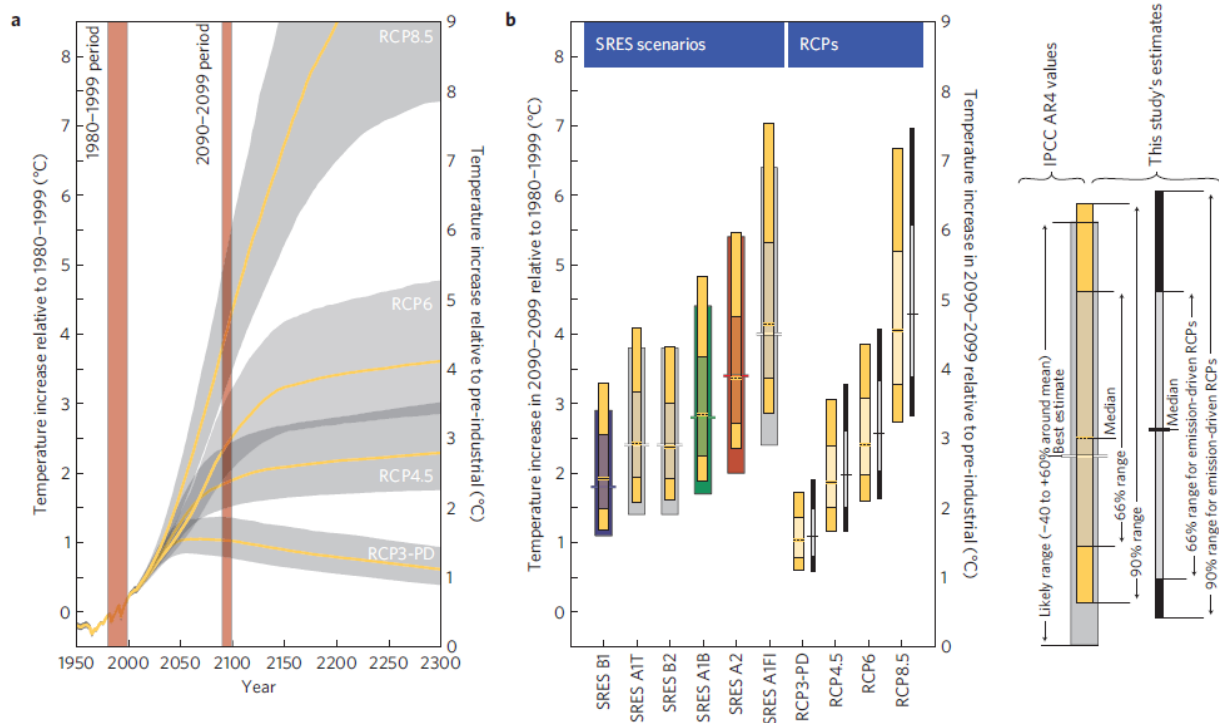
Figure A.2: Temperature increase obtained for SRES emission scenarios and RCPs based on CMIP3 and CMIP5 climate model simulations, respectively (Source: Rogelj et al., 2012 with permission).
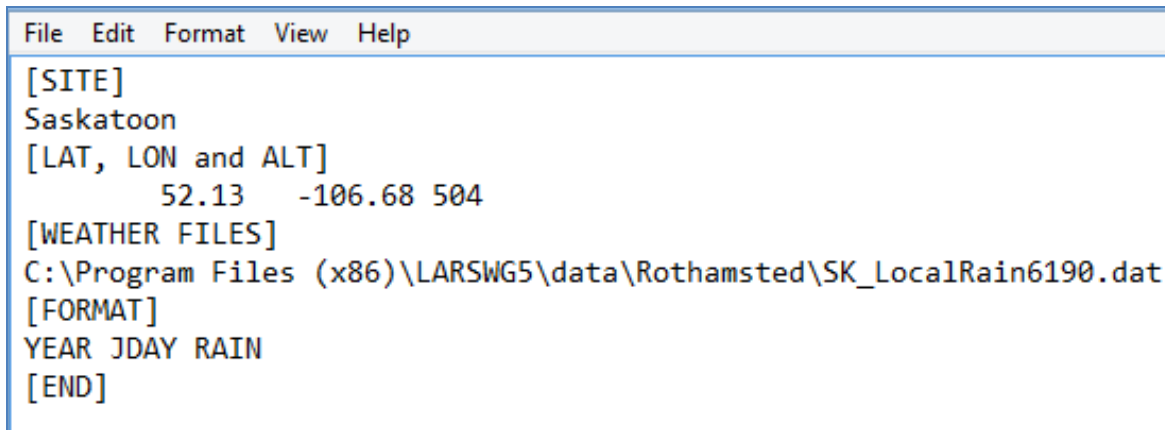
Appendix B

B.1 Steps involved in LARS-WG

Simulation of multiple realizations of daily precipitation using LARS-WG involves a number of steps as briefly described below.

(i) Site Analysis

The stochastic weather generation process in LARS-WG starts with *Site Analysis* in order to generate daily precipitation time series. It is necessary to update the information for Saskatoon in Site Analysis by specifying the local station name (e.g., Saskatoon), latitude, longitude, altitude, path of the folder where precipitation files are located, and format of the precipitation data files (as shown in Figure B.1).

```
File   Edit   Format   View   Help
[SITE]
Saskatoon
[LAT, LON and ALT]
        52.13    -106.68 504
[WEATHER FILES]
C:\Program Files (x86)\LARSWG5\data\Rothamsted\SK_LocalRain6190.dat
[FORMAT]
YEAR JDAY RAIN
[END]
```

Figure B.1: Updated Site Analysis file for Saskatoon

Site Analysis is performed when the file is updated using the Site Analysis option in LARS-WG, which produces three files namely a parameter file (Saskatoon.wgx), a statistics file (Saskatoon.stx), and a test file (Saskatoon.tst). LARS-WG uses the parameters located in the parameter file for generating synthetic precipitation time series, while the seasonal frequency distributions for wet/dry spell lengths and precipitation series are located in the statistics file. The statistical characteristics of the observed data and simulated data are compared and the results of comparison are located in the test file (Table B.1), where the simulated data are generated using the parameter files of the observed data. Among the important statistics, the test file contains test statistics (KS-, t-, and f-statistics) with the corresponding p-values, average wet/dry spell lengths for each month, and mean monthly precipitation amounts for each month. The statistics are used to assess the performance of LARS-WG by evaluating the corresponding p-values – evaluating if the observed and simulated data belong to the same distribution, i.e., the simulated precipitation is not significantly different from the observed data.

(ii) Generation of scenario files

Scenario files are required in LARS-WG for determining the perturbation rule of the weather generator parameters located in the parameter files. In case of generating synthetic precipitation series based on the parameters calculated from the observed precipitation data, no perturbation of the parameter values is applied so that the statistical characteristics of the simulated and observed precipitation series remain the same. However, relative change factors (RCFs) are calculated corresponding to the mean monthly precipitation amounts, and wet and dry spell lengths for each month, which are then included in the scenario file for generating future precipitation time series of arbitrary length under climate change scenarios by perturbing the parameter values obtained from the observed data. An example of a scenario file of LARS-WG is shown in Figure B.2. For detailed explanation of LARS-WG weather generation procedures, please refer to Semenov and Barrow (2002).

```
// LARS-WG5.5
//      Columns are:
//      [1]     month
//      [2]     relative change in monthly mean rainfall
//      [3]     relative change in duration of wet spell
//      [4]     relative change in duration of dry spell
//      [5]     absolute changes in monthly mean min temperature
//      [6]     absolute changes in monthly mean max temperature
//      [7]     relative changes in daily temperature variability
//      [8]     relative changes in mean monthly radiation
[VERSION]
LARS-WG5.5
[NAME]
Saskatoon_CGCM_RCP85_2071-2100
[BASELINE]
1975
[FUTURE]
2085
[GCM PREDICTIONS]
        Jan     1.29    1.28    0.92    0.00    0.00    1.00    1.00
        Feb     1.23    1.25    0.78    0.00    0.00    1.00    1.00
        Mar     2.12    1.81    0.79    0.00    0.00    1.00    1.00
        Apr     1.64    1.10    0.73    0.00    0.00    1.00    1.00
        May     1.50    0.99    0.71    0.00    0.00    1.00    1.00
        Jun     0.87    0.77    1.14    0.00    0.00    1.00    1.00
        Jul     0.69    0.84    1.49    0.00    0.00    1.00    1.00
        Aug     1.29    1.09    0.78    0.00    0.00    1.00    1.00
        Sep     0.94    1.05    0.91    0.00    0.00    1.00    1.00
        Oct     2.45    1.95    0.85    0.00    0.00    1.00    1.00
        Nov     1.39    1.30    0.79    0.00    0.00    1.00    1.00
        Dec     1.02    1.25    0.90    0.00    0.00    1.00    1.00
```

Figure B.2: Scenario file used in LARS-WG for the perturbation of parameter values obtained from the observed data

Table B.1: Relative change factors for CanESM2 during 2041-2070.

Month	Mean monthly precipitation			Wet spell length			Dry spell length		
	RCP2.6	RCP4.5	RCP8.5	RCP2.6	RCP4.5	RCP8.5	RCP2.6	RCP4.5	RCP8.5
Jan	1.13	1.09	1.29	1.05	1.01	0.99	0.80	0.91	0.94
Feb	0.96	0.84	1.13	1.01	1.12	1.11	0.86	0.99	0.84
Mar	1.61	1.55	2.02	1.34	1.30	1.54	0.97	0.88	0.77
Apr	1.64	1.90	1.38	1.11	1.27	1.21	0.78	0.81	0.90
May	1.01	1.40	1.37	0.95	0.93	1.00	0.97	1.01	0.82
Jun	1.00	0.78	1.14	0.93	0.94	0.89	1.07	1.00	0.88
Jul	0.98	0.84	0.81	1.14	0.93	0.96	0.99	1.23	1.15
Aug	1.22	0.98	1.30	1.07	0.92	0.96	0.90	0.93	0.79
Sep	0.80	1.12	0.99	1.07	1.03	1.07	0.94	0.90	0.87
Oct	1.48	1.58	1.84	1.33	1.23	1.40	0.78	0.78	0.91
Nov	0.90	1.22	1.38	1.27	1.28	1.27	1.01	0.98	0.91
Dec	1.37	1.47	1.20	1.29	1.27	1.45	0.95	0.80	0.91

Table B.2: Relative change factors for CanESM2 during 2071-2100.

Month	Mean monthly precipitation			Wet spell length			Dry spell length		
	RCP2.6	RCP4.5	RCP8.5	RCP2.6	RCP4.5	RCP8.5	RCP2.6	RCP4.5	RCP8.5
Jan	0.93	1.03	1.29	1.05	1.10	1.28	0.91	1.01	0.92
Feb	0.96	1.16	1.23	0.99	1.04	1.25	0.93	0.87	0.78
Mar	1.99	2.13	2.12	1.41	1.43	1.81	0.92	0.91	0.79
Apr	1.89	1.87	1.64	1.06	1.21	1.10	0.79	0.81	0.73
May	0.97	1.21	1.50	0.94	0.96	0.99	0.86	1.00	0.71
Jun	1.22	1.04	0.87	1.07	0.96	0.77	0.92	0.93	1.14
Jul	0.90	0.78	0.69	1.18	0.89	0.84	1.13	1.23	1.49
Aug	0.94	1.05	1.29	1.08	0.99	1.09	0.82	0.91	0.78
Sep	0.98	0.97	0.94	1.10	1.04	1.05	0.97	0.88	0.91
Oct	1.26	1.61	2.45	1.31	1.37	1.95	0.82	0.81	0.85
Nov	0.81	1.37	1.39	1.27	1.37	1.30	1.00	0.95	0.79
Dec	1.31	1.51	1.02	1.09	1.11	1.25	0.92	0.91	0.90

Table B.3: Relative change factors for HadGEM2-ES during 2011-2040.

Month	Mean monthly precipitation			Wet spell length			Dry spell length		
	RCP2.6	RCP4.5	RCP8.5	RCP2.6	RCP4.5	RCP8.5	RCP2.6	RCP4.5	RCP8.5
Jan	1.24	1.01	1.37	1.05	0.72	1.04	1.10	0.90	0.88
Feb	1.17	1.06	1.13	0.76	1.06	0.94	0.90	0.87	0.94
Mar	1.17	1.00	1.09	0.90	0.58	0.81	1.18	1.20	1.29
Apr	1.48	1.05	1.36	0.96	0.85	0.88	0.93	1.17	1.07
May	0.97	1.03	0.79	0.82	0.89	0.91	1.28	1.22	1.40
Jun	0.74	0.98	1.00	0.76	0.88	0.78	1.01	0.93	0.74
Jul	0.91	0.92	1.24	0.81	0.81	1.00	1.01	1.04	0.94
Aug	0.82	0.90	1.00	0.94	1.20	1.20	1.13	1.20	1.11
Sep	1.46	1.26	1.68	0.97	0.97	1.11	1.08	0.88	1.03
Oct	1.48	1.02	1.29	1.01	0.79	1.07	0.98	1.04	1.30
Nov	1.01	0.83	1.08	1.02	0.82	1.07	0.98	1.03	1.10
Dec	1.08	1.11	1.14	1.00	1.19	0.88	0.94	1.17	1.01

Table B.4: Relative change factors for HadGEM2-ES during 2041-2070.

Month	Mean monthly precipitation			Wet spell length			Dry spell length		
	RCP2.6	RCP4.5	RCP8.5	RCP2.6	RCP4.5	RCP8.5	RCP2.6	RCP4.5	RCP8.5
Jan	1.11	1.07	1.13	0.94	1.13	0.97	0.86	0.81	1.06
Feb	0.96	1.04	1.37	0.82	1.20	1.39	0.98	0.94	0.89
Mar	1.37	1.47	1.62	0.80	0.95	0.86	1.17	1.27	1.57
Apr	1.31	1.47	1.66	1.06	1.18	1.18	0.95	0.98	1.14
May	1.19	1.19	1.47	0.83	0.95	0.87	1.26	1.12	1.17
Jun	0.96	0.98	1.10	0.78	0.81	0.77	0.99	0.83	0.93
Jul	1.06	0.84	0.76	0.84	0.79	0.75	1.03	1.03	1.05
Aug	1.00	0.78	0.85	0.95	0.93	0.94	1.05	1.20	1.27
Sep	1.48	1.08	1.63	0.89	0.80	0.99	1.00	1.29	1.11
Oct	1.46	1.57	1.05	1.08	1.13	0.89	1.09	1.04	1.19
Nov	1.19	1.35	1.21	0.93	0.81	1.13	1.06	0.94	0.84
Dec	1.13	1.05	1.18	1.31	0.97	1.51	0.84	1.08	0.86

Table B.5: Relative change factors for HadGEM2-ES during 2071-2100.

Month	Mean monthly precipitation			Wet spell length			Dry spell length		
	RCP2.6	RCP4.5	RCP8.5	RCP2.6	RCP4.5	RCP8.5	RCP2.6	RCP4.5	RCP8.5
Jan	1.24	1.33	1.06	1.04	0.87	0.76	0.87	1.10	0.75
Feb	1.12	1.21	1.36	0.87	1.09	0.61	0.90	0.96	0.94
Mar	1.00	1.22	1.59	0.98	0.55	0.59	1.11	1.49	1.19
Apr	1.40	1.55	1.63	0.84	0.82	1.07	1.13	1.22	1.07
May	1.14	1.21	0.84	0.90	0.75	0.52	1.12	1.07	1.38
Jun	1.17	0.89	0.94	0.85	0.70	0.62	0.83	1.01	0.96
Jul	1.01	0.68	0.60	0.73	0.80	0.64	0.89	1.01	1.11
Aug	0.76	0.95	0.63	1.07	1.00	0.89	1.15	1.08	1.19
Sep	1.62	0.99	1.12	1.09	0.78	0.93	0.96	1.13	0.98
Oct	1.47	1.22	1.74	0.99	0.81	0.86	1.13	1.21	1.06
Nov	1.05	1.45	1.41	1.26	1.13	1.17	0.90	0.96	0.90
Dec	1.08	1.22	1.30	1.08	1.11	1.18	0.86	1.02	1.10
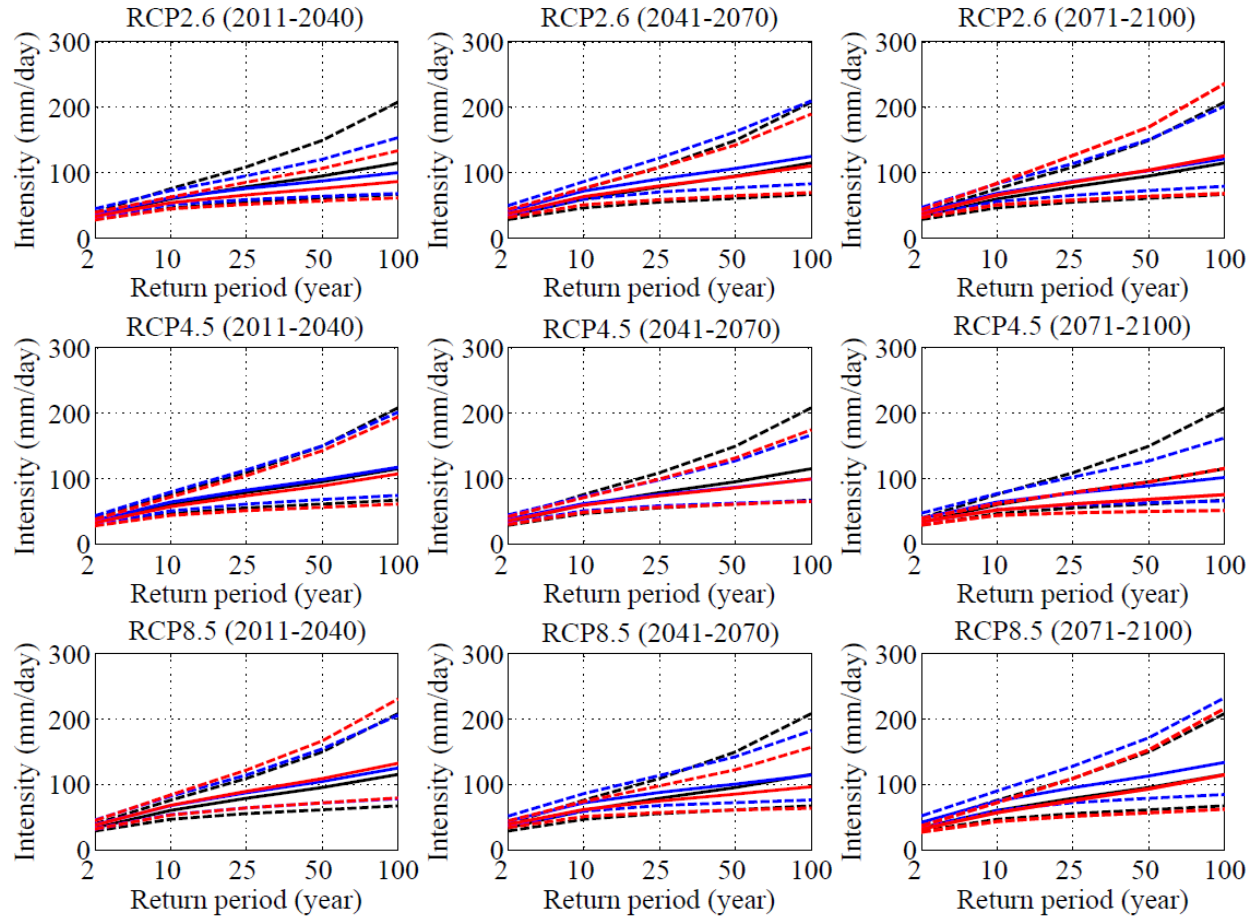
Figure B.3: Variations in the future projections of daily AMP quantiles in the City of Saskatoon according to HadGEM2-ES forced with three RCPs using two sets of change factors: with wet/dry spell (blue) and without wet/dry spell (red) effects. The expected quantiles (solid lines) and their 95% confidence intervals (dashed lines) are shown with the corresponding quantiles during the baseline period (black).
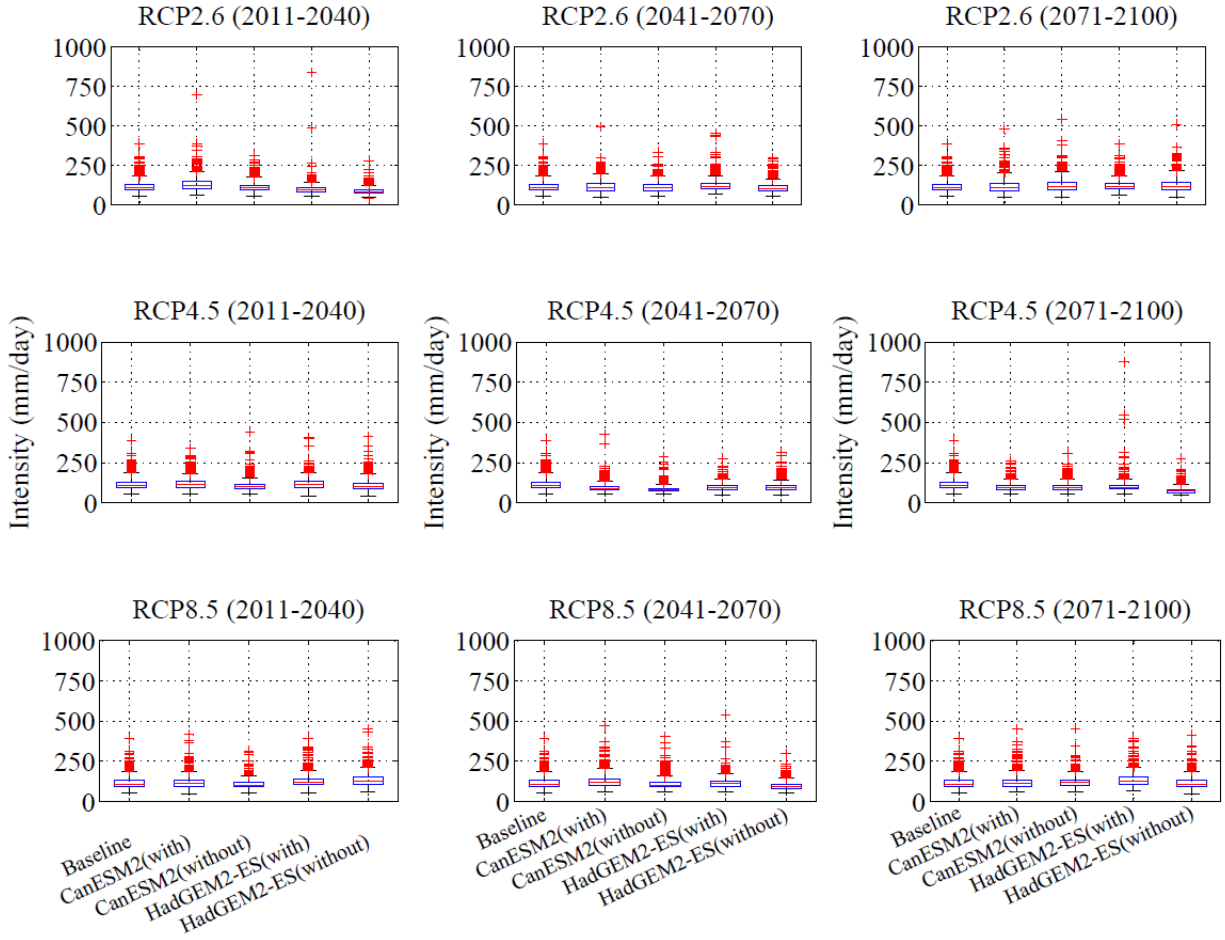
Figure B.4: Variations in the future projections of daily expected quantiles for **100-year** return period in the City of Saskatoon according to CanESM2 and HadGEM2-ES forced with three RCPs using two sets of change factors, i.e. with wet/dry spell and without wet/dry spell effects along with the corresponding daily expected quantiles during the baseline.

Appendix C

An attempt was made in this study to investigate the homogeneity of sub-hourly rainfall data recorded at four rain-gauges in the City of Saskatoon during the period 1992-2009 with missing records during 2002-2004. An attempt was also made to identify the representative rain gauge for the City of Saskatoon by evaluating the consistency between the rain gauges with comparison to the Environment Canada (EC) daily rainfall data during the same period.

C.1 Double mass curve analysis

Analysis of double mass curves was conducted for each of the four rain gauges to investigate the homogeneity of rainfall records over the period of operation. The double mass curves of the four rain gauges against EC measurement station show some fluctuations in the corresponding slopes. There are more fluctuations in slopes of the City Hall, the Diefenbaker Fire Hall (i.e., Diefenbaker), and the Warman Fire Hall (i.e., Warman) stations than that of the Acadia Reservoir rain gauge (i.e., Acadia). The slope of the Acadia record suggests that this gauge record might be more consistent with the EC data and thus, it might represent a reliable sub-hourly data series for the City of Saskatoon. Other rain gauges, i.e., City Hall, Diefenbaker, and Warman contain substantial missing data in their records, which is approximately 19% each, whereas Acadia gauge has 11% missing data during the period of sub-hourly rainfall record. The amount of missing data seems to affect the fluctuations in the slopes of the corresponding rain gauges. The comparison of double mass curves among the rain gauges in Figure C.1 shows that Diefenbaker and Warman gauges might be consistent in recording sub-hourly rainfall, while no other two rain gauges seem to demonstrate such consistency. Examination of Figure C.1 reveals that the Acadia gauge seems to keep consistency with EC rainfall record in the early few years, and later deviated from that trend during the last few years due to underestimation. On the other hand, the remaining three rain gauges seem to underestimate the EC rainfall values except in 1992 and part of 1993.
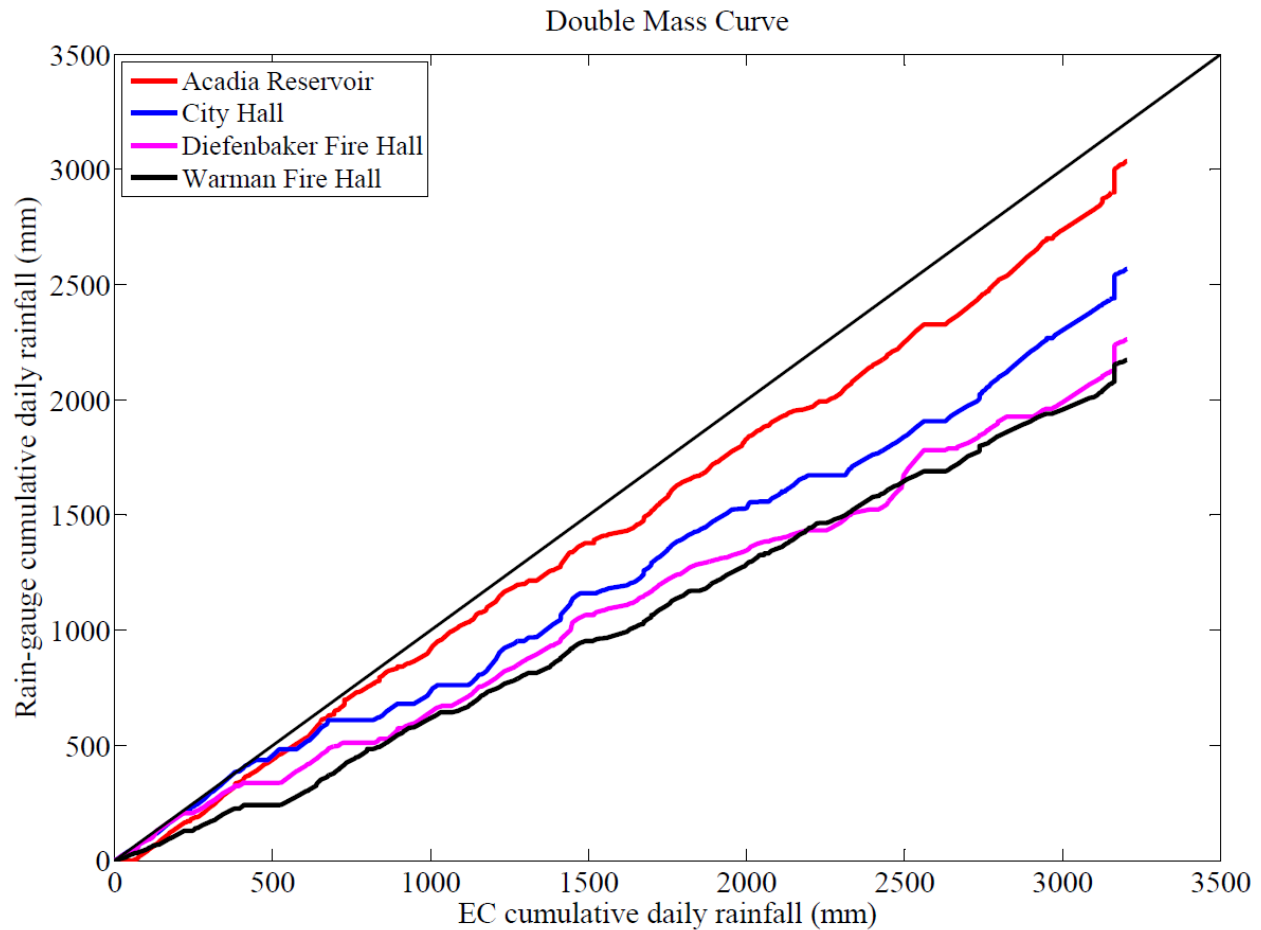
Figure C.1: Double mass curve of cumulative rainfall (mm)

C.2 Efficiency of rain-gauges as compared to EC records

The rain gauges seem to underestimate the annual total rainfall of EC in most of the years except in 1993, 1994, 2006 and 2007 where Acadia overestimated the EC annual total rainfall (Figure C.2). Overall, Acadia seems to estimate the annual total EC values better than the other rain gauges in most of the years, although some of the rain gauges estimate EC annual total rainfall quite closely in some years.
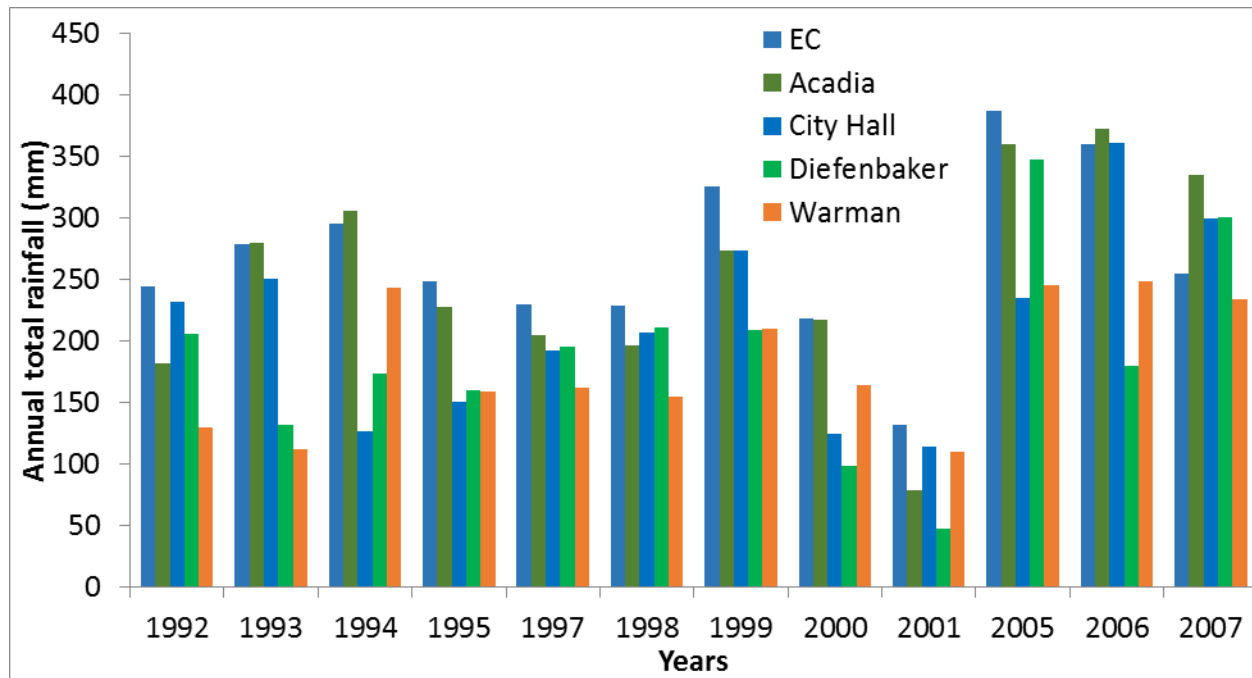
Figure C.2: Annual rainfall obtained from EC daily and Saskatoon's rain gauge sub-hourly rainfall data.

C.3 Tukey's multiple comparison test

The differences of mean between Diefenbaker-Acadia (D-A) and Warman-Acadia (W-A) rain-gauges are significant at 10% significance level, since the p-values are less than 0.10. Also the differences of mean between Environment Canada-Diefenbaker (E-D) and Warman-Environment Canada (W-E) are significant at 10% significance level since the p-values are less than 0.10 in Table C.1. Figure C.3 shows that the differences in mean levels for C-A, E-C, D-C, W-C and W-D rain gauges includes the zero-line within their intervals and so, the differences may become zero anytime leading to a non-significant difference between two means at 10% significance level. But the differences in the results between Diefenbaker and Acadia; and Warman and Acadia are comparatively large with the highest difference between Warman and Acadia (W and A) rain gauges. As compared to EC data, the differences in the mean between EC and Diefenbaker; and EC and Warman are comparatively large with the highest difference occurs between Warman and EC (W and EC) rain gauges. Overall, Acadia has the lowest difference in the mean in comparison to EC, which is also suggested by the corresponding p-value (i.e. p-value>>0.10).

Table C.1: Results of Tukey's test for comparison between differences in multiple means

Stations	Difference in mean	Lower limit	Upper limit	p-value
City Hall-Acadia	-0.209	-0.542	0.123	0.529
Diefenbaker-Acadia	-0.346	-0.678	-0.014	0.077
Environment Canada-Acadia	0.075	-0.257	0.408	0.981
Warman-Acadia	-0.386	-0.719	-0.054	0.034
Diefenbaker-City Hall	-0.137	-0.469	0.195	0.850
Environment Canada -City Hall	0.285	-0.047	0.617	0.216
Warman-City Hall	-0.177	-0.509	0.155	0.685
Environment Canada-Diefenbaker	0.422	0.089	0.754	0.016
Warman-Diefenbaker	-0.040	-0.372	0.292	0.100
Warman- Environment Canada	-0.462	-0.794	-0.129	0.006
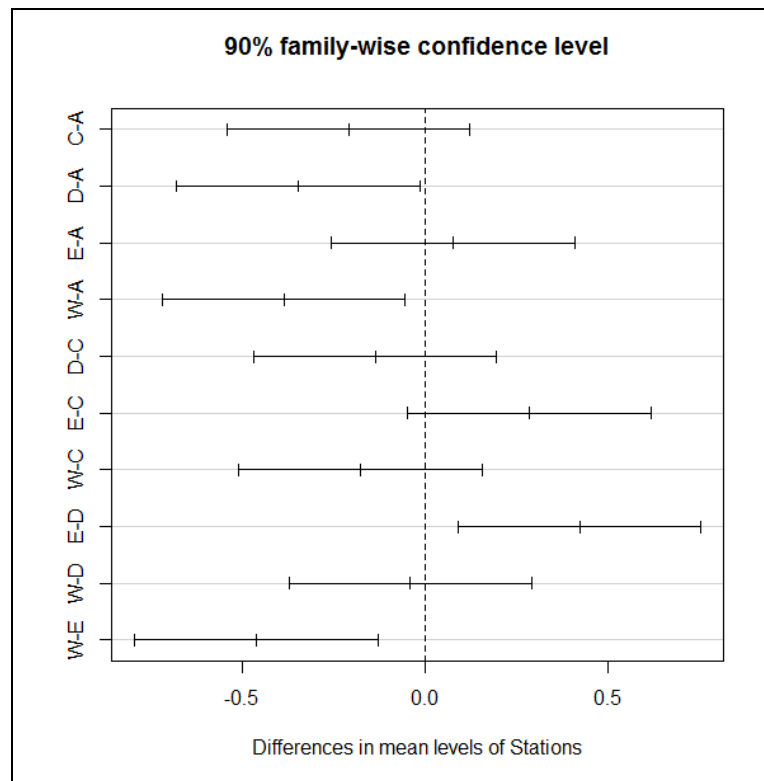
Figure C.3: Differences in mean rainfall between the rain-gauges and EC station

C.4 Extreme rainfall of the City rain gauges

The extreme rainfall can be analyzed by the identification of annual maximum rainfall of various temporal resolutions at the four rain gauges in Saskatoon. The annual maximum rainfall of different temporal resolutions (i.e., daily, 1-hour, 15-min, and 5-min) at each of the four rain gauges and the EC's daily rainfall at Diefenbaker Airport Station were used to compare the

variability in the extreme rainfall (Figure C.4). It is apparent from the previous results shown in Figures C.1 to C.3 that Acadia rain gauge is more consistent with the EC daily rainfall data than other rain gauges in the city. However, the remaining three rain gauges seem to perform quite similar to Acadia in terms of median and inter-quartile ranges of the corresponding extreme rainfall values. The median and inter-quartile ranges of the rain gauges fall within the inter-quartile range of the EC station in case of daily rainfall. The medians of extreme rainfall values at the rain gauges were not significantly different from each other in cases of other temporal resolutions. The annual maximum rainfall of 5-minute resolution at Acadia rain gauge shows quite similar variability as that of other rain gauges. However, the annual maximum rainfall of other temporal resolutions at Acadia rain gauge shows more variability than those of other rain gauges.
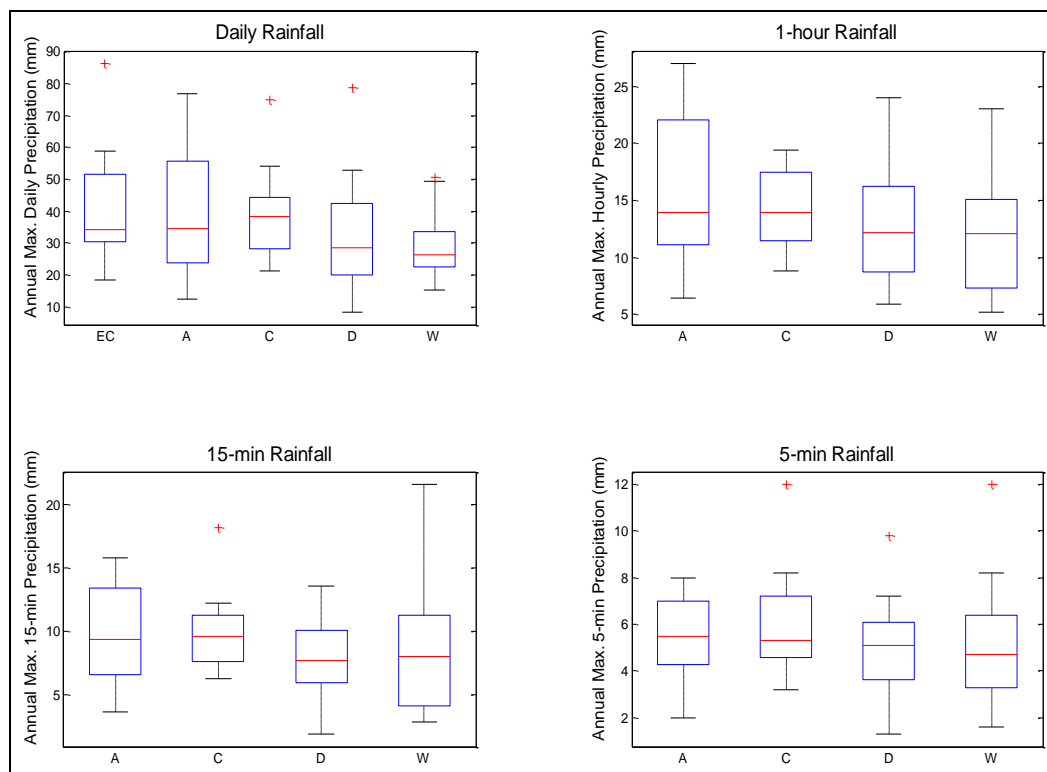
Figure C.4: Annual maximum rainfall of different temporal resolutions at the city rain gauges; A: EC: Environment Canada, Acadia, C: City hall, D: Diefenbaker, and W: Warman

The analysis of double mass curve and other performance evaluation criteria show that the Acadia rain gauge might be more reliable showing higher consistency with EC data having mean value, which is not significantly different from the EC mean rainfall value. Therefore, the sub-hourly rainfall data from Acadia rain gauge was considered for the hydrological study in the City of Saskatoon.

Appendix D

Table D.1: Internal parameters used in the GP search for extracting equations representing the relationships between the AMPs at the GCM (CanESM2 and HadGEM2) and the local scales

GP parameter	Type of parameter	Value
Inicmaxlevel	Variable parameters	19, 20
Dynamiclevel	(internal settings)	24, 25, 26
Realmaxlevel		30, 32, 35
Minprob		0.025, 0.08
Mathematical operations	Fixed parameters	$\{+, -, x, /, \exp(x), x^2\}$
Terminal		24

Table D.2: Internal parameters used in the GP search for extracting equations representing the relationships between the AMPs at the GCM (CGCM3.1) and the local scales

GP parameter	Type of parameter	Value
Inicmaxlevel	Variable parameters	17, 18
Dynamiclevel	(internal settings)	23, 24
Realmaxlevel		29, 30
Minprob		0.025, 0.08
Mathematical operations	Fixed parameters	$\{+, -, x, /, \exp(x), x^2\}$
Terminal		24

Table D.3: Equations extracted from GP based on CanESM2 and their performance statistics for training, validation and testing data sets

Duration (h)	Equations	Training				Validation				Testing			
		RMSE	R	MB	MARE	RMSE	R	MB	MARE	RMSE	R	MB	MARE
1	$Q_{Local}(x)=(Q_{GCM}(x)-24/Q_{GCM}(x)^2-2)(23-Q_{GCM}(x)/exp(Q_{GCM}(x)/24)+Q_{GCM}(x)/8)$	24.49	1.00	-5.78	0.02	16.00	1.00	-6.61	0.02	103.66	0.96	7.93	0.07
2	$Q_{Local}(x)=Q_{GCM}(x)^2/24+(36Q_{GCM}(x)+11Q_{GCM}(x)^2)/(Q_{GCM}(x)+12)+24$	9.36	1.00	1.74	0.01	5.25	1.00	1.82	0.01	52.71	0.97	8.08	0.07
3	$Q_{Local}(x)=10Q_{GCM}(x)+exp(24/Q_{GCM}(x))-48$	3.40	1.00	-0.69	0.01	2.55	1.00	-0.64	0.01	30.85	0.97	2.14	0.07
4	$Q_{Local}(x)=119Q_{GCM}(x)/24+2.7183Q_{GCM}(x)-exp(24/Q_{GCM}(x))-24$	3.24	1.00	0.56	0.01	2.48	1.00	0.51	0.01	24.06	0.98	2.81	0.08
5	$Q_{Local}(x)=145Q_{GCM}(x)/24-Q_{GCM}(x)^2/288-exp(24/Q_{GCM}(x)+1)$	3.05	1.00	-0.27	0.02	2.93	1.00	-0.35	0.02	20.94	0.97	1.42	0.08
6	$Q_{Local}(x)=31Q_{GCM}(x)/6-Q_{GCM}(x)^2/192-exp(24/Q_{GCM}(x))-1)$	4.57	1.00	-0.38	0.04	4.53	1.00	-0.61	0.04	17.69	0.97	0.93	0.09
7	$Q_{Local}(x)=4Q_{GCM}(x)-exp(Q_{GCM}(x)/24)/Q_{GCM}(x)+576/Q_{GCM}(x)exp(24/(exp(exp(Q_{GCM}(x)/24))))$	6.57	0.99	1.18	0.05	6.34	0.99	0.95	0.05	15.93	0.97	2.26	0.10
8	$Q_{Local}(x)=576/Q_{GCM}(x)^2+3Q_{GCM}(x)-576/Q_{GCM}(x)-exp(Q_{GCM}(x)/24)/Q_{GCM}(x)+46$	3.81	1.00	0.13	0.01	3.47	1.00	0.03	0.02	14.35	0.96	1.21	0.10
9	$Q_{Local}(x)=3Q_{GCM}(x)+24Q_{GCM}(x)^2/(Q_{GCM}(x)^2+576)+(24Q_{GCM}(x)-Q_{GCM}(x)^2)/(576-Q_{GCM}(x))$	3.24	1.00	0.99	0.03	3.21	1.00	0.84	0.03	13.76	0.96	1.89	0.09
10	$Q_{Local}(x)=3Q_{GCM}(x)+Q_{GCM}(x)^2/24exp(Q_{GCM}(x)/24)+Q_{GCM}(x)/24-Q_{GCM}(x)^2/288$	2.35	1.00	-0.90	0.03	2.35	1.00	-1.00	0.03	12.29	0.96	-0.22	0.08
11	$Q_{Local}(x)=25Q_{GCM}(x)/12-Q_{GCM}(x)^2/576+exp(24/Q_{GCM}(x))-576/Q_{GCM}(x)+47$	2.08	1.00	0.83	0.02	1.93	1.00	0.80	0.02	12.01	0.95	1.46	0.08
12	$Q_{Local}(x)=2Q_{GCM}(x)-Q_{GCM}(x)^2/288-552/Q_{GCM}(x)+47$	2.72	1.00	1.72	0.04	2.71	1.00	1.75	0.04	11.18	0.94	2.15	0.10
13	$Q_{Local}(x)=29Q_{GCM}(x)/24+(Q_{GCM}(x)^2+48Q_{GCM}(x))/(Q_{GCM}(x)+24+exp(Q_{GCM}(x)/24))$	3.40	0.99	0.86	0.05	3.31	0.99	0.69	0.06	9.43	0.96	1.12	0.08
14	$Q_{Local}(x)=Q_{GCM}(x)+24exp(1-24/Q_{GCM}(x))+24Q_{GCM}(x)^2/(576+Q_{GCM}(x)^2)+2.7183$	1.30	1.00	-0.07	0.01	0.86	1.00	-0.07	0.01	8.95	0.94	0.16	0.09
15	$Q_{Local}(x)=(576-Q_{GCM}(x)^2/12-3Q_{GCM}(x))/(exp(exp(24/Q_{GCM}(x)))+24)+2Q_{GCM}(x)$	1.50	1.00	0.66	0.02	1.57	1.00	0.68	0.03	9.16	0.94	1.08	0.10
16	$Q_{Local}(x)=(Q_{GCM}(x)-8)(48-Q_{GCM}(x)+1152/Q_{GCM}(x))/192+2Q_{GCM}(x)$	2.03	1.00	0.50	0.03	2.02	1.00	0.40	0.03	7.89	0.95	0.83	0.08
17	$Q_{Local}(x)=(48-Q_{GCM}(x)+24/Q_{GCM}(x))/exp(48/Q_{GCM}(x))+24/(exp(24/Q_{GCM}(x))+Q_{GCM}(x))+2Q_{GCM}(x)$	0.99	1.00	-0.02	0.01	0.82	1.00	-0.03	0.01	7.18	0.95	0.27	0.07
18	$Q_{Local}(x)=(24Q_{GCM}(x)-576)/(exp(Q_{GCM}(x)/24)+24)+25Q_{GCM}(x)/24-24/Q_{GCM}(x)+25$	1.37	1.00	0.58	0.02	1.49	1.00	0.60	0.02	6.44	0.96	0.71	0.02
19	$Q_{Local}(x)=((6912+48Q_{GCM}(x)^3)/Q_{GCM}(x))/(Q_{GCM}(x)^2+576)+Q_{GCM}(x)$	0.75	1.00	0.05	0.01	0.68	1.00	0.09	0.01	6.64	0.95	0.27	0.07
20	$Q_{Local}(x)=23Q_{GCM}(x)/24+331776Q_{GCM}(x)/(25Q_{GCM}(x)^2+576Q_{GCM}(x)+331776)$	0.82	1.00	0.02	0.02	0.80	1.00	-0.01	0.02	5.96	0.96	0.24	0.07
21	$Q_{Local}(x)=48/exp(24/Q_{GCM}(x))+exp(1-Q_{GCM}(x)^4exp(Q_{GCM}(x)/24-24))+Q_{GCM}(x)$	0.74	1.00	-0.31	0.01	0.46	1.00	-0.30	0.01	6.24	0.95	-0.04	0.07
22	$Q_{Local}(x)=Q_{GCM}(x)-exp(24/Q_{GCM}(x))-exp(2Q_{GCM}(x)/(Q_{GCM}(x)+24))+(24Q_{GCM}(x)-576)/(24+Q_{GCM}(x))+24$	1.41	1.00	0.09	0.02	1.19	1.00	0.09	0.02	6.11	0.95	0.39	0.06
23	$Q_{Local}(x)=(48-(96Q_{GCM}(x)-576)/(576-Q_{GCM}(x)))/exp(24/Q_{GCM}(x))+Q_{GCM}(x)$	0.55	1.00	0.45	0.01	0.57	1.00	0.46	0.01	5.76	0.95	0.65	0.07
24	$Q_{Local}(x)=24Q_{GCM}(x)/(exp(exp(Q_{GCM}(x)/576))(exp(Q_{GCM}(x)/24+1)+24))+Q_{GCM}(x)+24/exp(24/Q_{GCM}(x))$	1.30	1.00	-0.30	0.01	0.79	1.00	-0.29	0.01	5.19	0.95	-0.08	0.07

Units of RMSE and MB are mm/day.

Table D.4: Equations extracted from GP based on HadGEM2-ES and their performance statistics for training, validation and testing data sets

Duration (h)	Equations	Training				Validation				Testing			
		RMSE	R	MB	MARE	RMSE	R	MB	MARE	RMSE	R	MB	MARE
1	$Q_{Local}(x)=3Q_{GCM}(x)+Q_{GCM}(x)exp(1+Q_{GCM}(x)/24)-exp(49Q_{GCM}(x)/576)+73$	28.85	1.00	3.93	0.01	24.36	1.00	3.58	0.01	1112.32	0.94	11.78	0.07
2	$Q_{Local}(x)=Q_{GCM}(x)^3/288+4Q_{GCM}(x)-48/Q_{GCM}(x)+72$	9.32	1.00	-1.61	0.03	6.41	1.00	-2.07	0.03	46.48	0.97	1.06	0.08
3	$Q_{Local}(x)=71Q_{GCM}(x)/12+23Q_{GCM}(x)^3/13824+1$	1.53	1.00	0.56	0.01	1.39	1.00	0.57	0.01	28.09	0.97	1.82	0.06
4	$Q_{Local}(x)=48Q_{GCM}(x)^2/(552-2Q_{GCM}(x)-7.3891)+2Q_{GCM}(x)+31.3891$	4.03	1.00	-1.05	0.03	4.03	1.00	-1.23	0.03	16.68	0.98	-0.35	0.06
5	$Q_{Local}(x)=Q_{GCM}(x)^2/12+(Q_{GCM}(x)-24)/exp(Q_{GCM}(x)/12)+Q_{GCM}(x)/exp(8/(Q_{GCM}(x)+8))+Q_{GCM}(x)+24$	2.02	1.00	0.84	0.01	1.43	1.00	0.81	0.01	14.38	0.98	1.26	0.06
6	$Q_{Local}(x)=(27Q_{GCM}(x)+exp(Q_{GCM}(x)/24)+600)(Q_{GCM}(x)+1)./576+2Q_{GCM}(x)$	1.17	1.00	0.23	0.01	0.93	1.00	0.25	0.01	13.82	0.98	0.55	0.08
7	$Q_{Local}(x)=(21Q_{GCM}(x)^2+1632Q_{GCM}(x)+1152)./576$	0.59	1.00	0.19	0.00	0.44	1.00	0.18	0.00	12.83	0.97	0.48	0.08
8	$Q_{Local}(x)=Q_{GCM}(x)2/(48-Q_{GCM}(x)^2/(1152-Q_{GCM}(x)))+71Q_{GCM}(x)/24$	0.61	1.00	-0.20	0.01	0.64	1.00	-0.17	0.01	11.78	0.97	0.13	0.08
9	$Q_{Local}(x)=Q_{GCM}(x)^2/48+2.5Q_{GCM}(x)+exp(1-Q_{GCM}(x)/24)+exp(Q_{GCM}(x)/24)/24+exp(Q_{GCM}(x)/24)$	0.34	1.00	-0.05	0.00	0.31	1.00	-0.03	0.00	10.24	0.97	0.28	0.08
10	$Q_{Local}(x)=(Q_{GCM}(x)-2.7138)(Q_{GCM}(x)-24)/48+70Q_{GCM}(x)/24$	1.14	1.00	0.36	0.01	1.03	1.00	0.40	0.01	9.11	0.97	0.57	0.07
11	$Q_{Local}(x)=3Q_{GCM}(x)+(23Q_{GCM}(x)^2+Q_{GCM}(x)3)/13824-24/exp(exp(24/Q_{GCM}(x)^2))$	1.41	1.00	0.61	0.02	1.43	1.00	0.68	0.02	8.76	0.97	0.80	0.08
12	$Q_{Local}(x)=3Q_{GCM}(x)-24Q_{GCM}(x)/(exp(Q_{GCM}(x)/12)+2Q_{GCM}(x)-24+576/Q_{GCM}(x))$	1.30	1.00	-0.14	0.01	1.09	1.00	-0.11	0.01	8.00	0.97	-0.11	0.07
13	$Q_{Local}(x)=(Q_{GCM}(x)^2-Q_{GCM}(x)exp(1/(24-exp(Q_{GCM}(x)/24))))/(Q_{GCM}(x)+24)+45Q_{GCM}(x)/23$	0.81	1.00	0.03	0.01	0.73	1.00	0.06	0.01	7.62	0.97	0.04	0.07
14	$Q_{Local}(x)=69Q_{GCM}(x)/24+24/exp(Q_{GCM}(x)/24)-23$	0.72	1.00	0.24	0.01	0.74	1.00	0.25	0.01	6.74	0.97	0.23	0.07
15	$Q_{Local}(x)=Q_{GCM}(x)2/144+2Q_{GCM}(x)+1/exp(Q_{GCM}(x)/12)$	0.21	1.00	0.05	0.00	0.20	1.00	0.06	0.00	7.24	0.96	0.10	0.07
16	$Q_{Local}(x)=1-((5Q_{GCM}(x)-24)(24-Q_{GCM}(x)))/576+exp(Q_{GCM}(x)/24)/24+2Q_{GCM}(x)$	0.22	1.00	0.11	0.00	0.22	1.00	0.12	0.00	7.04	0.96	0.19	0.07
17	$Q_{Local}(x)=((3Q_{GCM}(x)-96)(exp(Q_{GCM}(x)/24)+2Q_{GCM}(x)-24))/576+2Q_{GCM}(x)$	0.37	1.00	-0.17	0.01	0.32	1.00	-0.15	0.01	5.98	0.97	-0.09	0.06
18	$Q_{Local}(x)=45Q_{GCM}(x)/24-Q_{GCM}(x)(24-Q_{GCM}(x))(24+Q_{GCM}(x))/13824$	0.95	1.00	-0.03	0.01	0.97	1.00	0.00	0.01	5.74	0.97	0.03	0.05
19	$Q_{Local}(x)=727.4067Q_{GCM}(x)/(387.7032-Q_{GCM}(x))-121Q_{GCM}(x)/576$	1.26	1.00	-0.18	0.02	1.20	1.00	-0.12	0.02	5.48	0.96	-0.15	0.06
20	$Q_{Local}(x)=25Q_{GCM}(x)/24+Q_{GCM}(x)^2/1152+(Q_{GCM}(x)^3/72+24Q_{GCM}(x))/(Q_{GCM}(x)+24)-1$	0.55	1.00	0.29	0.01	0.55	1.00	0.30	0.10	5.19	0.97	0.33	0.06
21	$Q_{Local}(x)=(Q_{GCM}(x)exp(Q_{GCM}(x)/24)-24Q_{GCM}(x))/(0.5Q_{GCM}(x)+47.9765)+2Q_{GCM}(x)$	1.04	1.00	-0.15	0.02	1.08	1.00	-0.10	0.02	5.48	0.96	-0.90	0.06
22	$Q_{Local}(x)=0.5exp(1+Q_{GCM}(x)/24-576/(Q_{GCM}(x)^2+24Q_{GCM}(x)))+1.5Q_{GCM}(x)-0.25$	0.99	1.00	-0.11	0.02	0.98	1.00	-0.06	0.02	5.27	0.96	-0.03	0.06
23	$Q_{Local}(x)=2Q_{GCM}(x)-(Q_{GCM}(x)-21.28)/(exp(Q_{GCM}(x)/24)+24/Q_{GCM}(x))-$	0.77	1.00	0.02	0.00	0.61	1.00	0.02	0.00	4.75	0.96	0.00	0.06
24	$Q_{Local}(x)=(2Q_{GCM}(x)^3-4Q_{GCM}(x)^2+192Q_{GCM}(x))/(Q_{GCM}(x)^2+120Q_{GCM}(x)-576)+Q_{GCM}(x)$	1.01	1.00	-0.03	0.02	0.99	1.00	0.00	0.02	4.50	0.96	-0.02	0.06

Units of RMSE and MB are mm/day.

Table D.5: Equations extracted from GP based on CGCM3.1 and their performance statistics for training, validation and testing data sets

Duration (h)	Equations	Training				Validation				Testing			
		RMSE	R	MB	MARE	RMSE	R	MB	MARE	RMSE	R	MB	MARE
1	$Q_{Local}(x)=0.31482Q_{GCM}(x)^2+0.31482Q_{GCM}(x)exp(Q_{GCM}(x)/24-exp(24/Q_{GCM}(x)))+96$	57.35	0.99	-4.84	0.10	54.84	1.00	-2.71	0.10	75.38	0.97	1.70	0.16
2	$Q_{Local}(x)=Q_{GCM}(x)^2/6+0.90558/exp(-0.03773(24+Q_{GCM}(x)))+83.36069$	23.23	0.99	3.10	0.07	21.78	1.00	3.19	0.07	42.79	0.97	7.07	0.12
3	$Q_{Local}(x)=Q_{GCM}(x)^2/12+2Q_{GCM}(x)+24/Q_{GCM}(x)+exp(Q_{GCM}(x)/24)+50$	5.41	1.00	0.95	0.02	5.14	1.00	0.93	0.02	34.59	0.96	3.09	0.11
4	$Q_{Local}(x)=(Q_{GCM}(x)+24)^2/24+Q_{GCM}(x)+Q_{GCM}(x)/8+exp(Q_{GCM}(x)/24)$	3.32	1.00	0.13	0.00	2.21	1.00	0.25	0.00	31.11	0.95	1.42	0.11
5	$Q_{Local}(x)=24/(Q_{GCM}(x)/24+24/Q_{GCM}(x))+25Q_{GCM}(x)/24+24+Q_{GCM}(x)(24+Q_{GCM}(x))/24$	2.75	1.00	-1.01	0.02	2.84	1.00	-1.15	0.02	25.25	0.95	0.14	0.11
6	$Q_{Local}(x)=4Q_{GCM}(x)+(576/Q_{GCM}(x)+Q_{GCM}(x))/exp(24/exp(Q_{GCM}(x)/24))+exp(Q_{GCM}(x)-24)/24))$	2.82	1.00	0.19	0.03	2.77	1.00	0.31	0.03	21.63	0.94	1.05	0.12
7	$Q_{Local}(x)=3Q_{GCM}(x)+(Q_{GCM}(x)^2-Q_{GCM}(x)+24)/(48+Q_{GCM}(x))+48exp(Q_{GCM}(x)/24)/Q_{GCM}(x)$	2.42	1.00	-0.18	0.02	2.57	1.00	-0.05	0.02	18.18	0.94	0.26	0.13
8	$Q_{Local}(x)=Q_{GCM}(x)^2/288+3Q_{GCM}(x)+72/Q_{GCM}(x)$	2.80	1.00	0.24	0.02	2.63	1.00	0.32	0.02	16.54	0.94	0.63	0.13
9	$Q_{Local}(x)=3Q_{GCM}(x)+72/Q_{GCM}(x)+(exp(Q_{GCM}(x)/24)-72)Q_{GCM}(x)/576$	3.04	1.00	-0.70	0.02	3.31	1.00	-0.58	0.02	15.97	0.93	-0.30	0.13
10	$Q_{Local}(x)=3Q_{GCM}(x)+24Q_{GCM}(x)/(72+2exp(24-Q_{GCM}(x))+exp(Q_{GCM}(x)/24))$	2.90	1.00	0.38	0.03	2.73	1.00	0.43	0.03	13.76	0.94	0.46	0.11
11	$Q_{Local}(x)=2Q_{GCM}(x)+72/Q_{GCM}(x)+7Q_{GCM}(x)/16$	2.12	1.00	0.03	0.02	2.08	1.00	0.09	0.02	12.86	0.93	0.25	0.12
12	$Q_{Local}(x)=2Q_{GCM}(x)-exp(2.5417+1/Q_{GCM}(x)-1/Q_{GCM}(x)^2)+24$	2.15	1.00	0.05	0.01	2.13	1.00	0.08	0.01	12.10	0.93	0.15	0.11
13	$Q_{Local}(x)=2Q_{GCM}(x)-Q_{GCM}(x)/(24+exp(24-Q_{GCM}(x))+Q_{GCM}(x))+6+24/Q_{GCM}(x)$	0.50	1.00	-0.01	0.01	0.53	1.00	0.00	0.01	10.78	0.93	0.05	0.11
14	$Q_{Local}(x)=2Q_{GCM}(x)+12/Q_{GCM}(x)-Q_{GCM}(x)/24+(3Q_{GCM}(x)+24)/Q_{GCM}(x)$	1.77	1.00	-0.24	0.02	1.84	1.00	-0.21	0.02	9.71	0.93	-0.16	0.12
15	$Q_{Local}(x)=23Q_{GCM}(x)/12+48/Q_{GCM}(x)-Q_{GCM}(x)/16.611+2$	1.21	1.00	0.01	0.02	1.28	1.00	0.04	0.02	9.32	0.93	0.12	0.11
16	$Q_{Local}(x)=1.5972Q_{GCM}(x)+Q_{GCM}(x)^2/864+8$	1.23	1.00	-0.64	0.02	1.18	1.00	-0.59	0.02	8.87	0.93	-0.54	0.10
17	$Q_{Local}(x)=1081Q_{GCM}(x)/576+48/Q_{GCM}(x)-24/exp(48/Q_{GCM}(x))$	1.33	1.00	0.18	0.02	1.25	1.00	0.21	0.02	7.65	0.94	0.30	0.10
18	$Q_{Local}(x)=Q_{GCM}(x)^2/192+25Q_{GCM}(x)/24+14$	0.91	1.00	0.10	0.02	0.92	1.00	0.07	0.02	7.05	0.95	0.22	0.08
19	$Q_{Local}(x)=1.5Q_{GCM}(x)+Q_{GCM}(x)exp(Q_{GCM}(x)/24)/1152+12/exp(Q_{GCM}(x)/24)$	1.02	1.00	-0.33	0.01	1.07	1.00	-0.29	0.01	6.75	0.95	-0.26	0.09
20	$Q_{Local}(x)=4Q_{GCM}(x)/3-Q_{GCM}(x)(48-Q_{GCM}(x))/300+8$	0.96	1.00	0.07	0.02	0.93	1.00	0.11	0.02	6.26	0.95	0.15	0.09
21	$Q_{Local}(x)=Q_{GCM}(x)^2/192+11Q_{GCM}(x)/12+12$	0.45	1.00	-0.41	0.01	0.46	1.00	-0.42	0.01	6.00	0.95	-0.28	0.08
22	$Q_{Local}(x)=Q_{GCM}(x)^2/576+13Q_{GCM}(x)/12+9$	1.38	1.00	-0.39	0.02	1.33	1.00	-0.37	0.02	6.10	0.95	-0.34	0.09
23	$Q_{Local}(x)=(144+4Q_{GCM}(x)+exp((Q_{GCM}(x)+24))/24+Q_{GCM}(x)$	1.01	1.00	-0.07	0.02	1.04	1.00	-0.01	0.02	5.85	0.94	0.00	0.09
24	$Q_{Local}(x)=Q_{GCM}(x)^2/576+25Q_{GCM}(x)/24+8/Q_{GCM}(x)+6.389$	0.58	1.00	-0.02	0.01	0.54	1.00	0.01	0.01	5.30	0.95	0.04	0.09

Units of RMSE and MB are mm/day.
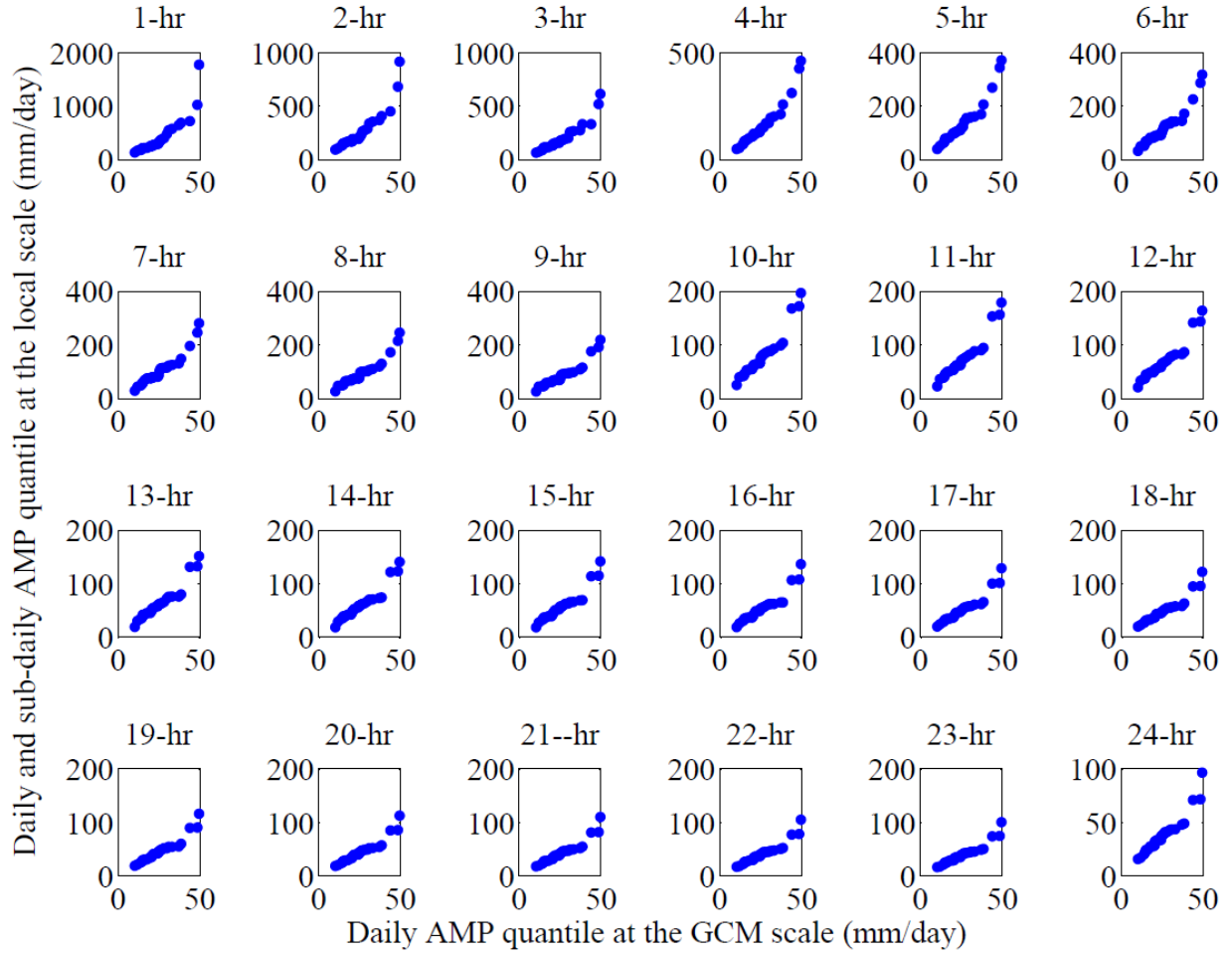
Figure D.1: Comparison between the GCM-scale (using output of HadGEM2-ES) daily AMP quantiles and the corresponding local-scale daily and sub-daily AMP quantiles during the baseline (1961-1990) period in Saskatoon (durations are indicated above the plots.)
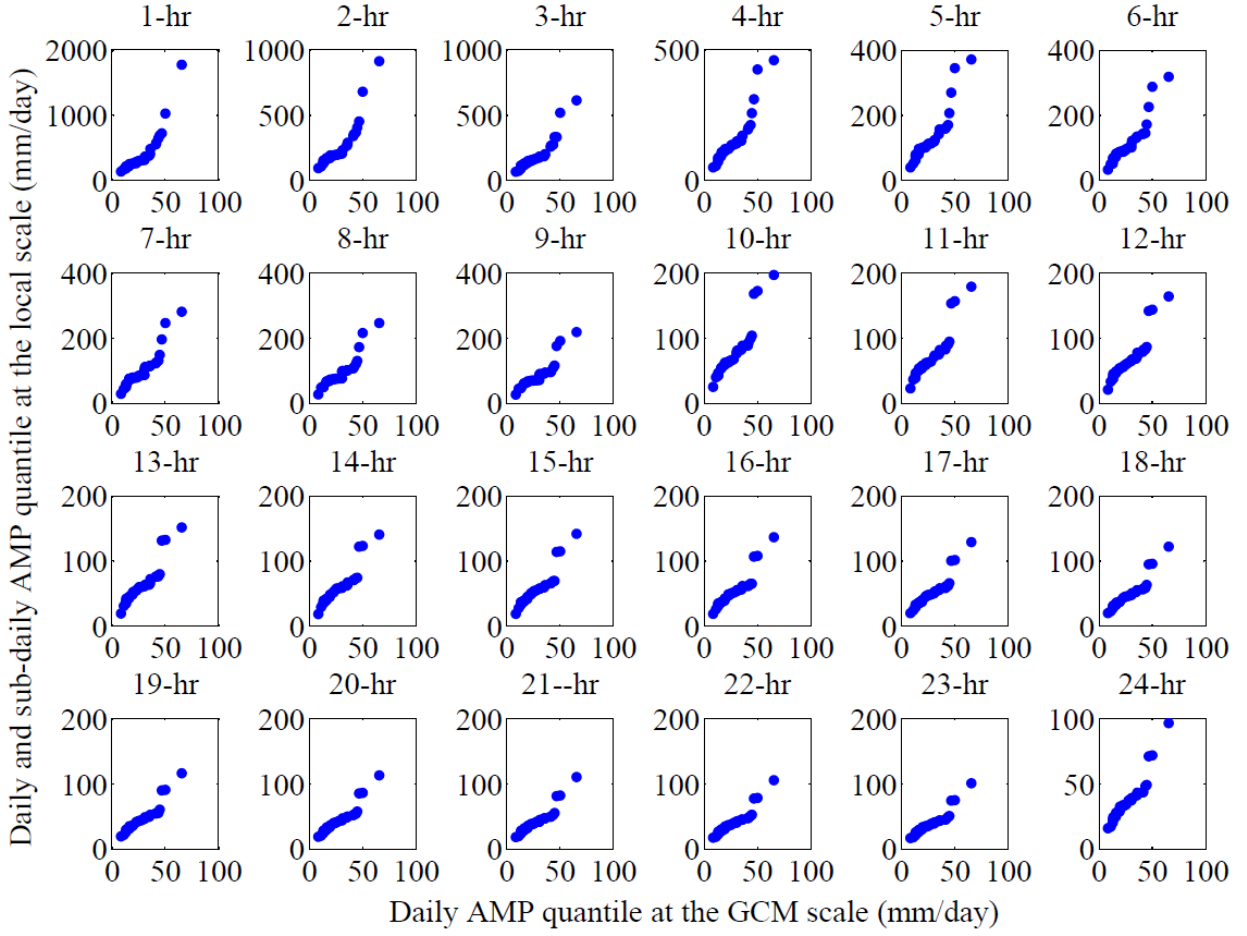
Figure D.2: Comparison between the GCM-scale (using output of CGCM3.1) daily AMP quantiles and the corresponding local-scale daily and sub-daily AMP quantiles during the baseline (1961-1990) period in Saskatoon (durations are indicated above the plots.)

Appendix E
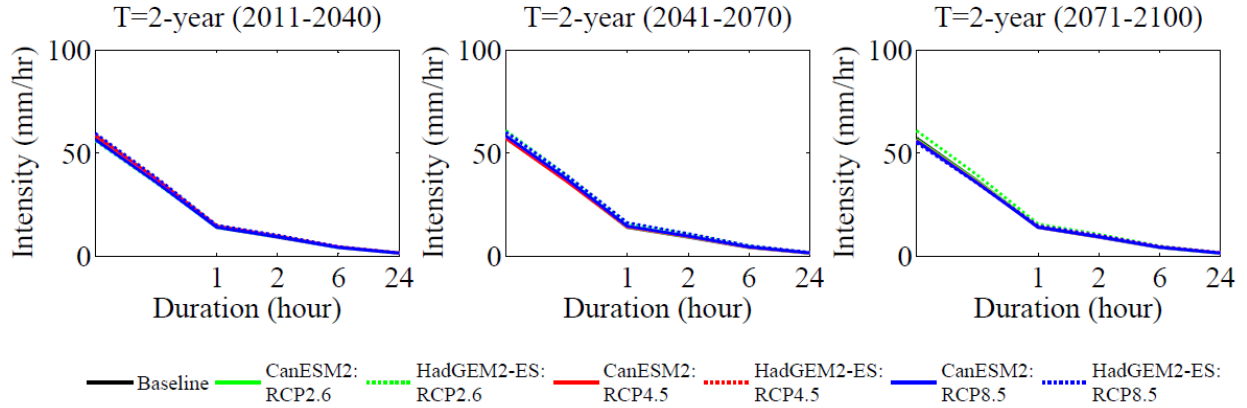
Figure E.1: Variations in the future IDF curves for 2-year return period in the City of Saskatoon according to CanESM2 and HadGEM2-ES based on three RCPs.
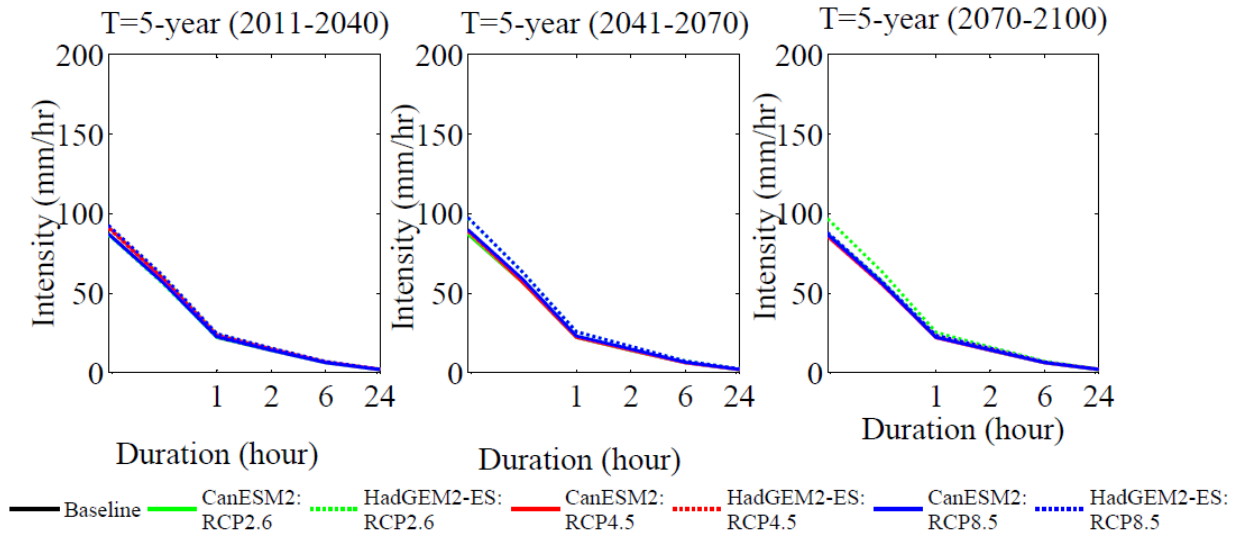
Figure E.2: Variations in the future IDF curves for 5-year return period in the City of Saskatoon according to CanESM2 and HadGEM2-ES based on three RCPs.
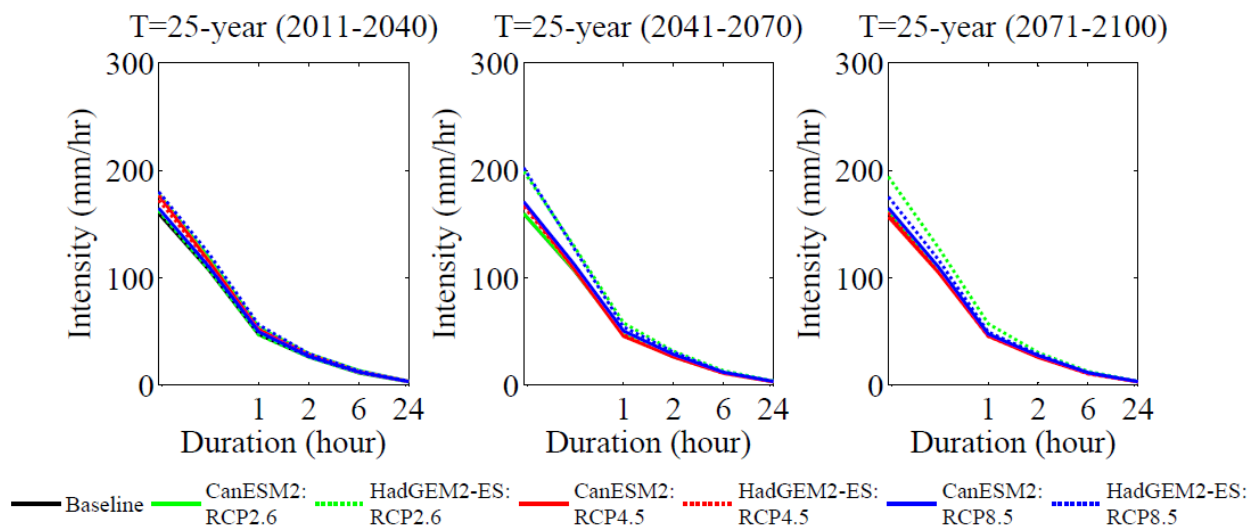
Figure E.3: Variations in the future IDF curves for 25-year return period in the City of Saskatoon according to CanESM2 and HadGEM2-ES based on three RCPs.
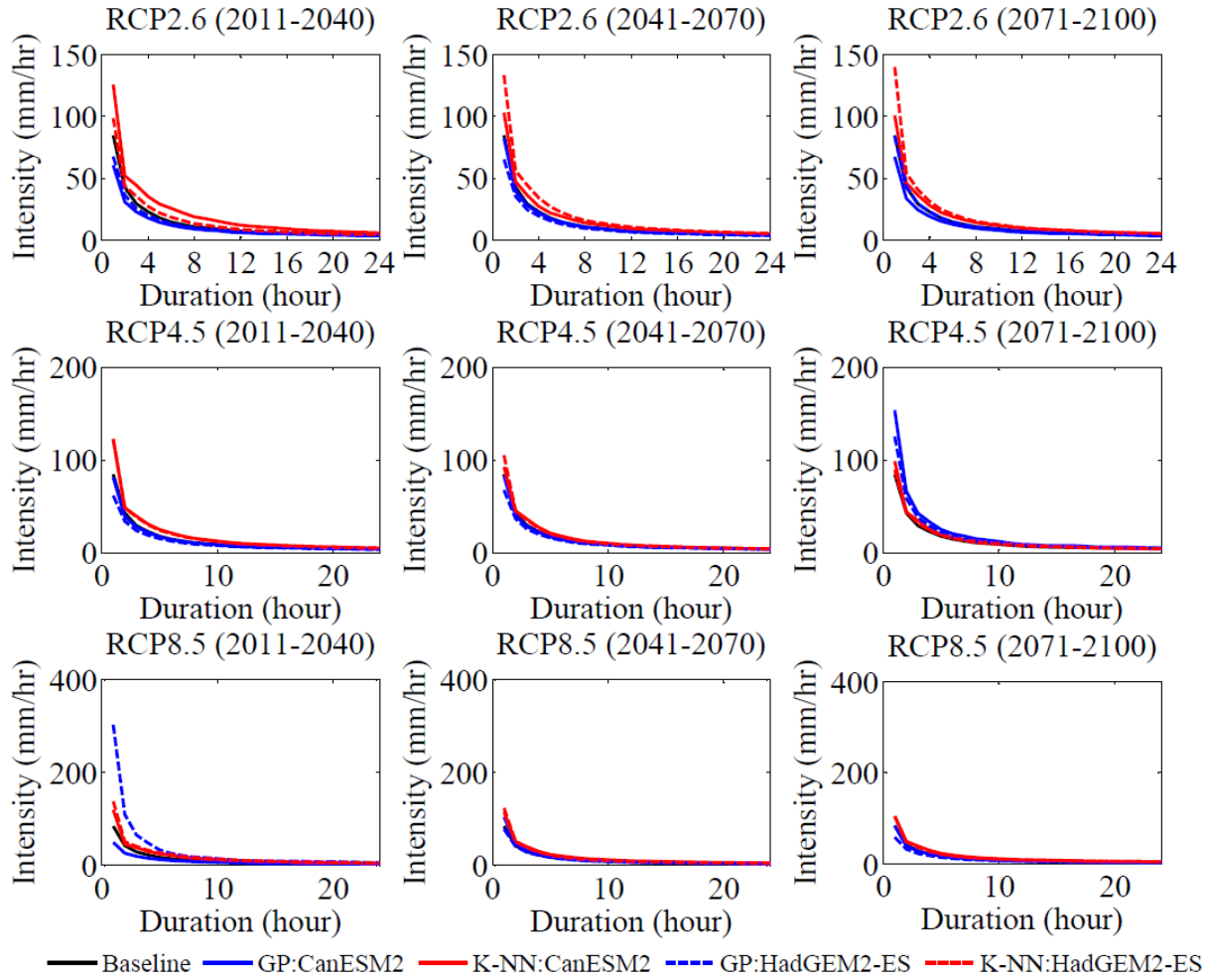
Figure E.4: Comparison between the future IDF curves (2011-2100) according to CanESM2 (solid lines) and HadGEM2-ES (dashed lines) based on three RCPs and 100-year return period obtained using two different downscaling approaches, i.e. GP method and LARS-WG combined with K-NN Hourly Disaggregation Model.

Table E.1: Comparison between the K-NN hourly disaggregation model and the GP method in simulating the expected precipitation intensity (mm/hr) for HadGEM2-ES based on three RCPs during the 21st century for various durations and return periods.

	GP Method												K-NN Hourly Disaggregation Model											
	(2011-2040)				(2041-2070)				(2071-2100)				(2011-2040)				(2041-2070)				(2071-2100)			
	Return period (year)												Return period (year)											
	2	5	25	100	2	5	25	100	2	5	25	100	2	5	25	100	2	5	25	100	2	5	25	100
HadGEM2-ES: RCP2.6																								
1-hr	15	22	39	68	19	29	48	65	17	27	51	84	13	22	48	99	15	25	59	133	15	25	60	140
2-hr	10	14	23	36	12	18	27	35	11	17	29	43	9	14	26	44	10	16	31	56	10	16	30	54
3-hr	8	11	17	25	10	14	20	25	9	13	21	29	7	11	20	35	8	12	24	44	8	12	23	41
4-hr	6	9	14	20	8	11	16	19	7	10	16	23	6	8	16	27	6	10	19	34	6	10	18	31
6-hr	5	6	10	13	6	8	11	13	5	8	11	15	4	6	11	19	5	7	14	22	5	7	13	21
12-	3	4	5	7	3	4	6	7	3	4	6	7	3	4	6	9	3	4	7	11	3	4	7	10
18-	2	3	4	5	2	3	4	5	2	3	4	5	2	3	4	6	2	3	5	7	2	3	5	7
24-	2	2	3	4	2	3	3	4	2	2	3	4	2	2	3	4	2	2	4	5	2	2	4	5
HadGEM2-ES: RCP4.5																								
1-hr	14	21	38	62	16	26	46	68	15	25	59	125	14	23	54	122	14	22	49	105	14	22	46	90
2-hr	9	13	23	34	11	16	27	36	10	16	33	58	10	15	28	48	9	14	26	45	10	15	27	44
3-hr	7	10	17	24	8	12	19	25	8	12	23	38	7	11	21	39	7	11	20	35	7	11	20	32
4-hr	6	8	13	19	7	10	15	20	6	10	18	29	6	9	17	30	6	9	16	26	6	9	15	24
6-hr	4	6	9	13	5	7	11	13	5	7	12	18	4	7	12	20	4	6	11	17	5	7	11	16
12-	3	4	5	6	3	4	6	7	3	4	6	8	3	4	7	10	3	4	6	8	3	4	6	8
18-	2	3	4	5	2	3	4	5	2	3	4	6	2	3	5	7	2	3	4	6	2	3	4	5
24-	1	2	3	4	2	2	3	4	2	2	4	5	1	2	4	5	2	2	3	4	2	2	3	4
HadGEM2-ES: RCP8.5																								

1-hr	14	26	89	303	17	28	51	78	15	25	42	59	14	24	58	139	16	25	56	124	14	23	51	104
2-hr	9	17	45	110	11	17	29	41	10	16	25	33	10	15	29	51	11	16	31	52	10	15	29	49
3-hr	7	13	30	66	9	13	21	28	8	12	18	23	7	12	23	41	8	12	23	39	7	11	21	37
4-hr	6	10	24	48	7	11	16	22	6	10	15	18	6	9	18	33	7	10	18	29	6	9	17	28
6-hr	5	8	15	26	5	8	11	14	5	7	10	12	5	7	13	23	5	7	12	19	5	7	12	18
12-	3	4	7	11	3	4	6	7	3	4	5	6	3	4	7	11	3	4	7	9	3	4	6	9
18-	2	3	5	9	2	3	4	5	2	3	4	4	2	3	5	7	2	3	5	6	2	3	5	7
24-	2	2	4	7	2	2	3	4	2	2	3	4	2	2	4	5	2	3	4	5	2	2	4	5
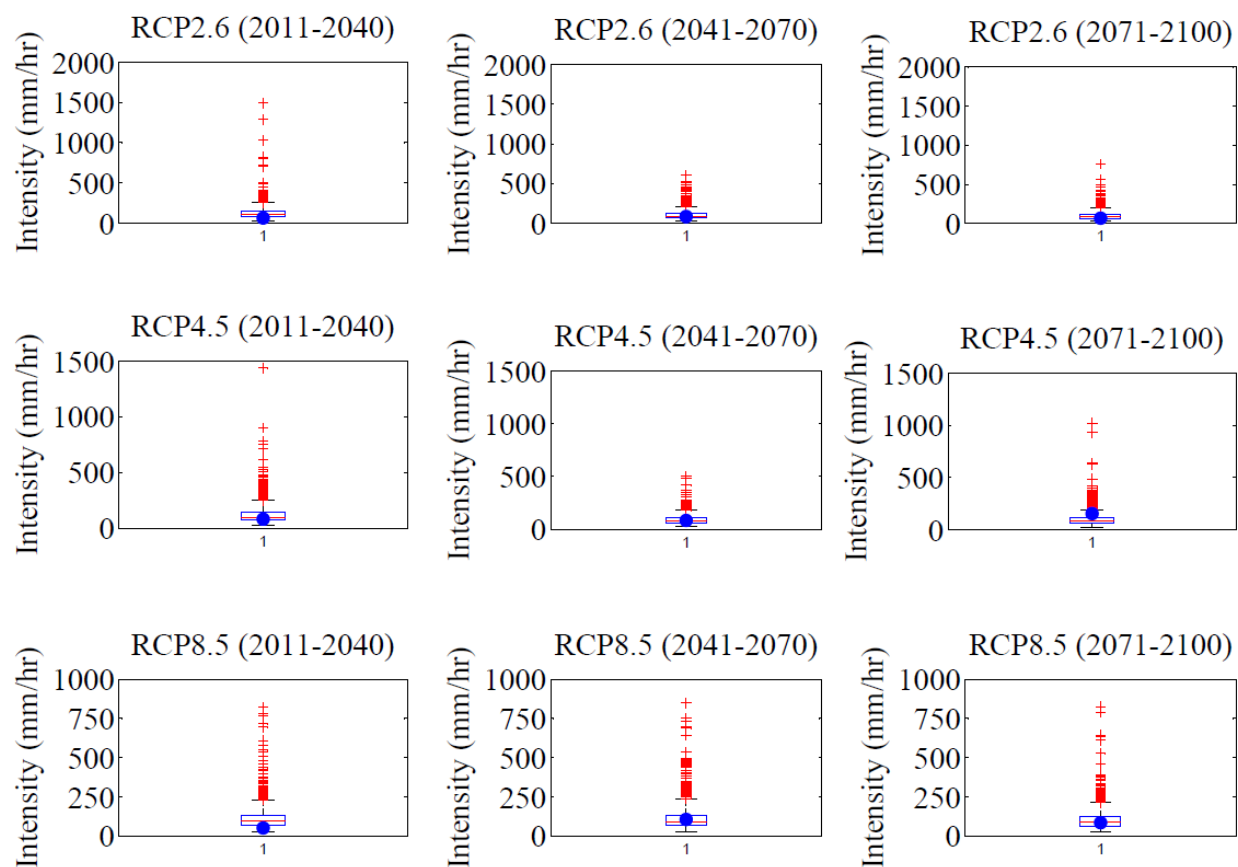
Figure E.5: Expected 1-hr AMP corresponding to 1000 realizations from LARS-WG and K-NN hourly disaggregation model (boxplot), and the same from GP method (blue dots) of **100-year** return period for **CanESM2** based on three RCPs during the 21st century.
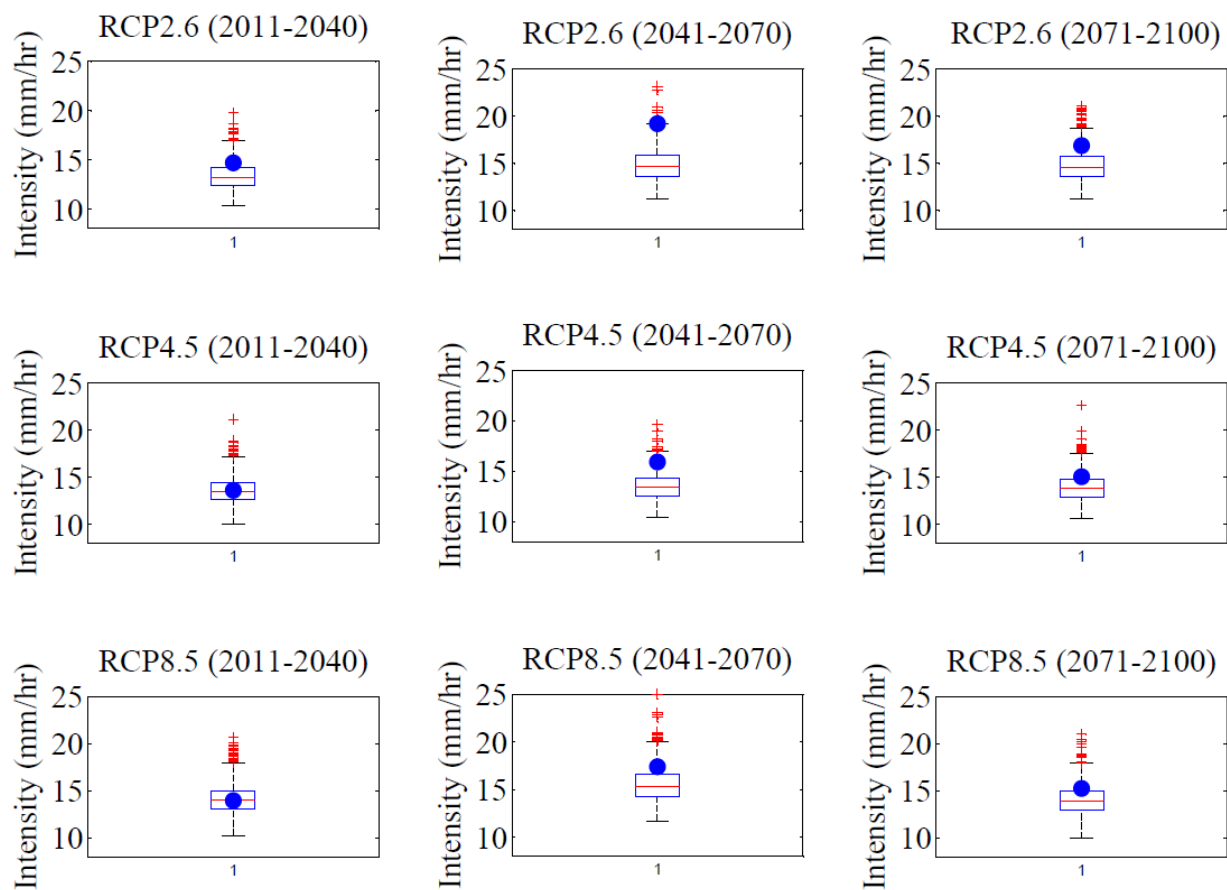
Figure E.6: Expected 1-hr AMP corresponding to 1000 realizations from LARS-WG and K-NN hourly disaggregation model (boxplot), and the same from GP method (blue dots) of **2-year** return period for **HadGEM2-ES** based on three RCPs during the 21st century.
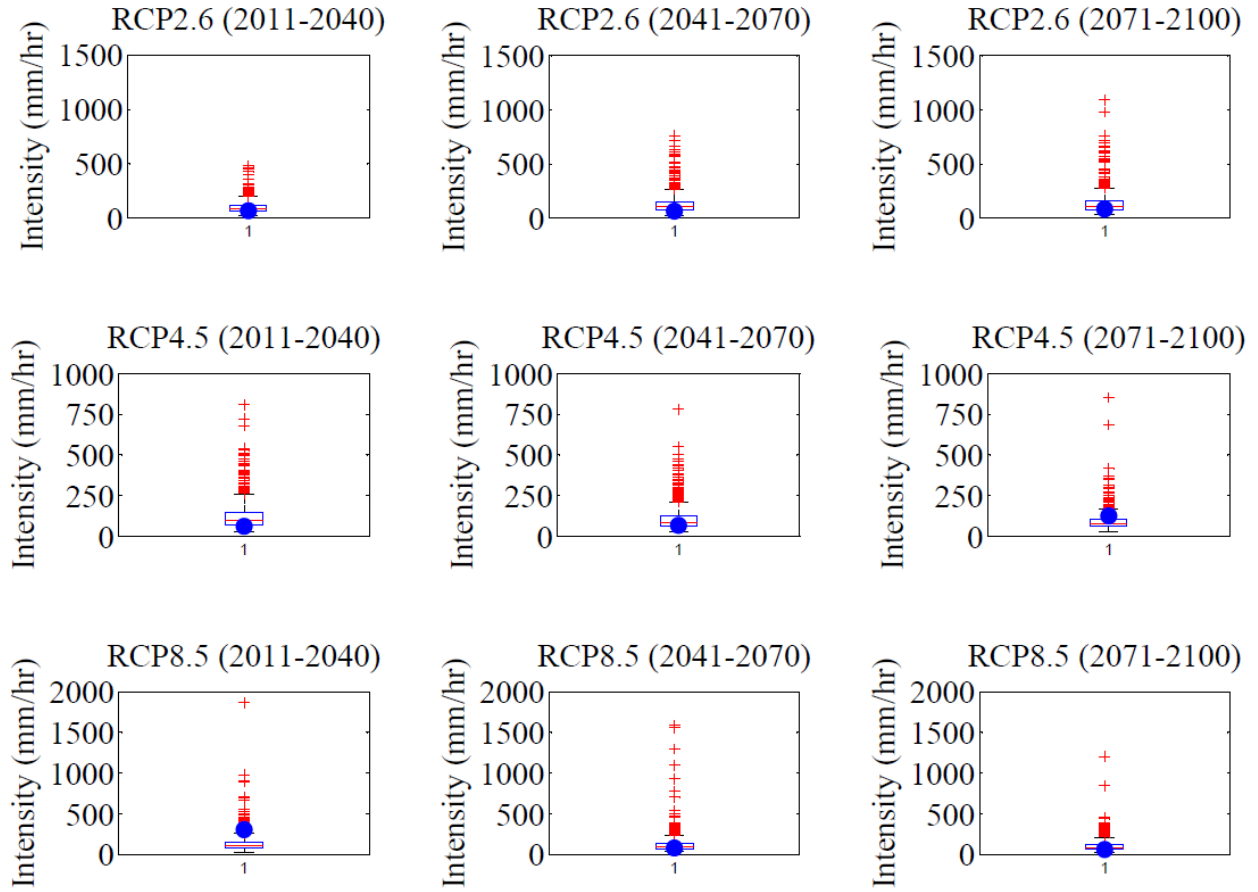
Figure E.7: Expected 1-hr AMP corresponding to 1000 realizations from LARS-WG and K-NN hourly disaggregation model (boxplot), and the same from GP method (blue dots) of **100-year** return period for **HadGEM2-ES** based on three RCPs during the 21st century.
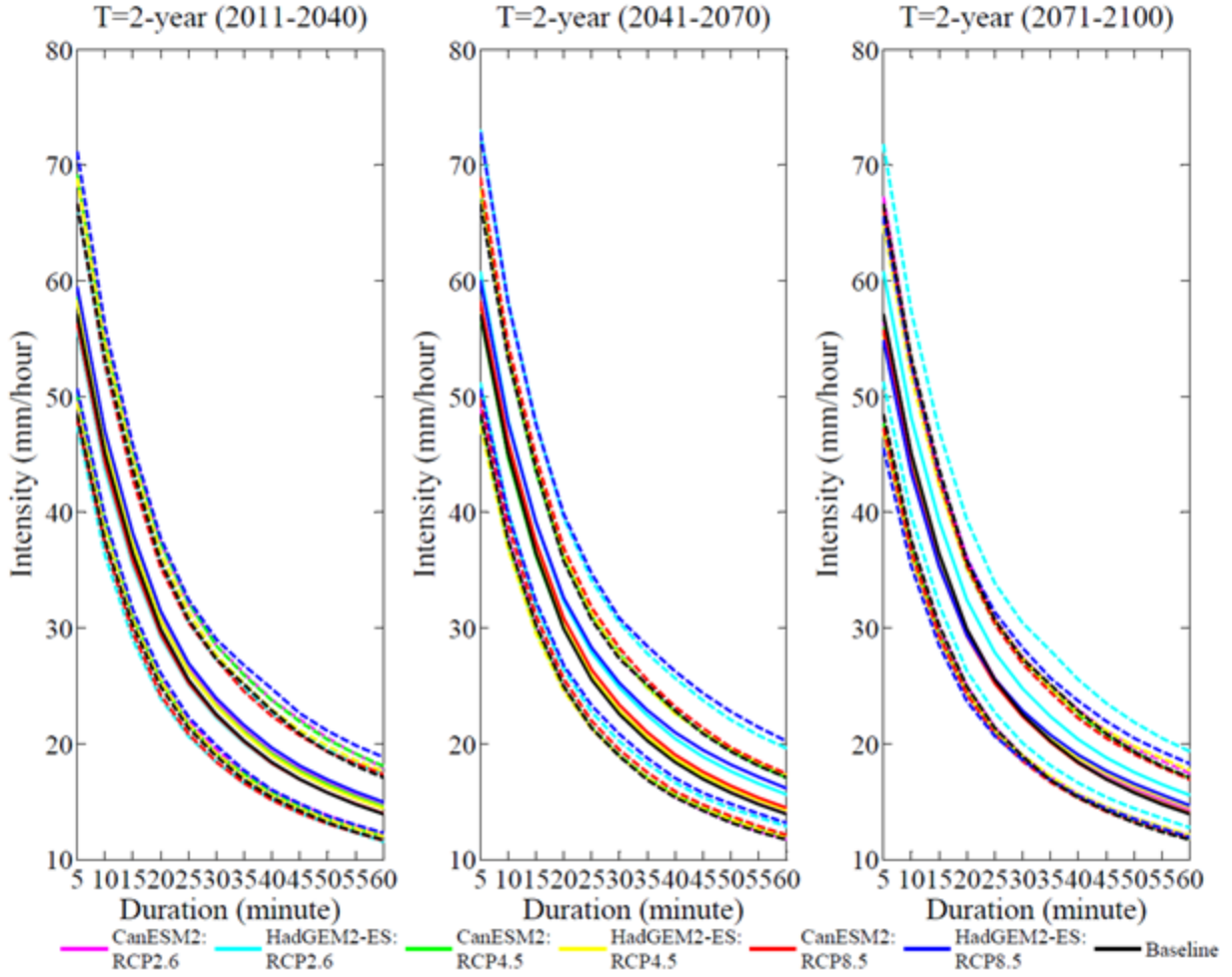
Figure E.8: Uncertainty in the projections of future extreme precipitation quantiles for 2-year return period based on two GCMs and three RCPs obtained from CMIP5 and quantified by using GEV shown as 95% confidence intervals (dashed lines).
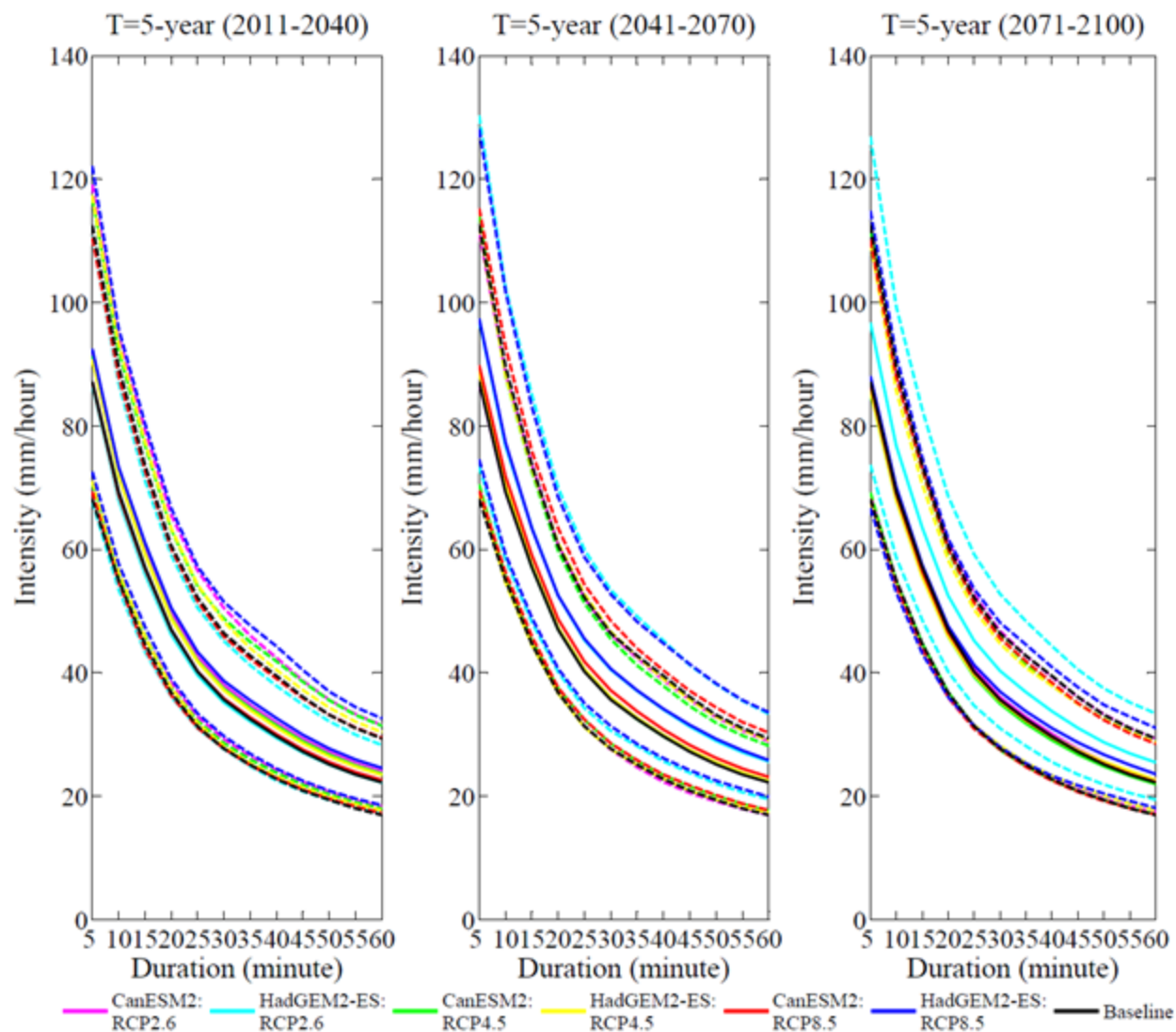
Figure E.9: Uncertainty in the projections of future extreme precipitation quantiles for 5-year return period based on two GCMs and three RCPs obtained from CMIP5 and quantified by using GEV shown as 95% confidence intervals (dashed lines).
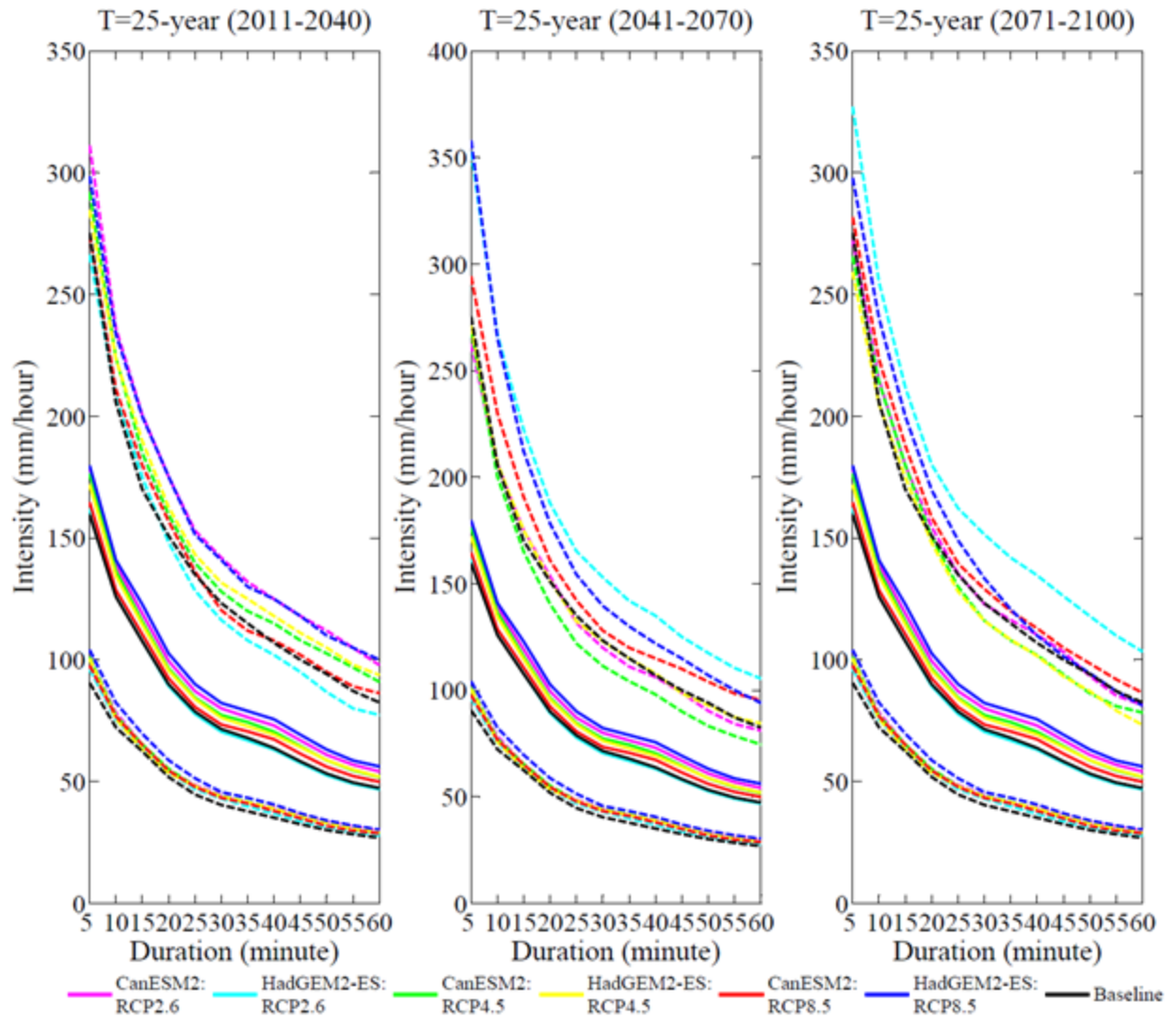
Figure E.10: Uncertainty in the projections of future extreme precipitation quantiles for 25-year return period based on two GCMs and three RCPs obtained from CMIP5 and quantified by using GEV shown as 95% confidence intervals (dashed lines).
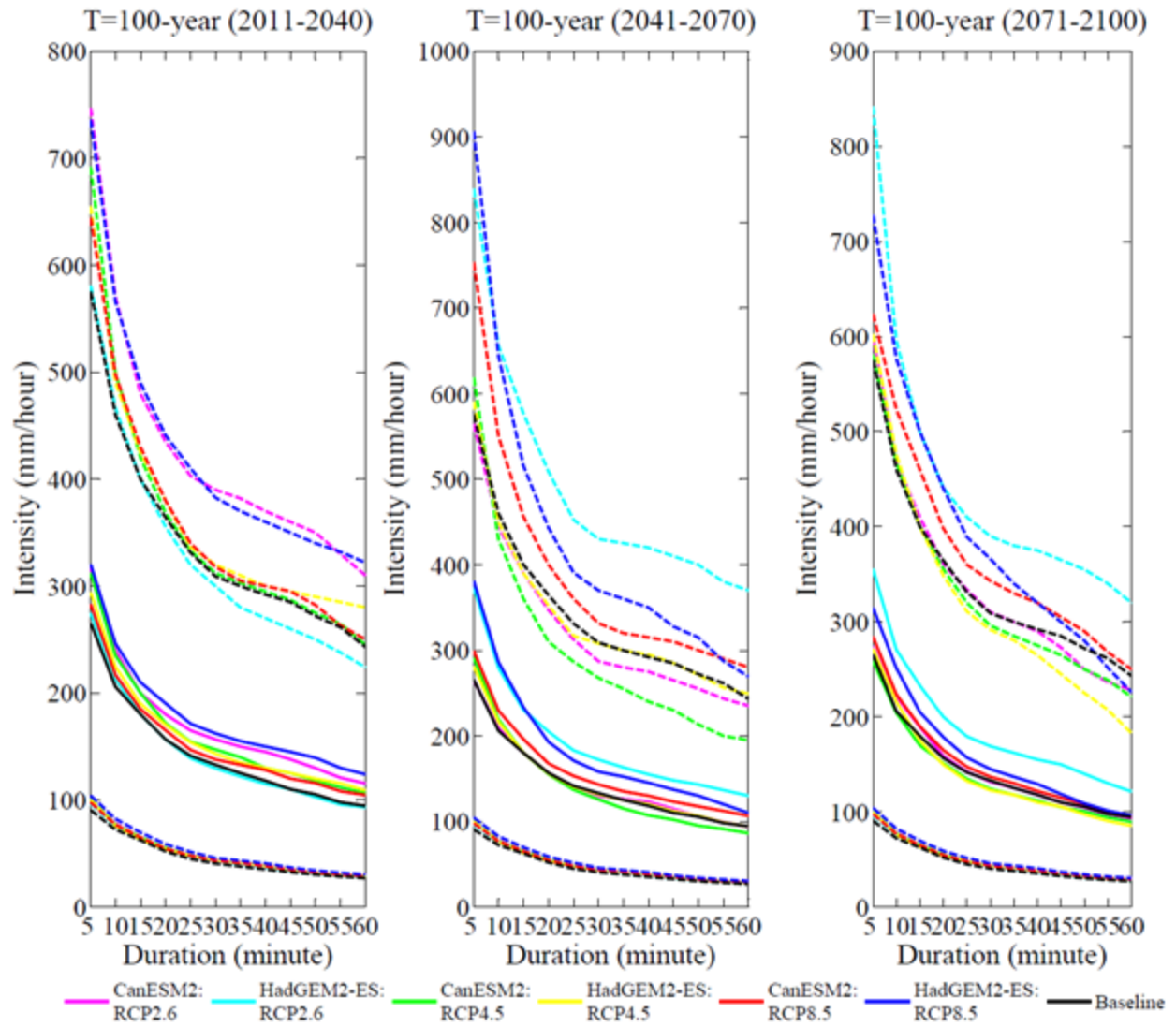
Figure E.11: Uncertainty in the projections of future extreme precipitation quantiles for 100-year return period based on two GCMs and three RCPs obtained from CMIP5 and quantified by using GEV shown as 95% confidence intervals (dashed lines).
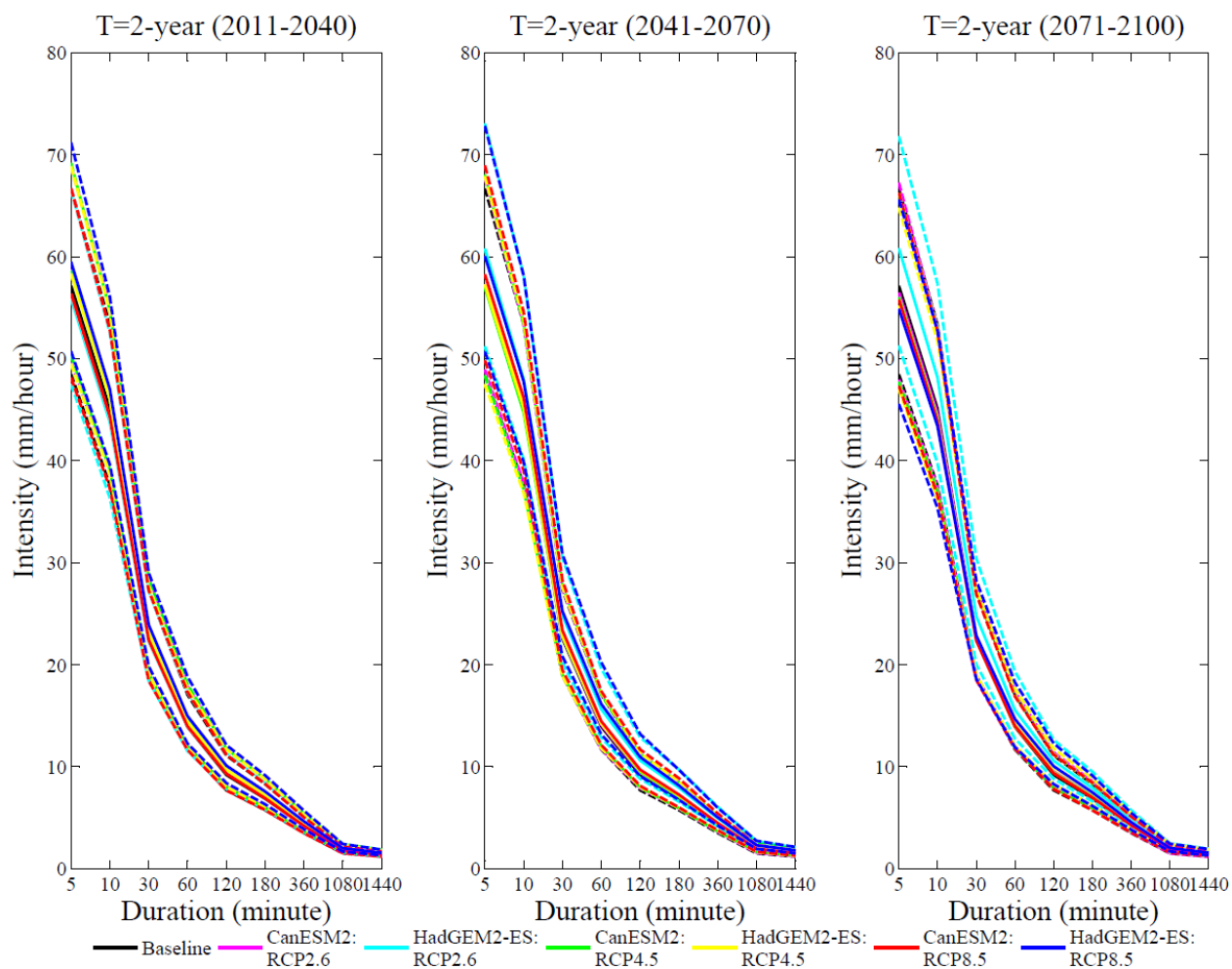
Figure E.12: Uncertainty in the projections of future extreme precipitation quantiles of durations from 5-min to 24-hour for 2-year return period based on two GCMs and three RCPs obtained from CMIP5 and quantified by using GEV shown as 95% confidence intervals (dashed lines).
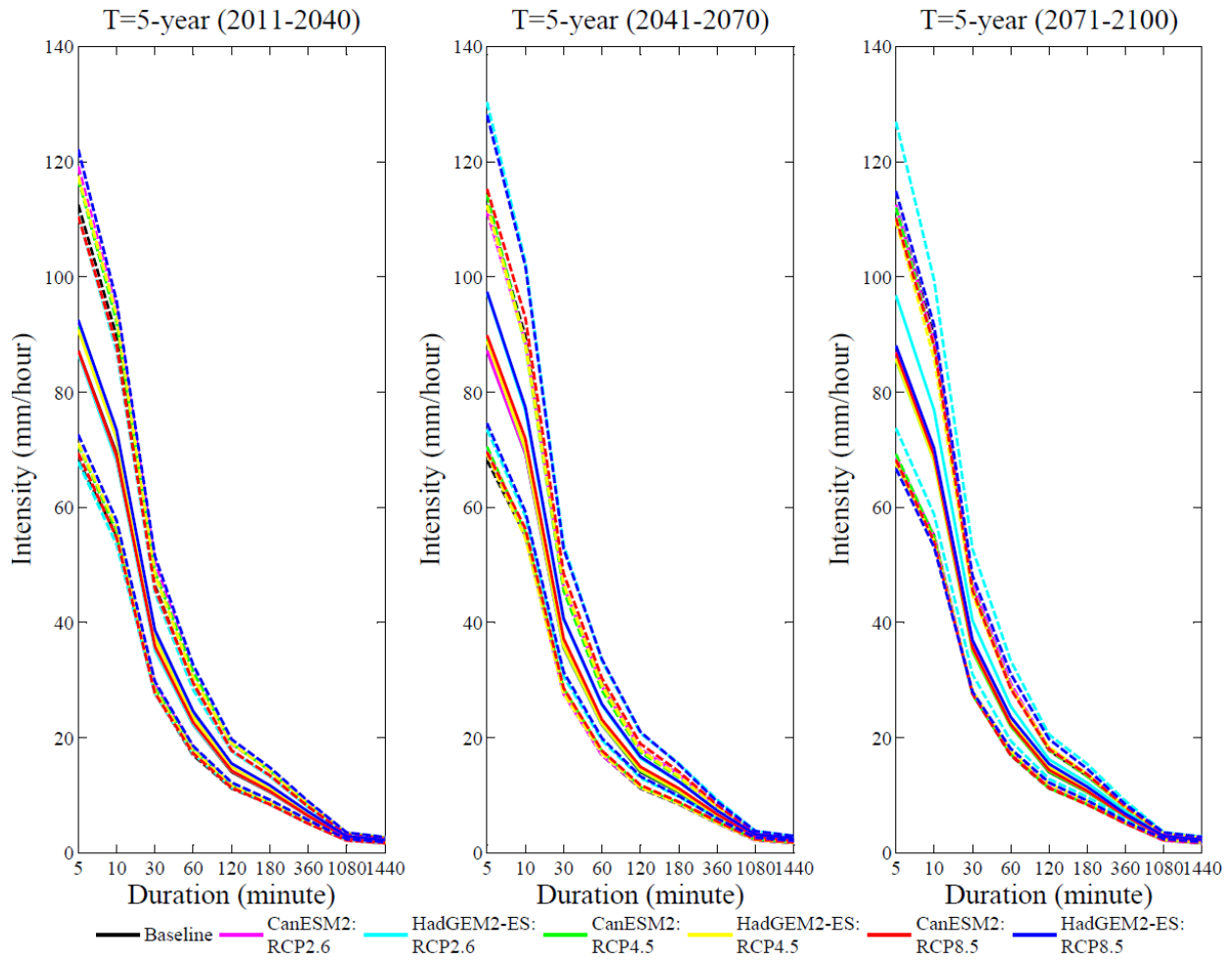
Figure E.13: Uncertainty in the projections of future extreme precipitation quantiles of durations from 5-min to 24-hour for 5-year return period based on two GCMs and three RCPs obtained from CMIP5 and quantified by using GEV shown as 95% confidence intervals (dashed lines).
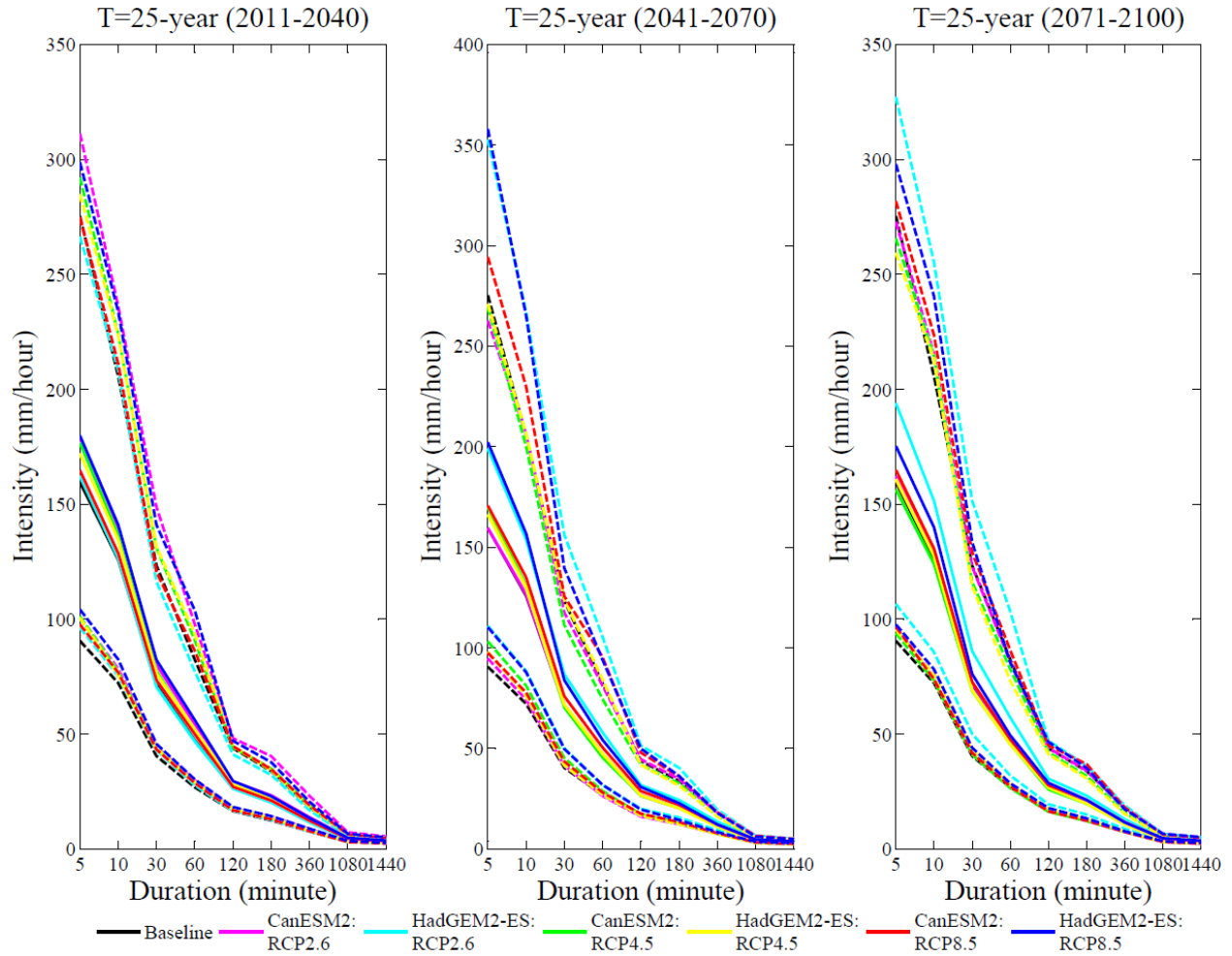
Figure E.14: Uncertainty in the projections of future extreme precipitation quantiles of durations from 5-min to 24-hour for 25-year return period based on two GCMs and three RCPs obtained from CMIP5 and quantified by using GEV shown as 95% confidence intervals (dashed lines).
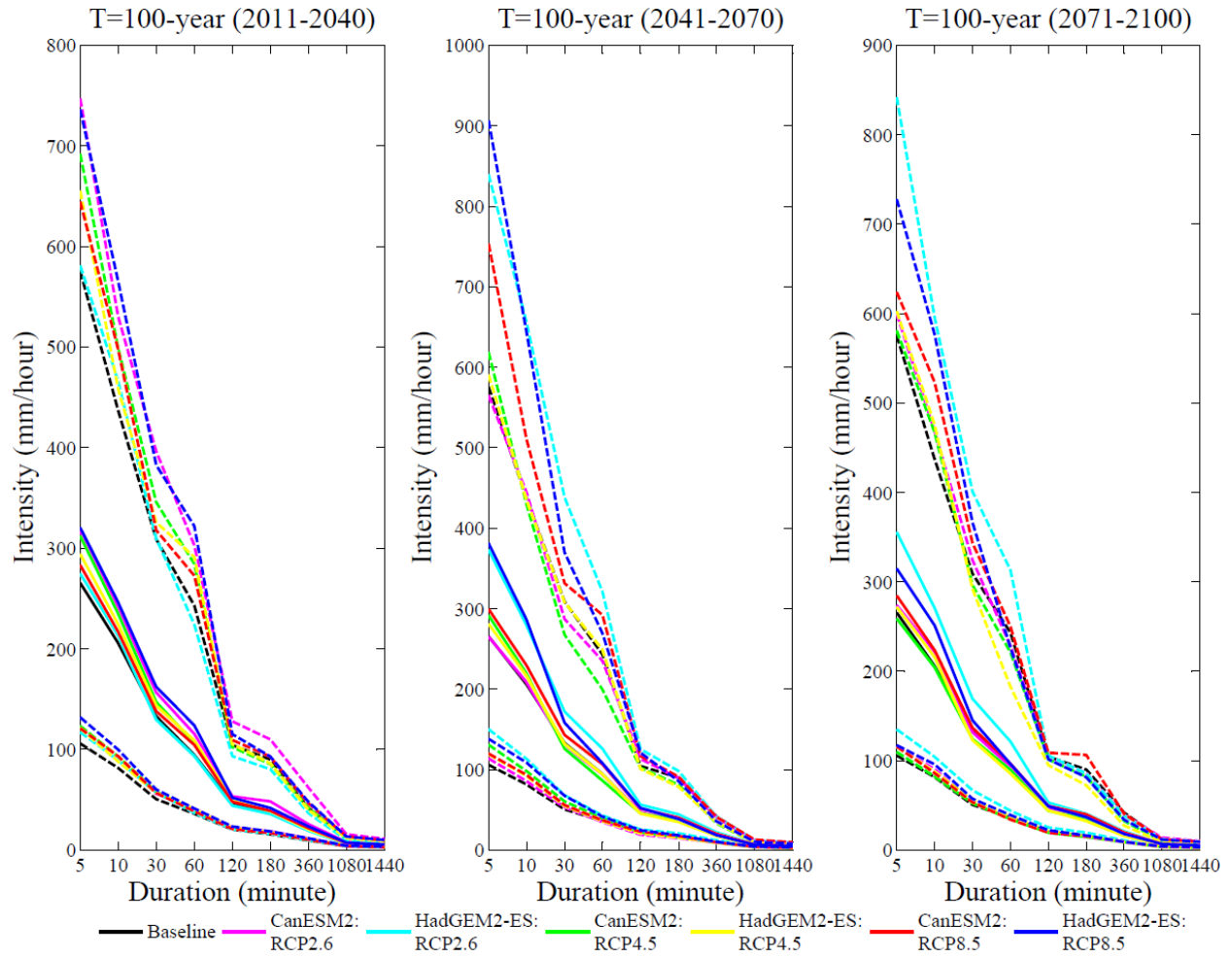
Figure E.15: Uncertainty in the projections of future extreme precipitation quantiles of durations from 5-min to 24-hour for 100-year return period based on two GCMs and three RCPs obtained from CMIP5 and quantified by using GEV shown as 95% confidence intervals (dashed lines).

Appendix F

F.1 Effect of wet and dry spell lengths
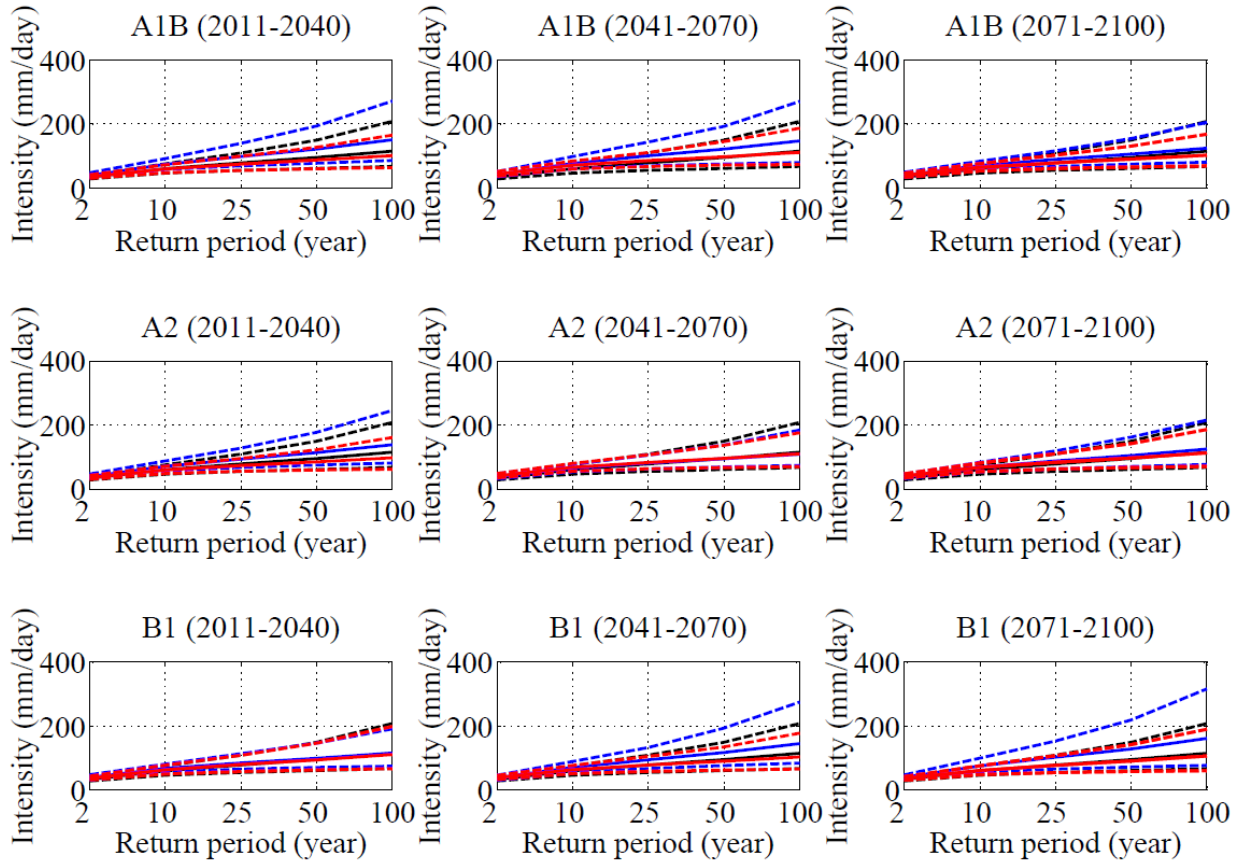
Figure F.1: Variations in the future projections of daily AMP quantiles in the City of Saskatoon according to CGCM3.1 forced with three emission scenarios using two sets of change factors: with wet/dry spell (blue) and without wet/dry spell (red) effects. The expected quantiles (solid lines) and their 95% confidence intervals (dashed lines) are shown with the corresponding quantiles during the baseline period (black).
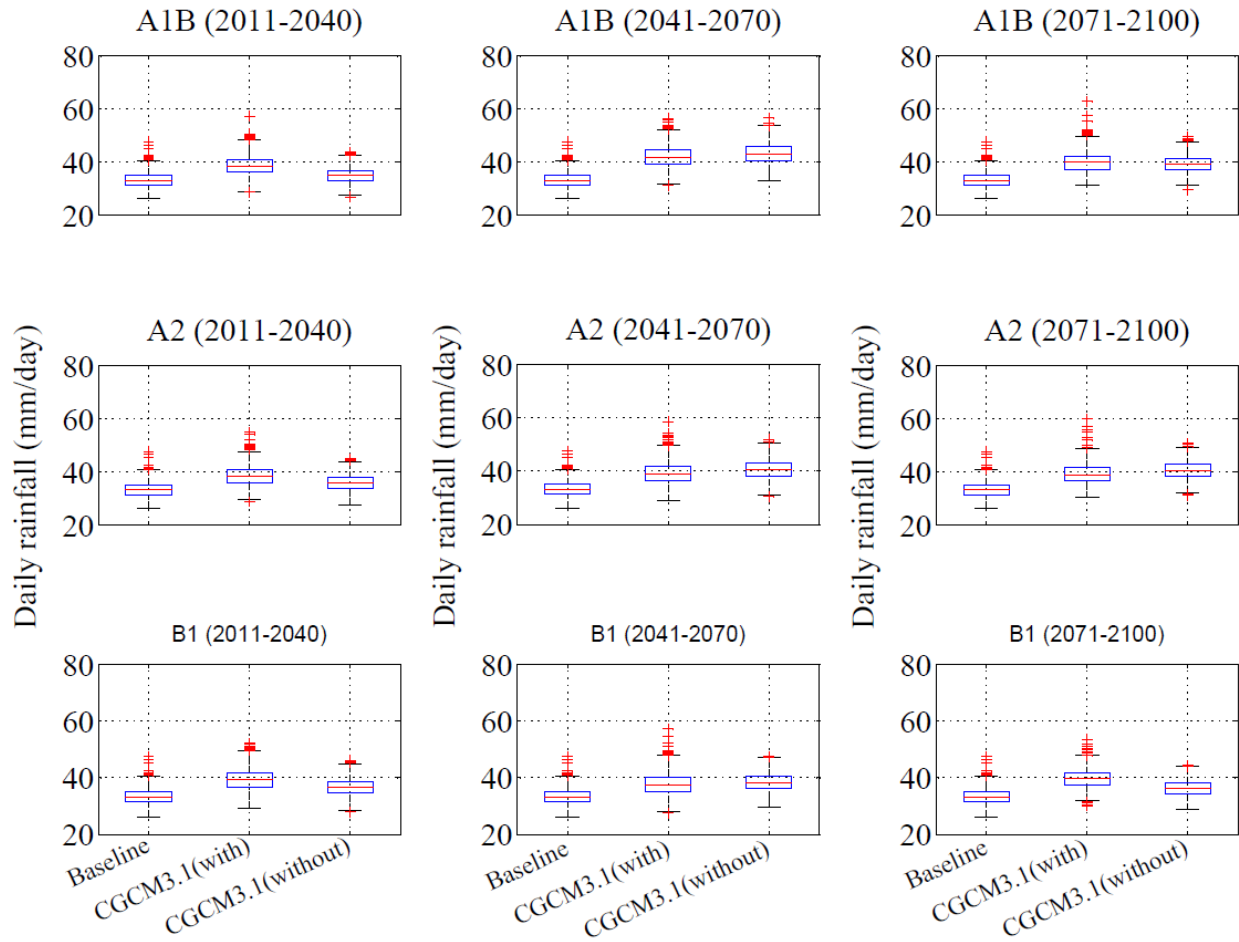
Figure F.2: Variations in the future projections of daily expected quantiles for 2-year return period in the City of Saskatoon according to CGCM3.1 forced with three emission scenarios using two sets of change factors, i.e. with wet/dry spell and without wet/dry spell effects along with the corresponding daily expected quantiles during the baseline.
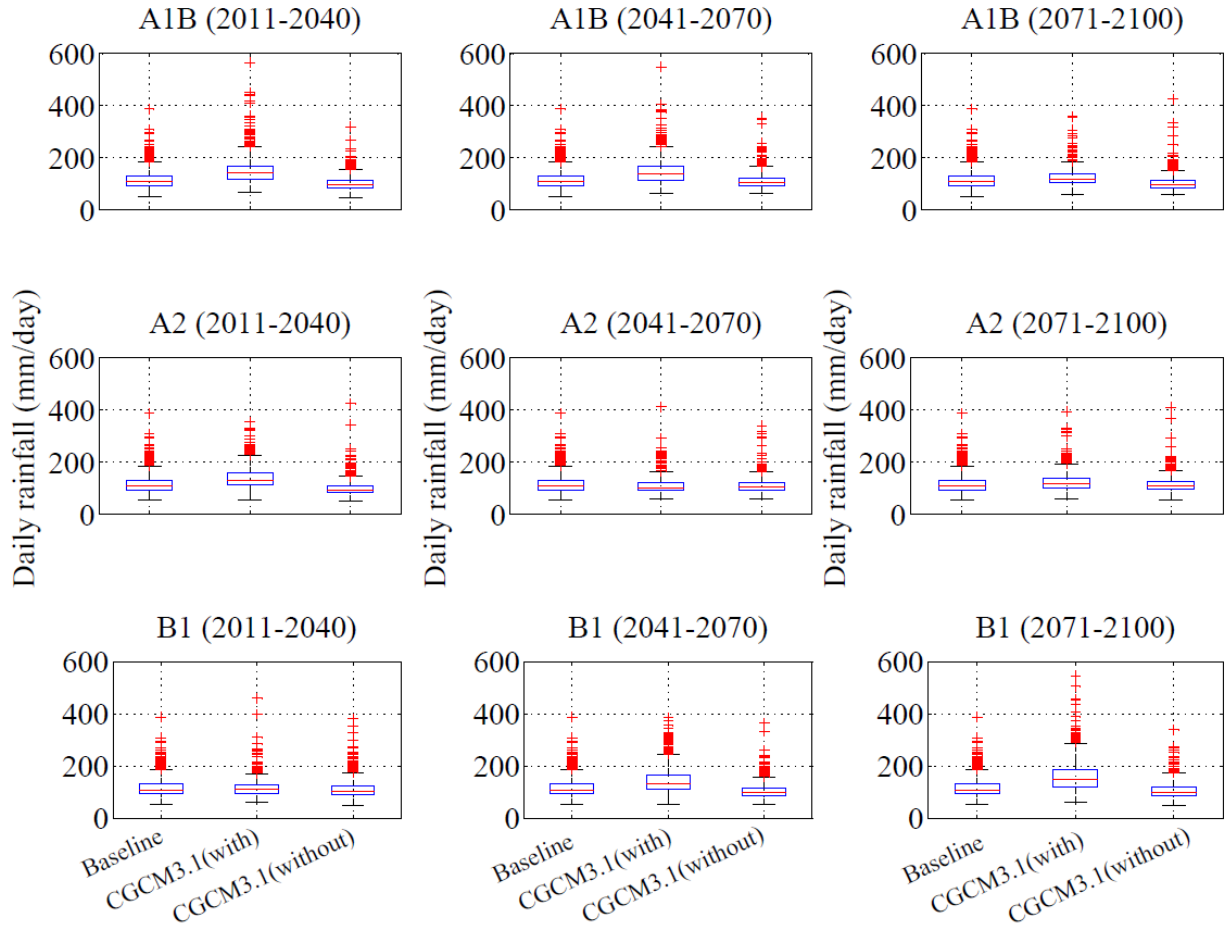
Figure F.3: Variations in the future projections of daily expected quantiles for 100-year return period in the City of Saskatoon according to CGCM3.1 forced with three emission scenarios using two sets of change factors, i.e. with wet/dry spell and without wet/dry spell effects along with the corresponding daily expected quantiles during the baseline.

F.2 Variations in the future IDF curves obtained for CMIP3 climate models
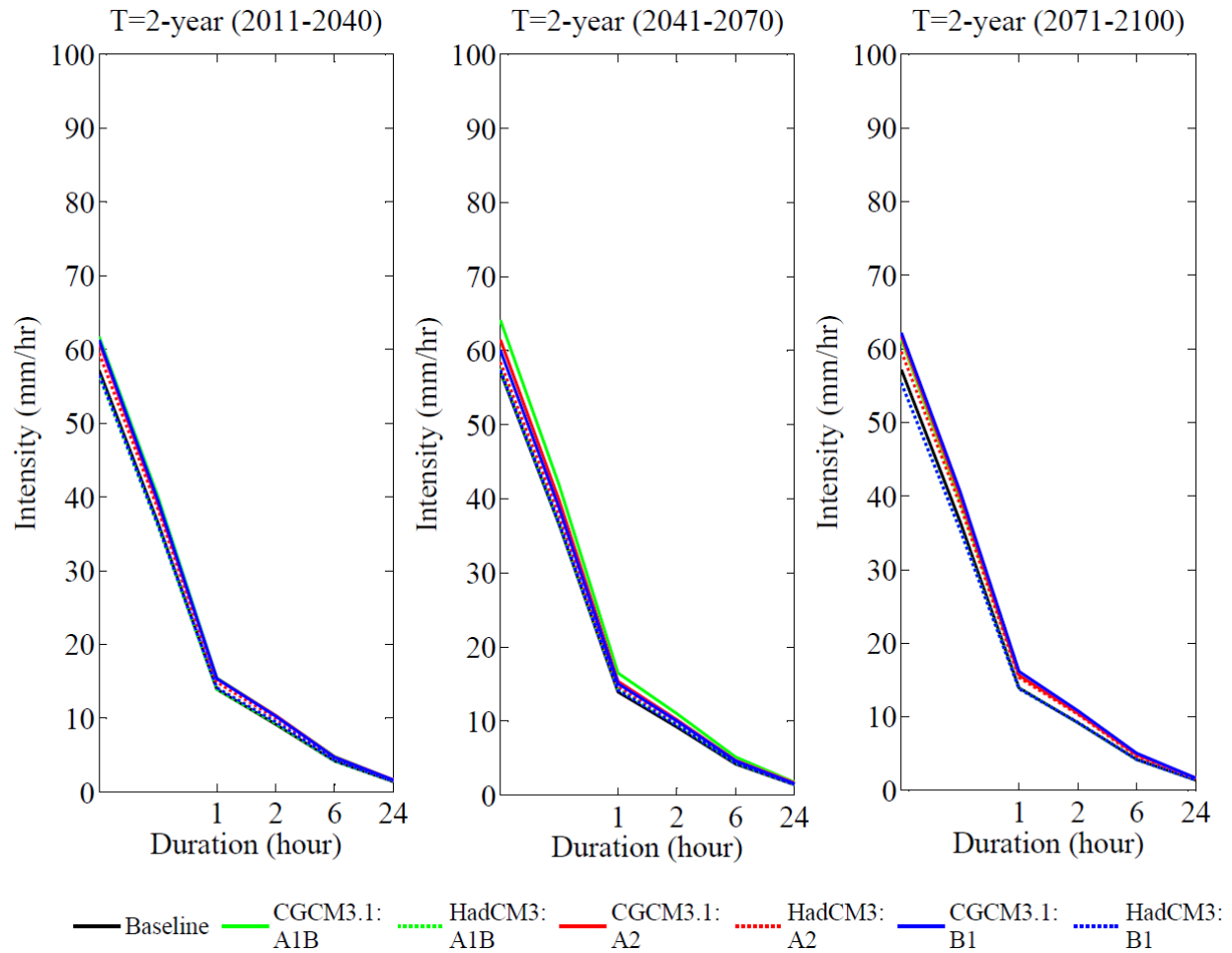
Figure F.4: Variations in the future IDF curves for 2-year return period in the City of Saskatoon according to CGCM3.1 and HadCM3 based on three AR4 emission scenarios.
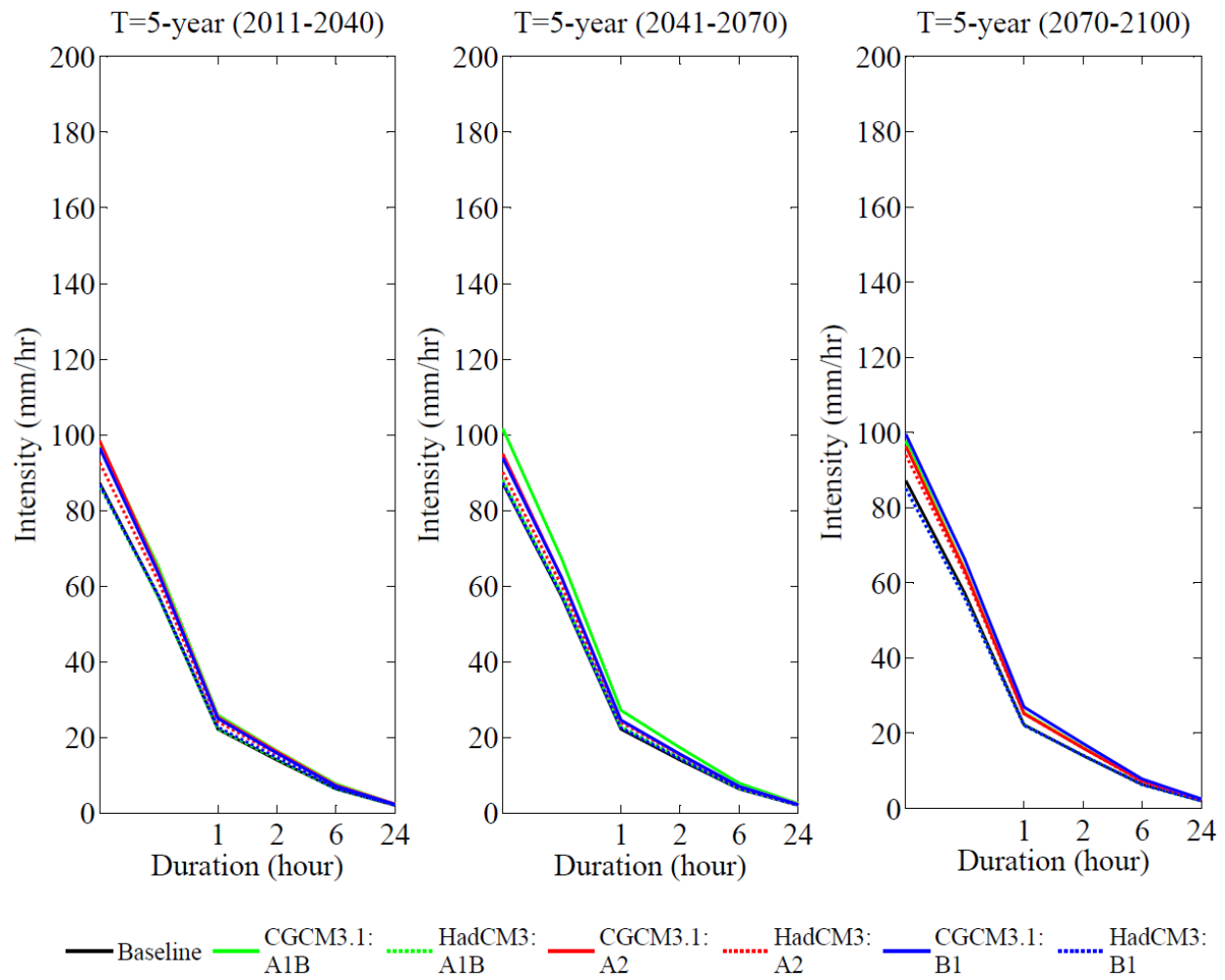
Figure F.5: Variations in the future IDF curves for 5-year return period in the City of Saskatoon according to CGCM3.1 and HadCM3 based on three AR4 emission scenarios.
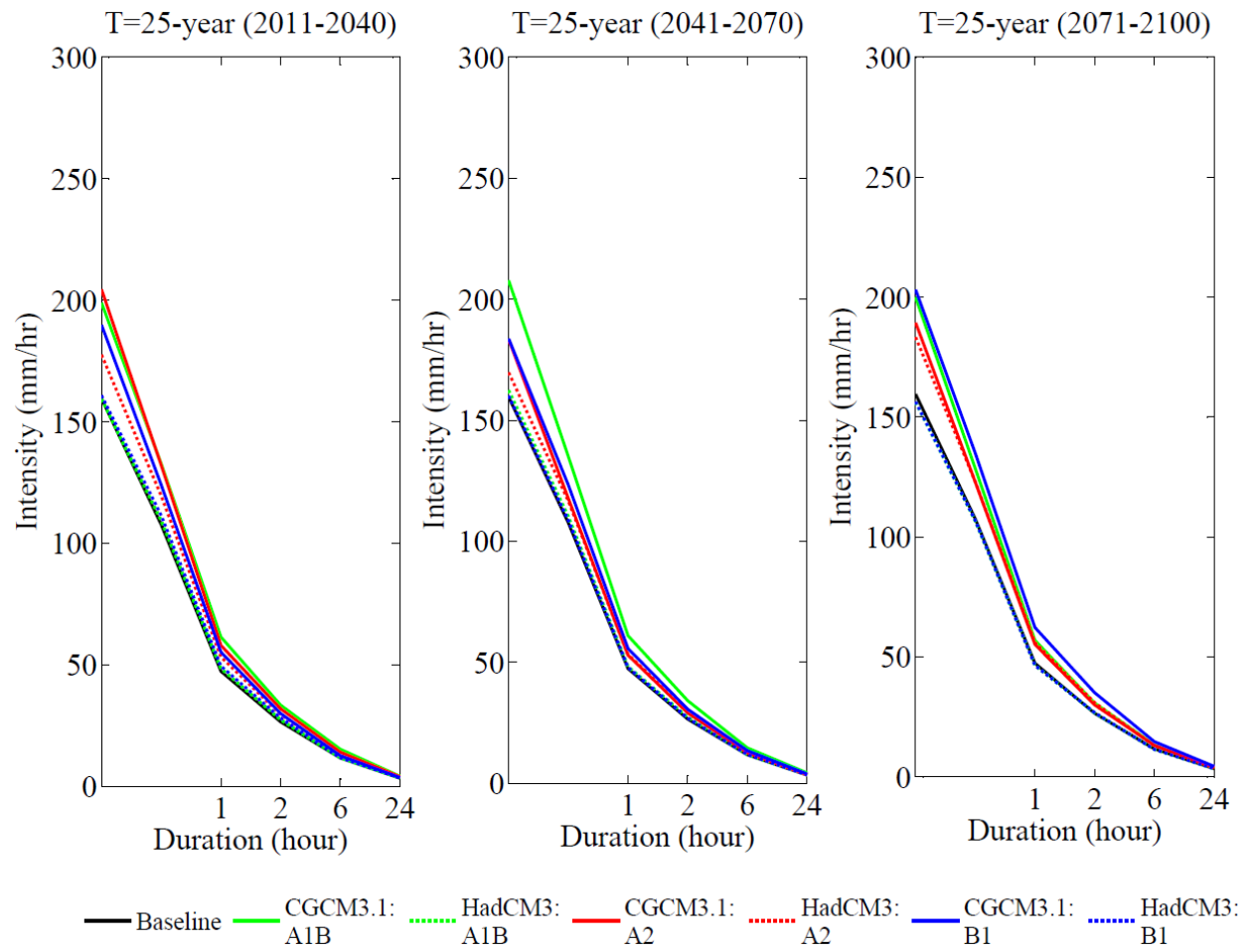
Figure F.6: Variations in the future IDF curves for 25-year return period in the City of Saskatoon according to CGCM3.1 and HadCM3 based on three AR4 emission scenarios.
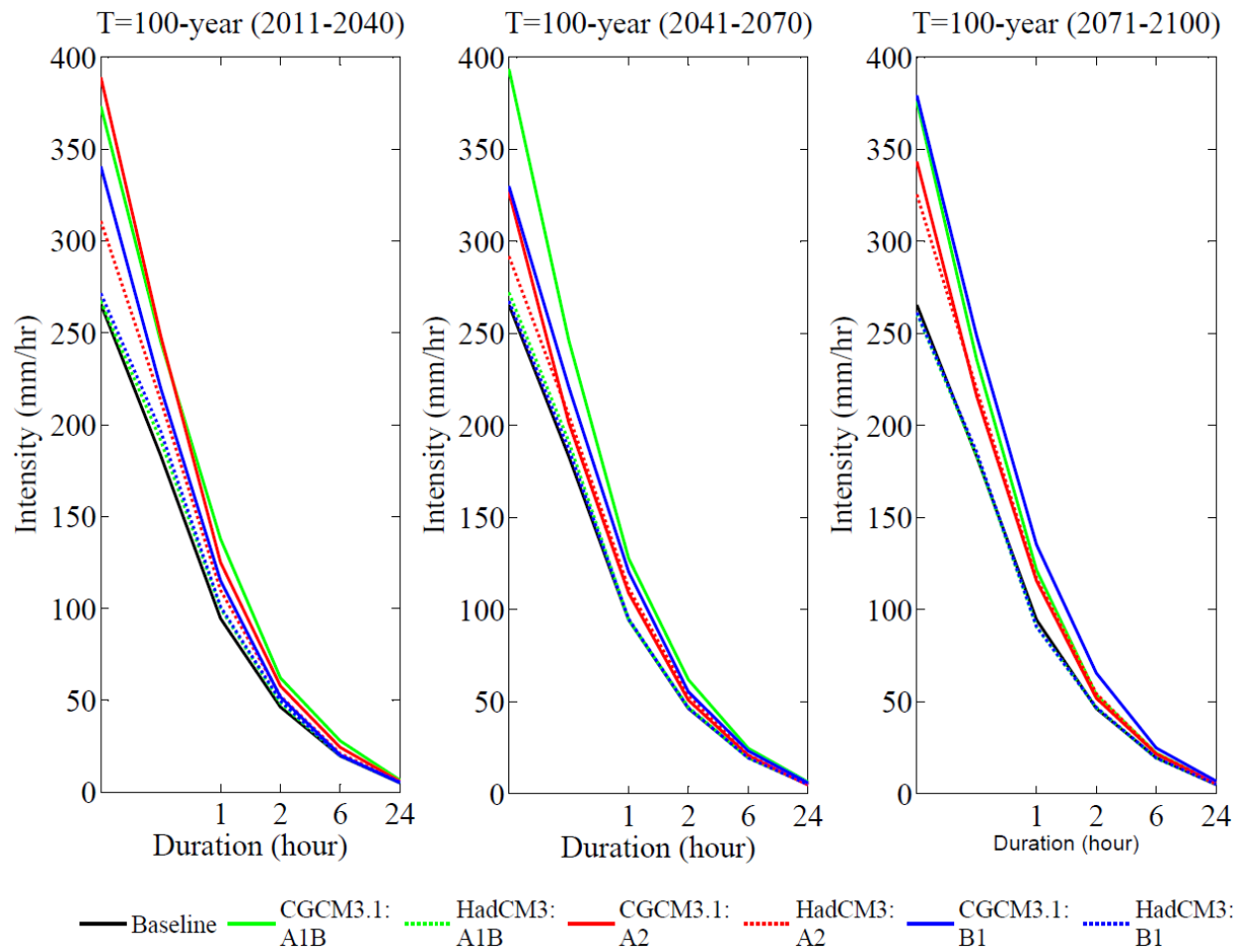
Figure F.7: Variations in the future IDF curves for 100-year return period in the City of Saskatoon according to CGCM3.1 and HadCM3 based on three AR4 emission scenarios.

Table F.1: The expected precipitation intensity (mm/hr) for CGCM3.1 and HadCM3 based on three AR4 emission scenarios obtained from CMIP3 during the 21st century for various return periods.

	(2011-2040)				(2041-2070)				(2071-2100)				(2011-2040)				(2041-2070)				(2071-2100)			
	Return period (year)																								
	2	5	25	100	2	5	25	100	2	5	25	100	2	5	25	100	2	5	25	100	2	5	25	100
CGCM3.1: A1B													HadCM3: A1B											
5-min	62	98	199	373	64	102	208	394	61	98	200	376	56	86	159	267	58	88	162	272	55	85	156	261
15-	40	65	133	245	42	67	135	246	39	63	129	236	36	57	109	191	37	58	110	191	35	56	107	184
1-hr	15	26	61	138	16	27	61	128	16	25	57	121	14	22	49	100	14	23	48	94	14	22	46	91
2-hr	10	16	33	62	11	17	34	62	11	16	31	54	9	14	27	48	10	15	27	47	9	14	27	47
6-hr	5	8	15	28	5	8	15	25	5	7	13	22	4	6	12	20	4	7	12	19	4	6	11	19
24-hr	2	2	4	6	2	3	4	6	2	2	4	6	1	2	3	5	1	2	3	5	1	2	3	5
CGCM3.1: A2													HadCM3: A2											
5-min	61	98	204	389	61	95	183	327	62	96	189	343	59	93	178	311	58	90	170	292	60	94	183	326
15-	39	64	132	248	40	62	118	201	40	63	123	216	38	61	120	213	38	60	117	205	39	62	123	220
1-hr	15	25	58	125	15	25	53	109	16	25	55	116	15	24	53	110	15	24	53	112	15	25	56	117
2-hr	10	16	32	58	10	16	29	51	11	16	30	52	10	15	30	52	10	15	30	53	10	16	31	54
6-hr	5	7	14	24	5	7	13	21	5	7	13	22	5	7	13	21	5	7	13	21	5	7	13	22
24-hr	2	2	4	6	2	2	3	5	2	2	4	5	2	2	4	6	2	2	4	6	2	2	4	6
CGCM3.1: B1													HadCM3: B1											
5-min	61	97	190	341	60	94	184	330	62	100	203	379	56	87	161	271	57	87	160	268	55	85	156	261
15-	40	63	124	220	39	62	123	221	41	66	135	249	36	57	111	196	37	58	109	187	35	56	107	186
1-hr	15	25	55	115	15	25	56	121	16	27	62	135	14	23	49	101	14	23	48	95	14	22	46	91
2-hr	10	16	30	52	10	16	31	55	11	17	35	66	10	15	28	50	9	14	27	46	9	14	27	47
6-hr	5	7	13	20	5	7	13	23	5	8	15	25	4	7	12	20	4	7	12	19	4	6	11	19
24-hr	2	2	4	5	2	2	4	6	2	3	4	7	1	2	4	5	1	2	3	5	1	2	3	5

With the advent of CMIP5 climate models and their corresponding simulations, the previously available simulations for CMIP3 climate models have become outdated. However, temperature projections of RCP4.5 show similarities with those of B1 emission scenario with similar mean temperature scenarios at the global scale by the end of 2100 (Rogelj et al., 2012). In this study, an attempt was made to investigate variations in the future extreme rainfall quantiles using the same GCM, i.e., CGCM3.1 and CanESM2 and the corresponding equivalent (based on temperature projections) emission scenarios, i.e., B1 and RCP4.5 obtained from CMIP3 and CMIP5, respectively (Table F.2). Both CGCM3.1: B1 and CanESM2: RCP4.5 show that the rainfall intensities increase in shorter durations and longer return periods. CGCM3.1: B1 shows the highest rainfall intensity of 379 mm/hr for 5-min duration and 100-year return period during 2071-2100, while CanESM2: RCP4.5 shows the highest rainfall intensity of 312 mm/hr for 5-min duration and 100-year return period during 2011-2040. The percentage change in rainfall intensity for the GCMs/RCPs is dependent on the duration, return period, and time slice. Generally, the percentage change in rainfall intensities with respect to the historical intensities for CanESM2: RCP4.5 is less than those for CGCM3.1: B1, which might be due to the inclusion of climate policies (i.e., adaptation and mitigation) in CMIP5 climate models.

Table F.2: Comparison between the expected rainfall intensity (mm/hr) for CGCM3.1: B1 and CanESM2: RCP4.5 obtained from CMIP3 and CMIP5, respectively, during the 21st century for various return periods.

	Rainfall intensity (mm/hr)												% Change in rainfall intensity											
	(2011-2040)				(2041-2070)				(2071-2100)				(2011-2040)				(2041-2070)				(2071-2100)			
	Return period (year)																								
	2	5	25	100	2	5	25	100	2	5	25	100	2	5	25	100	2	5	25	100	2	5	25	100
CGCM3.1: B1																								
5-min	61	97	190	341	60	94	184	330	62	100	203	379	7	11	19	28	5	8	15	24	9	14	27	43
15-min	40	63	124	220	39	62	123	221	41	66	135	249	8	10	15	20	6	9	14	21	11	16	25	36
1-hr	15	25	55	115	15	25	56	121	16	27	62	135	10	13	17	22	8	11	18	28	16	21	31	43
2-hr	10	16	30	52	10	16	31	55	11	17	35	66	12	13	13	12	9	11	15	20	18	23	33	42
6-hr	5	7	13	20	5	7	13	23	5	8	15	25	12	11	7	3	10	11	14	18	20	23	25	27
24-hr	2	2	4	5	2	2	4	6	2	3	4	7	16	14	7	1	10	11	14	18	20	23	30	40
CanESM2: RCP4.5																								
5-min	59	91	177	312	57	89	170	291	56	86	156	259	3	5	11	18	0	2	6	10	-2	-2	-2	-3
15-min	37	59	116	204	36	57	109	186	36	56	105	179	2	4	8	11	-1	0	1	1	-2	-3	-2	-2
1-hr	15	24	52	106	14	22	45	86	14	22	46	90	5	6	9	13	3	0	-4	-9	1	-1	-4	-5
2-hr	10	15	28	49	9	14	27	46	9	14	26	44	6	7	7	7	3	2	0	-1	3	1	-2	-6
6-hr	4	7	13	21	4	6	11	18	4	6	11	17	6	7	8	9	3	1	-4	-9	3	-1	-7	-14
24-hr	2	2	4	5	2	2	3	4	1	2	3	4	8	8	6	4	12	6	-5	-16	6	2	-6	-13

F.3 Variations obtained with the GP method and the K-NN hourly disaggregation model
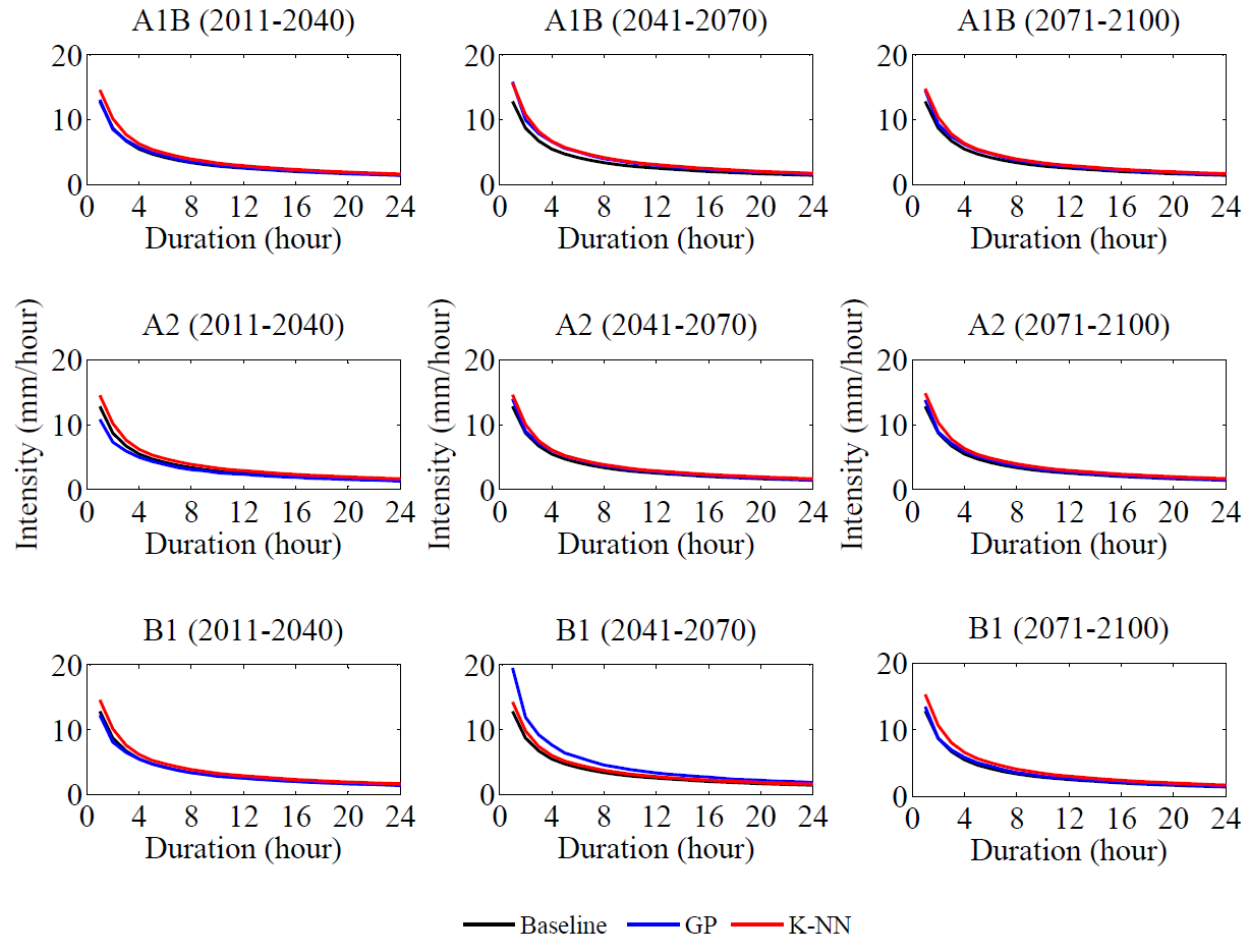
Figure F.8: Comparison between the future IDF curves (2011-2100) according to CGCM3.1 based on three AR4 emission scenarios and 2-year return period obtained using two different downscaling approaches, i.e. GP method and LARS-WG combined with K-NN Hourly Disaggregation Model.
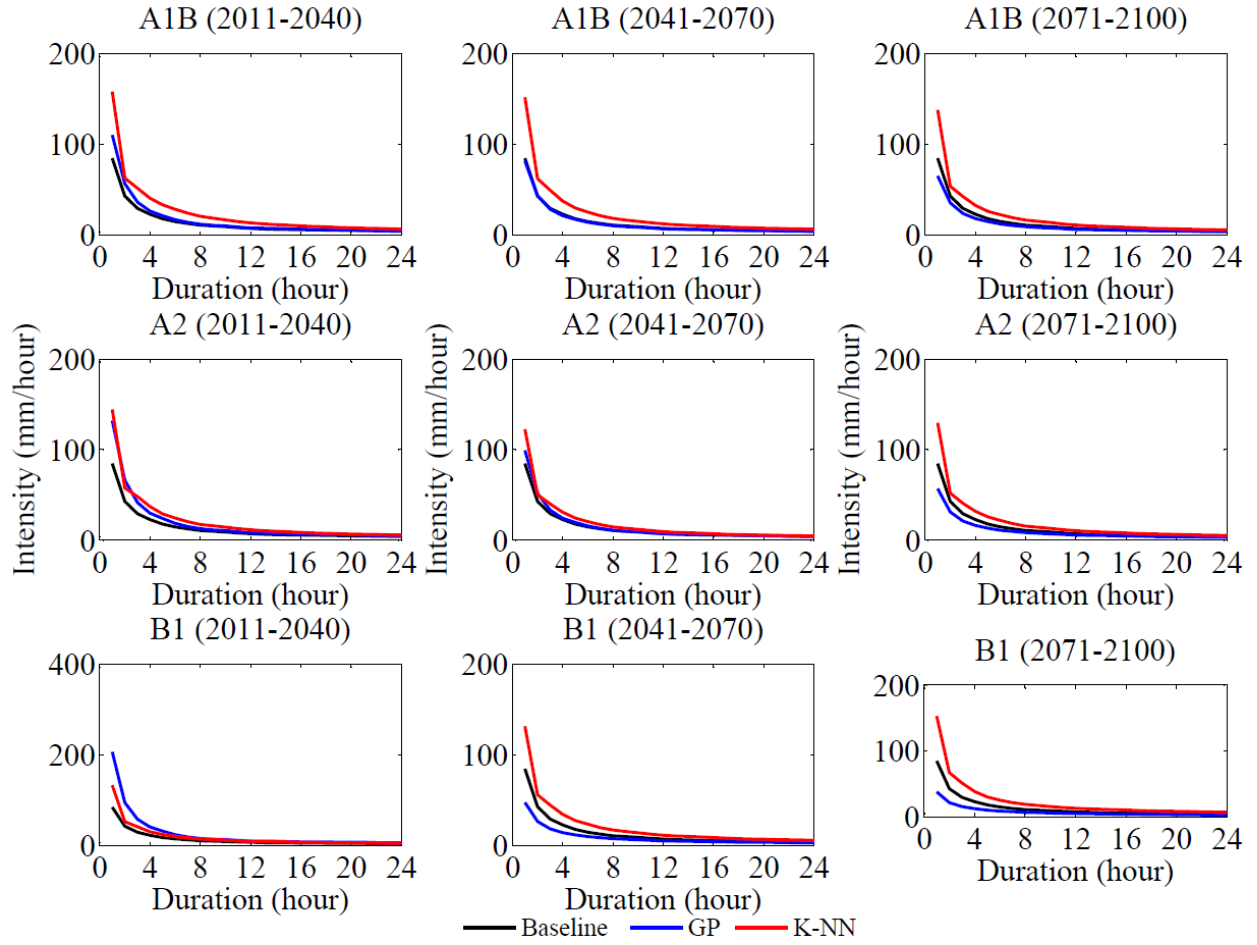
Figure F.9: Comparison between the future IDF curves (2011-2100) according to CGCM3.1 based on three AR4 emission scenarios and 100-year return period obtained using two different downscaling approaches, i.e. GP method and LARS-WG combined with K-NN Hourly Disaggregation Model.

Table F.3: Performance of the GP method based on CGCM3.1 in simulating the expected precipitation intensity (mm/hr) during the baseline period (1961-1990) for various durations and return periods.

Duration	Return period (year)				Return period (year)			
	2	5	25	100	2	5	25	100
	Historical (observed) hourly precipitation (1961-1990)				Simulated hourly precipitation (Using GP for CGCM3.1) (1961-1990)			
1-hr	12.8	21.0	44.9	84.6	12.3	22.8	50.2	88.4
2-hr	8.7	13.5	25.5	42.7	8.1	13.6	27.8	46.5
3-hr	6.7	10.4	18.7	29.3	6.5	10.3	19.2	30.2
4-hr	5.5	8.5	15.0	22.8	5.5	8.5	14.9	22.4
6-hr	4.2	6.3	10.3	14.7	4.2	6.3	10.2	14.6
12-hr	2.5	3.6	5.4	7.3	2.5	3.6	5.3	6.9
18-hr	1.8	2.5	3.9	5.3	1.8	2.5	3.8	5.2
24-hr	1.4	2.0	3.0	4.1	1.4	2.0	3.0	4.0

Table F.4: Comparison between the K-NN hourly disaggregation model and the GP method in simulating the expected precipitation intensity (mm/hr) for CGCM3.1 based on three AR4 emission scenarios during the 21st century for various durations and return periods.

	GP Method												K-NN Hourly Disaggregation Model											
	(2011-2040)				(2041-2070)				(2071-2100)				(2011-2040)				(2041-2070)				(2071-2100)			
	Return period (year)												Return period (year)											
	2	5	25	100	2	5	25	100	2	5	25	100	2	5	25	100	2	5	25	100	2	5	25	100
CGCM3.1: A1B																								
1-hr	13	25	58	110	16	28	53	81	15	24	44	65	15	25	64	158	16	27	64	152	15	25	59	138
2-hr	8	15	32	57	10	16	29	43	9	14	24	35	10	16	33	63	11	17	34	62	10	16	30	54
3-hr	7	11	21	36	8	12	20	28	7	11	17	24	8	12	26	52	8	13	26	49	8	12	23	42
4-hr	6	9	16	26	7	10	15	21	6	9	13	18	6	10	21	41	7	10	21	37	6	10	19	33
6-hr	4	7	11	17	5	7	11	14	5	7	9	12	5	8	15	28	5	8	15	25	5	7	13	22
12-hr	3	4	6	8	3	4	5	7	3	4	5	6	3	4	8	13	3	5	8	12	3	4	7	11
18-hr	2	3	4	6	2	3	4	5	2	3	4	4	2	3	5	9	2	3	5	8	2	3	5	7
24-hr	1	2	3	4	2	2	3	4	2	2	3	3	2	2	4	6	2	3	4	6	2	2	4	6
CGCM3.1: A2																								
1-hr	11	19	53	132	14	25	55	99	14	23	40	57	15	25	61	144	15	24	55	123	15	24	57	129
2-hr	7	12	29	66	9	15	30	52	9	14	23	31	10	16	31	58	10	15	29	50	10	16	30	52
3-hr	6	9	20	41	7	11	20	33	7	10	16	21	8	12	25	48	7	12	22	40	8	12	23	41
4-hr	5	8	15	30	6	9	16	24	6	9	13	16	6	10	20	37	6	9	18	31	6	10	18	32
6-hr	4	6	11	19	5	7	11	16	5	6	9	11	5	7	14	24	5	7	13	20	5	7	13	22
12-hr	2	3	5	8	3	4	6	7	3	4	5	6	3	4	7	11	3	4	7	10	3	4	7	10
18-hr	2	2	4	6	2	3	4	6	2	3	3	4	2	3	5	8	2	3	5	6	2	3	5	7
24-hr	1	2	3	5	1	2	3	4	1	2	3	3	2	2	4	6	2	2	3	5	2	2	4	5

CGCM3.1: B1

1-hr	12	21	64	207	19	30	41	48	13	20	30	38	15	24	58	133	14	24	57	132	15	26	65	153
2-hr	8	13	35	95	12	17	23	26	9	12	17	21	10	16	30	53	10	15	30	56	11	17	35	67
3-hr	6	10	23	58	9	13	16	18	7	9	13	15	8	12	23	41	7	12	24	45	8	13	27	51
4-hr	5	8	18	41	8	10	13	14	6	8	10	12	6	9	18	31	6	9	19	34	7	10	21	38
6-hr	4	6	12	24	6	7	9	10	4	6	7	9	5	7	13	20	5	7	13	24	5	8	15	25
12-hr	3	3	6	10	3	4	5	5	3	3	4	5	3	4	7	10	3	4	7	11	3	5	8	13
18-hr	2	2	4	8	2	3	3	4	2	2	3	3	2	3	5	7	2	3	5	8	2	3	6	9
24-hr	1	2	3	6	2	2	3	3	1	2	2	3	2	2	4	5	2	2	4	6	2	3	4	7
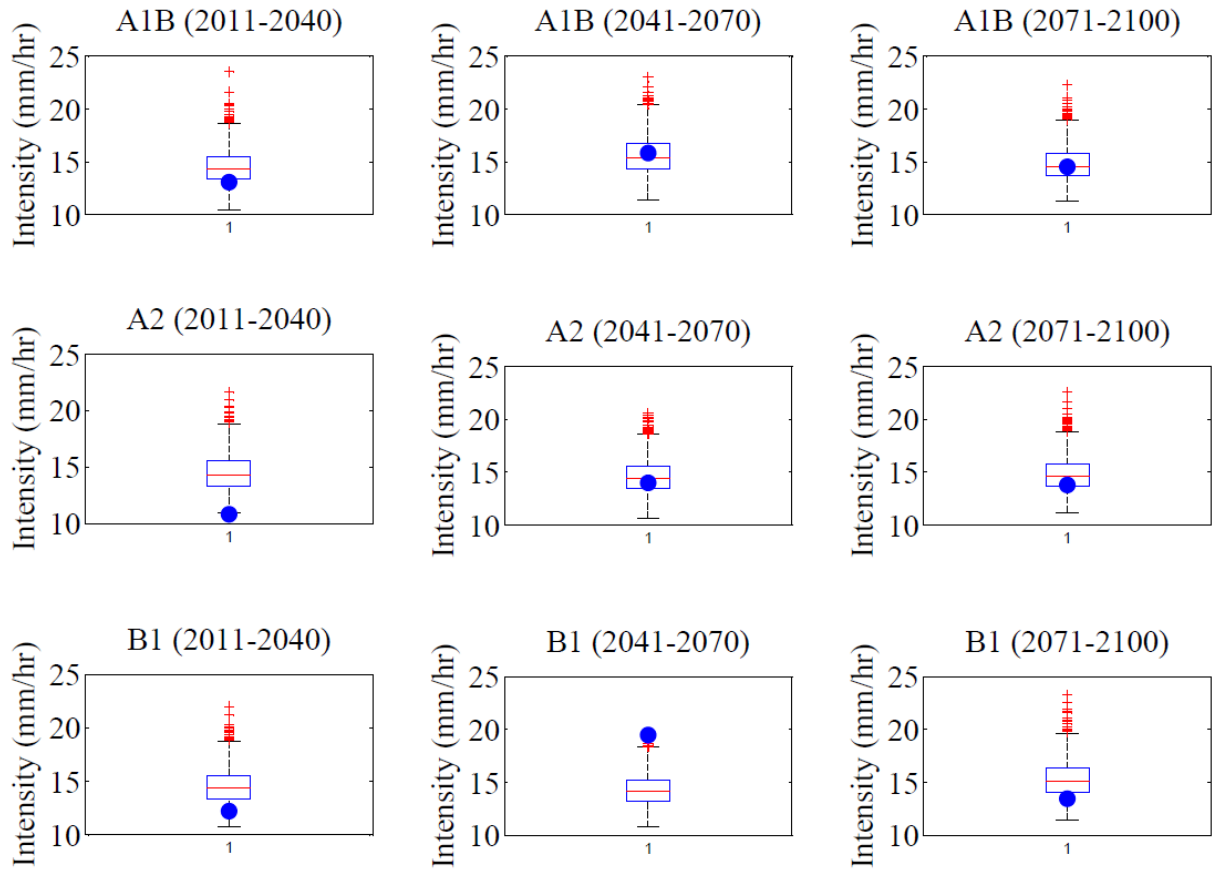
Figure F.10: Expected 1-hr AMP corresponding to 1000 realizations from LARS-WG and K-NN hourly disaggregation model (boxplot), and the same from GP method (blue dots) of 2-year return period for CGCM3.1 based on three emission scenarios during the 21st century.
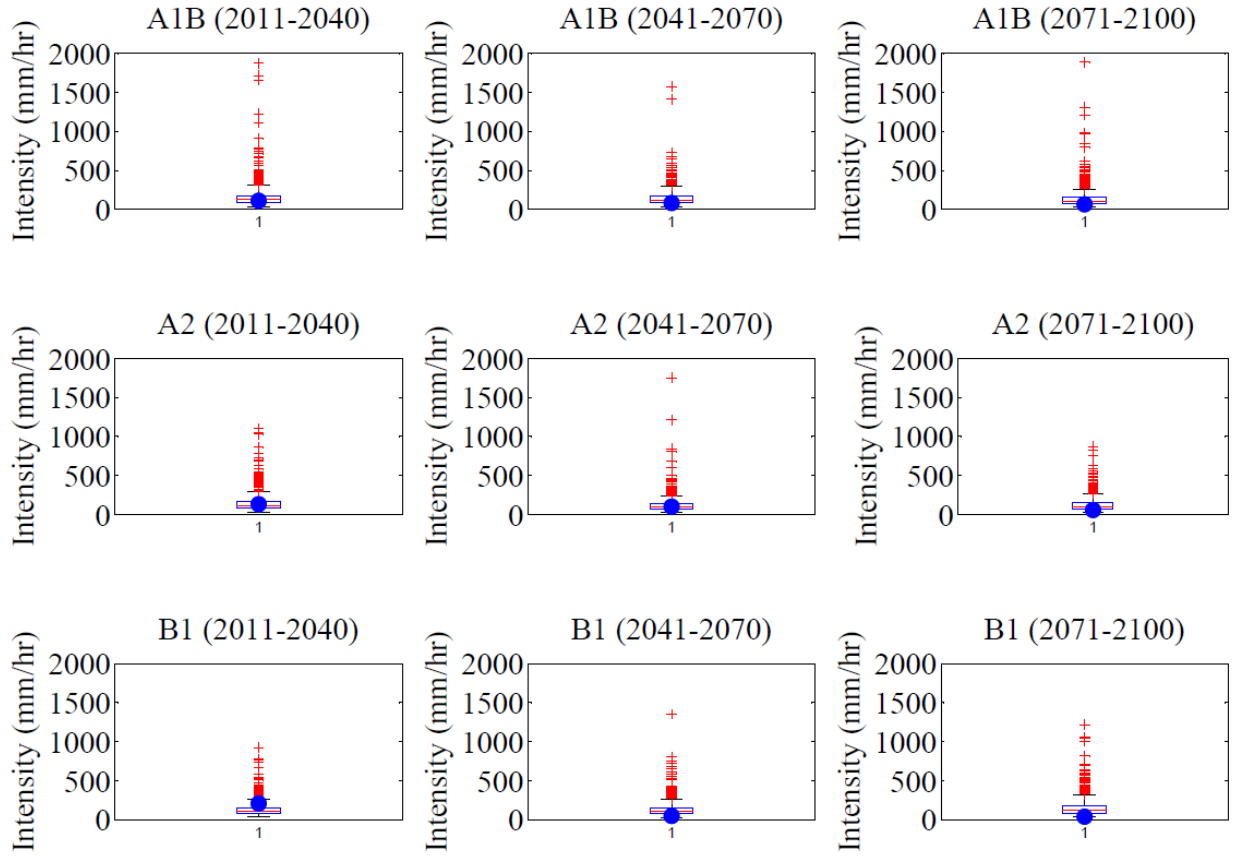
Figure F.11: Expected 1-hr AMP corresponding to 1000 realizations from LARS-WG and K-NN hourly disaggregation model (boxplot), and the same from GP method (blue dots) of 100-year return period for CGCM3.1 based on three emission scenarios during the 21st century.

F.4 Uncertainty in the projections of future IDF curves
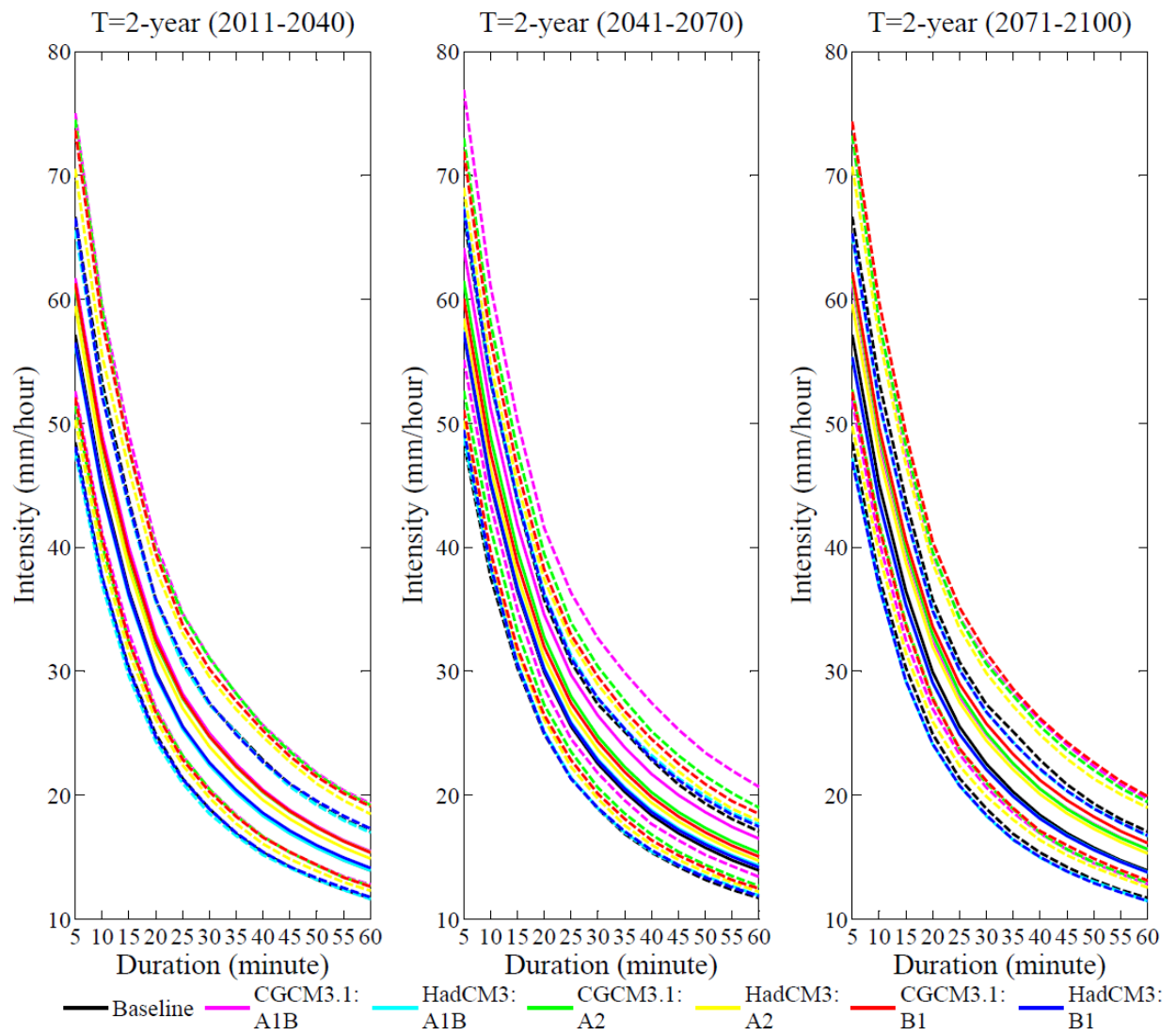
Figure F.12: Uncertainty in the projections of future extreme precipitation quantiles for 2-year return period based on two GCMs and three emission scenarios obtained from CMIP3 and quantified by using GEV shown as 95% confidence intervals (dashed lines).
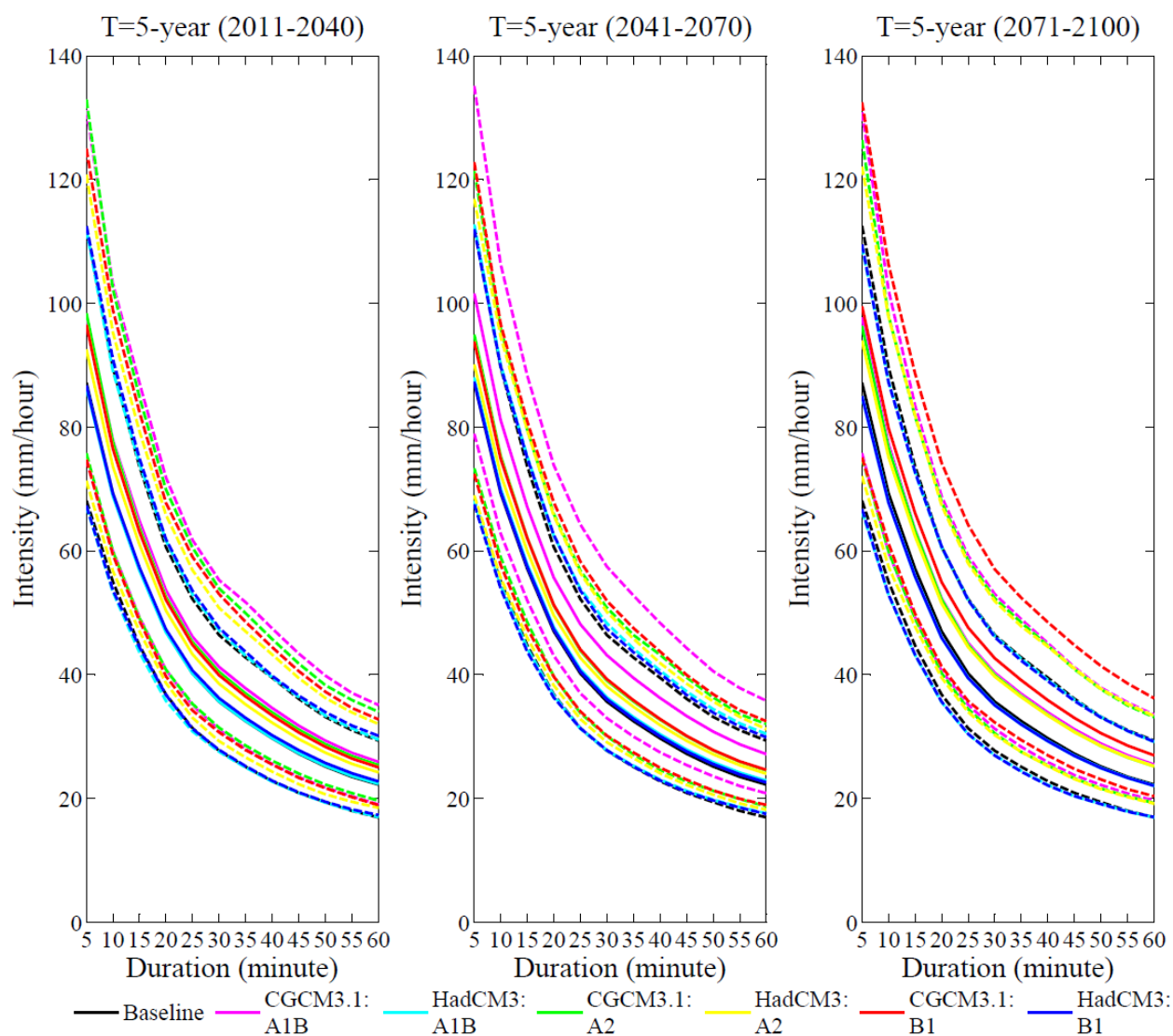
Figure F.13: Uncertainty in the projections of future extreme precipitation quantiles for 5-year return period based on two GCMs and three emission scenarios obtained from CMIP3 and quantified by using GEV shown as 95% confidence intervals (dashed lines).
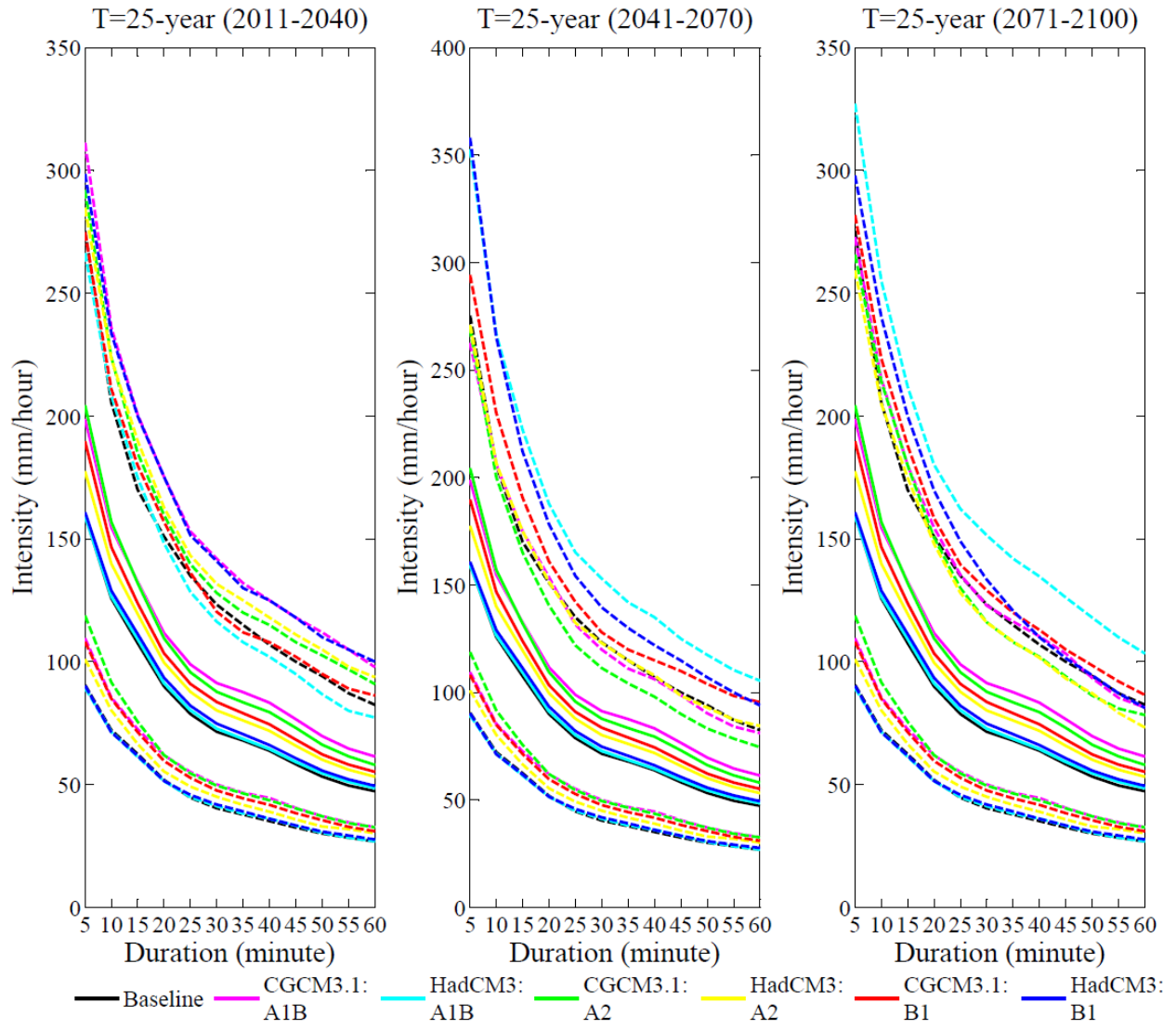
Figure F.14: Uncertainty in the projections of future extreme precipitation quantiles for 25-year return period based on two GCMs and three emission scenarios obtained from CMIP3 and quantified by using GEV shown as 95% confidence intervals (dashed lines).
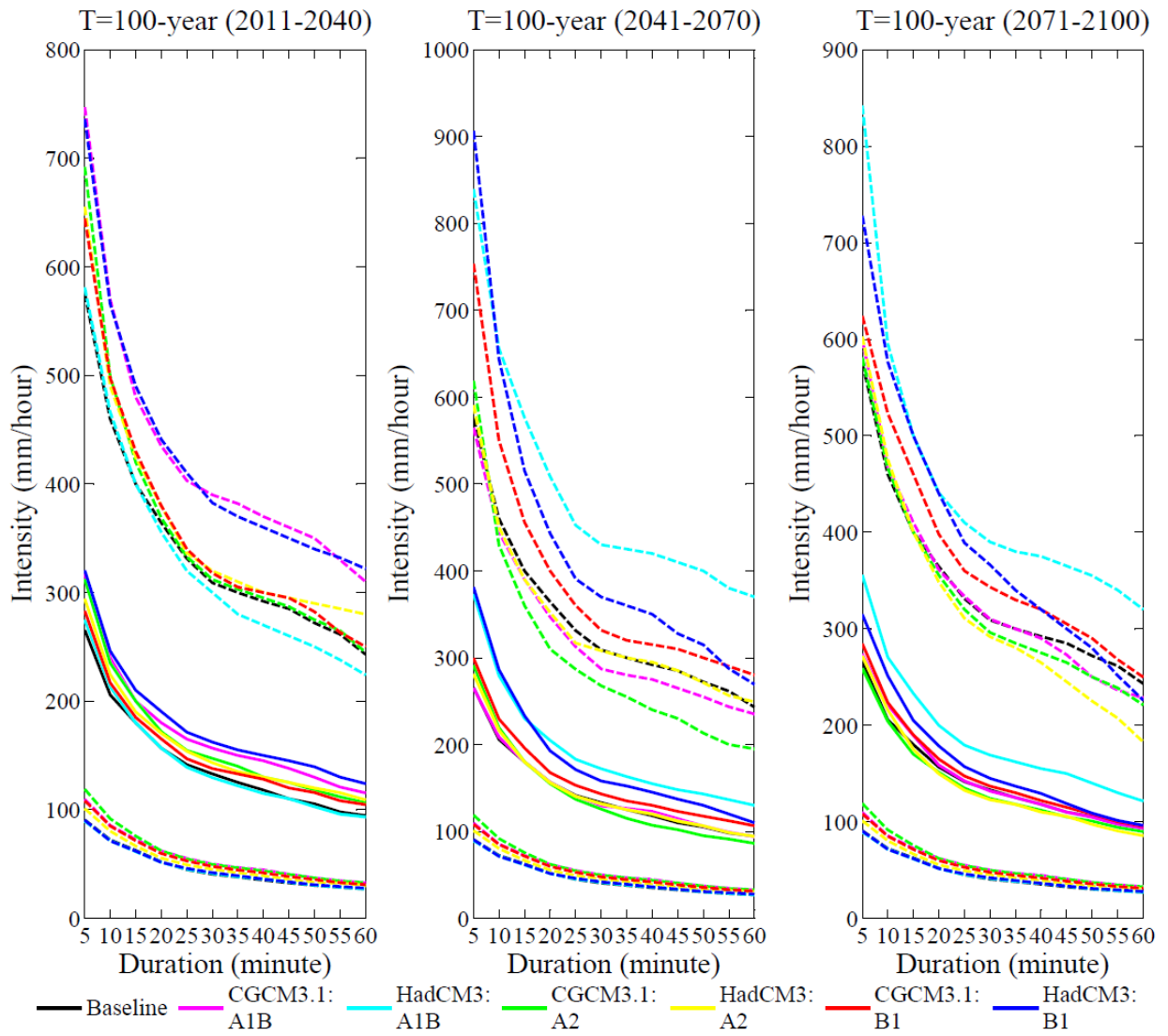
Figure F.15: Uncertainty in the projections of future extreme precipitation quantiles for 100-year return period based on two GCMs and three emission scenarios obtained from CMIP3 and quantified by using GEV shown as 95% confidence intervals (dashed lines).
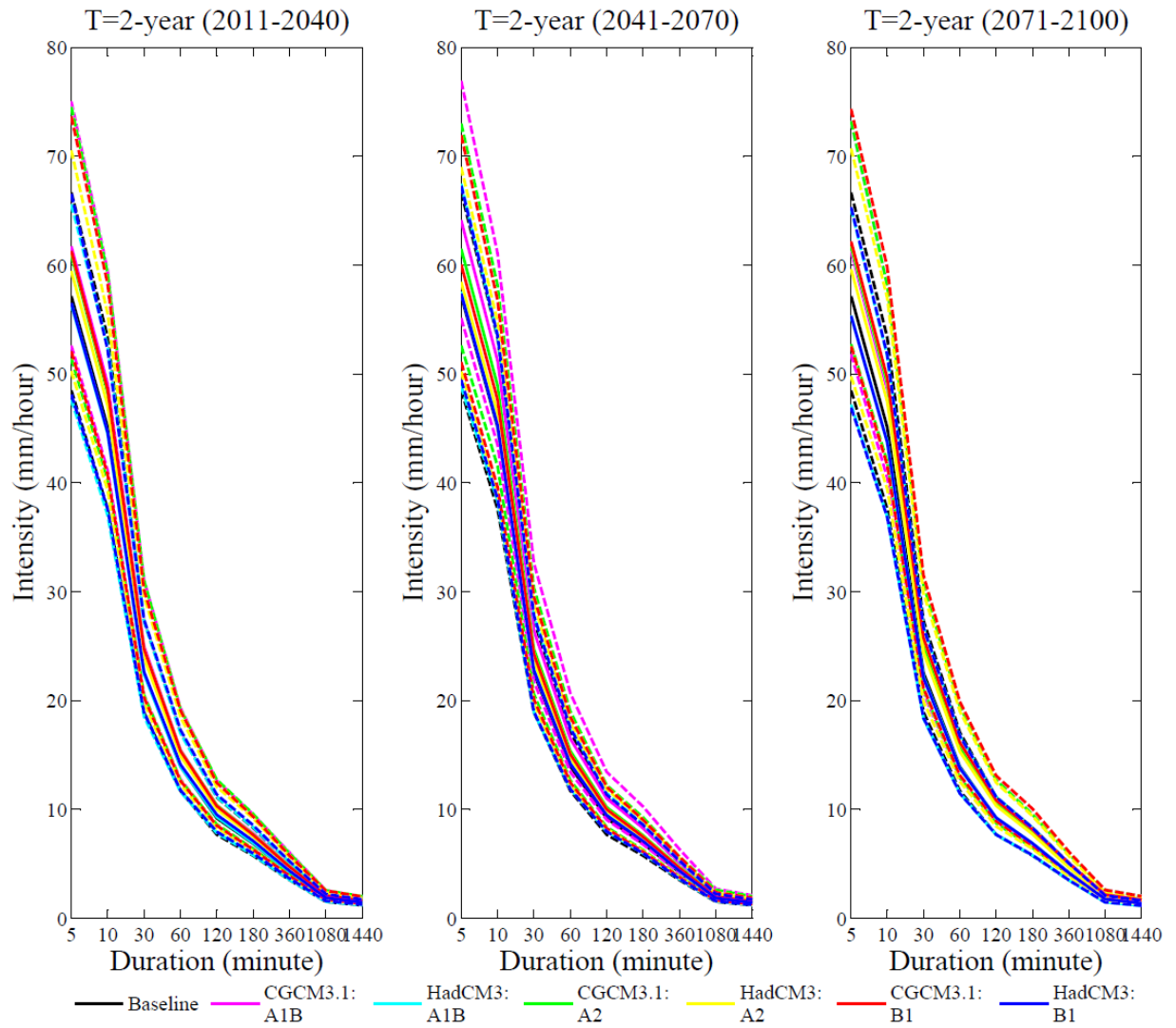
Figure F.16: Uncertainty in the projections of future extreme precipitation quantiles of durations from 5-min to 24-hour for 2-year return period based on two GCMs and three emission scenarios obtained from CMIP3 and quantified by using GEV shown as 95% confidence intervals (dashed lines).
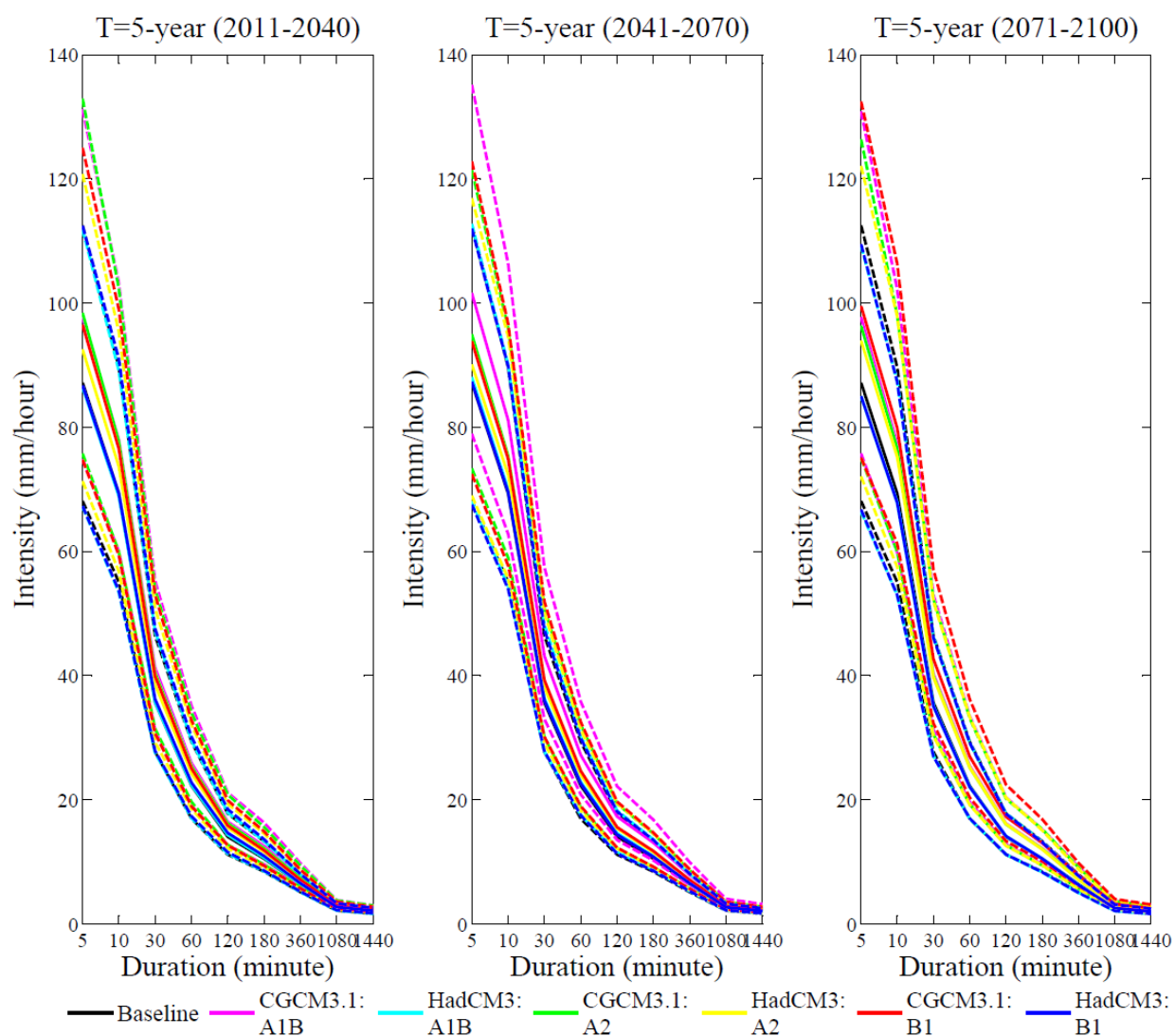
Figure F.17: Uncertainty in the projections of future extreme precipitation quantiles of durations from 5-min to 24-hour for 5-year return period based on two GCMs and three emission scenarios obtained from CMIP3 and quantified by using GEV shown as 95% confidence intervals (dashed lines).
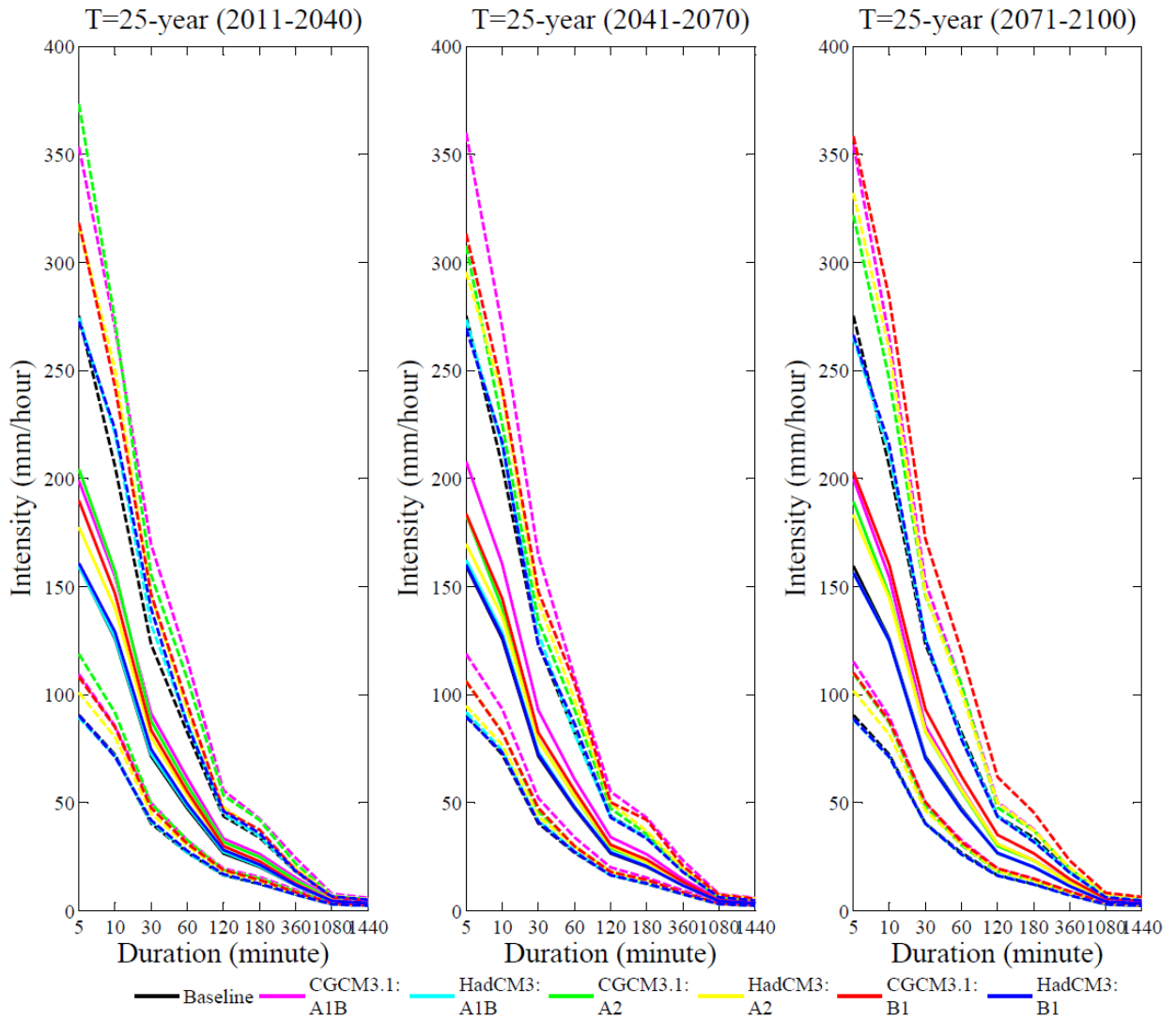
Figure F.18: Uncertainty in the projections of future extreme precipitation quantiles of durations from 5-min to 24-hour for 25-year return period based on two GCMs and three emission scenarios obtained from CMIP3 and quantified by using GEV shown as 95% confidence intervals (dashed lines).
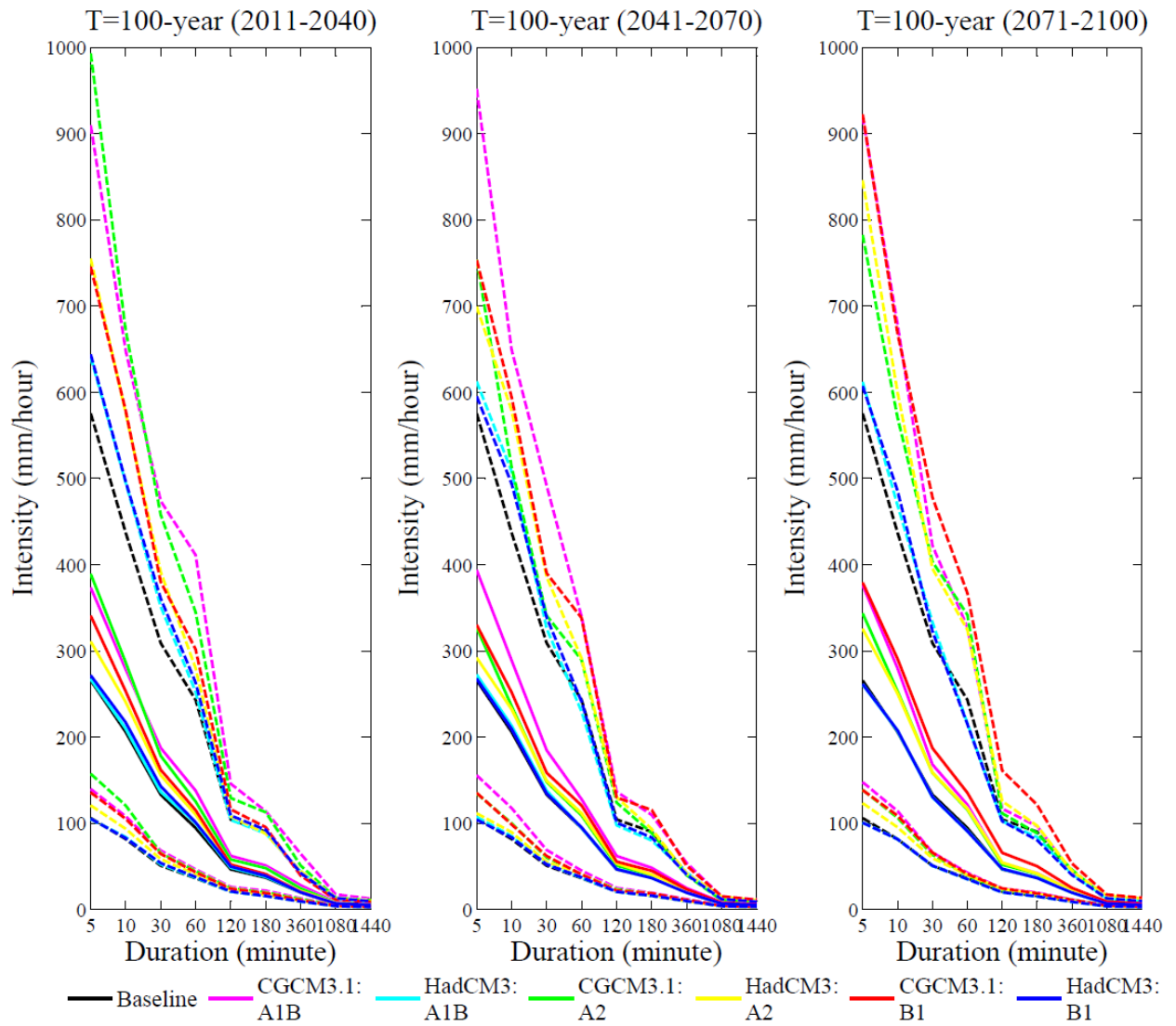
Figure F.19: Uncertainty in the projections of future extreme precipitation quantiles of durations from 5-min to 24-hour for 100-year return period based on two GCMs and three emission scenarios obtained from CMIP3 and quantified by using GEV shown as 95% confidence intervals (dashed lines).

F.5 Overall changes in the future IDF curves obtained from CMIP3 climate models

Table F.5: Historical and projected rainfall intensities based on two CMIP3 climate models (CGCM3.1 and HadCM3) and three emission scenarios for selected durations and return periods of storms in Saskatoon. Base means historical values, Min means the lowest of future projection, and Max is the highest value of future projections. The "bold" values represent the projected highest change.

Duration	Intensity (mm/hr)											
	2-year			5-year			25-year			100-year		
	Base	Min	Max	Base	Min	Max	Base	Min	Max	Base	Min	Max
5 min	57	55	64	87	85	102	159	156	**208**	265	261	**394**
15 min	37	35	42	57	56	67	108	107	**135**	183	184	**249**
1-hour	14	14	16	22	22	**27**	47	46	**62**	94	91	**138**
2-hour	9	9	**11**	14	14	**17**	27	27	**35**	46	46	**66**
6-hour	4	4	**5**	6	6	**8**	11	11	**15**	19	19	**28**
24-hour	1	1	**2**	2	2	**3**	3	3	**4**	5	5	**7**

Appendix G
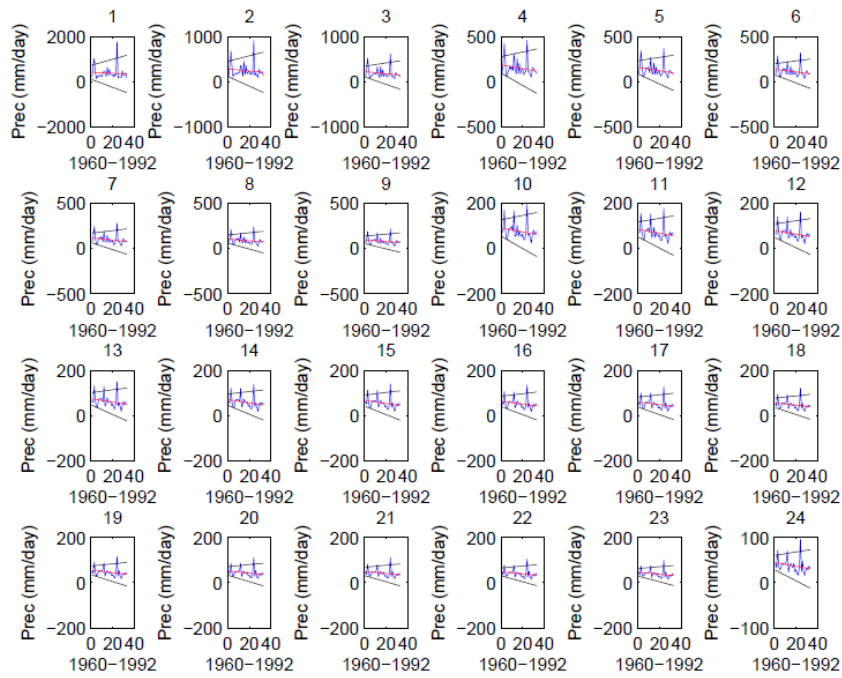
(a)
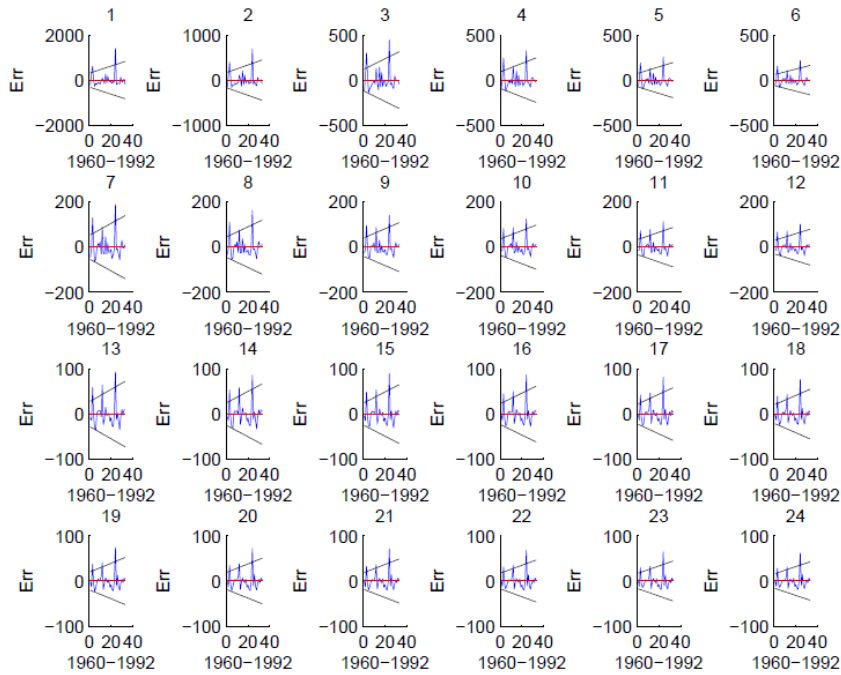
(b)

Figure G1. Performance of model L1; (a) best lines fitted to AMPs from 1-hr to 24-hr; (b) model residuals when fitted to Saskatoon's AMPs from 1-hr to 24-hr. Blue lines shows the original AMPs or associated errors. Black lines show the lower and upper bound limits for fitted lines or model residuals.
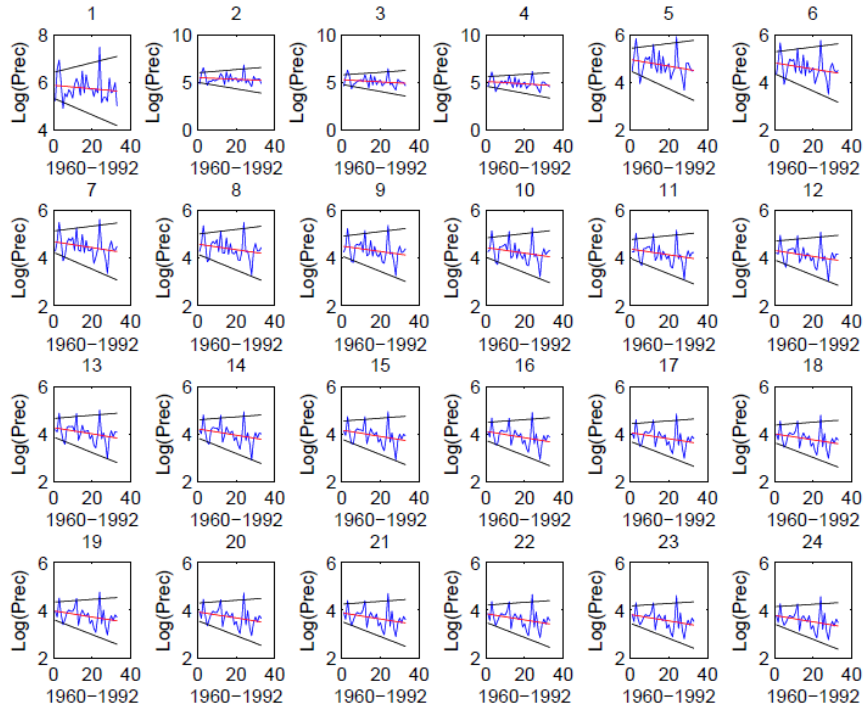
(a)
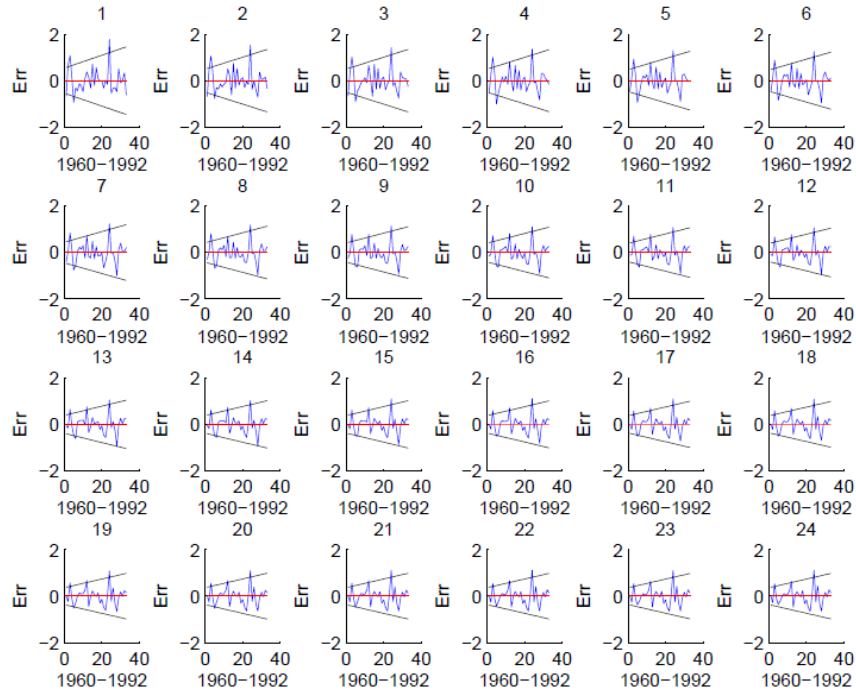
(b)

Figure G2. Performance of model L2; (a) best lines fitted to log-transformed AMPs from 1-hr to 24-hr; (b) model residuals when fitted to Saskatoon's log-transformed AMPs from 1-hr to 24-hr. Blue lines shows the log-transformed AMPs or associated errors. Black lines show the lower and upper bound limits for fitted lines or model residuals.
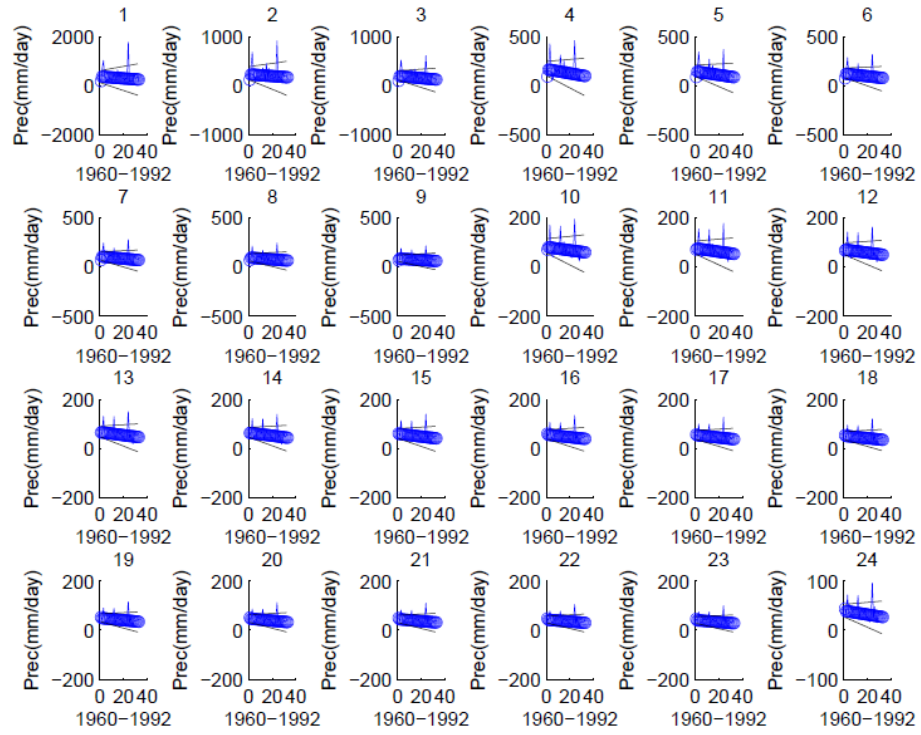
(a)
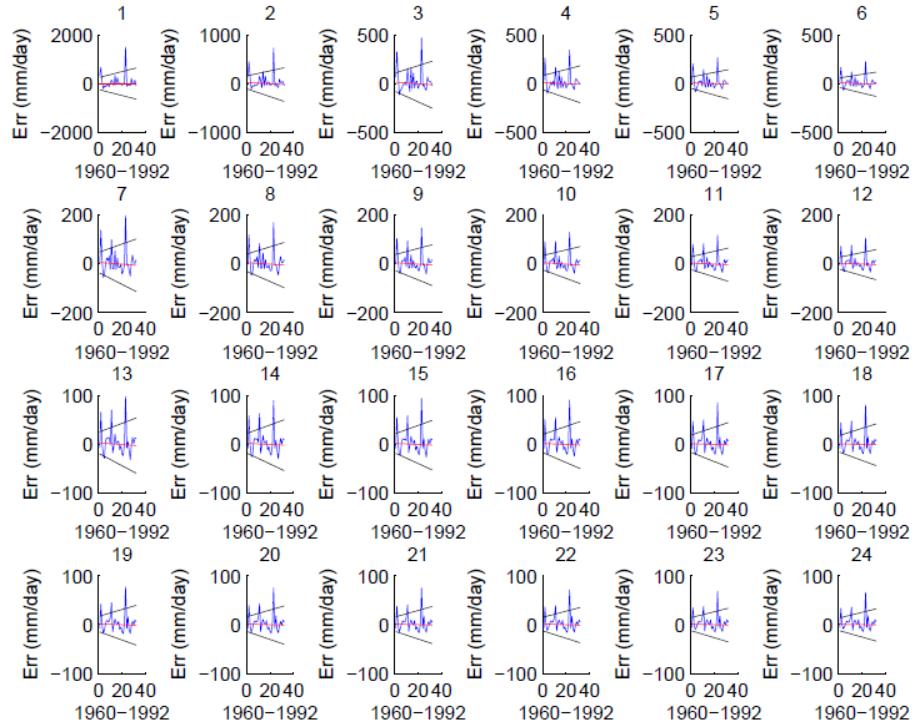
(b)

Figure G3. Performance of model L3; (a) best lines fitted to original AMPs from 1-hr to 24-hr; (b) model residuals when fitted to Saskatoon's original AMPs from 1-hr to 24-hr. Blue lines shows the original AMPs or associated errors. Black lines show the lower and upper bound limits for fitted lines or model residuals.

(a)

(b)
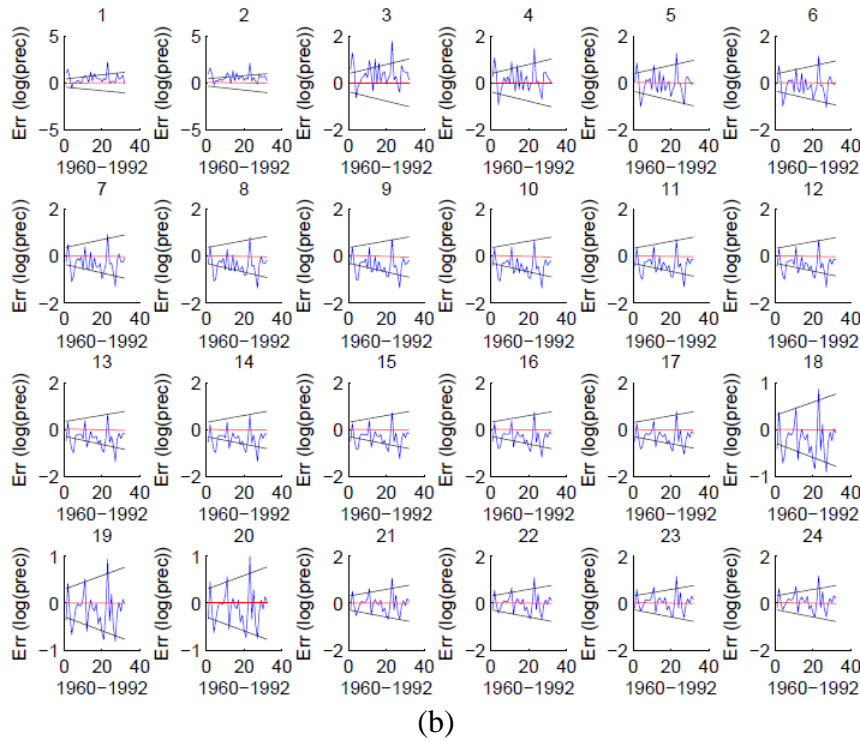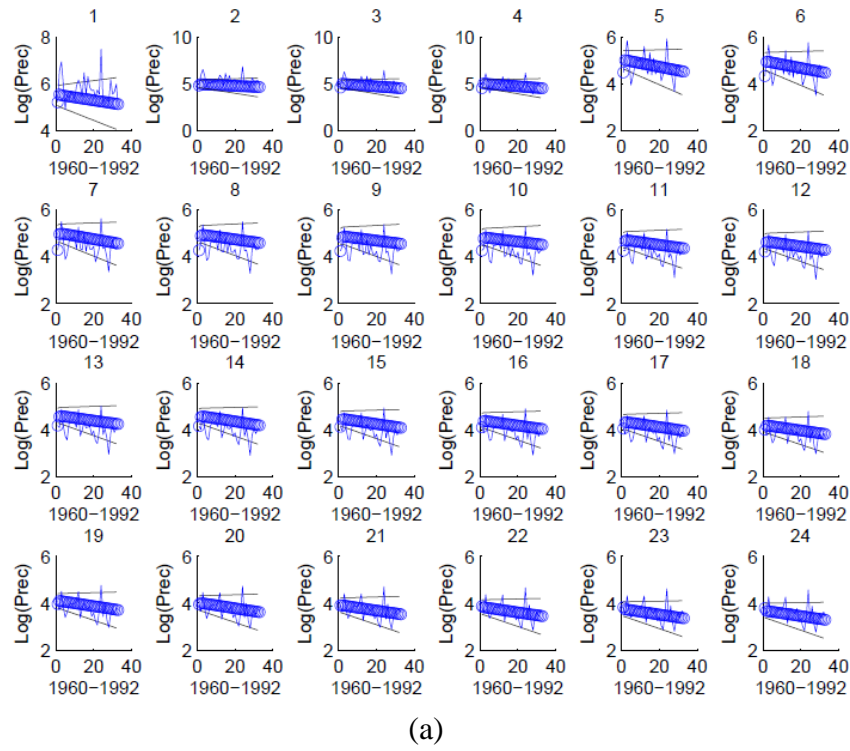
Figure G4. Performance of model L4; (a) best lines fitted to log-transformed AMPs from 1-hr to 24-hr; (b) model residuals when fitted to Saskatoon's log-transformed AMPs from 1-hr to 24-hr. Blue lines shows the original AMPs or associated errors. Black lines show the lower and upper bound limits for fitted lines or model residuals.
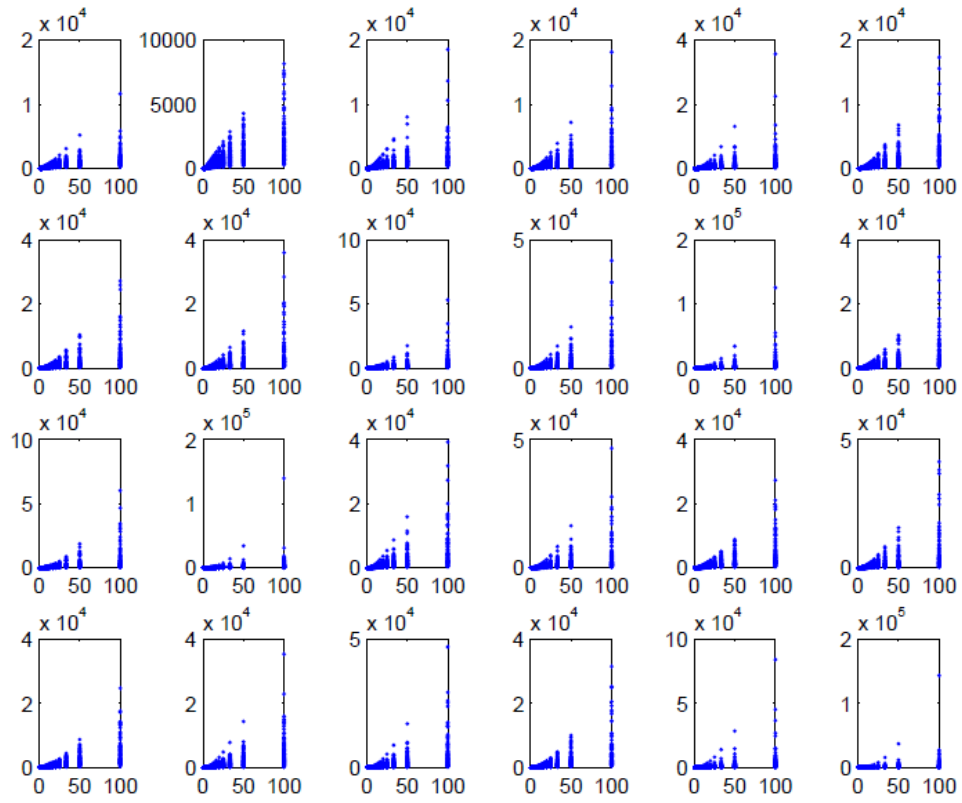
Figure G5. Future IDF curves (2021-2050) obtained by extending the historical trends using S2 model and generating random error terms with non-stationary variance – see Figure X7 for generated. The top left panel is related to 1-hr extremes and the bottom right panel is related to 24-hr.

Appendix H

Table H1. Lower bound, mean ensemble and upper bound values for Saskatoon's sub-daily extreme rainfall during 21st century according to projection of CanESM2 forced with RCP 2.6.

Extreme rainfall totals (mm); Lower bound – 0.025 non-exceedance probability																		
	1st control period (2011-2040)						2nd control period (2041-2070)						3rd control period (2011-2040)					
Duration	Return period (year)						Return period (year)						Return period (year)					
	2	5	10	25	50	100	2	5	10	25	50	100	2	5	10	25	50	100
1-hr	16.88	25.41	31.41	38.59	43.43	48.04	17.07	24.98	29.94	35.50	39.06	42.19	16.44	24.06	28.90	34.40	38.04	41.11
2-hr	19.34	28.71	35.42	43.41	48.99	54.04	19.50	28.39	33.99	40.10	44.35	47.89	18.78	27.35	32.83	38.67	42.33	45.84
3-hr	20.83	30.86	37.92	46.32	51.90	57.49	21.09	30.50	36.30	42.73	46.98	50.71	20.32	29.48	35.05	41.05	44.98	48.46
6-hr	23.36	34.33	41.97	51.03	57.58	63.72	23.76	33.99	40.28	47.26	51.78	55.61	23.03	32.75	38.77	45.22	49.38	53.18
12-hr	25.88	37.69	46.14	56.79	64.19	71.56	26.48	37.51	44.32	51.83	56.47	60.46	25.60	35.99	42.41	49.70	54.39	58.83
24-hr	29.07	42.00	50.96	64.03	73.98	83.70	29.91	41.73	49.30	56.58	61.37	65.53	28.87	39.71	47.19	55.51	60.70	65.12

Extreme rainfall totals (mm); Mean ensemble																		
	1st control period (2011-2040)						2nd control period (2041-2070)						3rd control period (2011-2040)					
Duration	Return period (year)						Return period (year)						Return period (year)					
	2	5	10	25	50	100	2	5	10	25	50	100	2	5	10	25	50	100
1-hr	20.56	31.98	42.14	59.42	76.85	99.86	20.31	30.54	39.09	52.81	65.89	82.28	19.73	29.85	38.50	52.68	66.49	84.13
2-hr	23.37	36.06	47.27	66.16	85.06	109.77	23.13	34.51	43.94	58.93	73.13	90.80	22.43	33.69	43.24	58.80	73.83	92.90
3-hr	25.17	38.59	50.36	70.08	89.74	115.43	24.94	36.95	46.82	62.41	77.07	95.23	24.20	36.10	46.17	62.45	78.09	97.78
6-hr	28.14	42.68	55.28	76.18	96.93	124.52	27.89	40.87	51.43	67.95	83.32	102.16	27.07	40.02	50.91	68.44	85.16	106.05
12-hr	31.08	46.66	59.97	81.68	102.64	129.13	30.74	44.65	55.92	73.43	89.60	109.24	29.79	43.72	55.43	74.21	92.02	114.13
24-hr	34.87	51.83	66.17	89.23	111.16	138.44	34.36	49.53	61.72	80.43	97.42	117.71	33.34	48.58	61.27	81.40	100.29	123.45

Extreme rainfall totals (mm); Upper bound – 0.975 non-exceedance probability																		
	1st control period (2011-2040)						2nd control period (2041-2070)						3rd control period (2011-2040)					
Duration	Return period (year)						Return period (year)						Return period (year)					
	2	5	10	25	50	100	2	5	10	25	50	100	2	5	10	25	50	100
1-hr	25.19	39.86	55.99	92.87	139.72	211.39	24.47	37.41	50.59	79.15	113.03	163.85	24.03	37.23	50.80	80.31	116.51	173.94
2-hr	28.61	44.92	62.17	101.79	151.62	231.15	27.55	41.93	56.56	87.79	125.69	181.87	27.20	41.82	56.67	88.33	127.53	187.51
3-hr	30.69	47.97	66.03	108.75	162.40	245.35	29.68	44.72	60.30	93.31	132.77	190.59	29.19	44.77	60.06	92.69	133.25	192.64
6-hr	34.20	52.80	71.81	116.10	171.77	255.96	33.03	49.28	65.32	99.24	139.29	198.53	32.43	49.29	65.51	99.03	140.22	199.32
12-hr	37.59	57.54	75.92	120.39	173.83	255.37	36.27	53.66	70.05	104.50	145.24	202.69	35.36	53.33	70.48	102.95	143.12	200.77
24-hr	41.95	63.45	81.42	123.43	173.14	244.68	39.86	59.28	76.44	110.44	149.40	203.96	39.48	58.64	76.35	110.59	154.69	216.94

Table H2. Lower bound, mean ensemble and upper bound values for Saskatoon's sub-daily extreme rainfall during 21st century according to projection of CanESM2 forced with RCP 4.5.

	Extreme rainfall totals (mm); Lower bound – 0.025 non-exceedance probability																	
	1st control period (2011-2040)						2nd control period (2041-2070)						3rd control period (2011-2040)					
Duration	Return period (year)						Return period (year)						Return period (year)					
	2	5	10	25	50	100	2	5	10	25	50	100	2	5	10	25	50	100
1-hr	17.00	25.50	31.45	38.19	42.77	46.81	17.28	25.06	29.85	35.01	38.52	41.44	17.31	25.35	30.36	35.60	38.83	41.31
2-hr	19.38	29.04	35.74	43.44	48.16	52.70	19.94	28.52	33.97	39.83	43.66	47.06	19.89	28.84	34.31	40.19	43.68	46.81
3-hr	21.06	31.42	38.44	46.62	51.98	56.74	21.75	30.90	36.49	42.84	46.91	50.35	21.68	31.26	37.09	43.12	47.06	50.31
6-hr	23.82	35.13	43.09	52.54	58.21	63.31	24.62	34.59	40.65	47.57	51.86	55.65	24.60	34.98	41.38	47.78	51.80	55.22
12-hr	26.42	38.81	47.78	57.97	64.65	70.37	27.47	38.04	44.69	52.32	57.31	61.67	27.43	38.65	45.00	51.74	55.88	59.34
24-hr	29.96	43.07	53.81	65.05	72.14	79.15	31.13	42.24	49.13	56.96	62.68	66.80	30.98	42.97	51.15	59.40	63.44	66.98

	Extreme rainfall totals (mm); Mean ensemble																	
	1st control period (2011-2040)						2nd control period (2041-2070)						3rd control period (2011-2040)					
Duration	Return period (year)						Return period (year)						Return period (year)					
	2	5	10	25	50	100	2	5	10	25	50	100	2	5	10	25	50	100
1-hr	21.21	32.41	41.80	56.89	71.28	89.32	21.04	31.14	39.17	51.49	62.75	76.37	20.74	30.73	38.74	51.12	62.52	76.43
2-hr	24.26	36.73	47.01	63.24	78.49	97.34	24.12	35.39	44.19	57.42	69.26	83.30	23.74	34.84	43.60	56.94	69.04	83.62
3-hr	26.29	39.49	50.21	66.88	82.29	101.09	26.19	38.13	47.32	60.93	72.94	87.01	25.73	37.48	46.64	60.40	72.74	87.47
6-hr	29.65	43.92	55.24	72.48	88.18	107.28	29.63	42.48	52.06	65.86	77.72	91.31	28.99	41.65	51.34	65.64	78.28	93.17
12-hr	33.01	48.24	60.00	77.45	92.85	110.89	33.08	46.69	56.45	70.05	81.35	93.94	32.16	45.65	55.80	70.57	83.43	98.42
24-hr	37.29	53.84	66.28	84.28	99.75	117.43	37.45	52.00	62.00	75.36	86.05	97.56	36.10	50.66	61.44	76.92	90.23	105.59

	Extreme rainfall totals (mm); Upper bound – 0.975 non-exceedance probability																	
	1st control period (2011-2040)						2nd control period (2041-2070)						3rd control period (2011-2040)					
Duration	Return period (year)						Return period (year)						Return period (year)					
	2	5	10	25	50	100	2	5	10	25	50	100	2	5	10	25	50	100
1-hr	25.78	39.57	53.79	84.40	121.72	177.34	24.99	37.32	49.16	73.36	102.17	143.50	24.69	37.17	49.35	74.70	104.76	148.55
2-hr	29.41	44.60	59.55	90.96	128.10	183.01	28.55	42.11	54.81	80.31	109.24	150.59	28.10	41.73	54.80	82.03	113.98	158.76
3-hr	31.82	47.63	62.77	94.18	131.76	186.55	30.96	45.05	57.73	83.55	112.67	153.60	30.34	44.75	58.34	85.67	117.27	160.99
6-hr	35.74	52.46	67.39	98.36	134.67	186.49	34.88	49.53	62.12	88.77	118.60	158.52	34.02	49.38	63.30	91.25	125.08	170.29
12-hr	39.80	56.98	71.21	101.11	135.79	185.66	38.93	53.94	65.81	91.22	118.75	155.80	37.39	53.56	67.83	98.32	133.43	182.39
24-hr	45.36	62.80	76.75	106.65	140.14	185.94	44.09	59.64	71.83	94.49	118.54	149.72	41.62	58.17	74.35	103.94	136.00	181.54

Table H3. Lower bound, mean ensemble and upper bound values for Saskatoon's sub-daily extreme rainfall during 21st century according to projection of CanESM2 forced with RCP 8.5.

	Extreme rainfall totals (mm); Lower bound – 0.025 non-exceedance probability																	
	1st control period (2011-2040)						2nd control period (2041-2070)						3rd control period (2011-2040)					
Duration	Return period (year)						Return period (year)						Return period (year)					
	2	5	10	25	50	100	2	5	10	25	50	100	2	5	10	25	50	100
1-hr	16.31	23.93	29.00	35.00	38.92	42.76	17.51	25.63	30.96	36.72	40.77	44.38	17.09	25.07	30.36	36.07	39.86	43.30
2-hr	18.57	27.06	32.75	39.43	43.61	47.45	20.05	29.18	34.96	41.31	45.38	49.15	19.67	28.64	34.29	40.71	44.79	48.43
3-hr	20.05	29.04	35.09	41.77	46.20	50.42	21.74	31.39	37.48	44.26	48.70	52.70	21.32	30.78	36.90	43.63	48.04	51.94
6-hr	22.52	32.26	38.52	46.04	51.02	55.61	24.53	34.97	41.34	48.87	53.32	57.54	24.04	34.32	40.93	48.44	52.79	56.81
12-hr	24.72	35.10	41.82	49.93	55.74	61.13	27.21	38.56	45.28	53.11	58.51	63.11	26.87	37.84	44.89	52.98	58.17	63.25
24-hr	27.66	38.83	46.01	55.13	61.76	67.97	30.48	43.06	50.26	58.82	64.99	70.61	30.16	42.04	49.97	59.61	66.20	71.56
	Extreme rainfall totals (mm); Mean ensemble																	
	1st control period (2011-2040)						2nd control period (2041-2070)						3rd control period (2011-2040)					
Duration	Return period (year)						Return period (year)						Return period (year)					
	2	5	10	25	50	100	2	5	10	25	50	100	2	5	10	25	50	100
1-hr	19.81	30.33	39.50	54.78	69.90	89.47	21.27	31.92	40.77	54.86	68.20	84.83	20.72	31.32	40.14	54.20	67.54	84.16
2-hr	22.51	34.19	44.26	60.90	77.23	98.22	24.27	36.13	45.88	61.23	75.61	93.32	23.70	35.49	45.17	60.41	74.68	92.28
3-hr	24.27	36.58	47.11	64.34	81.06	102.36	26.21	38.78	49.05	65.13	80.11	98.51	25.63	38.12	48.28	64.12	78.80	96.74
6-hr	27.11	40.38	51.63	69.85	87.38	109.54	29.38	42.98	54.01	71.15	87.01	106.34	28.82	42.34	53.20	69.92	85.23	103.76
12-hr	29.82	44.01	55.97	75.18	93.49	116.40	32.48	47.07	58.83	77.02	93.79	114.19	31.92	46.41	57.91	75.44	91.31	110.32
24-hr	33.40	48.82	61.61	81.86	100.83	124.14	36.39	52.23	64.87	84.23	101.86	123.08	35.74	51.46	63.80	82.37	98.95	118.48
	Extreme rainfall totals (mm); Upper bound – 0.975 non-exceedance probability																	
	1st control period (2011-2040)						2nd control period (2041-2070)						3rd control period (2011-2040)					
Duration	Return period (year)						Return period (year)						Return period (year)					
	2	5	10	25	50	100	2	5	10	25	50	100	2	5	10	25	50	100
1-hr	24.35	38.47	53.01	84.17	124.21	187.43	25.82	39.51	53.34	81.32	115.21	164.12	24.97	38.38	52.08	81.21	116.08	167.69
2-hr	27.70	43.08	58.72	92.77	135.28	199.75	29.33	44.46	59.53	90.30	127.09	180.60	28.49	43.23	57.93	89.25	125.29	177.94
3-hr	29.60	46.05	62.01	96.02	140.14	205.01	31.59	47.77	63.70	95.75	134.58	188.49	30.70	46.21	61.47	92.99	129.72	183.05
6-hr	33.02	50.20	66.35	101.61	144.90	209.11	35.20	52.58	69.32	102.55	142.90	202.01	34.31	50.88	66.81	100.41	139.25	195.89
12-hr	36.24	54.31	70.67	106.74	151.52	217.63	38.88	57.24	73.90	107.04	148.48	209.24	37.93	55.32	71.44	106.67	148.43	206.60
24-hr	39.91	59.93	75.62	112.19	159.80	227.30	43.40	62.56	79.55	115.50	158.10	218.95	42.33	60.57	77.93	114.36	153.03	205.91

Table H4. Lower bound, mean ensemble and upper bound values for Saskatoon's sub-daily extreme rainfall during 21st century according to projection of HadGEM2-ES forced with RCP 2.6.

	Extreme rainfall totals (mm); Lower bound – 0.025 non-exceedance probability																	
	1st control period (2011-2040)						2nd control period (2041-2070)						3rd control period (2011-2040)					
Duration	Return period (year)						Return period (year)						Return period (year)					
	2	5	10	25	50	100	2	5	10	25	50	100	2	5	10	25	50	100
1-hr	16.76	24.52	29.65	35.14	38.76	41.88	19.26	28.81	35.07	42.17	46.72	50.98	16.50	24.07	28.95	34.34	37.89	41.09
2-hr	19.26	28.01	33.59	39.64	43.49	46.49	21.94	32.97	40.06	47.66	52.37	56.90	18.85	27.32	32.66	38.61	42.41	45.84
3-hr	20.90	30.25	36.10	42.47	46.51	50.01	23.78	35.62	43.23	51.38	56.72	61.28	20.47	29.33	35.02	41.18	45.34	49.10
6-hr	23.71	34.02	40.62	47.66	52.17	56.24	26.95	39.80	47.98	57.59	63.82	69.35	23.07	32.67	38.79	45.32	49.75	53.94
12-hr	26.36	37.24	44.60	52.60	57.78	62.22	30.05	43.79	52.83	63.69	70.98	77.86	25.65	35.92	42.44	49.66	54.65	58.84
24-hr	29.68	40.93	48.70	59.09	65.19	70.16	33.96	48.02	58.22	70.92	80.40	89.12	28.85	39.80	47.32	55.65	60.68	65.00
	Extreme rainfall totals (mm); Mean ensemble																	
	1st control period (2011-2040)						2nd control period (2041-2070)						3rd control period (2011-2040)					
Duration	Return period (year)						Return period (year)						Return period (year)					
	2	5	10	25	50	100	2	5	10	25	50	100	2	5	10	25	50	100
1-hr	20.70	30.91	39.25	52.35	64.62	79.78	23.94	36.10	46.21	62.32	77.62	96.79	19.78	29.91	38.55	52.70	66.48	84.10
2-hr	23.70	35.06	44.18	58.31	71.39	87.45	27.42	40.97	52.03	69.34	85.45	105.18	22.46	33.69	43.20	58.60	73.42	92.13
3-hr	25.69	37.73	47.29	61.91	75.29	91.56	29.73	44.08	55.63	73.49	89.89	109.81	24.21	36.10	46.12	62.25	77.67	96.98
6-hr	28.93	41.92	51.98	67.00	80.35	96.11	33.48	48.98	61.19	79.65	96.23	115.91	27.07	39.95	50.74	68.04	84.46	104.92
12-hr	32.08	45.88	56.30	71.47	84.57	99.61	37.16	53.66	66.38	85.20	101.72	120.92	29.79	43.65	55.25	73.79	91.29	112.94
24-hr	36.00	50.87	61.78	77.17	90.07	104.45	41.66	59.48	72.97	92.60	109.54	128.93	33.34	48.52	61.09	80.92	99.39	121.90
	Extreme rainfall totals (mm); Upper bound – 0.975 non-exceedance probability																	
	1st control period (2011-2040)						2nd control period (2041-2070)						3rd control period (2011-2040)					
Duration	Return period (year)						Return period (year)						Return period (year)					
	2	5	10	25	50	100	2	5	10	25	50	100	2	5	10	25	50	100
1-hr	25.38	38.59	50.88	77.77	110.40	158.84	29.24	44.09	59.16	91.92	131.14	188.67	24.02	37.29	51.20	80.77	116.74	171.12
2-hr	28.92	43.50	57.34	85.60	120.76	171.02	33.36	49.60	65.75	100.43	140.54	199.03	27.17	41.77	56.67	88.13	126.90	185.19
3-hr	31.22	46.55	60.84	90.41	125.15	176.67	36.11	53.06	69.43	103.69	143.35	200.66	29.19	44.69	60.33	92.47	131.54	189.52
6-hr	35.07	51.40	65.49	94.59	128.77	175.77	40.69	58.53	74.84	109.43	149.04	204.38	32.41	49.29	65.53	99.17	139.20	197.99
12-hr	38.88	56.14	69.88	98.32	128.92	171.04	45.58	63.71	79.58	113.85	152.22	206.60	35.41	53.53	70.26	103.09	142.73	199.39
24-hr	43.88	62.15	75.07	100.72	128.36	165.46	51.83	70.30	85.50	120.91	159.45	211.09	39.45	58.80	76.32	110.48	151.69	210.43

Table H5. Lower bound, mean ensemble and upper bound values for Saskatoon's sub-daily extreme rainfall during 21st century according to projection of HadGEM2-ES forced with RCP 4.5.

	Extreme rainfall totals (mm); Lower bound – 0.025 non-exceedance probability																	
	1st control period (2011-2040)						2nd control period (2041-2070)						3rd control period (2011-2040)					
Duration	Return period (year)						Return period (year)						Return period (year)					
	2	5	10	25	50	100	2	5	10	25	50	100	2	5	10	25	50	100
1-hr	17.18	25.44	30.77	37.01	40.96	44.62	17.81	25.97	30.91	36.20	39.42	42.11	18.39	26.65	31.68	36.75	39.72	42.24
2-hr	19.64	28.92	34.76	41.56	45.91	49.98	20.51	29.72	35.15	40.77	43.99	46.91	21.24	30.49	36.02	41.49	44.91	47.53
3-hr	21.30	31.06	37.37	44.54	49.34	53.54	22.32	32.07	37.92	43.65	47.06	49.95	23.15	33.07	38.96	45.11	48.77	51.71
6-hr	24.00	34.67	41.61	49.56	54.59	59.20	25.37	35.95	42.46	48.92	53.04	56.45	26.31	37.36	43.74	50.07	53.78	56.57
12-hr	26.51	37.89	45.67	53.72	58.56	63.27	28.15	39.72	46.83	54.15	58.47	62.34	29.41	41.53	48.22	54.41	57.53	60.11
24-hr	30.19	42.22	50.74	57.62	61.63	65.49	31.52	44.41	52.89	61.19	66.10	70.78	32.81	46.47	53.61	60.31	63.60	66.47
	Extreme rainfall totals (mm); Mean ensemble																	
	1st control period (2011-2040)						2nd control period (2041-2070)						3rd control period (2011-2040)					
Duration	Return period (year)						Return period (year)						Return period (year)					
	2	5	10	25	50	100	2	5	10	25	50	100	2	5	10	25	50	100
1-hr	21.00	31.91	41.03	55.66	69.61	87.12	21.31	31.30	39.24	51.40	62.50	75.89	21.93	32.03	39.75	51.14	61.16	72.85
2-hr	23.96	36.07	46.06	61.85	76.69	95.06	24.42	35.51	44.16	57.12	68.69	82.37	25.19	36.43	44.85	57.01	67.50	79.54
3-hr	25.91	38.72	49.15	65.43	80.53	98.95	26.46	38.20	47.22	60.57	72.35	86.14	27.38	39.31	48.12	60.69	71.38	83.53
6-hr	29.10	42.95	54.02	70.96	86.35	104.77	29.80	42.45	51.93	65.66	77.49	91.05	30.96	43.84	53.12	66.06	76.84	88.84
12-hr	32.19	47.03	58.75	76.48	92.43	111.36	33.04	46.49	56.40	70.50	82.46	96.01	34.42	48.09	57.73	70.91	81.66	93.44
24-hr	36.06	52.19	64.84	83.92	101.09	121.55	37.02	51.59	62.14	76.90	89.18	102.82	38.42	53.09	63.22	76.81	87.72	99.47
	Extreme rainfall totals (mm); Upper bound – 0.975 non-exceedance probability																	
	1st control period (2011-2040)						2nd control period (2041-2070)						3rd control period (2011-2040)					
Duration	Return period (year)						Return period (year)						Return period (year)					
	2	5	10	25	50	100	2	5	10	25	50	100	2	5	10	25	50	100
1-hr	25.43	39.19	53.26	83.71	119.25	171.61	25.58	38.01	49.78	74.23	102.86	143.36	26.14	38.31	49.71	71.96	96.93	132.30
2-hr	29.00	44.14	59.11	91.08	128.66	184.57	29.25	42.75	55.29	80.54	108.81	148.51	29.91	43.32	55.25	78.40	103.96	139.29
3-hr	31.22	47.17	62.59	94.92	132.44	188.10	31.54	45.83	58.63	83.81	112.60	152.06	32.52	46.48	58.75	82.16	108.43	143.81
6-hr	35.00	52.08	67.80	100.12	137.80	190.65	35.35	50.44	63.43	89.05	116.64	154.60	36.51	51.41	63.92	88.02	114.79	150.01
12-hr	38.51	56.66	73.19	106.05	142.95	195.21	39.08	54.76	67.88	93.99	123.27	163.95	40.38	55.92	68.25	92.86	119.88	154.20
24-hr	43.26	62.15	80.61	116.66	156.75	212.65	43.81	60.46	74.15	100.29	129.00	167.59	45.41	62.37	73.56	100.32	130.19	168.80

Table H6. Lower bound, mean ensemble and upper bound values for Saskatoon's sub-daily extreme rainfall during 21st century according to projection of HadGEM2-ES forced with RCP 8.5.

Extreme rainfall totals (mm); Lower bound – 0.025 non-exceedance probability																		
	1st control period (2011-2040)						2nd control period (2041-2070)						3rd control period (2011-2040)					
Duration	Return period (year)						Return period (year)						Return period (year)					
	2	5	10	25	50	100	2	5	10	25	50	100	2	5	10	25	50	100
1-hr	16.34	23.92	28.95	34.83	38.83	42.85	17.54	25.66	30.66	36.56	40.40	43.77	17.10	24.98	30.17	35.96	39.54	42.94
2-hr	18.65	26.98	32.48	38.80	42.87	46.82	20.12	29.19	34.92	41.14	45.25	48.74	19.64	28.43	34.18	40.70	44.68	48.37
3-hr	20.12	28.94	34.72	41.32	45.98	50.07	21.80	31.42	37.40	43.75	48.06	51.94	21.30	30.72	36.75	43.41	47.95	51.64
6-hr	22.56	32.12	38.33	45.61	50.98	55.67	24.56	35.08	41.30	48.25	53.11	57.22	24.15	34.35	40.91	48.06	52.69	57.02
12-hr	24.79	35.07	41.67	49.74	55.68	61.27	27.23	38.43	45.05	52.76	58.02	62.74	26.87	37.84	44.83	52.89	58.09	62.63
24-hr	27.62	38.75	45.94	55.22	61.84	67.74	30.40	42.86	50.03	58.83	65.05	70.86	30.16	42.12	49.96	59.57	66.02	71.33
Extreme rainfall totals (mm); Mean ensemble																		
	1st control period (2011-2040)						2nd control period (2041-2070)						3rd control period (2011-2040)					
Duration	Return period (year)						Return period (year)						Return period (year)					
	2	5	10	25	50	100	2	5	10	25	50	100	2	5	10	25	50	100
1-hr	19.85	30.39	39.56	54.81	69.89	89.43	21.26	31.91	40.78	54.95	68.42	85.26	20.72	31.30	40.10	54.13	67.44	84.04
2-hr	22.56	34.22	44.27	60.81	76.99	97.75	24.27	36.12	45.87	61.25	75.70	93.55	23.69	35.49	45.18	60.45	74.74	92.37
3-hr	24.32	36.62	47.14	64.31	80.97	102.14	26.21	38.75	48.99	65.05	80.03	98.45	25.64	38.14	48.31	64.17	78.88	96.85
6-hr	27.14	40.40	51.63	69.79	87.26	109.33	29.35	42.92	53.91	71.00	86.80	106.08	28.81	42.35	53.24	70.05	85.49	104.22
12-hr	29.83	44.02	55.96	75.12	93.33	116.03	32.45	47.00	58.74	76.90	93.60	113.88	31.94	46.44	57.96	75.53	91.47	110.61
24-hr	33.40	48.81	61.60	81.82	100.76	124.01	36.35	52.17	64.82	84.26	102.05	123.56	35.73	51.45	63.80	82.38	98.96	118.48
Extreme rainfall totals (mm); Upper bound – 0.975 non-exceedance probability																		
	1st control period (2011-2040)						2nd control period (2041-2070)						3rd control period (2011-2040)					
Duration	Return period (year)						Return period (year)						Return period (year)					
	2	5	10	25	50	100	2	5	10	25	50	100	2	5	10	25	50	100
1-hr	24.48	38.24	52.51	83.78	122.76	183.49	25.80	39.37	53.63	83.16	118.60	171.09	25.00	38.36	52.08	81.06	115.75	165.99
2-hr	27.62	43.06	58.36	92.39	134.22	199.31	29.32	44.37	59.73	91.33	127.14	182.63	28.53	43.34	58.06	89.69	126.30	180.87
3-hr	29.65	45.82	61.54	96.40	139.38	205.35	31.62	47.61	63.69	95.93	134.27	190.37	30.70	46.27	61.37	93.79	130.06	182.76
6-hr	33.11	50.20	66.26	101.00	143.70	208.02	35.22	52.34	69.08	102.31	140.94	198.33	34.30	50.91	66.73	100.60	140.90	199.17
12-hr	36.40	54.38	70.36	106.12	149.96	216.94	38.78	57.06	73.85	107.33	147.66	205.87	37.97	55.21	71.75	107.69	149.23	207.99
24-hr	39.93	59.99	75.38	112.13	159.34	229.77	43.41	62.65	79.83	117.12	160.25	223.16	42.38	60.61	77.69	114.75	153.33	207.34

Abbreviations

AAFC-WG	Agriculture and Agri-Food Canada Weather Generator
ACCESS1.0	Australian Community Climate and Earth-System Simulator 1.0
AMP	Annual Maximum Precipitation
ANN	Artificial Neural Network
AOGCM	Atmospheric Ocean General Circulation Model
AR4	Fourth Assessment Report
AR5	Fifth Assessment Report
BCCCSM1.1	Beijing Climate Center Climate System Model 1.1
CanESM2	Second generation Canadian Earth System Model
CDCD	Canadian Daily Climate Data
CESM1-BGC	Community Earth System Model, version 1-Biogeochemistry
CGCM3	The third generation Coupled Global Climate Model
CHRM	Climate High Resolution Model
CMIP3	Coupled Model Intercomparison Project, phase 3
CMIP5	Coupled Model Intercomparison Project, phase 5
CO_2	Carbon dioxide
CRCM	Canadian Regional Climate Model
CSIRO-Mk3.6.0	Commonwealth Scientific and Industrial Research Organization, Mk3.6.0 version
ECDF	Empirical Cumulative Distribution Function
ESM	Earth System Model
GCM	Global Climate Model
GEV	Generalized Extreme Value
GLM	Generalized Linear Model
GLM-WG	Generalized Linear Model-based Weather Generator
GP	Genetic Programming
GSR	Genetic Symbolic Regression
HadCM3	Hadley Centre Coupled Model, version 3
HadGEM2-ES	The Earth System configuration of the Hadley Centre Global Environmental Model, version 2
HadRM	Hadley Center Regional Model
IAM	Integrated Assessment Model
IDF	Intensity-Duration-Frequency
INM-CM4	Institute of Numerical Mathematics Climate Model, version 4.0
IPCC	Intergovernmental Panel on Climate Change
K-NN	K-Nearest Neighbor
LARS-WG	Long Ashton Research Station Weather Generator
MARE	Mean Absolute Relative Error
MB	Mean Bias
MIROC-ESM	Model for Interdisciplinary Research on Climate-Earth System Model
MM5	Fifth Generation Pennsylvania State University/National Center for Atmospheric Research Mesoscale Model
MRI-CGCM3	Meteorological Research Institute-third generation Coupled Global Climate Model
PCMDI	Program for Climate Model Diagnosis and Intercomparison
R	Pearson's correlation coefficient
RCF	Relative Change Factor
RCM	Regional Climate Model

RCP   Representative Concentration Pathway
RegCM   Regional Climate Model System
RMSE   Root Mean Squared Error
SDSM   Statistical Downscaling Method
SED   Semi-Empirical Distribution
SRES   Special Report on Emission Scenarios
WGEN   Weather Generator
WG-PCA   K-NN Weather Generator with Principal Component Analysis